Radar remote sensing of a semi-arid environment: a case study in central tunisia.

Stone, Rosemary Jane

Radar Remote Sensing of a Semi-arid Environment: A Case Study in Central Tunisia.

In two volumes.

Volume 1.

By

Rosemary Jane Stone B.Sc. A.K.C.

Thesis submitted for the degree
of Doctor of Philosophy,
University of Durham.

Department of Geography

December 1988

Radar Remote Sensing of a Semi-arid Environment: A Case Study in Central Tunisia.

Abstract

This work examines the potential of spaceborne microwave remote sensing for the discrimination and analysis of morphological and surface cover-features in semi-arid Tunisia. The study area in central Tunisia comprises a region of overlap between two satellite radar passes: namely Seasat and SIR-A. This allows the influence of two different radar depression angles, look directions and resolutions upon image appearance to be determined. Both these systems operated at a wavelength of 23cm and hence the characteristic responses of semi-arid surfaces at this wavelength are assessed. This is achieved through visual and digital image interpretation and discriminant analysis of image data.

As SIR-A data is available only in optical format, the image had to be digitised before digital image processing could be undertaken. Several radiometric and geometric pre-processing procedures have to be accomplished.

Despite the time-lag and calibration difficulties involved, the dominant ground controls on radar backscatter are identified through statistical analysis of information collected in the field. Surface relief, feature geometry and surface roughness are the most important parameters for both systems. The difference in depression angle causes relief information to dominate the Seasat image, while roughness information dominates the SIR-A image.

The availability of Landsat Thematic Mapper data for part of the SIR-A swath west of the coastal study area provides a valuable opportunity to assess the complementary nature of data from the visible, infra-red and microwave parts of the electromagnetic spectrum. This is examined through digital and statistical analysis of image data. In the mountain environments, slope angle and aspect are found to be the dominant parameters influencing SIR-A backscatter through their effect on local radar incidence angle.

The special quality of radar is its sensitivity to relief and roughness information. This is exploited in a number of applied studies that assess the contributions of radar to environmental management in semi-arid areas. Finally, recommendations are made for future research in the light of the multi-parameter radar systems due to be launched in the 1990s.

Declaration

This thesis is the result of my own work undertaken in the Department of Geography, University of Durham. It has not been accepted in partial or complete fulfilment of any other degree or professional qualification. All information taken from, or provided by, other authors is credited to them at the appropriate place in the text.

Statement of Copyright.

Radar Remote Sensing of a Semi-arid Environment: A Case Study in Central Tunisia.

Contents of Volume 1

Page

Page

Page

Page

Contents of Volume 2

List of Figures.

Page

Page

Page

Chapter 9.

List of Tables.

Page

Page

Page

List of Plates.

(All plates can be found in Volume 2 of this thesis.)

Page

Chapter 2.

Page

Page

Page

Page

Page

Page

Page

Chapter 7.

Acknowledgements.

Financial support for this research came from the Natural Environment Research Council under research studentship GT4/84/GS/22.

I would like to express my gratitude to Dr Ray Harris for his supervision during the first two years of this research project and for his continued interest after his departure from Durham. Many thanks go to Dr Ian Evans for taking me on and offering me so much help, support and encouragement during the later stages of this work.

I would like to thank John Ford (JPL) and Philip Rebillard (SEP) for the Seasat and SIR-A imagery and Nigel Gammage of Joyce Loebl Ltd. for his help with the SIR-A digitization. Many thanks go to Angela Morrison, Alison Reed and the rest of the NERC image analysis team for their cheerful assistance during my image processing marathons at Swindon, Wallingford and Keyworth.

Many thanks go to Dr Alois Sieber, Dr Rupert Haydn and Dr Barbara Theilen-Willige for all the help and advice they gave me during my European Remote Sensing tour in 1985. Sincere thanks go to Barbara for her spontaneous hospitality and understanding.

I am grateful to Professor John Townshend and Dr Andy Millington of the Department of Geography at Reading University for allowing me to join their expedition to Tunisia in 1986. Without their help I would never have been able to visit many of my field areas. My thanks go to Pam Kennedy and Kevin White of Reading University for their assistance in the field and to Sinclair Sutherland of Durham University for his cheerful company in the hills and valleys around Hadjeb el Ayoun. I am grateful to Ali Hamza of the Tunisian Ministry of Agriculture for all his support during my time in Tunisia and to the staff at the Tunisian Meteorological Office and the Office of Aerial Surveys.

My thanks go to Joan Dorril and Mike Alexander for setting my on the right path in the soils laboratory. I shall always be endebted to Bob Nelson for picking up the pieces on that Sunday afternoon in July 1986 and to all those who cared for me during my absence from Durham.

I would like to thank Peter Dodds, Bob Nelson, Danny Donoghue, Dr Tim Munday and Richard Leaver for their help and advice, particularly on the computing front. I am grateful to Alam for letting me use his GIMMS programmes for the calculation of soil loss. My sincere thanks go to Peter for making me smile!

Many people have helped me with the production of this thesis and I am most grateful to all of them. My thanks go to William Reed, Catherine Reed and Joyce Carse for typing the manuscript and to my Mother, Norma Stone, for coping so valiantly with the tables. I am very grateful to my parents and to Phil for proof reading the text. I would like to thank Linda Scott, Derek Hudspeth and Andrew Hudspeth for the long hours they have had to spend in the dark room on my behalf. Finally, I want to express my gratitude to Alison for letting me take over her word processor for so many hours.

I am grateful to the Overseas Section of the Transport and Road Research Laboratory for offering me a future in Applied Remote Sensing.

A big 'thank you' goes to Tony, Alison, Alam, Sinclair, Carl, Bill, Susan, Phil, Jane and Annabel and to all my friends who have worked so hard to keep me sane. Sincere thanks go to Professor John Pugh and to Wilf and Betty Dodd for their cheerful encouragement. Thank you, Tony, for helping me find the greatest gift of all!

The biggest 'thank you' goes to my parents, who have lovingly supported me through all my ups and downs. I could never have done it without them.

Glossary of Arabic Words Used in the Thesis.

CHOTT = Salt marsh or lake.

DJEBEL = Mountain range.

KEF = Cliff.

OUED = Wadi or river bed.

SAHEL = Coast or shore.

SEBKHA = Salt lake (often dry).

SIDI = Master (usually a prefix to a Holy man's name).

Chapter 1. Introduction.

Satellite radar remote sensing provides the environmental scientist with a valuable new tool for the identification and assessment of earth surface features and land cover types. Data generated by a radar system is dependent upon the interaction of the radar signal with the surface, and is influenced largely by the geometry of that surface at the macro- and micro-scale, together with surface dielectric properties (see Chapter 3). However, due to the inherent differences between radar data and imagery from conventional systems such as aerial surveys and the Landsat satellites, the full information content of radar imagery is only poorly understood.

A review of microwave remote sensing techniques for land surface and hydrological applications, prepared for the Natural Environment Research Council in 1984, concluded:

> "... the level of understanding of the qualitative information content of remotely sensed microwave data is currently inadequate." (Harris et al., 1984).

The report recommended an increase in microwave remote sensing research, particularly in the environmental sciences, with emphasis on the interaction between radar signal and ground surface characteristics. A number of key areas were identified in which research should be concentrated. They included:

(i) The development of quantitative criteria for assessing the effects of system parameters on the interpretability of a radar image.

(ii) Topographic, structural and lineament mapping.

(iii) Development of stereo and radargrammetric techniques.

(iv) The definition of surface roughness and volume roughness.

(v) The measurement of the complex dielectric constant for a range ofenvironments.

(vi) Vegetation mapping and assessment.

(vii) The improvement of radar calibration techniques.

(viii) Ground and airborne sampling at the time of spaceborne radar overpasses.

(ix) Assessment of suitable image processing and classification techniques for the analysis of radar data.

The report also suggested that microwave remote sensing should be promoted:

> "... as a tool, both in its own right, and as a data source complementary to visible and infrared remote sensing."(Harris et al., 1984).

This research project was designed to meet some of the recommendations of the NERC report by providing an opportunity for research into environmental science applications of satelite radar. The areas noted in i, iv, vi and ix are all addressed.

At the project design stage, only two satellite radar systems had been in operation: namely Seasat (1978) and the Shuttle Imaging Radar-A (SIR-A : 1981). It was decided to include data from both these satellites in the research framework to allow comparison of the effects of their different system parameters (look direction, depression angle and resolution) upon radar return. For this to be done effectively, an area of overlap between the two image products had to be identified.

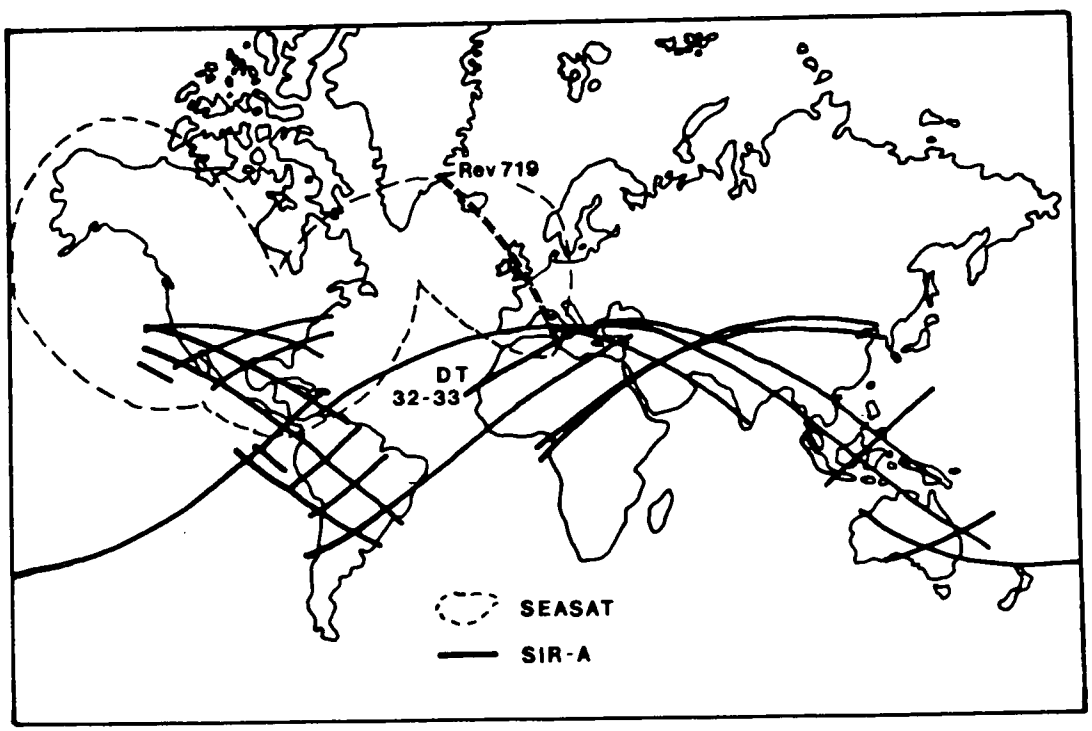

Figure 1.1 Coverage of the Seasat and SIR-A systems.

Few such areas exist outside northern and central America (Figure 1.1). One suitable region of overlap lies on the coastal plain of central eastern Tunisia, near the main tourist centres of Sousse and Monastir (Figure 2.1). This semi-arid environment has a number of characteristics that make it ideal for a comparative study of radar imagery. Firstly, the area includes examples of some typical semi-arid environments and geomorphological features, allowing general conclusions to be made about radar-terrain interactions in semi-arid areas. Secondly, the limited vegetation cover over large parts of the area enables the effect of surface roughness upon radar imagery to be assessed. Furthermore, the effective angle between the two satellite passes is 93° , thereby allowing comparisons to be made between imagery recorded at perpendicular look directions. These considerations, coupled with existing departmental research interests in Tunisia, led to the adoption of the Tunisian overlap area as the basis for the research project.

The SIR-A coverage of Tunisia extends westwards from the coast across the centre of the country (Figure 2.1). Availability of Landsat Thematic Mapper data for part of this extension provides a valuable opportunity to assess the complementary nature of SIR-A and Landsat TM imagery. Consequently, a second study area was defined in the mountainous environments of central Tunisia to evaluate the relative merits of information recorded in the visible, infrared and microwave parts of the electromagnetic spectrum. The Landsat data is used for comparative purposes only and, as such, is not analysed in detail.

The second study area in central Tunisia includes several characteristic semi-arid surfaces and features not found nearer the coast; namely those associated with mountainous areas and piedmonts. Together, the two study areas provide contrasting environments in which the application of satellite radar remote sensing may be assessed.

Given the field area and radar imagery described above, the principal aim of this research has been to investigate the potential of spaceborne microwave remote sensing in the discrimination and analysis of morphological and surface cover features in semi-arid Tunisia. Beyond this, a number of key research objectives has been defined. These are as follows:

(1) To identify the dominant ground controls on radar backscatter through fieldwork and image analysis, (as far as calibration problems and time-lag considerations will allow).

(2) To identify the characteristic responses of semi-arid environments in the L-band microwave region.

(3) To determine the influence of radar incidence angle and look direction upon the radar response from semi-arid surfaces.

(4) To assess the relative merits of Seasat and SIR-A as imaging radar systems.

(5) To assess the suitablility of SIR-A for discriminating environments within upland and lowland areas.

(6) To evaluate the complementary nature of satellite radar and Landsat imagery and the relative contributions of each.

(7) To determine methods appropriate for image processing and classification of radar imagery.

(8) To make recommendations about research needs in the light of future remote sensing programs.

The main body of this thesis begins with a description of the study area in central Tunisia in Chapter 2. The information presented in this section was used to design the fieldwork program and as an aid to image interpretation. This is followed by a review of the background and theory of microwave remote sensing in Chapter 3. The various radar system and ground parameters are considered in most detail, as they provide the basis for the radar image analysis.

In Chapter 4 the acquisition and pre-processing of the two radar scenes is discussed. Various pre-processing operations were necessary before either image could be analysed by digital image processing techniques. Image analysis techniques, together with the visual interpretations of the imagery, are discussed in Chapter 5.

The fieldwork undertaken in Tunisia, together with the laboratory analysis of samples collected in the field, is discussed in Chapter 6. This chapter also describes the statistical analyses applied to the field data and to corresponding image data, and the results obtained from inter-relating them. This allows the dominant parameters influencing radar image appearance to be identified.

Classification of the imagery by discriminant analysis is reviewed in Chapter 7.

General conclusions drawn from the results discussed in Chapters 5 to 7 are presented in Chapter 8. Recommendations are made for future research into environmental science applications of satellite microwave remote sensing, in the light of future radar programs. Finally, possible applications of radar imagery to environmental problems in semi-arid areas are discussed in Chapter 9.

Chapter 2. The Study Area in Eastern Central Tunisia.

2.1. General Information: Site and Situation.

The SIR-A imagery available for Tunisia covers a central belt approximately 60km wide from the transitional area locally known as the Sahel of Sousse in the east to the Algerian border just west of Kasserine (Figure 2.1). Seasat imagery of the Sahel provides coverage for the coastal area, extending northwards to Enfidaville. Preliminary analysis of the combined radar cover led to the selection of two study areas for the research project.

The first comprises the region of overlap of the SIR-A and Seasat radar passes in the coastal plain of Sousse. It covers an area of 60km^2 from Sousse (Latitude 39°80'N, Longitude 9°20'E) (Figure 2.2a) in the north to Mahdia in the south. The regionally-important town of Kairouan lies just outside the area to the north-west. The area is characterised by generally low relief associated with Tertiary and Quaternary deposition. The greatest relief can be found in areas of hill country to the south and east where the land rises to between 100m and 200m above sea level (Plate 2.1). The most prominent features are the large inland sebkhas of Sidi el Hani and Kelbia, resulting from slow subsidence of the Sahel zone in the Quaternary. Towards the coast is the fossil sebkha associated with the Monastir tombolo, also formed during the early Quaternary. Drainage in the area is intermittent, with most of the wadis located around the sebhkas and on the coastal plain.

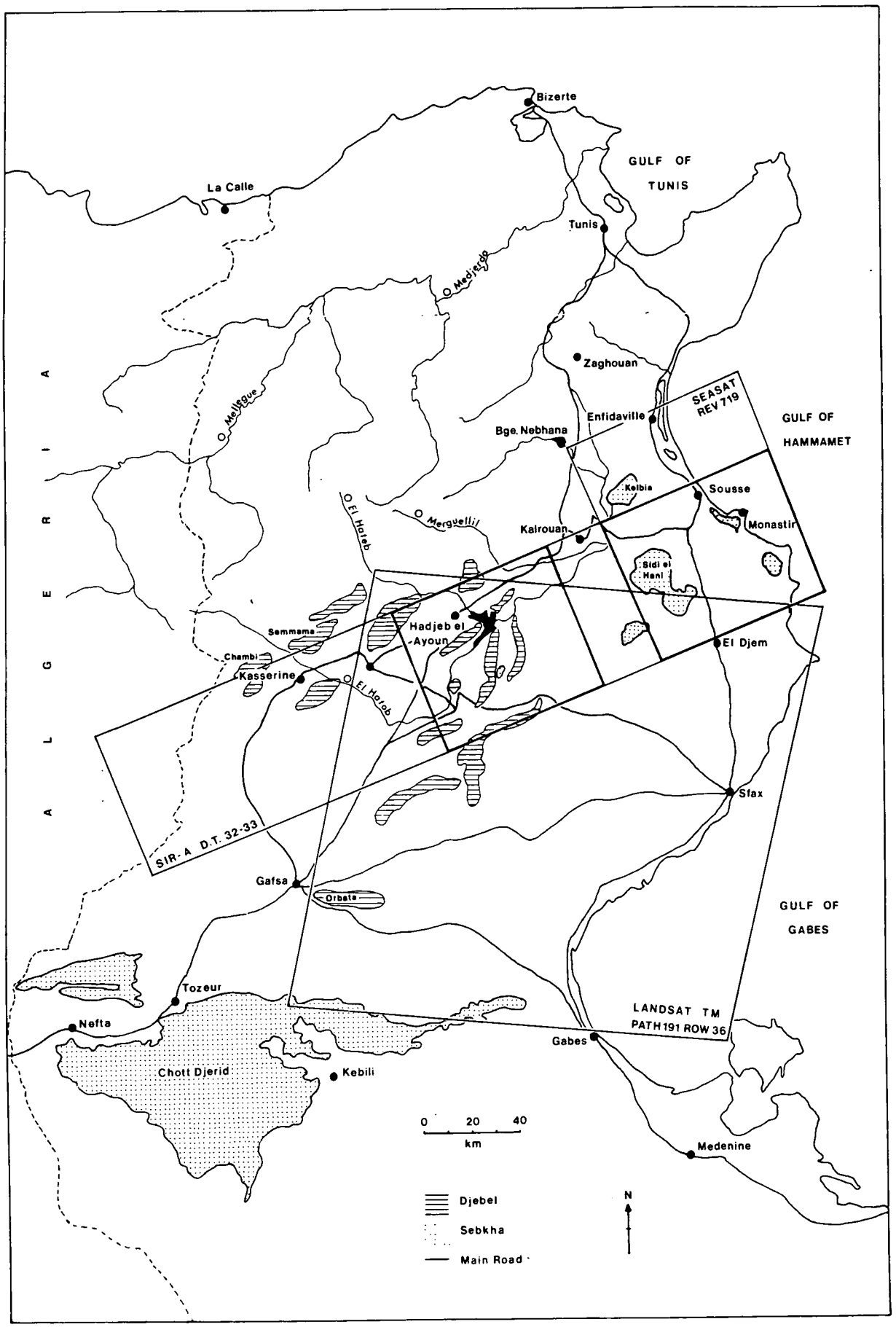

Figure 2.1 Location of satellite data in central Tunisia.

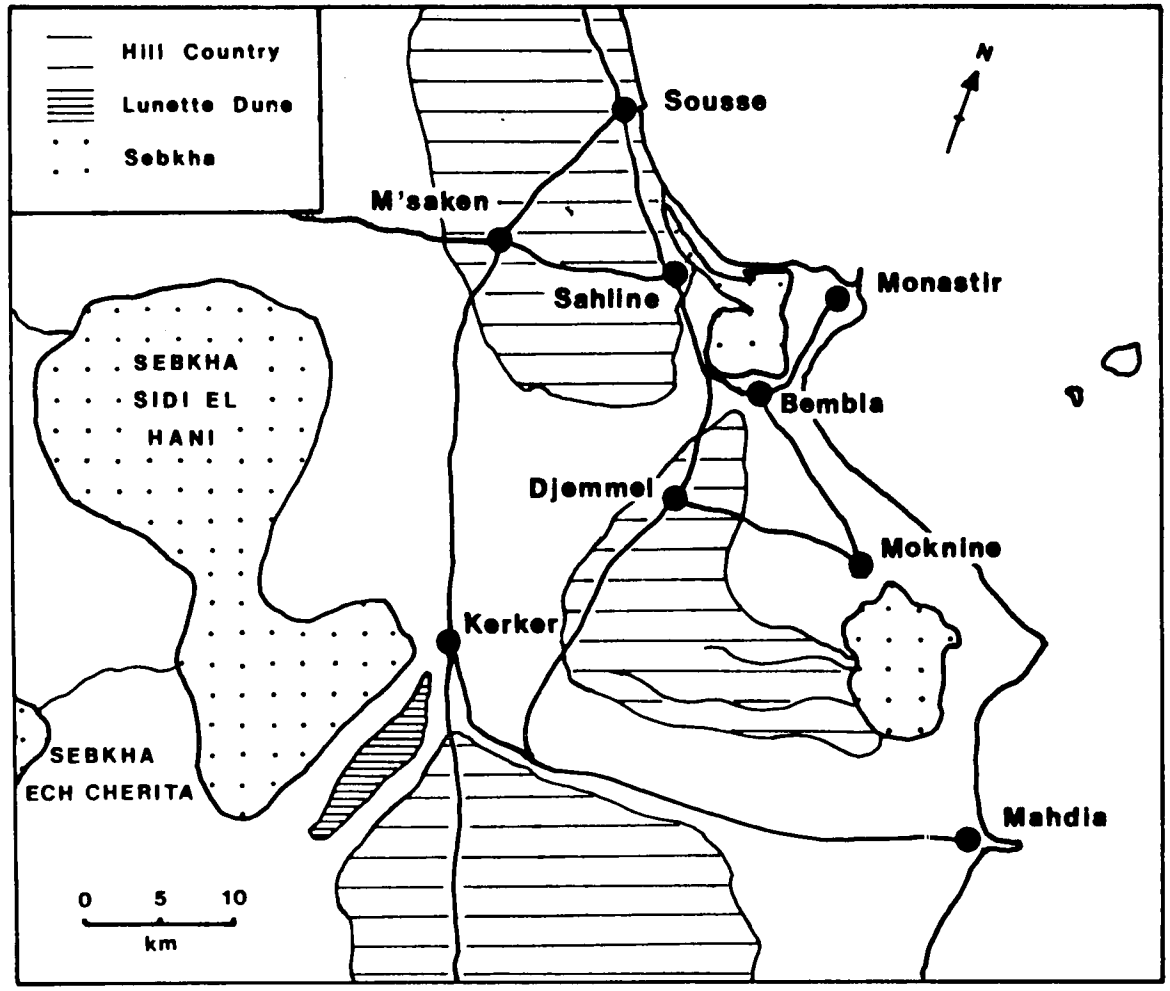

Figure 2.2a Eastern study area on the coastal plain of Sousse.

The natural steppe grassland has been replaced largely by extensive olive cultivation and pockets of arable farming to the north. The main settlements are located around the coast where fishing has long been an important industry. Today the larger towns of Sousse and Monastir have bowed to the influence of Tunisia's growing industry, tourism, which modifies increasingly the land use of coastal areas.

The second study area is of a similar size and lies west of the Sahel zone near the town of Hadjeb el Ayoun, at approximately 39°32'N, 8°00'E. The northern edge lies along the main road between the historically-important centres of Kairouan and Sbeitla (Figure 2.1; Figure 2.2b). The dominant features here are the complex series of anticlines associated with the tectonically-significant Tunisian "North-South Axis". These djebels, with their pediments and duricrust formations, form a prominent series of mountain ranges, rising to heights of over 600m above the surrounding plains of Hadjeb el Ayoun and Sidi Bouzid. Their topography has been modified considerably by fluvial dissection. The plain is dissected by the wadis of Zeroud and el Hadjel which converge at the site of the recently-constructed Sidi Saad dam. L'Oued el Hadjel is a discordant tributary of the Oued el Hatob, which flows past Kasserine into the Sidi Bouzid plain. The larger Oued Zeroud flows eastwards into the coastal plain, feeding the sebkhas with a seasonal supply of water and sediment. The drainage basin of the Oued el Hadjel covers an area of about 21,000 hectares fed by a number of deep gullies which have dissected the valley since Roman times. In contrast, the Cherahil valley to the east is a smooth agricultural plain, supporting irrigated arable farming and olive plantations. Agriculture has largely replaced

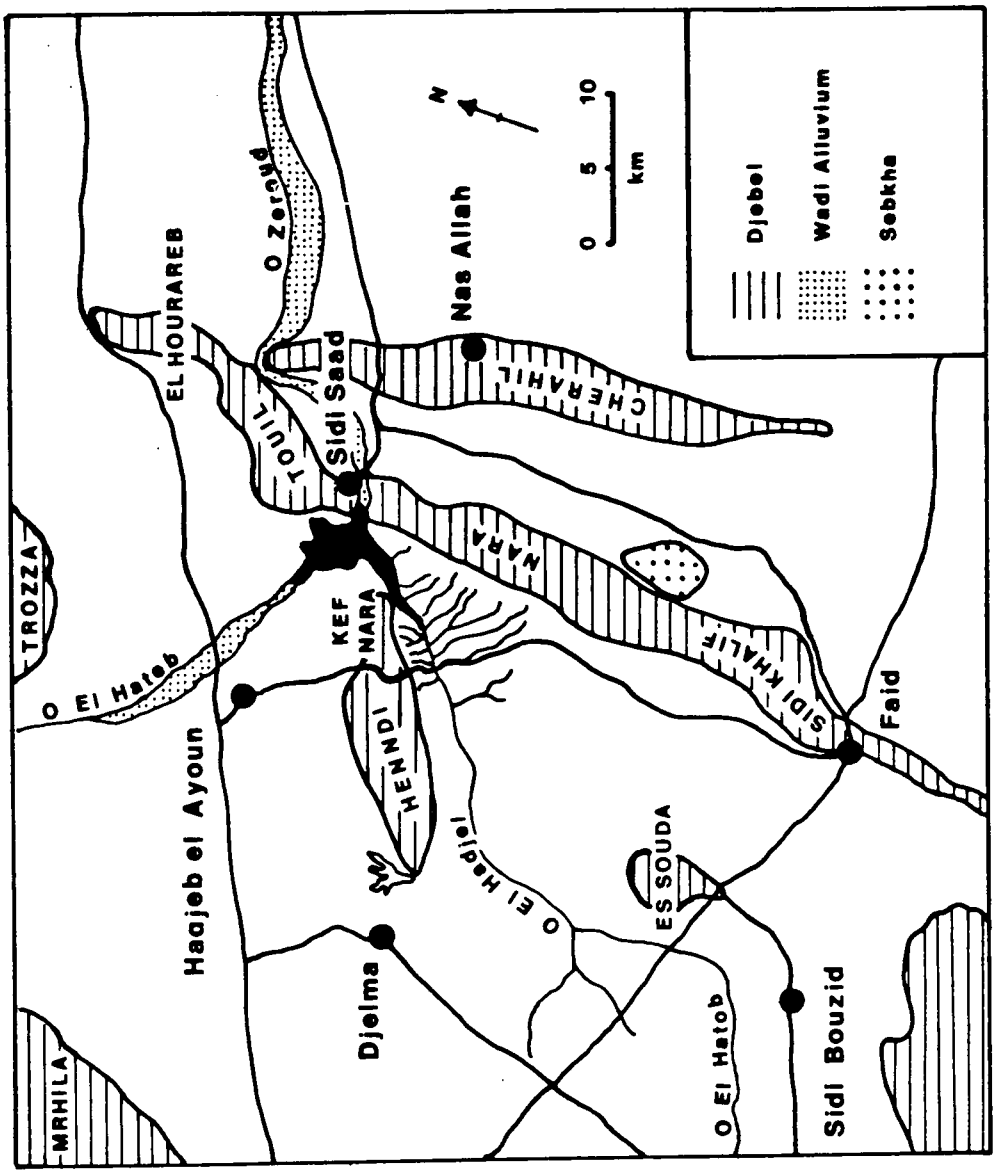

Figure 2.2b Western study area near Hadjeb el Ayoun.

the natural alfa and juniper steppe vegetation on all but the steeper slopes of the djebels.

The two areas provide contrasting environments for investigation and exploration. Together they cover a wide range of semi-arid landforms and land cover types, making the area as a whole a suitable stage for testing the interactions of satellite radar with semi-arid environments. In the following sections, information pertaining to landscape evolution and the present-day environments of the central Tunisian study belt is presented. It is a general synthesis, serving only as a basis for field investigations and image interpretation. Detailed information is presented only where it is deemed necessary for understanding the human and physical environment that we see today.

2.2. The Climate of Central Tunisia.

The study area in central Tunisia experiences a semi-arid climate, with a mean annual rainfall of around 200-300mm and temperature of around 20°C. Local climatic variations are considerable, with coastal areas experiencing higher temperatures and rainfall figures than areas inland. Figures for five regionally-important weather stations within the central belt are presented in Table 2.1. In the spring and autumn, precipitation intensities are high, with up to 30mm of rainfall recorded in the first 15 minutes of some events. This has a considerable influence on runoff and soil movement in exposed areas (République Tunisienne, 1976). Dominant wind directions vary seasonally, with onshore winds common from April to August and north-westerly winds prevalent in winter and autumn.

STATION WITH ALTITUDE	MEAN ANNUAL PRECIPITATION	MEAN ANNUAL TEMPERATURE
MONASTIR 2m	370mm (1951-1980: Met. Office)	19.5°C (1951-1980: Met. Office)
KAIROUAN 60m	340mm (1951-1980: Met. Office)	19.1°C (Period unknown: Hollis and Kallel, 1986)
HADJEB EL AYOUN 343m	320mm (1963-1972: République Tunisienne, 1976)	18.4°C (1963-1972: Rép. Tun., 1976)
SBEITLA 661m	310mm (1963-1972: Rép. Tun., 1976)	17.2°C (1963-1972: Rép. Tun., 1976)
SIDI BOUZID 354m	276mm (1951-1980: Met. Office)	18.0°C (1963-1972: Rép. Tun., 1976)

Table 2.1 Rainfall and temperature data for five regional stations in central Tunisia.

2.3. The Geology of Central Tunisia.

This section describes the geological formation of central Tunisia as an aid to understanding the structure and lithologies seen in the landscape today. A tectonic map of Tunisia, showing the main areas of uplift and subsidence, is given in Figure 2.3. It should be compared with the study area maps in Figures 2.2a and 2.2b. Unfortunately, detailed maps of solid geology and surficial deposits were unavailable for this project, although a brief study was made of Sheet 78 of the Tunisian Geological Survey (Hadjeb el Ayoun) at the University of Tunis. This map is simplified in Figure 2.4. The location of two schematic cross-sections of the valley of L'Oued el Hadjel (Figure 2.5) are shown on this map. Further reference is made to these cross-sections in Section 2.4 (see below). The stratigraphic sequence for Mediterranean regions is listed in Table 2.2.

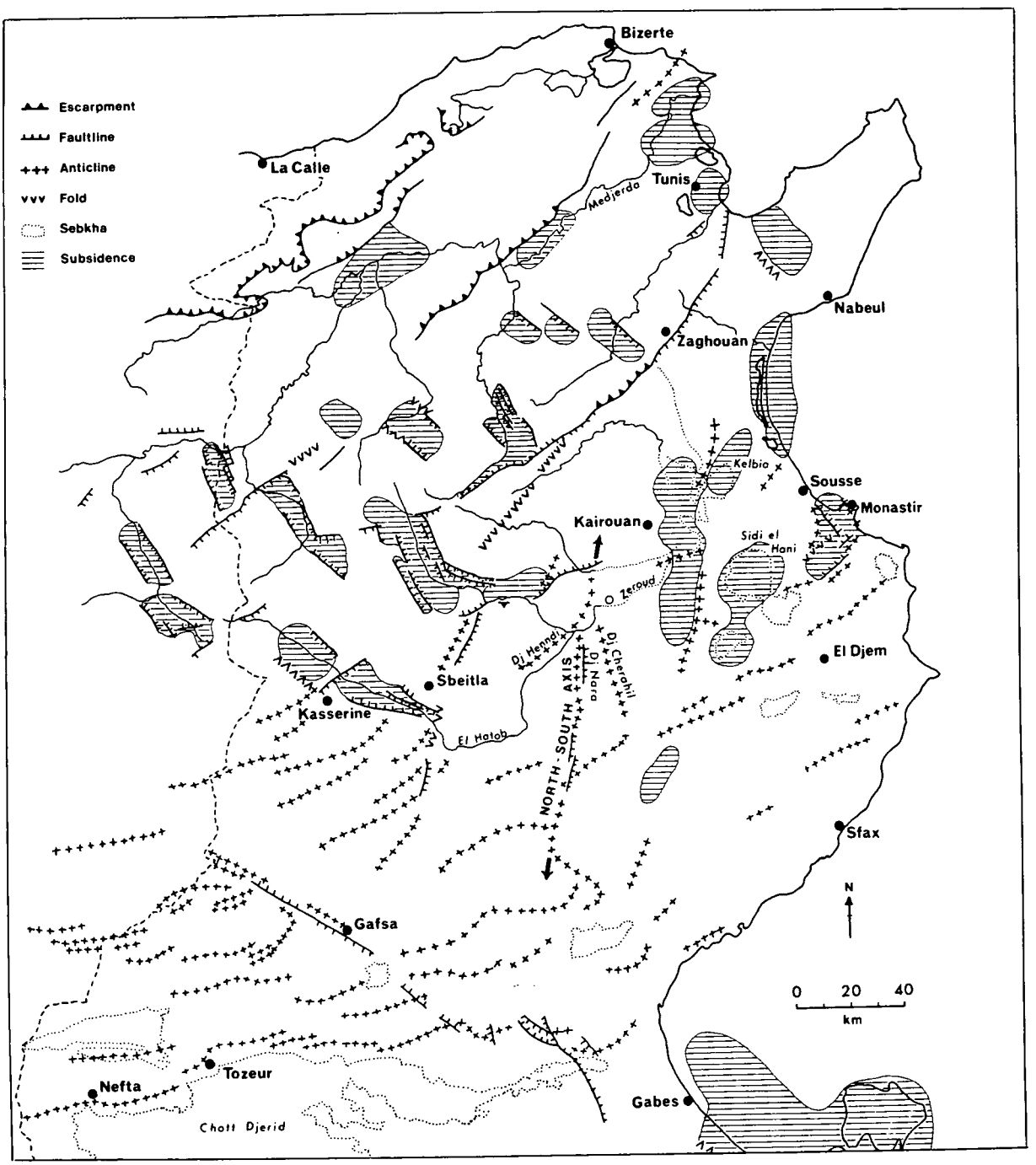

Figure 2.3 Tectonic map of Tunisia showing main areas of relief and subsidence (after Coque and Jauzein, 1965)

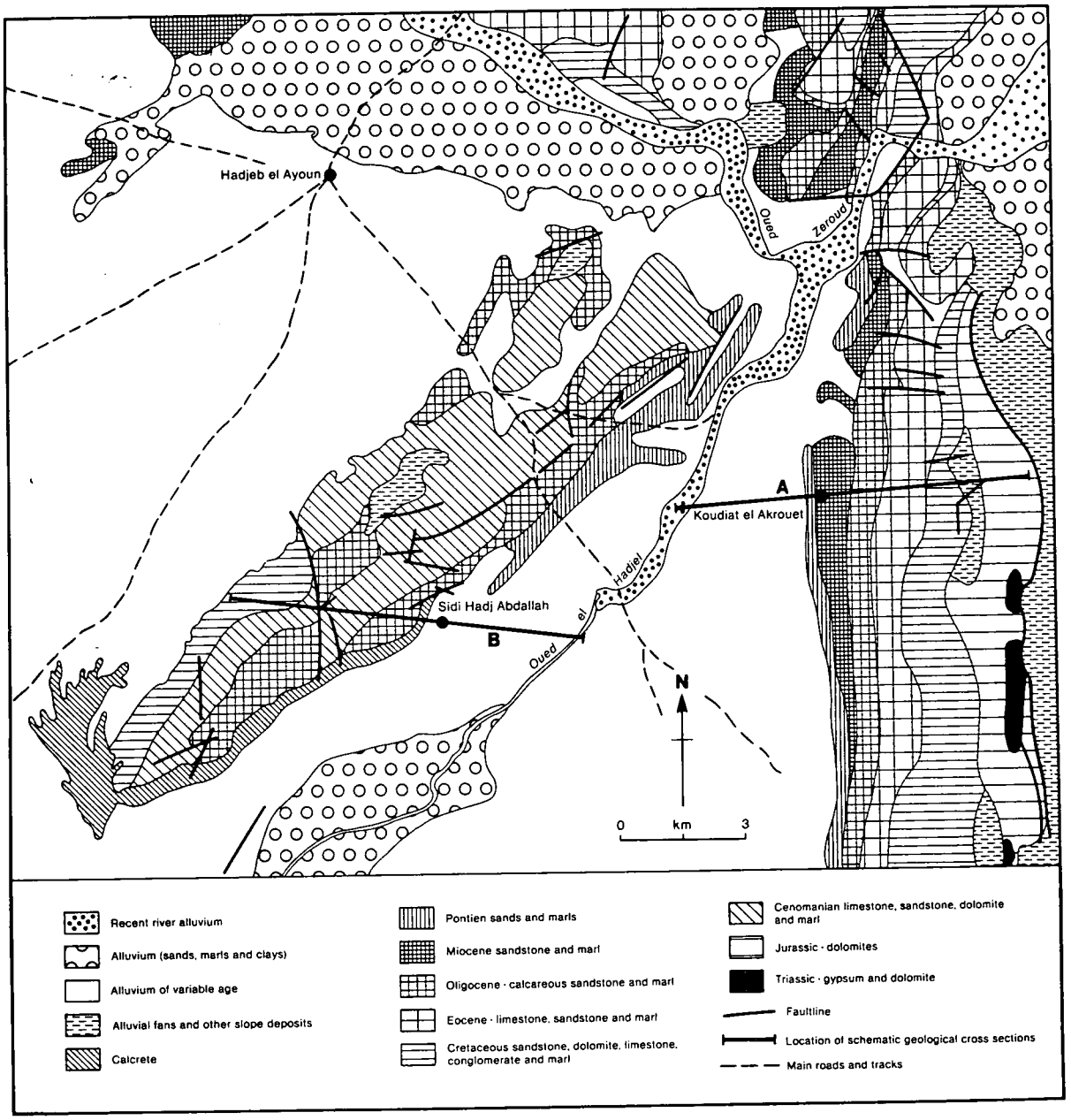

Figure 2.4 Geological map of the Hadjel Valley (based on sheet 78 of the Tunisian Geological Survey: Hadjeb el Ayoun).

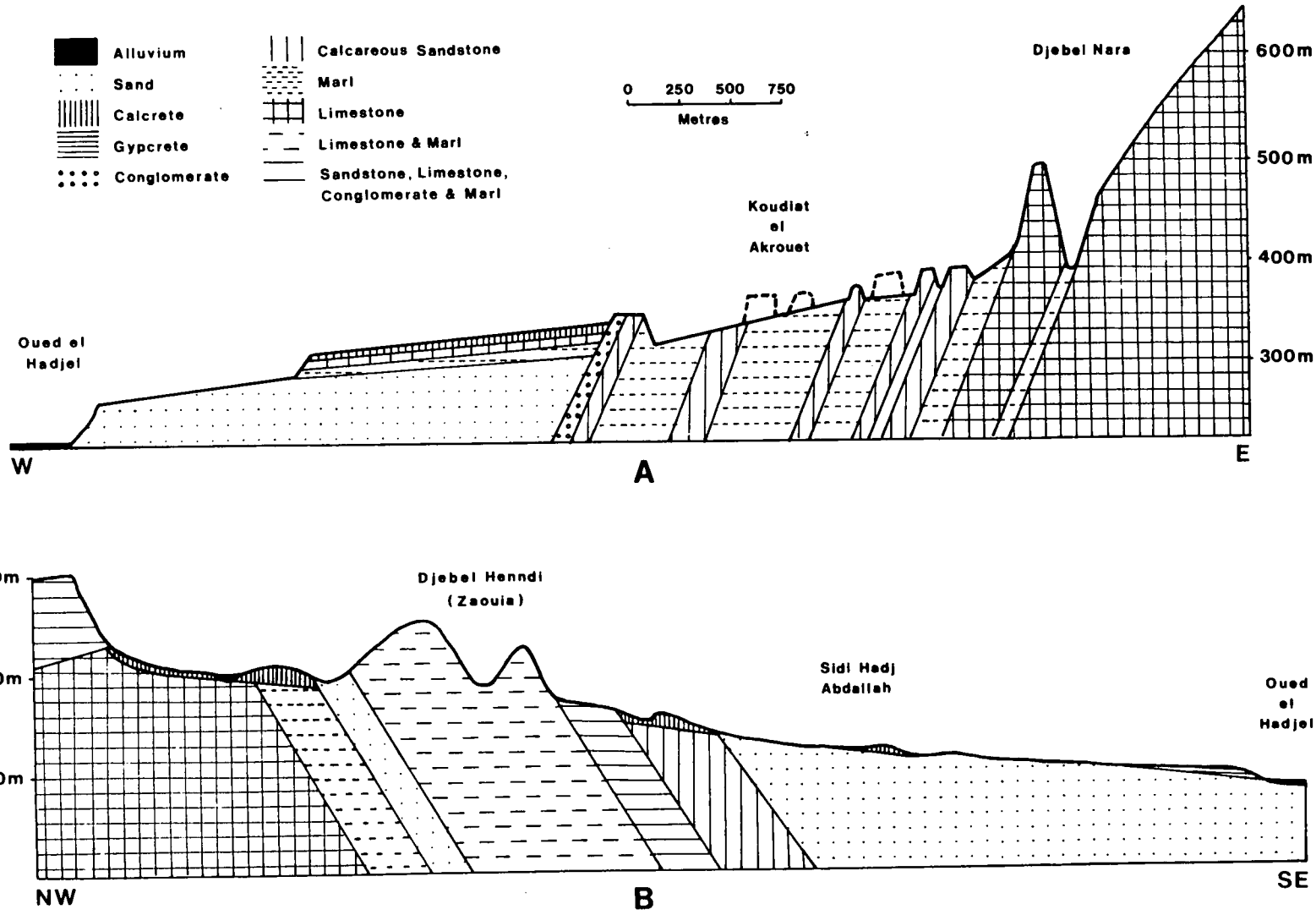

Figure 2.5 Cross sections across the Hadjel Valley (For locations see Figure 2.4)

ERA	PERIOD	EPOCH	STAGE AND EVENT
CENOZOIC	QUATERNARY	HOLOCENE PLEISTOCENE	FLANDRIAN
	Neogene	PLIOCENE MIOCENE	TUNISIAN ATLAS OROGENY
	TERTIARY Palaeogene	OLIGOCENE EOCENE PALAEOCENE	WESTERN MEDITERRANEAN OROGENY
MESOZOIC	CRETACEOUS	UPPER (SENONIAN) MIDDLE LOWER (NEOCOMIAN)	APTIAN
	JURASSIC	UPPER MIDDLE LOWER	
	TRIASSIC	UPPER MIDDLE LOWER	
PALAEOZOIC Upper	PERMIAN CARBONIFEROUS DEVONIAN		HERCYNIAN OROGENY
PALAEOZOIC Lower	SILURIAN ORDOVICIAN CAMBRIAN		CALEDONIAN OROGENY
	PRE-CAMBRIAN		

Table 2.2 Geological Sequence for Mediterranean regions (After Anderson, 1978).

Most of Tunisia, along with Libya and southern Algeria, is part of the Saharan platform which was intensely folded and uplifted during the Precambrian, but has since suffered only minor phases of uplift and downwarping. Throughout the Palaeozoic, North Africa experienced a series of marine transgressions and regressions, but the only rocks of that era exposed in Tunisia are the red and green shales of Permian origin found in the parallel hogsback ridges of Djebel Tabaga, 25km north-west of Medenine in the south of the country (Baird, 1967). These outcrops are unique in their stratigraphic expression due to the subsequent downwarping of many northern areas of the Saharan Shield after the Hercynian Orogeny.

In the Triassic, thick deposits of evaporites were laid down throughout North Africa (Busson, 1967). Although Triassic evaporites crop out in some areas, Jurassic rocks dominate the geology of most of northern and central Tunisia. Deep drilling in the 1950s and 1960s revealed the presence of thick sequences of Jurassic limestones and shales in a large depositional trough, sometimes more than 1500m deep, stretching from Kairouan in the north to the eastern margins of the Chott Djerid in the south (Buchanan and Schwab, 1966; Castany, 1967).

Today, Jurassic rocks are clearly evident on the eastern side of the Nara-Touil-Hourareb ranges, which form the North-South axis in the centre of the country (Figure 2.4). Much of the detailed stratigraphy and fossil record can be distinguished only poorly due to dolimitization, but yellow-grey silty limestones, interbedded with silty marls and ferruginous limestone lenses, have been identified dating from the mid-Jurassic. These are

overlain by upper Jurassic grey-blue crystalline limestones interbedded with yellow shale and calcareous pyritic limestone.

The dolomites of Djebel Nara are overlain by the Sidi Khalif shales and marls, which are evident also in the surrounding Djebels of Mrhila and Cherahil. The shales were deposited during the Aptian Transgression, after a period of local deformation and erosion. They mark the Jurassic-Cretaceous boundary within the Nara chain. This transgression continued well into the Tertiary, but increasing orogenic activity resulted in deposition becoming more localized. The Eocene saw thick deposits of gypsum and white limestone laid down along Djebel Nara and Djebel Cherahil on top of phosphates dating from the early Palaeogene (Burrollet, 1967).

Increased orogenic activity in the Oligocene led to the deposition of thick sandstones over central Tunisia. These are well in evidence in the Nara Chain where they are interbedded with marls and shales. Gypsum dating from this period is also evident in the northern part of Djebel Nara. Tertiary rocks exposed in Djebel Henndi to the west of the Hadjel valley are mainly Palaeogene limestones, conglomerates and shales. Some ferruginous sandstones can be found at the eastern end of this Djebel in an area known locally as Kef Nara.

Tertiary deformation associated with the western Mediterranean and Alpine orogenies uplifted and faulted the deposits of central Tunisia, creating the complex series of Djebels that dominate the area today. The North-South Axis of Djebel Nara, Djebel Touila, Djebel Hourareb and Djebel Cherahil, together with the Henndi Range, emerged towards the end of the Cretaceous and was

accentuated during the Palaeogene (Figure 2.3). Deformation resumed in the Neogene, uplifting these Djebels still further. At this time, the Nara-Cherahil Complex formed the southern apex of a huge fold system running through Zaghouan into the Gulf of Tunis. To the west was the stable shelf of the Kasserine Island (Bishop, 1975; Coque and Jauzein, 1965). To the east and north widespread subsidence occurred, leading to the formation of low-lying regions of the central Tunisian study areas. Subsidence was particularly important in the Sahel of Sousse, Quaternary deposits obscuring much of the evidence of Mesozoic and Tertiary sedimentation.

Thus the Tunisian North-South Axis was born. Faulting further accentuated this axis in the upper Neogene (Figure 2.3), evidence of which can be seen today in the core of Djebel Nàra. Today the anticlines of the North-South-Axis rise above the plains of Hadjeb el Ayoun and Kairouan, forming a prominent boundary to the eastern Sahel zone. Their formation also provides a clear temporal boundary, between the major relief building events of the Mesozoic and Tertiary and the geomorphological modifications active throughout the Quaternary.

2.4. The Geomorphology of Central Tunisia.

Quaternary landforming processes have modified the Tertiary landscape of central Tunisia to a varying extent. To the west of the study belt, geomorphological processes have altered a pre-existing lithological and tectonic framework. In contrast, the dominant landforms of the eastern Sahel zone beyond the North-South Axis have only appeared in the Quaternary, largely obscuring the record of previous geological periods. The following subsections provide a general appraisal of the results of the major

landforming events of the past ten million years. The two study areas are discussed in turn allowing easier evaluation during field and image analysis.

As this thesis is devoted to the study of radar backscatter from the major landforms and land use patterns of central Tunisia, the descriptions below concentrate on the dominant features in each study area, namely pediments and duricrust formations in the mountainous regions of Hadjeb el Ayoun, and sebkhas and lunette dunes in the coastal zone around Sousse. The features described are not necessarily peculiar to each region. For example, small sebkhas occur in the Cherahil valley near Hadjeb el Ayoun, and pockets of calcrete are present towards the coast at Monastir (Figure 2.7). However, the radar response from these minor features in each area is largely overshadowed by that from surrounding landforms, land use and cover types, and is, therefore, difficult to evaluate.

2.4.1. The Mountain Environments of Hadjeb el Ayoun.

The morphology of the environs of Hadjeb el Ayoun which is seen today is a reflection of the underlying geology, gradually modified by Quaternary landforming processes. The exposed blocky slopes of the limestone Djebels are fringed by gently-sloping pediments, typical of arid and semi-arid regions. These 'erosional surfaces of low relief' (Hadley, 1967) were probably formed by weathering and rill-wash erosion beginning in the Tertiary, with additional shaping by lateral planation in the early stages of development (Bryan, 1935). The nature of pediments varies considerably, usually as a direct result of the lithology beneath. The influence of lithology on pediment form, though not necessarily formation, is clearly exemplified in the Hadjel valley,

where the gentle slopes of the north-west (Figure 2.5a) are strangely contrasted with their counterparts to the south-east of the Oued el Hadjel (Figure 2.5b).

The alternating limestones, sandstones and marls exposed on the western side of the faulted anticline of Djebel Nara have been differentially eroded during the Quaternary, creating the irregular steps of the pediment plain seen today (Plate 2.2). Within this pediment, two main erosion surfaces can be distinguished. In the upper reaches of the valley, exposures of Palaeogene and Neogene limestones and calcareous sandstones rise above the weaker Nara Marls to form the Tertiary glacis, which lies some 25m above the Pontien level (République Tunisienne, 1976). Only this newer erosion level can be clearly identified in the western and southern regions of the Hadjel valley.

Differential erosion of the western pediment of the Cherahil Range has produced a series of stepped outcrops aligned with the northern part of the eroded anticline. These striking morphological features rise like sleeping dinosaurs above the flat plains of the Cherahil valley (Plates 2.3 and 2.4). Erosion of rocks weakened by intense deformation also produced an area of inverted relief within Djebel Cherahil (Plate 2.5) and Djebel Nara (Plate 2.6). Most of the pediments in the Hadjeb el Ayoun region are covered by duricrusts. These layers of encrustation are common to many low-angle surfaces in semi-arid areas and have been studied extensively in North Africa (Boulaine, 1958; Coque, 1962; Noureddine, 1979). More recent accounts by Goudie (1973, 1985) have provided a wealth of information about these:

> "Product[s] of terrestrial processes within the zone of weathering in which...calcium carbonate (in the case of calcrete) or other compounds...have dominantly accumulated in and/or replaced a pre-existing soil, rock or weathered material to give a substance which may ultimately develop into an indurated mass" (Goudie, 1973).

Calcrete is most common in Tunisia, as illustrated in Figure 2.6, but in many southern areas it grades into gypsum which is morphologically similar (Goudie, 1973). Both are found in the Hadjeb study area (Figure 2.5), with pockets of deep gypcrete covering the western banks of the Oued el Hadjel (République Tunisienne, 1976).

Calcretes usually have a hardened upper crust underlain by "friable nodule horizons" (Goudie, 1985). The whole mass is commonly several metres deep (Bonvallot and Delhoume, 1978), with thicknesses of up to 15m having been recorded in Tunisia (Dutcher and Thomas, 1966). The hardened crust makes them resistant to erosion, thus preserving the ancient pediment level (Coque and Jauzein, 1967). However, once this upper layer is breached, the friable mass beneath becomes highly susceptible to erosion by water and wind. This is clearly illustrated by the raised calcrete banks which emanate from the slopes of Djebel Mrhila, now several metres proud of the surrounding plain (Plate 2.7). Another interesting example can be found at the western tip of Djebel Henndi. Here a series of shallow finger-like channels have been cut into the calcrete mass by concentrated runoff from the Djebel (Figure 2.2b; Plate 2.8). The channels flow southwards where they join the Oued el Hadjel, although drainage reversal is likely to have happened some time in the Quaternary.

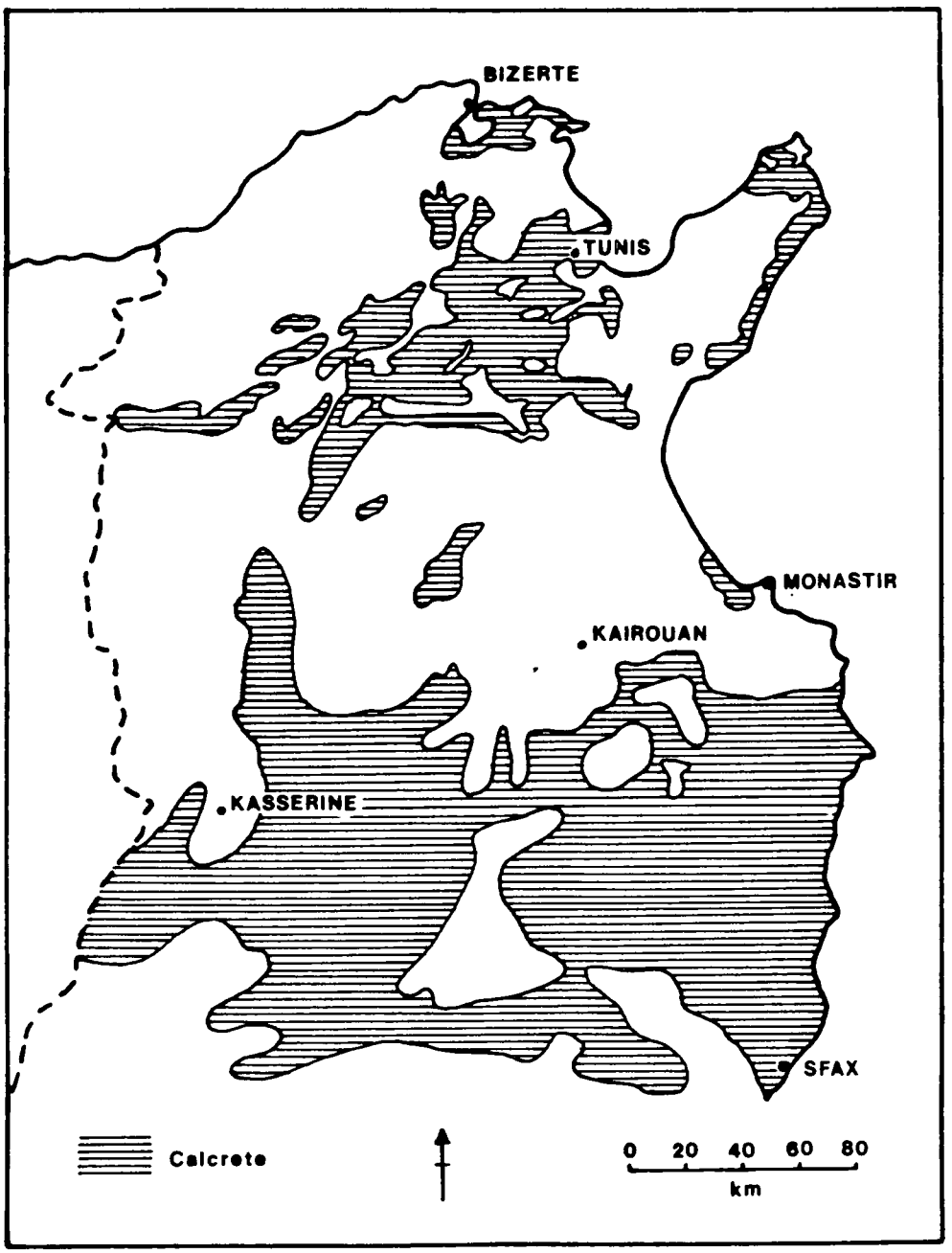

Figure 2.6 Calcrete in Northern Tunisia (after Goudie, 1973).

Numerous models have been proposed for calcrete formation. None is universally accepted owing to the inaccessibility of source areas and the differing nature of deposits within these areas. Without further detailed field study it is impossible to say with any degree of certainty whether any model may be entirely discounted. Previous studies in Tunisia have favoured the formation of calcrete by cementation of alluvium or debris material from the mountain slopes above (Coque and Jauzein, 1967), with some input of finer material by wind. Coque (1955, 1958) and Bonvallot and Delhoume (1978) suggested that calcareous crusts in Tunisia are relics of periods of aridity which occurred during the Quaternary. These periods were interrupted by catapluvials and pluvials, where transport and erosion processes became more dominant. Therefore, the two duricrust levels, superimposed upon the two pediments of the Hadjel valley, could be said to mark the end of periods of slope formation. However, recent recognition of the current formation of calcrete in many semi-arid areas has given credence to the idea that most crusts are fairly recent phenomena (Smith and Whalley, 1982). Indeed, ages of 8,000 to 9,500 years have been attributed to Tunisian duricrusts by Page (1972), an age which differs widely from the Villafranchian origin proposed by Horta (1979).

As mentioned above, duricrusts are highly resistant to erosion, but when the hard crust is removed spectacular erosion features may occur. One interesting feature associated with the erosion of encrusted slopes is the 'flat-iron'. Magnificent examples of these triangular slope facets can be found in the field area on the western slopes of Djebel Nara and Djebel Cherahil (Plate 2.9).

The power of water as an agent of erosion is well in evidence in the Hadjel valley, where spectacular gullying has taken place (Plate 2.10). Badlands of the Hadjel valley and elsewhere in the region owe their origin to the removal of natural vegetation and intense cultivation since the Roman period (Le Houerou, 1959; Bonvallot, 1977; Bannour et al., 1981; Hamza, 1985). Agricultural activity destroyed the calcareous crust and ancient alluvial cover leaving the friable matrix beneath open to erosion, which now averages 850,000 m^3 per year for the Hadjel valley alone (République Tunisienne, 1976; Hamza, 1977). Material from the gullies drains into the Oued el Hadjel and flows northwards into the Oued Zeroud. Reconnaisance work for the construction of the Bourguiba Reservoir at Sidi Saad allowed measurements of suspended sediment load to be made at the point of entry into Oued Zeroud. Indeed, the load has been sufficiently high to cause a substantial silting problem since the completion of the reservoir in 1981 (Hamza,1986, personal communication).

Where duricrusts are not present, other deposits often cover the Quaternary pediment levels. In the lower parts of the Hadjel valley a blanket of recent alluvium has been deposited on the wadi floor and most recent erosion level. To the south of the valley, alluvial fans coalesce to fringe the south-eastern slope of Djebel Sidi Khalif (Plate 2.11). These fans are relatively small in comparison with the larger fans of Djebel Orbata, 80km to the south (White, 1987).

2.4.2 The Sahel of Sousse.

The dominant features of the eastern coastal plain are the large inland sebkhas of Sidi el Hani and Kelbia and the near coastal sebkha at Monastir. The first two features owe their existence to the subsidence associated with the end of the Tunisian Atlas orogeny in the Pliocene. This subsidence disrupted the existing drainage patterns of L'Oueds Nebhana-Merguellil and Zeroud, which previously drained into the sea, creating a series of closed depressions seasonally fed by wadi discharge (Coque and Jauzein, 1967). This tectonic origin makes these 'flat areas of clay, silt and sand...often encrusted with salt' typical of the thousand or more 'inland sebkhas' recorded in North Africa (Glennie, 1970; Cooke and Warren, 1973). There is strong evidence to support the theory that subsidence is continuing in these areas today as large volumes of sediments are incorporated into the sebkhas with no noticeable rise in surface elevation (Coque and Jauzein, 1965, 1967).

Inland sebkhas receive their water from a variety of sources, ranging from intermittent flooding by wadis to capillary movement from a near-surface water table. Recent work by Hollis and Kallel (1986) has concluded that Sebkha Kelbia is fed by the waters of three large wadi systems and artesian groundwater flow, with some minor input from direct rainfall in the wet season. Sebkha Kelbia is indeed unique in the Sahel zone in its ability to discharge into the sea through the Plain of Enfidaville. Sidi el Hani has no discharge route, its only outlets being evaporation and infiltration.

Major and minor flood discharges are both very important in the maintenance of water level in the two

inland sebkhas. High post-flood levels are associated with low salinity, which gradually increases with decreasing water level. Occasional dessication occurs in both sebkhas, although, once again, Sebkha Kelbia is unique in North Africa in that it never develops a dry salt crust (Hollis and Kallel, 1986). Evaporation of the waters of Sidi el Hani, on the other hand, frequently leads to salt-crust formation (Plate 2.12). Sodium chloride is brought to the surface in groundwater solution by capillary action where evaporation occurs leaving a halite crust. When a new influx of permeable sediment, such as sand, enters the sebkha, the upward flow of groundwater causes solution of the crust and recrystallisation at the surface (Glennie, 1970). If clay-sized particles are deposited, however, upward flow is limited and salt lenses tend to remain beneath the surface. Large salt polygons are common in areas of Sidi el Hani.

The arid and semi-arid periods of the late Quaternary in Tunisia have been conducive to the formation of 'aeolian ridges' or 'lunette dunes' in the vicinity of the sebkhas. Seasonal dessication of sebkha surfaces allows removal of material by strong unidirectional winds and deposition on the downwind sebkha margins. The nature of the dune feature is largely dependent upon the deflated sediment. Classic lunette dunes described in North Africa have a substantial clay content of between 20% and 30% (Bowler, 1973). In the Sahel of Sousse, however, there is a greater proportion of sand-sized material and the resultant dunes are therefore sandy and elongated (Coque and Jauzein, 1976). Much of this material is pseudo-sand, formed by the flocculation of clay during salt crystallization. Once the material has been deposited the particles coalesce during the next wet season and leaching returns the soluble salts to the sebkha basin. The ridge

may become vegetated but its friable nature renders it highly susceptible to erosion. Excellent examples of the dissected low-angle dunes can be found to the south and east of both the large inland sebkhas of the Sahel zone (Figure 2.2b).

As in the western study area, it is the recent influence of man that has accelerated the process of erosion in many of the marginal agricultural lands of the Sahel region. The gullies to the south of Sidi el Hani formed when the natural vegetation cover of the unstable aeolian ridge was removed. The problem quickly spread. A similar soil erosion problem has been identified in the hill country around the town of M'saken. Once channels have been established, climatic conditions and not anthropogenic factors are largely responsible for wadi form (Brierley, 1981).

The sahel of Sousse also provides an excellent example of a near-coast inland Sebkha blocked by a tombolo and coastal dune complex (Glennie, 1973). A Flandrian dune ridge now separates the old coastal sebkha at Monastir from perennial marine influence (Figure 2.7) and has allowed considerable accumulation of Quaternary alluvium and saline soils. The tombolo is linked to the mainland by a pre-Flandrian dune ridge, now the site of Monastir airport. Regarding ancient shorelines, Coque and Jauzein (1967) wrote:

> "There is little probability of finding traces of very old shorelines along the coastal areas of the eastern plain of Tunisia, due to the continued subsidence of the area and to the effects of recent sedimentation."

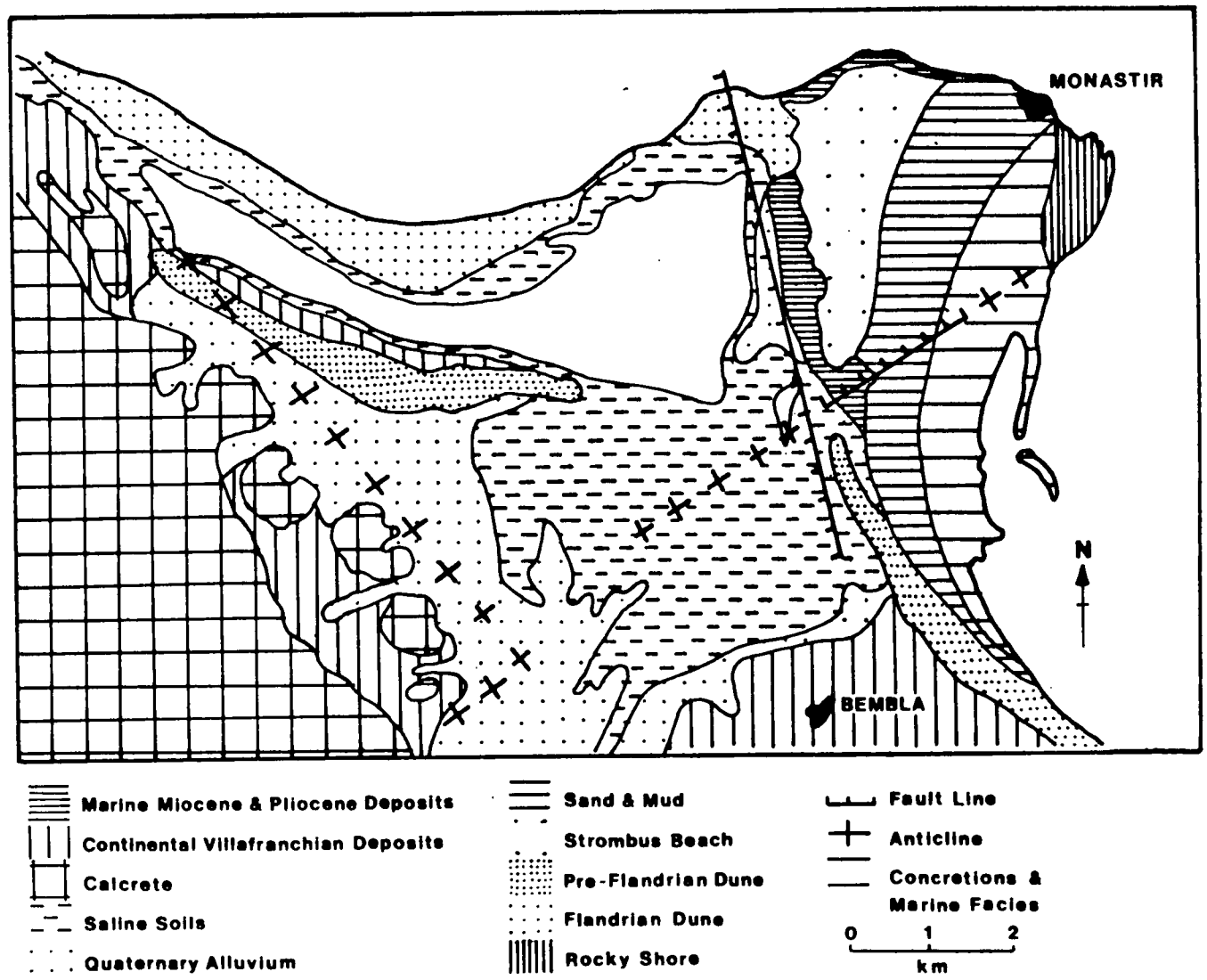

Figure 2.7 The geology of the Monastir area (after Coque and Jauzein, 1967).

However, Monastir provides one of the finest locations of evidence of marine incursion in Tunisia. This supports the view expressed previously that the features of the Sahel of Sousse are largely products of Quaternary landforming processes which have buried much of the Tertiary geology.

2.5. The soils of Central Tunisia.

The soils of the central Tunisian study area, with its mean annual rainfall of 200-300mm and long dry season, are undergoing significant physical weathering. Stony soils are common on the limestones, conglomerates, marls and gypsum of the foothills and on the duricrusts of the Nara chain. A characteristic example of this type of soil can be seen on the gently-sloping pediment on the eastern flank of Djebel Sidi Khalif . Here, surface pebble count decreases markedly with increasing distance downslope (Brechtel and Rohmer, 1980).

The skeletal soils of the southern foothills grade into brown or yellow-brown semi-desert soils with little profile definition and considerable sodium chloride salinity. Under present climatic conditions these soils are thin, with a high sand and low clay content making them susceptible to wind erosion (Brechtel and Rohmer, 1980). Further north in the Hadjel valley increased concentrations of clay and silt render the soils more susceptible to fluvial erosion and less susceptible to deflation. These brown valley soils are characteristic of large areas of the central steppe. Deeper brown calcareous soils or gypsiferous soils are found in the vegetated areas, particularly in alfa and olive growing regions (République Tunisienne, 1976).

East of the North-South Axis, there is a tendency for saline and saline-alkaline soils to predominate around the sebkha areas of the Sahel zone. For example, Brechtel and Rohmer described considerable variations in amounts of chlorides and sulphates in soils within a 5km radius to the east and south of Kairouan. These results are borne out by evidence from other sites in the Sahel zone (Hollis and Kallel, 1986), the salt works at Sahline providing excellent proof of high salinity near the Monastir coast. Salinity levels rise sharply within the sebkhas themselves. Active salt production can be found today in extensive areas along the southern margins of Sidi el Hani. Loamy silts and clays interspersed with sand are common in all sebkha and near-sebkha regions of the Sahel.

2.6. The vegetation of Central Tunisia.

The natural vegetation of central Tunisia has largely disappeared under the influence of man. In the upland areas around Hadjeb el Ayoun, alfa (Stipa tenacissima) and rosemary (Rosmarinus ericolyx) steppe vegetation has gradually encroached upon the natural pine (Pinus halepenensis) and juniper (Juniperus phonenecia) forests (République Tunisienne, 1976). The percentage cover of each species is a function of topography, soil and anthropogenic factors. At present 30% of the calcrete and pediment areas are covered by dense alfa steppeland.

The deeper soils in and around the Hadjel valley have been cultivated since Roman times, when the area was an important agricultural region (Brogan, 1967). The northern plains of the Hadjel and Cherahil valleys remain important areas of cereal, olive, apricot and almond production, particularly with the advent of effective irrigation from the Sidi Saad and El Houraréb reservoir schemes (Plate

2.4). In the Hadjel valley itself, where soils are more sandy, the removal of the natural vegetation cover and the intense cultivation of the Roman period led to increased deflation of exposed soils, culminating in a severe soil erosion problem extended by continuing poor agricultural practices (Hamza, 1985; Rapp and Hellden, 1979). Since the 1960s, attempts made by the Tunisian Ministry of Agriculture to control the spread of erosion have included the planting of stabilizing cactus hedges (Opuntia cambrensis) and small pine plantations on the southern flank of Djebel Henndi. However, large areas of cereals and plantations remain, covering over 7,000 hectares in the Hadjel valley alone (Figure 2.8; Plate 2.13; République Tunisienne, 1976).

Similar vegetation types characterise much of the Sahel zone (White, 1983). Interspersed with pockets of arable farming and rough grazing, large olive, apricot and almond plantations cover much of the area between the sebkhas and the coast (Plate 2.14). Individual plantations may cover many hundreds of hectares and although the tree spacings vary widely throughout the region, within-plot spacings are fairly constant. On the more fertile soils, a second or even third level of bush or cereal crops are grown beneath the tree canopy (Plate 2.15). This multi-layer agriculture has become increasingly common in the irrigated areas around Sousse and Monastir, where waters from the Nebhana reservoir scheme have allowed a level of cultivation hardly seen since the Roman period (République Tunisienne, 1984). However, the employment prospects offered by the growing tourist centres of Sousse and Monastir have proved more attractive than farming, leading to an increase in fallow and grazing land and a decrease in sub-plantation cereal agriculture. This is especially

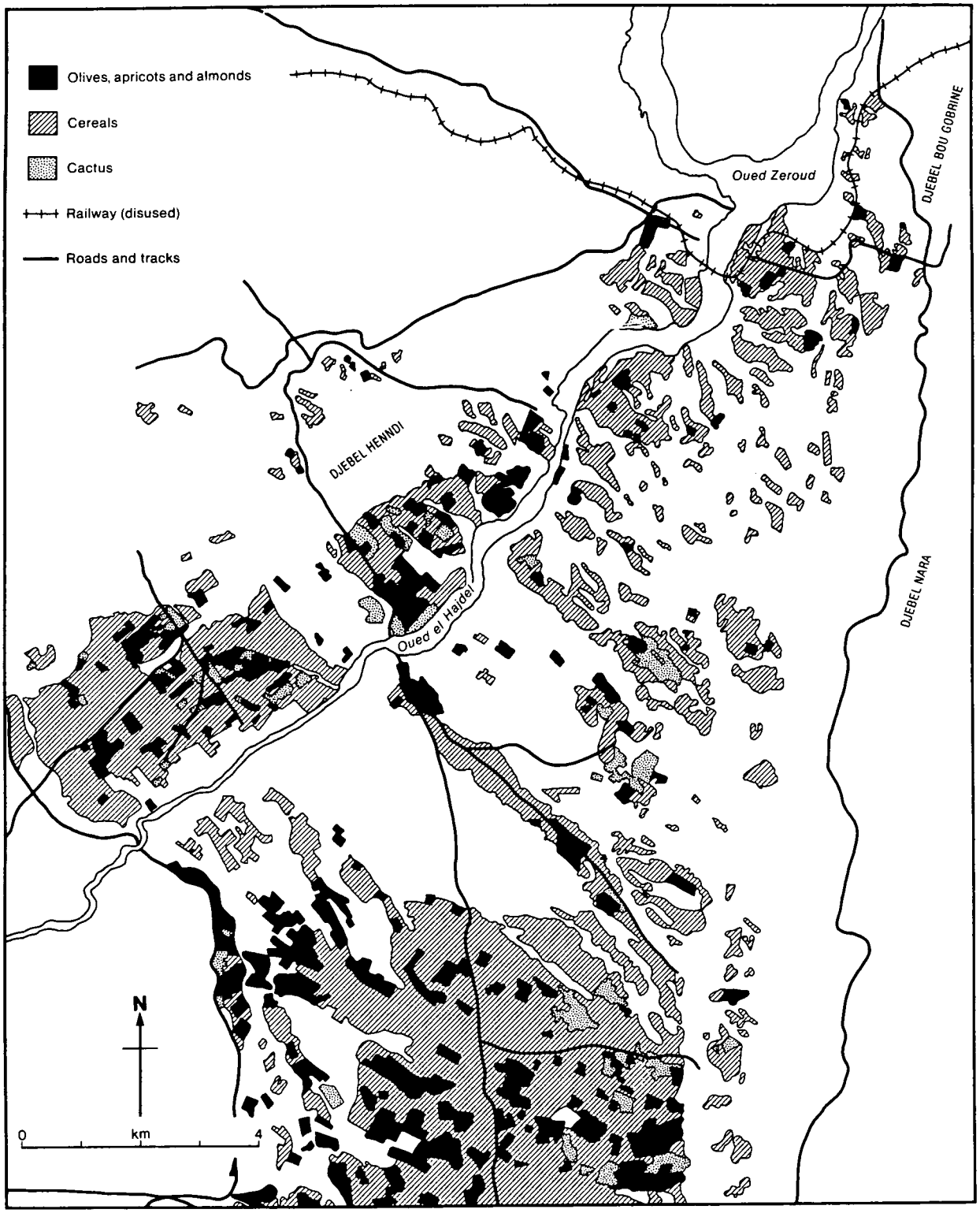

Figure 2.8 Vegetation in the Hadjel Valley (after République Tunisienne, 1976).

visible around the town of Sahline, about 8km west of Monastir.

The more saline soils surrounding the sebkhas of the coastal plain and inland basins support halophytic and scrub vegetation, Atriplex halimius and Lygeuni being amongst the most common varieties. The southern shores of Sidi el Hani are further delineated by eucalyptus forest which extends into the hill country south of the lunette dune. On the lunette dune itself rough grazing and thorn bushes predominate (Plate 2.16), the latter helping to protect the dune from the prevailing winds of the coastal plain.

Chapter 3 Radar Remote Sensing of the Environment: Theory and Practice.

3.1. Introduction: The Electromagnetic Spectrum.

Energy is produced and transmitted by electromagnetic radiation at various positions within the electromagnetic spectrum. The bands of the spectrum are defined by wavelength, and range from gamma rays with a wavelength of less than 0.1nm to very high frequency radio waves of up to 3x10 km in wavelength (Figure 3.1). In practice, the atmosphere blocks energy from large areas of the spectrum and transmission is only possible within three 'atmospheric windows'. These regions are:

(1) Visible and near infra-red (0.3μm-3μm)
(2) Thermal infra-red (3μm-14μm), and
(3) Microwave (1mm-1m).
Their location within the spectrum is represented in figure 3.1.

The visible part of the spectrum is subdivided into colours which can be observed by the human eye (blue, green, red, etc.). Together with the near infra-red, the visible wavebands are often used in remote sensing systems, the best known being the multispectral scanner (MSS) used by the early Landsat satellites. The value of the thermal infra-red waveband for environmental remote sensing has also been identified, particularly in soil moisture and heat loss applications. It has been combined with the visible and near infra-red wavebands in the Thematic Mapper (TM) operated by the more recent Landsat satellites. Both these sensors detect the 'passive' radiation of energy from a surface, and hence are dependent upon external illumination from an energy source, usually the sun.

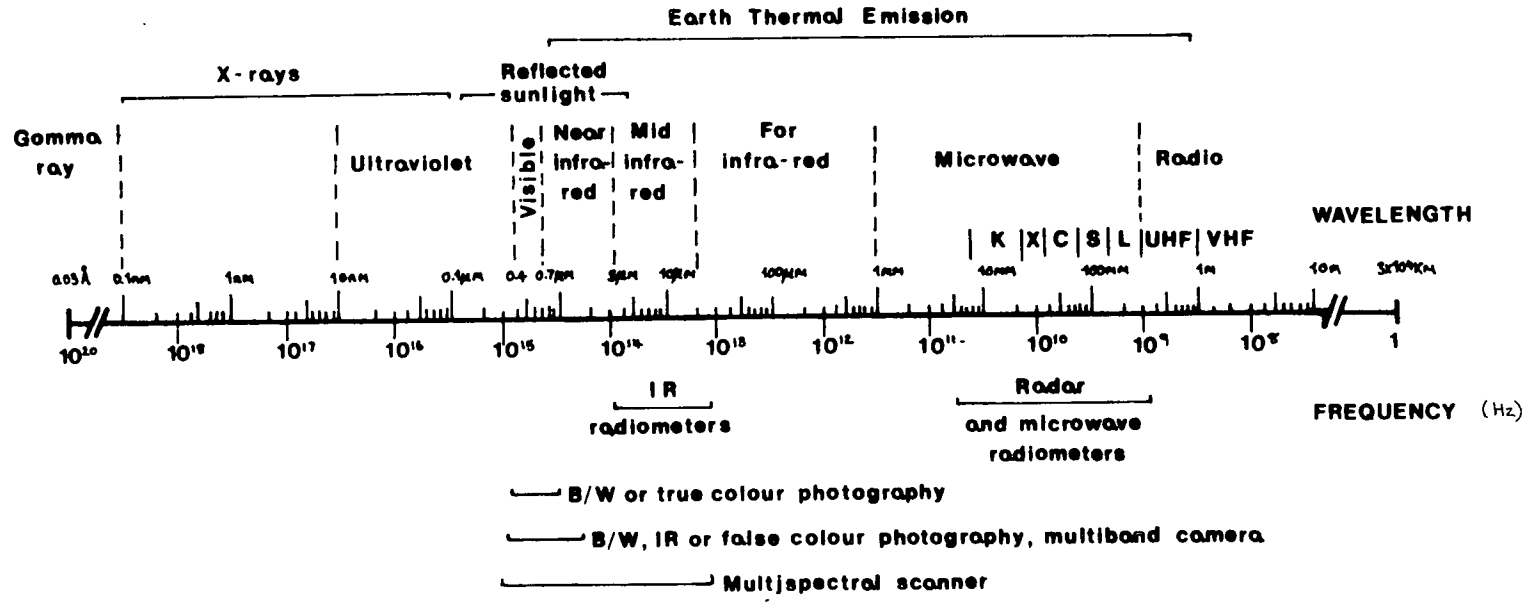

Figure 3.1 The Electromagnetic Spectrum (Trevett, 1986).

The microwave portion of the electromagnetic spectrum is much wider than those identified above, covering wavelengths from 1mm to 1m. It too is divided into bands with the letters K, X, C, S, L and F, as shown in Figure 3.1. The terminology is arbitrary, chosen during the Second World War in an attempt to confuse the enemy. Microwaves occur naturally and can be measured passively by microwave radiometers. However, microwave remote sensing usually relies on the transmission of microwave energy from a source to the surface of interest, the return signal from which is measured by the sensor. This type of 'active' remote sensing is used by all imaging radar systems, radar being an acronym for 'Radio Detection and Ranging'. Microwaves are capable of penetrating haze, cloud and light rain while still retaining their wave forms (Trevett, 1986).

Matter-energy interactions in all portions of the electromagnetic spectrum yield varying amounts of information about the environment. Certain surfaces, or vegetation cover types, have characteristic spectral responses, or fingerprints, at particular wavelengths, allowing them to be easily distinguished. This separability is dependent upon the interaction of the energy source with the substance in question, be it soil moisture, chlorophyll content or mineral composition. Much investigation has been made into the response of surfaces at visible and infra-red wavelengths and, although it cannot be claimed that the scientific basis is understood completely, the field is generally regarded as established. Satellite remote sensing at microwave wavelengths, however, is still in its infancy. Although widely recognised as a powerful new tool for interpretation and analysis of earth surface features, complementary to information recorded at shorter wavelengths, the full information content and potential

value of radar data are poorly understood (Harris et al., 1984; Trevett, 1986). This thesis attempts to extend the knowledge of radar as a remote sensing tool by examining the response of surfaces to microwave energy, particularly at the longer wavelengths of the L band. The findings are compared with complementary information obtained from the Landsat Thematic Mapper to allow reassessment of their value in the field of environmental remote sensing.

The operation of radar systems is a complex procedure and would require several volumes if it were to be described fully. A general knowledge of radar operation is vital for a good understanding of the images produced. However, it should always be borne in mind that a radar image is an interpretation tool, not an end in itself; thus a full understanding of sensor theory is only necessary when it serves to explain the nature of the image it produces. The following sections describe the historical development and the theory behind the use of radar as a remote sensing tool. Particular emphasis is placed upon microwave environmental science applications and radar interaction with land surfaces. A description of the response of other surfaces such as ocean waves and sea ice, at microwave wavelengths, has been omitted as it lies outside the boundary of the research project. The theory and operation of the Landsat Thematic Mapper Satellite is briefly summarised in Section 3.6.

3.2. Radar Remote Sensing: Background and Theory.

The reflection of radio waves from solid objects was first noted by Heinrich Hertz as early as 1886, and later by Hulsmeyer in 1904. It had also been observed that these waves were "scattered" upon reaching an irregular surface and could only be recorded if amplified sufficiently by a sensitive receiving device. Research on both sides of the

Atlantic by A.H. Taylor and James Watson Watt in the 1920s and 1930s led to the development of the Plan Position Indicator (PPI) radar for navigation and military target location. This system used a rotating antenna and provided information about the terrain in circular format using a cathode ray tube display.

By the beginning of the Second World War ground radar stations were in operation along the eastern and southern coasts of Great Britain. These stations could detect aircraft up to a range of 150 miles and were updated to detect low-flying aircraft once the war had begun (Hallows, 1947). PPI radars were also operated from a fixed antenna under an aircraft and generated high quality image products yielding a considerable amount of terrain-related information (Macdonald, 1980b).

During the early use of radar the appearance of objects other than specific military targets was regarded as 'ground clutter' and attempts were made to remove this from the image (Trevett, 1986). When PPI radar data became declassified in the 1950s civilian scientists realized that the previously unwanted ground clutter afforded useful geological and ground cover information. In addition, radar's cloud-penetrating capability prompted further research into this new method of environmental observation. A continuous-strip airborne radar was soon developed, which operated from an antenna directed perpendicularly to the flight path. These side-looking airborne radar systems, or SLARs, allowed the collection of reconnaissance imagery without the need to fly over unfriendly regions (Sabins, 1978), and were operated at shorter and shorter wavelengths, giving improved resolution over PPI imagery.

A SLAR system operates by sending an electromagnetic signal of constant wavelength and time from a pulse-generating device through a transmitter into the radar antenna. The antenna sends and receives the radar pulse alternately, controlled by an electronic switching device or duplexer. The signal received is a product of the interaction between the radar signal and the terrain and the time taken for it to travel to and from that terrain. The former regulates the intensity of the signal on the cathode ray tube (the highest returns producing the brightest signals) while the latter determines the position of the feature in the image. This is converted to distance so that rapidly-returning signals appear close to the flight path on the image and slower signals appear at the far range. This time response, together with the angle of transmission, determines the width of the radar image in the range direction, with distances in the azimuth direction controlled merely by the flight path of the host aircraft.

The speed at which the image film is advanced is usually adjusted to maintain the same scale in the azimuth and the range directions. The distance-time relationship can cause problems in range positioning, as objects in 'slant-range' format (direct distance between sensor and target) will have different horizontal spacings (ground range) (Figure 3.2). Non-linear sweeping can be applied to the cathode ray tube to obtain equivalent ground-range positioning, but this leads to severe distortion in mountainous terrain (Ulaby et al., 1981). Nevertheless, ground-range images are preferred for stereo viewing and mosaic preparation (Moore, 1983). The recording of data on optical film has gradually given way to digital storage in more recent years.

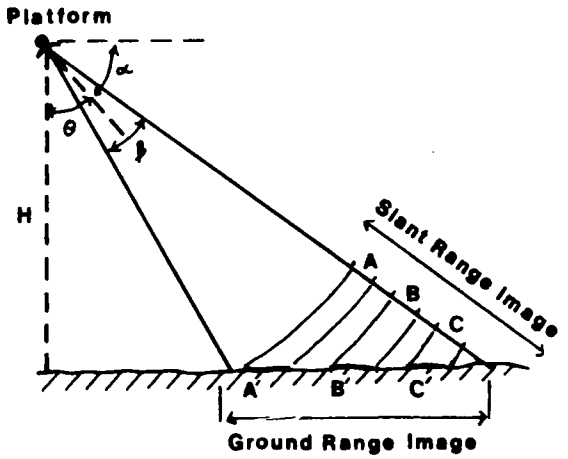

Figure 3.2 Slant Range and Ground Range radar geometry (after Wu et al, 1981).
α Depression angle
θ Incidence angle
β Antenna beamwidth
H Spacecraft altitude

Two types of SLAR system were developed in the 1950s. These came to be known as the Real Aperture Radar (RAR), and the Synthetic Aperture Radar (SAR). The two systems differ in their means of achieving resolution in the azimuth, or long-track direction.

In all RAR systems azimuth resolution is proportional to antenna beam width, which is determined in turn by the wavelength of the radar pulse and the physical size of the antenna being carried by the host aircraft. Two objects at the same range along track will only be resolved if they are separated by a distance greater than the antenna beam width at their range (Jensen et al., 1977). As antenna beam width increases in the range direction a systematic

decrease in resolution occurs. Thus, even aircraft supporting large radar antennas have limited azimuth resolution capabilities, especially at far range. A short-wave signal produces the finest azimuth resolution, but this advantage is offset by increased absorption of energy by atmospheric moisture in the form of cloud and haze (Long, 1983). RAR range resolution on the other hand is dependent upon pulse length, a short pulse generating a high resolution. Pulse length can easily be reduced to yield a finer range resolution. SLAR imagery obtained from Real Aperture Radar commonly has a resolution finer in the range direction than in the azimuth direction.

Realization of the limitations of RAR prompted research into Synthetic Aperture Radar (SAR) or coherent SLAR. SAR was invented by Carl Wiley, who named it the 'doppler beam sharpener' for reasons that will be discussed later. A Synthetic Aperture Radar is able to achieve fine resolution using a short antenna by recording the signal from a target at sequential positions within the radar beam as the host platform moves along track. As a target enters the beam, the distance from the radar is given as the time delay between signal transmission and reception. As the radar moves, the slant range distance between antenna and target alters producing a doppler frequency shift or phase change in the signal (Harger, 1970). The receiver records the time-delay and doppler frequency shift and uses it to synthesize a small aperture giving a theoretical resolution of:

$$Ra = L/2 \qquad \text{(Equation 3·1)}$$

where Ra = Azimuth resolution and L = Length of radar antenna.

Azimuth resolution is constant with range, as the increasing beam width generates an effective increase in synthesized antenna length at far range (Trevett, 1986). SAR operation is represented diagrammatically in Figure 3.3.

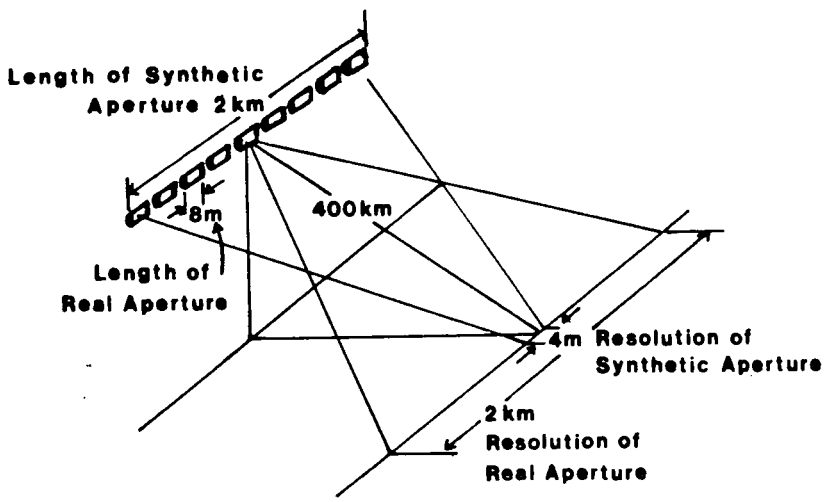

Figure 3.3 Synthetic Aperture versus Real Aperture resolution for spacecraft operating at a wavelength of 4cm (Ulaby et al, 1981).

SAR data are recorded on film as a complex series of opaque and transparent dashes which represent a one-dimensional phase interference pattern between the transmitted and recorded signal. The width of a dash corresponds to the length of the radar pulse whilst its distance from the edge of the film represents the target position in range (Jensen et al., 1977). The film onto which this information is recorded is a radar hologram. When this hologram film is illuminated by a coherent light source each dash scatters the incoming wave onto a lens

that recreates the pattern of radar waves received by the antenna in visible-light form. Since the hologram is a record of all the data from a terrain throughout the antenna beam width, the resolution of the created image is that of the synthetic-aperture and not the real-aperture antenna (Jensen et al., 1977).

At first sight the radar signal film is virtually uninterpretable and has to be carefully processed before it can be used in remote sensing applications. The processing can be optical or digital. Optical processing allows preparation of two types of final image product: the survey quick-look and the precision-processed image. The former can be used by the surveyor to determine the standard of the radar image, while the latter is used by most image interpreters and earth scientists.

Precision-processing of radar imagery is a complicated procedure requiring an optical correlator, of which few exist. The two main commercial systems are held by Goodyear Aeroservices and the Earth Resources Institute of Michigan (ERIM) (Trevett, 1986) (see Figure 3.4). Good optically processed SAR images are of high quality and can be used for most remote sensing applications (Trevett, 1977). They have the advantage of being able to be produced within an acceptable time limit.

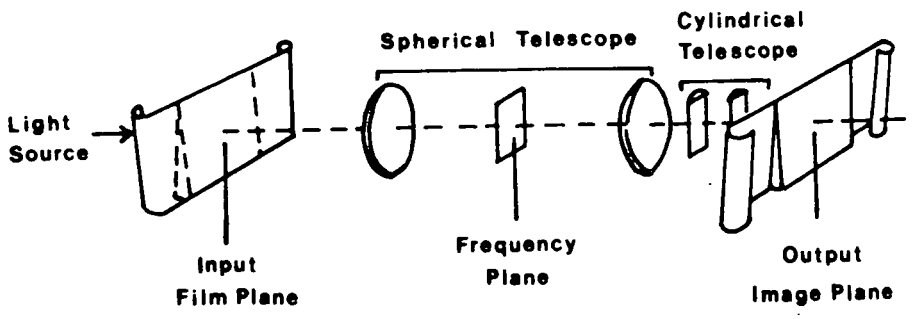

Figure 3.4 ERIM optical processor (Trevett, 1986).

Digital SAR processing systems do not have such an advantage. All radar signals returning from the terrain are recorded at high speed and onto high density digital tapes (HDDTs). Generally, a digital SAR system will contain a bandpass prefiltering mechanism, that divides the doppler return into equal parts (usually four) which are processed separately. Each section is called a 'sub-aperture' or 'look' and, once combined they form a complete image with significantly reduced 'speckle' (Wu et al., 1981). Look filtering also serves as a data reduction tool, an important consideration in digital SAR processing.

In addition, a digital SAR processor undertakes to correct for errors of 'range migration' or 'range curvature' caused by the change in slant range generated by the doppler effect. At satellite altitudes this condition is pronounced due to the motion and curvature of the earth, and is described as 'range walk'. The processor samples data in a way that minimizes geometric distortion in the final image product (Leaver, 1985, personal communication).

Once all the corrections described above have been undertaken, the final data are output either as a digitally-processed, optically-written image or as a computer compatible tape (CCT). The latter are coming into more common use, especially with the increase in satellite SAR systems. Digital data collection and storage allows an interpreter to combine and compare images with other digital remote sensing data such as Landsat data. The obvious advantage has a trade-off with the time taken to process the digital data. As yet, real-time, high-resolution digital SAR processing remains unfeasible, although this is likely to change in the future.

3.3. The Rise of Airborne Radar Remote Sensing in the Environmental Sciences.

The declassification of airborne radar data in the 1950s led to the wider use of SLAR imagery by civilian earth scientists and surveyors. Early observations of volcanic terrains as a pilot study for radar lunar investigations highlighted the potential of radar in geology and geomorphology (Bienvenu and Pascucci, 1962; Simons and Beccasio, 1964; Cambell and Ulrichs, 1969). In 1964 an interdisciplinary radar group was set up under the joint patronage of NASA and the U.S. Geological Survey. Over the next few years the group was responsible for the acquisition of large quantities of high quality SLAR data of the United States using a Westinghouse Ka-band RAR system (Matthews, 1975; Leberl, 1978; Macdonald, 1980a; Harris et al., 1984).

Numerous publications resulted from these studies, those of Dellwig and Moore (1966) and Dellwig et al. (1966) being among the most important in the historical development of radar remote sensing. Using like- and cross-polarized Westinghouse data, Dellwig and Moore (1966) identified the importance of terrain slope and surface roughness on radar backscatter from contrasting lithological units in the Pisgah crater area of California. They were among the first to suggest that it is the surface expression of lithology in terms of roughness that is important, rather than the lithological units themselves. They concluded that radar resolution, polarization and look angle were additional influential factors in the appearance of the final image, thus paving the way for the study of radar data in terms of system and ground parameters. These parameters are fully explained in Section 3.5.

In 1967 and 1969 the all-weather capability of radar was exploited in the first large-scale SLAR mapping project in a tropical area. The Westinghouse survey, known as project RAMP (Radar Mapping of Panama), covered much of Panama and northern Colombia and resulted in the preparation of regional topographical, hydrological, geological, geomorphological and vegetation maps at a scale hitherto made difficult by the inaccessibility of the terrain and thick cloud cover. Much of the data was examined in detail by Macdonald (1969), who concluded that radar was the only practical tool for reconnaissance mapping in humid tropical areas (Harris et al., 1984) on account of the thick cloud cover and difficult terrain. The reports of radar's ability to reveal hydrological features in tropical forests are also well documented. This capability results largely from the high backscatter recorded from sharp breaks in the forest at the margins of water courses facing the incoming radar signal, and the corresponding radar shadow at forest edges facing away from the sensor (Trevett, 1986). Other studies of RAMP data are documented by Wing (1970), Wing and Dellwig (1970), Lewis (1971), and Macdonald and Wing (1972).

Perhaps the largest and most famous of all the radar surveys was project RADAMBRAZIL, originally called project RADAM (Radar of the Amazon) in 1971. A total area of 8.5 million km^2 was covered by Goodyear Aeroservice X-band SAR to produce a huge radar mosaic. The survey was commissioned by the Ministry of Mines and Energy, but provided a wealth of geomorphological and vegetation information, further highlighting the importance of radar in tropical forest surveys (Correa, 1980; Ford and de Cunha, 1985; Trevett, 1986). The project was one of the first radar surveys to be supported by an extensive field program, giving vital access to concurrent ground conditions (Macdonald, 1980b).

Other areas in which early radar surveys were undertaken included Venezuela, Nicaragua and Nigeria, all showing the advantages of radar as a cloud-penetrating tool for tropical surveys (Parry and Trevett, 1979; Vincent, 1980; Trevett, 1986). In 1976 the NIRAD project in Nigeria yielded large amounts of strip imagery extending from the forests of the humid south to the arid Sahel in the north. The survey was conducted by Motorola Aerial Remote Sensing Inc., with Hunting Technical Surveys Limited undertaking field mapping and image interpretation. The survey is important in the history of radar remote sensing as it was the first real insight into the value of radar in arid environments. Whilst recognising the advantage of radar penetration through the "harmattan" dust haze in the north, Parry and Trevett (1979) considered that "...radar would possibly be less effective in the more arid areas". They were surprised to find that radar provided an excellent means of determining soil moisture in sparsely-vegetated areas, as the arrival of the rainy season generated different signal responses in strips flown at various times during the survey. Comparative studies made by Koopmans (1982, 1986) stressed the complementary nature of NIRAD survey data with that of traditional air surveys and the Landsat Multispectral Scanner.

European airborne radar surveys began in earnest in the 1980s with the instigation of the European SAR-580 campaign by the European Space Agency and the Joint Research Centre of the European Commission. The campaign, which took its name from the Canadian Convair 580 used as the host aircraft, had many objectives:

> "...the most important was to create an opportunity for the European Scientific community to work with airborne multi-channel and dual-polarization synthetic aperture radar, and to try to determine the future role of SAR in complementing optical sensors" (Koopmans, 1985),

in preparation for the launch of the European ERS-1 satellite (see Section 3.4.5.).

Over a period of four years from 1980 to 1984 large amounts of digital and optical data were collected from various test sites throughout Europe. Publications by principal investigators in each test site describe conflicting views as to the value of such radar surveys. Results from hydrological and soil surveys in England and Wales produced no clear evidence of a relationship between soil moisture and radar backscatter (Blyth, 1984). In 1986, Evans and Carroll went as far as to conclude that radar is likely to have little role to play in soil surveys in England and Wales. In contrast, the "distinct potential" of multi-frequency, multi-polarization SAR in crop classification was described by Sieber and Trevett in 1983 for two test sites in southern Germany. Rott (1983, 1984b) also described the value of airborne radar data in geomorphological studies of the Austrian Alps.

For all its problems, the European SAR-580 campaign focussed attention on the need for further investigation into the role of radar in all the environmental sciences (Trevett, 1984). Investigators came to realize the limitations in current knowledge of microwave surface and volume scattering , for example, and the need for further investigations, "particularly in arid and hyperarid areas" (Koopmans, 1985). Stereo modelling and coregistration of radar with information from the visible and infrared have

been recognised as important steps in the future of microwave remote sensing. These questions have been addressed in this research project, in the hope that understanding may be advanced.

3.4. Satellite Radar Remote Sensing: Systems Past Present and Future.

3.4.1. Introduction.

During the 1960s, NASA commissioned a study of potential possibilities offered by satellite borne radar systems for lunar surface mapping. Tests carried out over analogous terrestrial geological sites soon highlighted the great wealth of information that could be gleaned by radar. Further investigations in the 1970s demonstrated the potential of radar in ocean monitoring applications. These findings resulted in the launch of the Seasat satellite in 1978.

3.4.2. Seasat

Seasat was launched from the Western Test Range, Vandenberg Air Force Base, California on 26th June 1978 into a near-circular orbit 800km high at a nominal inclination of 108°. The satellite carried five sensors each having the primary objective of global oceanographic monitoring. The five sensors were:

(1) Radar Altimeter (ALT)
(2) Scatterometer (SASS)
(3) Scanning Multichannel Microwave Radiometer (SMMR)
(4) Visible and Infrared Radiometer (VIRR)
(5) Synthetic Aperture Radar (SAR).

Evaluation of the technology and performance of the first four sensors is beyond the scope of this project and can be found in several reports (Lipes et al., 1979; McClain and Marks, 1979; Born et al., 1979; Allan, 1983; Thomas and Minnett, 1986). The following paragraphs will describe the operation and performance of the Seasat SAR.

The Seasat SAR looked to the starboard of the satellite platform, its 100km swath centred 20.5° from nadir, as shown in Figure 3.5). Because of the curvature of the earth the incidence angle at the ground was approximately 3° greater than the complement of the depression angle (Ford, 1980; Koopmans, 1980; cf. Figure 3.5). The radar used an L-band signal with a wavelength of 23cm (frequency of 1.25 GHZ) and HH polarization. The SAR achieved a 23m resolution in range and 6m in azimuth. However, the azimuth illumination time was divided into four 'looks' to obtain a higher signal-to-noise ratio in each resolution element (Pravdo et al., 1983). Thus, the final image data had an approximate resolution of 25m x 25m. The various system parameters of Seasat are given in Table 3.1.

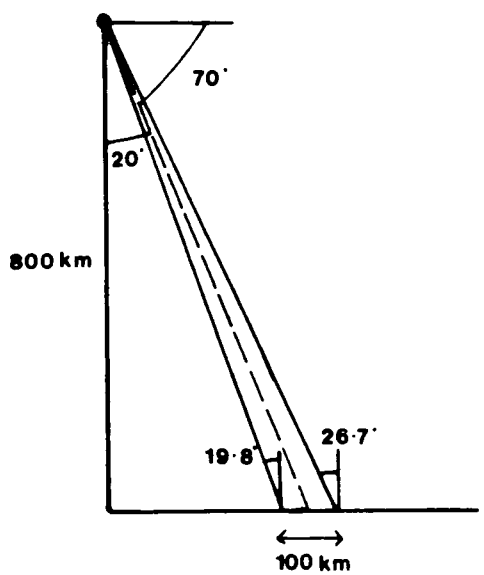

Figure 3.5 Seasat SAR imaging geometry (after Ford, 1980).

PARAMETER	SEASAT	SIR-A
Active Period	June - October 1978	November 1981
Orbit inclination	Polar 108°	38°
Altitude	794 km	c. 260 km
Frequency	1.275 GHz	1.282 GHz
Wavelength (λ)	23.5 cm	23.5 cm
Depression Angle	70° ± 3°	43° ± 3°
Incidence Angle (θ) (from vertical)	23° ± 3°	50° ± 3°
Polarization	HH	HH
Resolution	25 m	40 m
Number of looks	4	4 - 7
Swath width	100 km	50 - 55 km
Processing	Optical and digital	Optical

Table 3.1 Seasat and SIR-A system parameters.

The SAR was in operation for 106 days when on October 10th 1978, a massive short circuit in the electrical system brought the mission to an end. However, during its 1503 revolutions of the earth (14 each day) Seasat had collected around 10 million km^2 of imagery between latitudes 72° north and south. In December 1978 the Seasat Data Utilization Project was formed to determine the utility of Seasat as an oceanographic observation tool. The final report, published in July 1982 (Born et al., 1982), concluded that Seasat had indeed achieved accuracies equal to, or in excess, of the original goals. However, the extent to which the results could be extrapolated to other areas or times was unclear as:

> "...only a limited number of comparisons of satellite and in situ data were made, and these comparisons were for a few locations, for a few times" (Born et al., 1982).

The importance of time lag between image and ground data collection in the Tunisian study area is considered in Chapters 5 to 8.

Seasat had no provision for on-board data recording so data were telemetered to five ground-receiving stations over an analogue data link (Wu et al., 1981). The signal was digitised and recorded onto a High Data Rate Recorder (HDRR). Processing, which consisted of range compression, doppler estimation, azimuth correlation and multiple-look overlay, was then undertaken. Most of the Seasat SAR data was optically processed by ERIM's Precision Optical Processor (Figure 3.4). A small proportion of the data (3%) were digitally processed using the Interim Digital Processor (IDP) at JPL. Because of the location of the five receiving stations, 65% of the data covers land areas in North America, the Caribbean and Western Europe (Figure

1.1; Pravdo et al., 1983). With these points in mind it is extremely fortunate that digital Seasat imagery is available for the study area in eastern Tunisia. The image used for the research project (Revolution 719) was recorded on August 16th 1978 at an approximate time of 6.40 GMT at Oakhanger receiving station (see Figure 1.1, Plate 3.1).

Optically processed Seasat imagery had many sources of radiometric and geometric calibration error resulting from antenna gain problems, resolution degradation and the limited dynamic range of signal and image films (Pravdo et al., 1983), and is therefore not suitable for quantitative measurement of backscatter. Digital processing of Seasat imagery has provided improvements over optical data products, although data skew problems and limited radiometric calibration ensure that careful quantitative image assessment only should proceed (Stewart et al., 1980). Measurements of image tone cannot be directly related to radar backscatter (Ford et al., 1980), but can be used as directional indicators in quantitative studies. Additional information on the data processing and performance of Seasat SAR can be found in: Jordan and Rodgers (1976), Brown et al. (1979), Jordan (1980), Bennet et al. (1980), Wu et al. (1982), Benson (1984) and ESA (1984).

In addition to the numerous studies of oceanographic application of Seasat SAR (Gonzalez et al., 1979; Harris et al., 1984), many excellent geological and vegetation investigations were carried out over land. The large depression angle of Seasat caused severe foreshortening and layover in mountainous areas (see Section 3.5.5) (Martin-Kaye and Lawrence, 1983a; Martin-Kaye et al., 1983; Rott 1984b) but the value of Seasat data for geological interpretation in areas of more moderate relief

has been stated widely (Elachi, 1971; Sabins et al., 1980; Blom et al., 1984; Wadge and Dixon, 1984; Dixon et al., 1985; Mackenzie and Ringrose, 1986). In their study of the vegetated limestone regions of Jamaica, Wadge and Dixon (1984) found that they could differentiate between areas of different karst geomorphology on the basis of variations in SAR image texture. Blom et al. (1984) detected igneous dykes buried beneath 2m of alluvium when analysing a Seasat image of Means Valley in the Mojave Desert. Several authors found that digital image analysis of Seasat data yielded important additional information (Daily, 1983; Dixon et al., 1985). These studies bode well for the Tunisian project, suggesting that Seasat SAR imagery can provide a wealth of terrain related information.

3.4.3. Shuttle Imaging Radar-A (SIR-A).

The Shuttle Imaging Radar-A was carried on the second flight of the space shuttle Columbia on November 12th 1981 with the primary objective of furthering the understanding of radar signatures of geological features (Cimino and Elachi, 1982). This SAR system was modelled on the design for the Seasat system. It too used an L-band (23cm) wavelength and HH polarization, but other system parameters differ considerably. The main difference between the systems is the shallower 43° depression angle of SIR-A which was designed with geological applications in mind. A further difference is the reduced (40m) resolution of SIR-A, as opposed to the 25m resolution achieved by Seasat. This resolution was determined using a corner-reflector array in the Lake Henshaw area of California (Cimino and Elachi, 1982). Comparison of the Seasat and SIR-A system parameters can be found in Table 3.1.

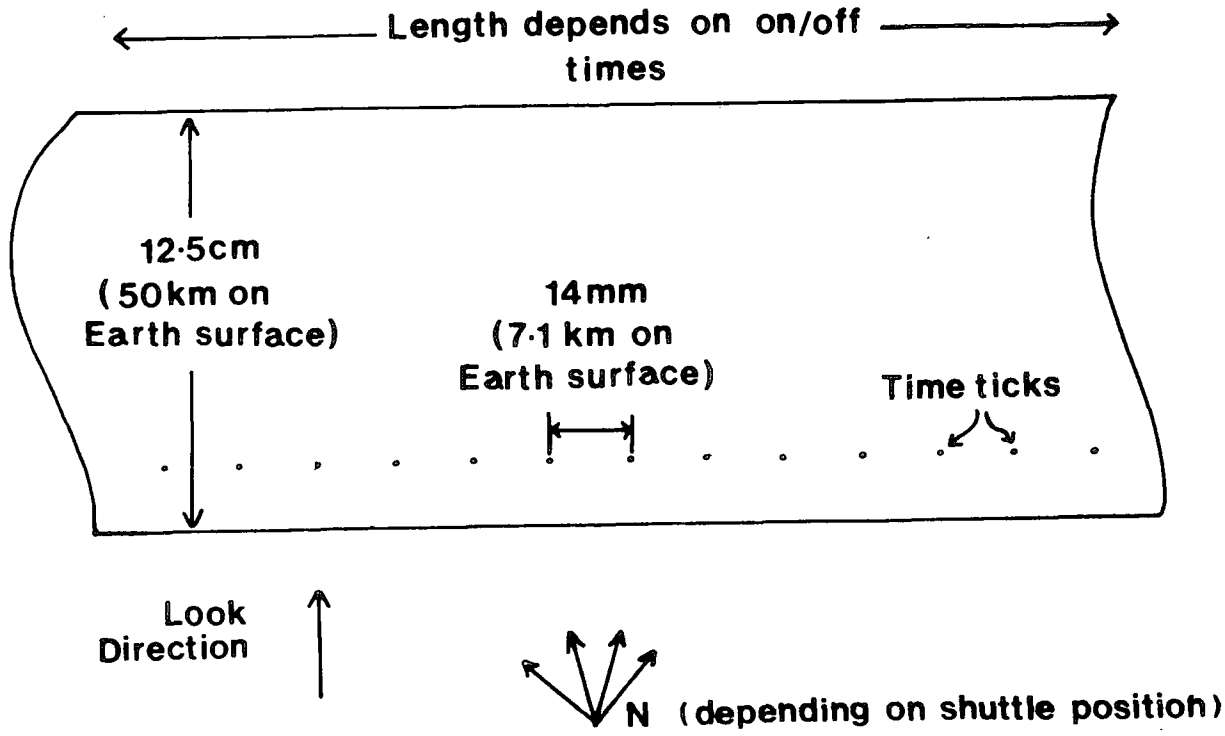

Figure 3.6 SIR-A film image format (Cimino and Elachi, 1982).

SIR-A achieved a near circular orbit with an inclination of 38° and average altitude of 259km. Unfortunately, the flight was cut short and the original SIR-A flight plan had to be abandoned (Martin-Kaye and Lawrence, 1983a), but the on-board optical film recorder was able to record about 10 million km^2 of imagery with a 50km swath width between latitude 40.8°N and 35.6°S. The signal film was then processed in an optical correlator at JPL into image film format (Figure 3.6). Each image can be identified by a data-take number and geographical location (Cimino and Elachi, 1982). The SIR-A image swath can be found in Data Take 32-33 of November 4th 1981. The location of the swath, together with other SIR-A and Seasat data is shown in Figure 1.1 and Plates 3.2 and 3.3.

Like Seasat, SIR-A had no calibration facility and no attempt was made to calibrate the sensor so that absolute measurements of radar backscatter could be made. However, quantitative interpretation and limited quantitative analysis is valid (Cimino and Elachi, 1982). It is possible to use the backscatter profile with range of a smooth ocean target to overcome some of the optical-processing calibration problems (Cimino and Elachi, 1982). Use of such information for image correction in the Tunisian study area is discussed in Chapter 4.

The SIR-A mission will be best remembered for its dramatic revelation of the subsurface palaeo-drainage patterns of the Eastern Sahara (McCauley et al., 1982; Breed et al, 1983; McCauley et al., 1986; Schaber et al., 1986). A considerable amount of geological and land use information was gleaned from SIR-A images of other climatic areas ranging from semi-arid to humid-tropical (Martin-Kaye and Lawrence, 1983b; Theilen-Willige, 1984, 1985; ; Ford and Sabins, 1985). Sabins (1983b) concluded that the low depression angle of SIR-A enhanced subtle

topographic features in mountainous regions of Indonesia. These topographic features could well be the surface expression of geological features. Similar conclusions were recorded by Longoria (1985) in north-eastern Mexico. Uses of SIR-A imagery in land use and settlement pattern applications have been documented by Lo (1984) and Jiyuan et al., (1986). There have been two excellent overviews of the SIR-A mission published by scientists at JPL (Ford et al., 1983; NASA-JPL, 1983). The complementary nature of data obtained from SIR-A (or Seasat) and the Landsat Satellites has been stressed in many publications and will be discussed in Section 3.6.

3.4.4. Shuttle Imaging Radar-B (SIR-B)

Previous comparative studies of SAR imagery from Seasat and SIR-A recognised the importance of dual incidence angle imagery in providing relief and roughness information (e.g. Elachi et al., 1982). Such studies resulted in the implementation of a multiple incidence angle SAR in the SIR-B flight of 1984. With its variable depression angle of 15°-60°, SIR-B was the first in a series of proposed multi-parameter SAR's as radar scientists became more aware of the opportunities these offered (NASA, 1982, 1983). Unfortunately, the mission was beset with problems ranging from antenna mis-orientation to problems in data transmission, which led to the cancellation of many of the proposed experiments (Trevett, 1986). Nevertheless, as more and more research into SIR-B image analysis is published the value of multi-incidence angle imagery is clearly evident.

Several important studies were undertaken in arid regions to further the understanding of SAR penetration capabilities (Berlin et al., 1984; Schaber, 1984; Taranik, 1984; Richards, 1984). Computer image processing of SIR-B

imagery from the Al Labbah Plateau, Saudi Arabia, in conjunction with field investigations resulted in increased understanding of the nature of L-Band signal penetration (Berlin et al., 1986). Other important geological investigations of SIR-B imagery are reported in Cimino and Wall (1985), Farr and Massonnet (1985), Lynne and Taylor (1986), Fielding et al. (1986) and Lowman et al., (1987). Application of SIR-B imagery to pedological and vegetation mapping (Wang, 1984; Hoffer, 1984) has also yielded important information on the relationship between radar incidence angle and surface-related backscatter (Wang et al, 1986; Cimino et al., 1986b; Dobson and Ulaby, 1986). Detailed investigation into SIR-B coverage of agricultural areas in Germany was undertaken by scientists at DFVLR and the University of Stuttgart. Sieber (1984) and Sieber and Noack (1986) chronicle the results of airborne SAR and ground studies undertaken during the SIR-B flight of 1984. Although the revised flight plan left many areas devoid of coverage reducing the amount of calibrated imagery, the results afforded encouraging prospects for future multi-parameter missions of agricultural areas (Sieber, Personal Communication). Interesting results were obtained from SIR-B images of flooded areas (Richards et al., 1987; Imhoff et al., 1987). Imhoff et al. (1987) suggest that digital analysis of SAR data can aid the delimitation of flood boundaries and help in management programs.

Some of the most important results of the SIR-B mission were in the region of stereo-radargrammetric mapping. The multiple incidence angle allowed investigation into the possibilies afforded by stereo analysis in a number of test areas (Kobrick, 1984). A series of studies of such imagery over Argentina provided encouraging results (Domik et al., 1986; Leberl et al, 1986).

3.4.5. Future SAR Missions.

> "Although traditional methods will continue to be used, imaging radar science is clearly evolving toward a much more quantitative and analytical approach as multiparameter calibrated SAR's become available" (NASA-JPL, 1982).

The 1990s promise to be an exciting period for spaceborne radar, with several multi-parameter missions planned in various parts of the world.

(a) SIR-C and SIR-D.

Two further missions are planned for the early 1990's (Elachi, 1983; Evans et al., 1985). In addition to having multiple incidence angles of 15°-55°, SIR-C will operate a multiple wavelength, multiple polarization SAR with 30m resolution. L-band, C-band (and possibly X-band) imagery will be available across the whole range of like- and cross-polarization (NASA-JPL, 1983, 1986; Ottl and Valdoni, 1985). Two flights are planned, thereby providing dual-season coverage for vegetation and hydrological studies. All imagery will be digitally collected and processed and emphasis will be placed upon improved geometric and radiometric calibration.

NASA-JPL (1986) considers this multiparameter system in three-dimensional parameter space defined by wavelength, polarization and incidence (Figure 3.7). If one compares the parametrical possibilities offered by the fixed-parameter Seasat and SIR-A systems (and even the multi-incidence and SIR-B) with SIR-C, the improvement is dramatic. The possibilities offered to geological and land-cover investigations are also dramatic. The dual-wavelength facility will allow quantification of the

roughness dependence of backscatter from a whole series of surfaces from geomorphological features to forest stands. Multi-polarization will allow studies of surface and volume scatter to be undertaken from calibrated imagery. In addition, research into multiple-incidence stereo-radar imagery and radargrammetry will continue.

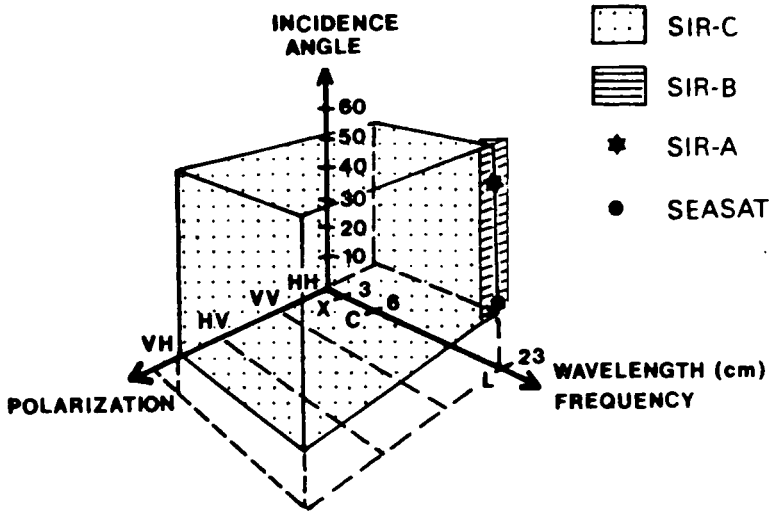

Figure 3.7 System parameter coverage of Seasat and the Shuttle Imaging Radars (NASA, 1986).

Three further satellite SAR missions are planned for the 1990s: The European Earth Resources Satellite (ERS-1), its Japanese Equivalent (JERS-1) and the Canadian Radarsat project.

(b) ERS-1

The European Space Agency's ERS-1 satellite, due for launch in 1989 from the Kourou Space Centre in French Guiana, is primarily designed for ocean monitoring and coastal and ice applications. The satellite will have a sun-synchronous circular orbit with a 3-day repeat cycle, inclined at an angle of 98.5° at an altitude of 780km (ESA, 1984). The design for ERS-1 is being undertaken by

an industrial consortium headed by Dornier Systems of Germany (Haskell, 1983a; Dornier, 1984).

The satellite will use the multi-mission platform developed for the French SPOT satellite on which various instruments will be deployed. These will include a wind scatterometer, a radar altimeter, an along-track scanning radiometer, a precise range and range-rate experiment (PRARE) and an active microwave instrument (AMI). The AMI will be capable of operating in imaging or wave mode, the former allowing acquisition of SAR imagery. The SAR parameters are fixed: C-band wavelength, HH polarization, 30m resolution and 23° incidence angle; essentially being a C-band equivalent of Seasat. The SAR signal data will be telemetered to the ground receiving station at Kiruna in Sweden and then digitally processed using a multi-look high-throughput and high precision processor (Jones et al., 1983; BNSC, 1987; George and Guignard, 1987; Noack et al., 1987). Emphasis has been placed upon system calibration, although scientists have been quick to stress the problems of calibrating such a complex system (Haskell, 1983b; Francis, 1983; Hartl, 1983).

The satellite will be followed by ERS-2 and ERS-3 as a continuation and back-up facility (Trevett, 1986). Both will have the same system specifications as ERS-1, but ERS-3 will be a land-orientated platform (Haskell, 1983c). The use of a C-band SAR could present problems for terrain applications as little C-band data has been available so far. This problem should be overcome by pre-flight image simulation (ESA, 1985).

(c) JERS-1

The Japanese Space Agency plans to launch its own orbiting SAR satellite in the 1990s. JERS-1 will be an L-band SAR with an incidence angle of 33°. Signal data will

be received at the Japanese receiving station and other ground stations.

(d) Radarsat.

The Canadian Centre of Remote Sensing (CCRS) is in the final planning stages of its spaceborne SAR, Radarsat. Primarily designed for ocean and ice studies, the C-band Radarsat will also be capable of recording data for land applications on a global basis (Trevett, 1986). The system will have HH polarization and a variable incidence angle of 20°-45°. Signal data will be sent to the ice information centre in Ottawa where it will be digitally processed. Emphasis has been placed upon the development of a fast processing system to allow maximum use of the ice monitoring information (Harris et al., 1984). The project had an initial British involvement in platform design but a recent government decision necessitated withdrawal through lack of funding. The project now promises to be a joint Canadian-United States venture with the platform due to be launched from the Space Shuttle in the early 1990s.

All four of these proposed systems will provide much valuable information at microwave frequencies about the earth's oceans and land surfaces. At the end of the coming decade great advances will have been made in the understanding of the interaction of radar with the environment, allowing this wealth of information to be extracted. The comparison of Seasat and SIR-A imagery in this project makes some contribution to the advance of SAR multi-parameter understanding.

3.5. Radar and the Environment: System and Target Considerations.

3.5.1. General Characteristics of Radar Return.

Radar system performance is described by the radar equation which relates the power received to the characteristics of the system and the nature of the target. The SAR radar equation may be written:

$$Pm = 2(4\pi)^3 KT \frac{F(S/N)_o \alpha R^3 V}{G^2 \lambda^3 \sigma_o X} \qquad \text{(Equation 3·2)}$$

Where:

Pm = Mean transmitted power
F = Receiver noise factor
$(S/N)_o$ = Minimum signal to noise ratio at processor output
α = System and propagation losses
R = Maximum range
V = Maximum track velocity
G = Antenna gain
σ_o = Minimum terrain echo area per unit area (scattering coefficient)
X = Linear azimuth per range resolution

(After Harris et al, 1984)

In general, the average scattering coefficient, σ_o, is a function of radar wavelength, polarization and look angle together with the geometric and dielectric properties of the target. Thus backscatter can be described as:

$$\sigma_o = f(\lambda, \phi, \rho, \theta, \varepsilon, \Gamma_1, \Gamma_2, \nu) \qquad \text{(Equation 3·3)}$$

Where:

- λ = Wavelength
- ϕ = Angle of incidence
- ρ = Polarization of incident wave
- θ = Aspect angle
- ε = Complex dielectric constant
- Γ_1 = Surface roughness on a microscale greater than /10 of the air/solid boundary
- Γ_2 = Sub-surface roughness of a second layer where the signal can penetrate the first layer to a significant degree
- ν = Complex volume-scattering coefficient in heterogeneous media

(After Simonett and Davis, 1983)

The three system characteristics are usually held constant by radar design, effectively ensuring that return power is solely dependent on the nature of the target (Fung and Ulaby, 1983). Nevertheless, variation of radar parameters over the same target will yield a changing backscatter response.

Intrinsically, a radar image appears similar in character to a traditional air photograph in which analysis is based upon interpretation of image texture, tone and context. Early radar surveys adopted similar methods of interpretation, often with high degrees of success. Traditional interpretational skills certainly have their place in the analysis of radar imagery, but the significance of target interactions with an active microwave signal cannot be ignored. A full understanding of the interaction between ground and sensor parameters and their influence on radar return is vital to valuable use of radar imagery in the environmental sciences. Indeed, backscatter models seem to be the way forward in the scientific evaluation of radar data as "...the quantitative use of radar data in a number of application areas is rapidly approaching" (Blanchard, 1980).

The following sections describe the various radar system and ground parameters. Although they are discussed separately they have a high degree of interaction and should not be regarded as mutually exclusive (Stone, 1985). In addition, system parameters specific to the SIR-A and Seasat satellite systems are discussed so that parameters relevant to the research project may be identified.

3.5.2. Radar System Parameters: Resolution.

Radar resolution is a complex parameter to understand as, unlike conventional remote sensing systems, it is 'detectability' rather than 'resolvability' that is important (Macdonald, 1980b; Harris *et al.*, 1984). In theory, a radar resolution cell is determined by resolution in the range and azimuth directions, as explained in Section 3.2, with SAR azimuth resolution being far superior to that of RAR (see Figure 3.3). In

practice, it is possible for objects much smaller than the given resolution to be detected and vice versa. If a target has higher backscatter properties than the surrounding area (a corner reflector, for example), it may well be detected on the resultant image. An excellent example of this 'detectability' is cited by Trevett (1986), who described the appearance of highly-reflectant street lamps on a road bridge while the bridge itself (which is larger than the resolution cell but has a smooth, low-backscatter surface) is invisible on the radar image. Realization of the dependence of radar on target properties is vital in subsequent image interpretation.

Unfortunately there is a trade-off between spatial and radiometric resolution for most SAR systems, the radiometric resolution being a

> "...measure of accuracy with which the microwave reflectivity of the terrain can be ascertained" (Frost, 1984).

Simonett and Davis (1983) define radiometric or 'grey-level' resolution as:

> "...the ratio of the 90 percent level to the 10 percent level on the signal-fading distribution for a number of independent samples averaged for each pixel"

and state that:

> "...the value of the grey-level resolution decreases as the number of independent samples averaged for each pixel increases",

causing an inverse relationship between pixel dimensions and radiometric resolution. The number of independent samples, and hence radiometric resolution, can be increased by increasing the number of 'looks' or 'sub-apertures' in the image, thereby reducing speckle (Li et al., 1983, 1985). The trade-off has been explored by several radar scientists though textural discrimination studies (Simonett and Davis, 1983; Frost et al., 1984). Frost et al. (1984) found that a radar system with four looks and a 25m spatial resolution enabled five natural texture signatures to be discriminated. A decrease in looks or spatial resolution led to a decreased capacity to separate the textures. In his survey of user preferences, Ford (1982) found that, in geological applications, higher spatial resolution was more important than a greater number of looks.

An understanding of the implications of radar spatial resolution and number of looks averaged is necessary for image interpretation and analysis. The Seasat SAR and SIR-a systems differ in both these capacities (Table 3.1). Seasat achieves a spatial resolution of 25m in azimuth and range as opposed to the 40m resolution of SIR-A. This difference is largely due to radar processing functions determined by various algorithms and has been confirmed by observations of corner reflectors in the field (Wu et al., 1981; Cimino and Elachi, 1982). To some extent the spatial deficiency of SIR-A is counteracted by the use of up to 7 looks (6 in the azimuth direction) capable of achieving a higher radiometric resolution than the 4-look Seasat system. In most instances, however, SIR-A used 4-5 looks, bringing it into line with the Seasat filter. The relevance of resolution differences between the two satellite systems is examined in Chapters 5 to 8.

3.5.3. Radar Wavelength.

The width of the microwave portion of the electromagnetic spectrum was discussed earlier in Section 3.1. Each band within the microwave region (Figure 3.1) covers a much greater range of wavelengths than the corresponding subdivisions within the visible and infrared. As wavelength is largely dependent upon radar antenna design, it becomes more difficult for a radar system to have a multi-wavelength capacity, something taken for granted in conventional multispectral remote sensing (Trevett, 1986). Most radar systems are designed to operate within a specific waveband: generally X, K or L and, more recently, C. It is important to have a clear understanding of the difference between target/signal response at each wavelength.

The significance of radar wavelength (λ) is largely a function of backscatter variations caused by signal interaction with geometrical and dielectric ground properties (Schaber et al., 1976, 1980). In general terms, the use of shorter wavelengths (K or X band) will yield more surface roughness information than long wavelengths (L band). As a general rule, it can be said that a surface will appear 'smooth' on a radar image, if the average height and spacing of irregularities is less than a quarter of the wavelength of the signal. If irregularities exceed this, the surface will appear 'rough'. On the whole, therefore, surfaces will appear relatively more smooth at longer wavelengths such as the 23.5cm wavelength (L-band) used by the Seasat and SIR-A (Sabins et al., 1980). This is an important consideration to bear in mind in image evaluation. The relationship between wavelength and roughness has been described by various equations, and is explained more fully in Section 3.5.8.

Longer wavelengths have other capabilities. Depending on the moisture content and other dielectric properties of the soil (Section 3.5.7), L-band radar signals are capable of penetrating the surface to reveal subsurface features at depths of up to 3m (Podwysocki et al., 1985; McCauley et al.,1986). The spectacular results from the L-band SIR-A and SIR-B coverage of hyperarid areas of the eastern Sahara are well documented (McCauley et al., 1982, 1986; Breed et al., 1983; Dixon, 1984; Elachi et al., 1984). The revelation of palaeodrainage channels and subsurface geology in these areas led to a major revision of previous theories of morphological and hydrological evolution. The extent to which an L-band signal can penetrate soils with higher moisture contents is incompletely understood, although it is generally believed that a small increase in moisture content dramatically reduces penetration (McCauley et al., 1982). Careful field and laboratory analysis is necessary in various environments before empirical and mathematical models will have developed sufficiently for them to contribute to image understanding (McCauley et al, 1982; Schaber 1984). The possibility of some penetration in the Tunisian study area must not be discounted, although the effect may be difficult to assess.

Wavelength not only determines ground surface penetration, but also the amount of penetration through a vegetation or crop layer. Some degree of penetration may be required for studies of geology or soil moisture conditions beneath a vegetation canopy (Sieber, 1984; Trevett, 1986), precluding the use of short wavelength signals. On the other hand, vegetation and crop-type discrimination is possible at short wavelengths (X and C) which allow less canopy penetration (Sieber and Trevett, 1983; Sieber and Noack, 1986) although L-band radar has

proved capable of discriminating large-grain agricultural crops (Mehta, 1984).

Convincing studies of L-band radar backscatter from forest stands have been made by Ford et al. (1985), Simonett et al (1987) and Richards et al (1987b). Simonett et al (1987) found that, at L-band, radar backscatter is largely dependent upon ground and trunk interaction with the canopy serving only as an absorption medium. The effect of this interaction proportionally increases with tree spacing. SIR-A and Seasat backscatter from olive trees in examined in Chapters 6 and 7.

In any radar survey it is desirable to appreciate the influence of radar wavelength upon backscatter before any valuable interpretation may be made. Much work still needs to be done before the full effects of wavelength are known. Recent multi-frequency systems such as the European SAR-580 radar, have provided interesting and useful results supporting the view that multi-frequency radar is desirable in geomorphological and vegetation mapping (Schaber et al., 1976; Jackson, 1980; Stewart et al., 1980; Haskell and Sorensen, 1982). Continued research should enable environmental scientists to be in a much stronger position when discussing system requirements for future radar surveys.

3.5.4. Radar Polarization.

> "The polarization of an electromagnetic wave describes the orientation of the electric field strength vector at a given point in space during one period of oscillation" (Macdonald, 1980b)

Most imaging radar systems transmit an horizontally-polarized waveform and record the returned signal in the

same polarization. This 'like-polarized' signal is given the notation 'HH' or horizontal-transmit-horizontal-return. On reaching the surface some degree of depolarization of the signal occurs, depending upon the geometry of the target and the roughness and homogeneity of the surface materials. This depolarization can be recorded by adding a vertically-polarized receiving antenna to the radar system (Trevett, 1986). This signal is given the notation 'HV' and is referred to a being 'cross-polarized'. Similarly, a like-polarized VV signal or cross-polarized VH signal can be used.

Radar images of the same surface at different polarizations exhibit different characteristics, largely due to the physical interaction of the signal with the surface. Daily et al (1978, 1979) found that like-polarized radar backscatter is dependent upon the size of surface irregularities in relation to the wavelength of the signal, while cross-polarized backscatter is dependent upon the overall roughness character of the surface, including particle shape and packing density. The relationship between depolarization, wavelength and surface roughness has been studied by many scientists (Rebillard, 1980; Blom and Elachi, 1981; Fung and Eom, 1983; Evans et al., 1985; Blom et al., 1987), and is further examined in Section 3.5.8.

Differing image characteristics between like- and cross-polarized backscatter can be exploited to allow discrimination between lithological units and surface types (Dellwig and Moore, 1966; McCauley, 1972: Daily et al., 1978; Elachi et al., 1980; Macdonald, 1980b; Blom et al., 1987). Blom et al (1987) conclude that, based on results from two test areas in the United States, HH polarization is useful for discriminating lavas, while sedimentary rocks can be discriminated more easily from VV

polarized imagery. Although Blom et al (1987) admit that their results could be heavily dependent upon the surface material used in the study and cannot necessarily be universally applied, the importance of surface properties on radar depolarization should not be underestimated.

More recently, there has been concentration of research upon examination of the effects of vegetation cover upon radar signal depolarization (Ford et al., 1985; Evans et al., 1986; Wu and Sader, 1987; Ulaby et al, 1987). Ford et al (1985) found that in forested areas distinct polarization could be correlated with tree size, distribution and density, with widely-spaced trees producing a high like-polarization (HH) response and areas of dense forest with understorey giving a high cross-polarized (VH) response. Later studies by Evans et al., (1986) and Wu and Sader (1987) have confirmed these results.

As described in Section 3.4., the SIR-A and Seasat satellite SAR systems used a like-polarized HH signal. As yet, no cross-polarized radar imagery is available from space altitudes, making a comparative study of polarization effects impossible in this research area. This uniformity of polarization (and wavelength) achieved by a combined study of Seasat and SIR-A data does allow the effect of surface roughness upon radar backscatter to be evaluated more easily (see Section 3.5.8. and Chapter 6). Recognition of the advantages of multipolarized imagery led to proposals for a multipolarization facility to be included on the future SIR-C and SAMEX (Shuttle Active Microwave Experiment) Satellite (Evans et al., 1985; Trevett, 1986). It has been suggested that multipolarized radar data is of more use in target discrimination than multiwavelength data. Undoubtedly, it is technically more feasible and is a cheaper option, and will have an important role in future SAR programs.

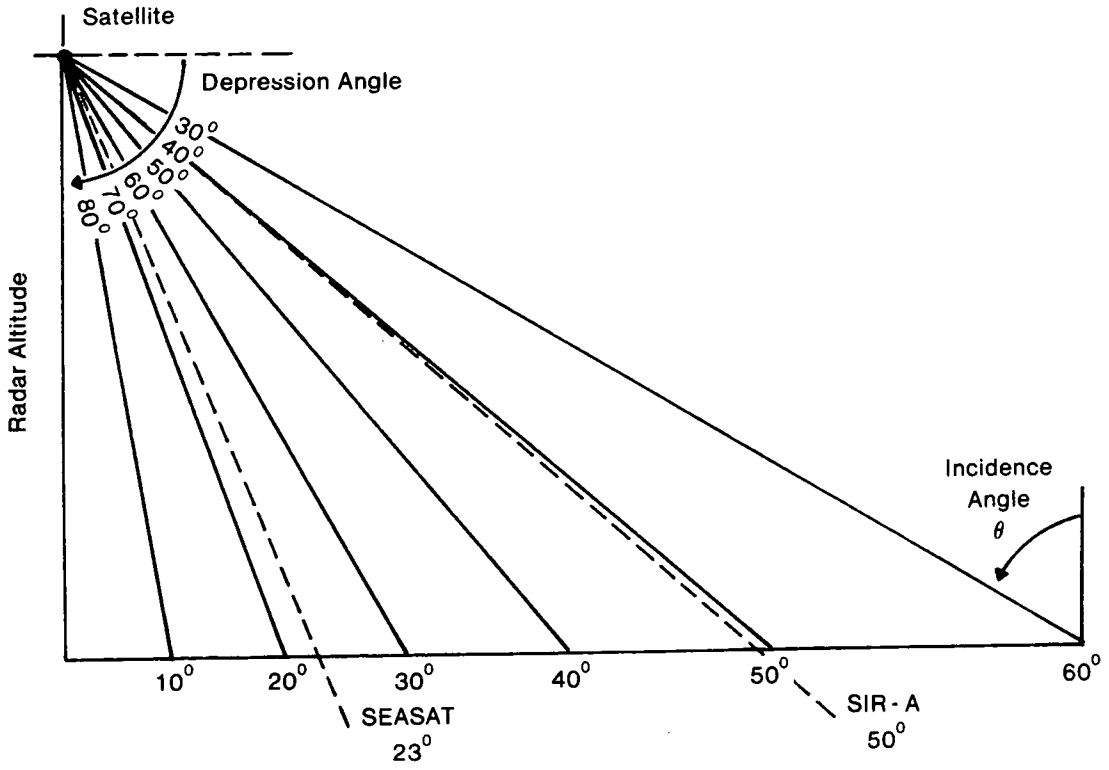

Figure 3.8 The relationship between radar depression angle and incidence angle.

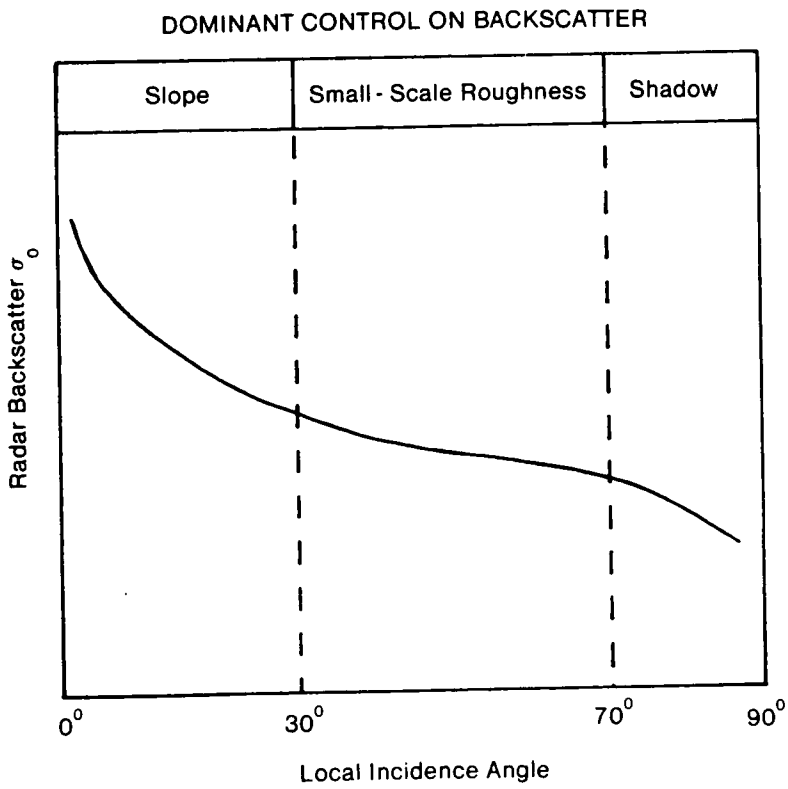

Figure 3.9 The dominant controls on radar backscatter.

3.5.5. Radar Depression Angle/Incidence Angle and Radar Geometry.

The depression angle (α) of a radar system is the angle between the radar antenna, or mid line of the scan, and the horizontal (Trevett, 1986). On a flat surface, the complement of the depression angle is known as the incidence angle (θ) which can be defined as:

> "...the angle formed by an impinging beam of radar energy (propagational vector that is perpendicular to radar wavefront) and perpendicular to the incident surface at the point of incidence" (Harris et al., 1984).

The relationship between depression angle and incidence angle is illustrated in Figure 3.8. The differing depression angles of the Seasat and SIR-A systems are also shown on this diagram. At satellite altitudes the curvature of the earth influences this geometrical relationship and, for a horizontal surface, the depression and incidence angles of a radar are no longer complementary (Koopmans, 1980). For both Seasat and SIR-A the difference is 3° (Table 3.1).

In practice, the local angle of incidence on a surface is a function of the radar depression angle and the slope angle and orientation of that surface (Foody, 1986). Therefore, effective local incidence will vary with local changes in terrain slope. For slopes oriented towards the incoming radar look direction, backscatter will increase with slope angle until a 0° incidence angle is reached. Maximum backscatter will occur at this point, which is also equivalent to the depression angle of the radar system. Conversely, for slopes oriented away from the radar signal, zero backscatter occurs at the maximum

incidence angle, where slope angle is approximately equivalent to the depression angle (Fung and Eom, 1981; Harris et al., 1984). This condition is known as 'grazing', with radar depression angle often referred to as 'grazing angle'. Thus, radar backscatter can be said to be inversely proportional to local incidence angle (Farr, 1983).

Radar incidence angle is obviously dependent on terrain slope through the angular relationship described above. At low depression angles (high incidence) radar backscatter is largely determined by surface topography, while at high depression angles, other surface factors, such as roughness or moisture become more important (NASA-JPL, 1984; Mo et al., 1984). These surface factors are described in Sections 3.5.7. to 3.5.9. A diagram showing the dominant controls on radar backscatter with incidence angle is given in Figure 3.9. Small elevation changes are sufficient to severely affect the detection of surface features and boundaries in radar imagery (Stiles et al., 1982). The disruption is largely dependent upon the depression angle as, at large angles, changes in slope of only a few degrees result in a change in amplitude of the backscatter cross-section by a factor of two or more (Elachi, 1980).

Comparison of the Seasat and SIR-A imagery of Tunisia provides and excellent opportunity to study the dependence of radar backscatter upon incidence angle. The 70° and 43° respective depression angles of Seasat and SIR-A have been shown to provide different, sometimes complementary, information about the areas over which they have been used (NASA-JPL, 1982; Elachi et al., 1982; Rebillard et al., 1984). The steep incidence angle of Seasat provides excellent roughness and hydrological information in lowland areas, but suffers from severe distortions in

areas of high relief. On the other hand, the shallower incidence angle of SIR-A offers tremendous potential in upland areas while providing less information in lowland regions (NASA-JPL, 1982; Koopmans, 1983; Martin-Kaye and Lawrence, 1983a; Rott, 1984a). The relationship between radar incidence angle, terrain slope and backscatter is examined in Chapter 6, where local incidence angles are calculated for various test areas in the field.

Examination of radar backscatter as a function of incidence angle was one of the primary objectives of the multi-angle SIR-B mission. The question of optimum depression angle for geological and vegetation mapping was addressed in many areas, some scientists preparing a library of radar signatures at various incidence angles (Farr, 1984; Parr, 1984; Farr and Massonnet, 1985; Ford and Sabins, 1985). The effect of incidence angle upon surface penetration was also analysed (Schaber, 1984; Taranik, 1984) following the conclusive studies of SIR-A penetration capabilities (Elachi et al., 1984). SIR-B also provided an opportunity to study the stereo viewing capability or radar images with the same look direction but differing depression angles (Leberl et al., 1985, 1986a, 1986b; Cimino et al., 1986; Domik et al., 1986). The value of dual-angle stereo radar imagery was recognised by Kaupp et al. (1983), who suggested that four incidence angles of 20°, 40-45°, 60° and 70-75° would provide the maximum topographic and lithological information.

Over and above the conditions described, there are three further characteristics of radar imagery that are associated with incidence angle, namely radar shadow, foreshortening and layover. These characteristics are described in turn below.

(a) Radar Shadow.

Shadows will appear in a radar image when the backslope of an area of relief exceeds the depression angle (Lewis and Waite, 1973; Harris et al., 1984). As depression angle decreases the shadows lengthen in proportion to the increasing slant-range distance (Figure 3.10 c and d). It is possible to have maximum illumination of a backslope at near range, while the same slope at far range would be in shadow (Macdonald, 1980b). Thus, a radar image of homogeneous terrain can appear very different at near and far range.

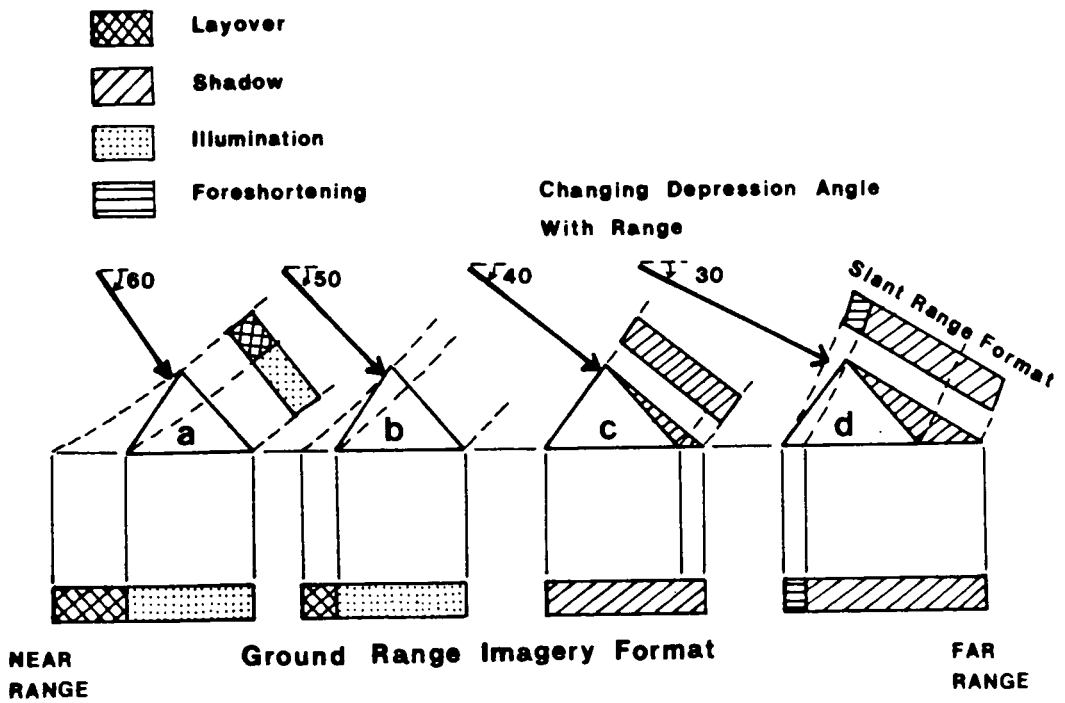

Figure 3.10 Distortions in radar imagery as a function of slope and depression angle (after Macdonald, 1980b).

The relationship between depression angle, target geometry and shadow length can be quantified through the following equations (Trevett, 1986):

$$Ss = \frac{LSr}{H} \qquad \text{(Equation 3.4a)}$$

and

$$Ss = \frac{L}{\sin\alpha} \qquad \text{(Equation 3.4b)}$$

where:

Ss = Slant range distance of target from platform

Sr = Slant range distance of end of shadow to platform

L = Length of shadow

h = Height of target

α = Radar depression angle

H = Radar platform altitude

These equations provide the radar interpreter with some method of relief assessment from shadows on the image, although, at satellite altitudes, the effects of earth curvature cannot be ignored. Lewis and Waite (1973) found that radar-derived slope measurements were comparable with similar measurements derived from topographic maps, being more realistic in mountainous regions.

Quantitative and qualitative information derived from shadows on a radar image can aid topographic and geological interpretation in areas of moderate relief (Macdonald, 1969), with the texture of the shadow often adding further information about vegetation or geomorphology (Simonett and Davis, 1983). However, in high mountainous areas low depression angles create excessive radar shadowing, hindering image interpretation (Macdonald and Waite, 1971a; Harris et al., 1984).

(b) Radar Foreshortening.

Radar foreshortening is a distortion in the image caused by:

> "...the variation in the length of equal terrain slopes when the slope measurements are taken at different incidence angles" (Macdonald, 1980b).

It causes a shortening of slopes on an image at all incidence angles except grazing angle, at which there is no distortion. Like radar shadow, foreshortening varies with range relative to slope and incidence angle (Figure 3.10d). In the case described in this diagram, effective incidence angle is so great that it concentrates all the incoming radar energy in a smaller area than that of the ground projection. The return from the ground is thus concentrated in a small area of the image, producing a brighter response than normal. Backscatter from the backslope of the relief feature is negligible, producing a darker than normal response (Trevett, 1986). Foreshortening can pose severe image interpretation problems at high incidence angles (McCoy and Lewis, 1976; Kaupp et al., 1982).

(c) Radar Layover.

When incidence angles are less than terrain slope, a different form of image displacement occurs in the form of radar layover. The curvature of an incoming radar signal causes the top of a tall feature, such as a mountain, to return energy to the system in advance of its base. This produces a displacement of the feature's top on the image towards the near range (Figure 3.10 a and b). Layover is most pronounced at large depression angles and high relief and tends to occur in the near-range rather than the far-range. It can lead to problems in geological and morphological interpretation in mountainous terrain, especially at large depression angels such as that used by the Seasat system (Ford, 1980; Martin-Kaye and Lawrence, 1983a).

It can be seen from the above that there is a trade-off between radar depression angle and type of displacement in images of mountainous terrain. High depression angles produce severe layover, especially at near range, while low angles result in radar foreshortening. Shadows characterize the far range portions of most mountainous areas, particularly when low depression angles are used (Kaupp et al., 1983; Harris et al, 1984). Nevertheless, in all but the highest mountains, low-to-medium depression angles are generally regarded as providing more useful information.

The interdependence of radar incidence angle and the slope angle is very clear. Thus much of the information discussed in this section is also relevant to Section 3.5.7. The importance of incidence angle upon discrimination of terrain roughness and moisture will be further examined in Sections 3.5.8. and 3.5.9. respectively.

3.5.6. Radar Look Direction.

The azimuth or look direction of a radar system is an important system parameter, particularly for geological and geomorphological interpretation. Radar look direction is the term given to the orientation of the radar beam from north and is usually perpendicular to the flight direction of the host platform. It has further influence on feature direction, over and above that of illumination geometry described in the previous section, by determining local incidence angle and the amount of layover and shadow produced (see Section 3.5.7). Features oriented in a direction perpendicular to radar look direction will cast shadows which are easily discriminated on the resultant image. Hence drainage patterns and lineaments, or

> "...linear features of a surface...which differ distinctly from the patterns of adjacent features (O'Leary et al., 1976)

perpendicular to radar look direction will be preferentially enhanced (Ford, 1980; Koopmans, 1980, 1983). Conversely, features normal to the look direction will be subdued (McDonough and Deane, 1979; Harris et al.,(1984).

There have been numerous studies of the effect of illumination upon feature detection in radar imagery (Dellwig and Moore, 1966; Dellwig et al., 1968; Eppes and Rouse, 1974; Gelnett, 1978; Bryan, 1979; MacDonald, 1980; Blom and Elachi, 1981; Elachi et al., 1982; Sabins, 1983a; Ford et al., 1983). Most of these studies conclude on the advantage of perpendicular look directions for geological and topographic mapping. In their studies of sand dunes, Blom and Elachi (1981) went as far as to suggest that only

linear features oriented within 60° of the perpendicular to radar illumination would be detected satisfactorally, although Nithack (1982) found that rows of trees could be discriminated on SLAR imagery irrespective of look direction. An independent study of lineament enhancement in Japan by Yamuguchi (1985) supports the findings of Blom and Elachi (1981). Today, it is universally believed that two opposing look directions are desirable if all linear features are to have the same likelihood of detection (McCoy and Lewis, 1976; Blom and Elachi, 1981). The SIR-B radar mission was designed to acquire imagery from various azimuth directions to enable this direction dependency to be examined (Harris et al., 1984; Taranik, 1984; Borengasser and Taranik, 1985).

The satellite flight paths of the Seasat and SIR-A systems (Figure 1.1) gave rise to a situation of near-perpendicular look directions in the region of data overlap in Eastern Tunisia. The Seasat system provides an illumination direction from the west (248°) while SIR-A look direction is from the south (155°). This has considerable implications for the interpretation and analysis of each image. These implications were highlighted by Rebillard et al. (1984) and Rebillard and Nguyen (1982) in this region and other similar areas of North Africa. The effects on feature detection are examined more closely in Chapters 5 to 7. In addition, azimuth angles are used to compute local incidence angles for slopes studied in the field (see Section 6.4).

3.5.7. Radar Ground Parameters: Surface Relief.

As described in the previous two sections, the slope angle and aspect of a feature influence the backscatter from that feature by determining local incidence angle (see Chapter 6). In addition, surface relief influences the amount of shadowing and distortion in a radar image. Steep slopes suffer from severe layover, making it difficult to build up an accurate picture of hydrology and geology in an area, although some degree of shadowing is useful in morphological interpretation. The influence of surface relief upon SIR-A radar return in the study area around Hadjeb el Ayoun is examined in Chapters 5 to 7.

3.5.8. Surface Roughness.

Surface roughness has a larger influence on radar return than any other terrain parameters because of its control over the nature and extent of backscatter from the terrain. It can be defined as:

> "...a composite of the vertical and horizontal dimensions and spacings of small scale features, together with the geometry of the individual features that make up the surface" (Harris et al., 1984).

For remote sensing applications surface roughness is commonly categorized through measurement of:

(a) the standard deviation of surface height variations (or root-mean-square 'rms' height); and
(b) surface correlation length (Ulaby, 1982; Ulaby et al., 1982a). (See Figure 3.11).

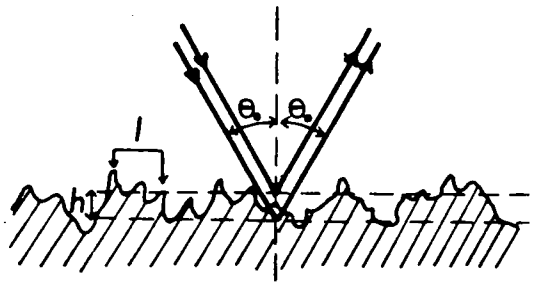

Figure 3.11 Geometry for the definition of roughness criteria: standard height deviation 'h' and correlation length 'l' (after Schanda, 1986).

Both have been used to good effect by Ulaby et al., (1978), Blyth (1984) and Eom and Boerner (1986). Both have their influence on signal polarization, with like-polarized backscatter dependent upon the relative size of scatterers, and cross-polarized backscatter related to the density of these scatterers (Daily et al., 1978, 1979) (see Section 3.5.4). Natural surfaces are complex, making it very difficult to define them mathematically or geometrically (Jackson, 1980). This complexity prompted Mo et al., (1984) to suggest that rms height and spacing of irregularities were not "...adequate descriptions of surface roughness". However, for all but the most intricate of studies of signal-surface interaction it is often sufficient to define roughness by variations in surface height alone. This suggestion was endorsed by Engman and Wang (1987) who, contrary to Choudhury et al. (1979), question the importance of correlation length in estimations of relative roughness.

The behaviour of an incident radar wave at a boundary surface is determined by the roughness of that surface. The three classic roughness situations are described in Figure 3.12. Where the incident wave is reflected away from the radar antenna by the plane surface, the resultant backscatter is described as 'coherent' because the phase front of the wave is preserved (Figure 3.12i) (Schanda, 1986). The second situation (Figure 3.12ii) describes an increase in diffuse or 'non-coherent' scattering as the incident wave comes into contact with a surface having minor undulations. The diffuse scatter component increases with increased surface roughness (Figure 3.13iii) until, in the case of a Lambertian surface, a large proportion of signal backscatter is returned to the antenna. Obviously there are many cases between these extremes but, as a general rule, the rougher the surface, the greater the amount of returned energy and the brighter the signal on the radar image (Trevett, 1986).

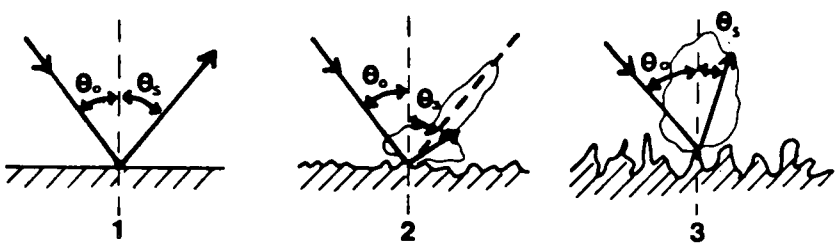

Figure 3.12 Coherent and diffuse scatter as a function of surface roughness (1) specular reflection (coherent scatter) on a perfect plane, (2) scatter from a slightly rough surface with a large coherent and small incoherent component and (3) diffuse scatter from a very rough surface (after Schanda, 1986).

Evaluation of the surface roughness and hence radar backscatter is closely linked to signal wavelength and incidence angle (Schaber et al., 1976; Daily et al., 1979). The importance of the latter has been discussed in Section 3.5.5. (see Figure 3.9) and is extended here. The relationship between incidence angle, radar wavelength and surface roughness can be described by a series of boundary criteria. The Rayleigh criterion (Beckman and Spizzichino, 1963) considers a surface to be smooth when:

$$h < \frac{\lambda}{8\cos\gamma} \qquad \text{(Equation 3·5)}$$

where:

λ = Radar wavelength

γ = Angle between the surface and the incident wave (equal to the depression angle for a horizontal surface)

h = Height of surface irregularities

This equation gives transition values of 8.5cm and 4.0cm for Seasat and SIR-A respectively. The Rayleigh criterion is an excellent first-order classifier of surface roughness, but a more robust measure is needed for models of natural surfaces (Schanda, 1986). Ulaby et al., (1982a) propose the Fraunhofer criterion which considers a surface to be smooth if:

$$h < \frac{\lambda}{32\cos\gamma} \qquad \text{(Equation 3·6)}$$

Neither of these criteria considers the larger-scale roughness component from slopes and geomorphological features that contribute considerably to the overall brightness of a pixel (NASA, 1986). Nevertheless, they provide an excellent means of general roughness determination.

The main drawback of the Rayleigh and Fraunhofer criteria is that neither considers the intermediate area between a smooth and rough surface. To overcome this problem Peake and Oliver (1971) modified the Rayleigh criterion to generate a region of intermediate roughness between smooth and rough criteria. The smooth criterion considers a surface to be smooth when:

$$h < \frac{\lambda}{25 \sin \gamma} \qquad \text{(Equation 3·7)}$$

while the rough criterion defines the lower limit of a rough surface where:

$$h > \frac{\lambda}{4{\cdot}4 \sin \gamma} \qquad \text{(Equation 3·8)}$$

Peake and Oliver's roughness criteria have been used extensively by Sabins and others to evaluate the effect of roughness on radar backscatter at various wavelengths and depression angles (Sabins, 1978, 1983b; Sabins *et al.*, 1980; McCauley, 1982). In all these studies the observed radar signatures of different rock types were in good

agreement with calculations of surface roughness. The dependence of calculated values upon system parameters is illustrated in Figure 3.13. The category limits increase with wavelength and incidence angle, the intermediate category becoming significantly more important at angles greater than 50°, especially at L-band. If we consider the limits for Seasat and SIR-A at their respective incidence angles of 23° and 50° (see Figure 3.13), it is clear that surfaces that appear rough on a Seasat image will still lie within the intermediate category for SIR-A. Similarly, a smooth surface, according to calculations for a SIR-A image, will have a characteristic intermediate return on a Seasat image of the same area. The availability of L-band Seasat and SIR-A imagery for the same test area in Tunisia provides a rare opportunity to explore the possibilities of these general roughness equations. The theoretical and practical application of the equations are examined in Chapter 6.

A comparative study of Seasat and SIR-A imagery, made by Rebillard and Nguyen (1982) found that the SIR-A image was dominated by roughness information on account of its high incidence angle. Similar studies of roughness from SIR-A imagery can be found in the following: Woldai (1983a, 1983b), Merrifield and Yang (1985); Sood et al., (1985); Theilen-Willige (1987). The majority of these highlight the importance of radar-roughness discrimination in geomorphological and geological applications. The importance cannot be disputed, although it should be stressed that it is roughness, a second order property of surface materials rather than the materials themselves that is the basis for discrimination (Blom et al., 1987). Problems arise when one tries to distinguish two areas of contrasting lithology but similar roughness on a radar image (Malin et al., 1978).

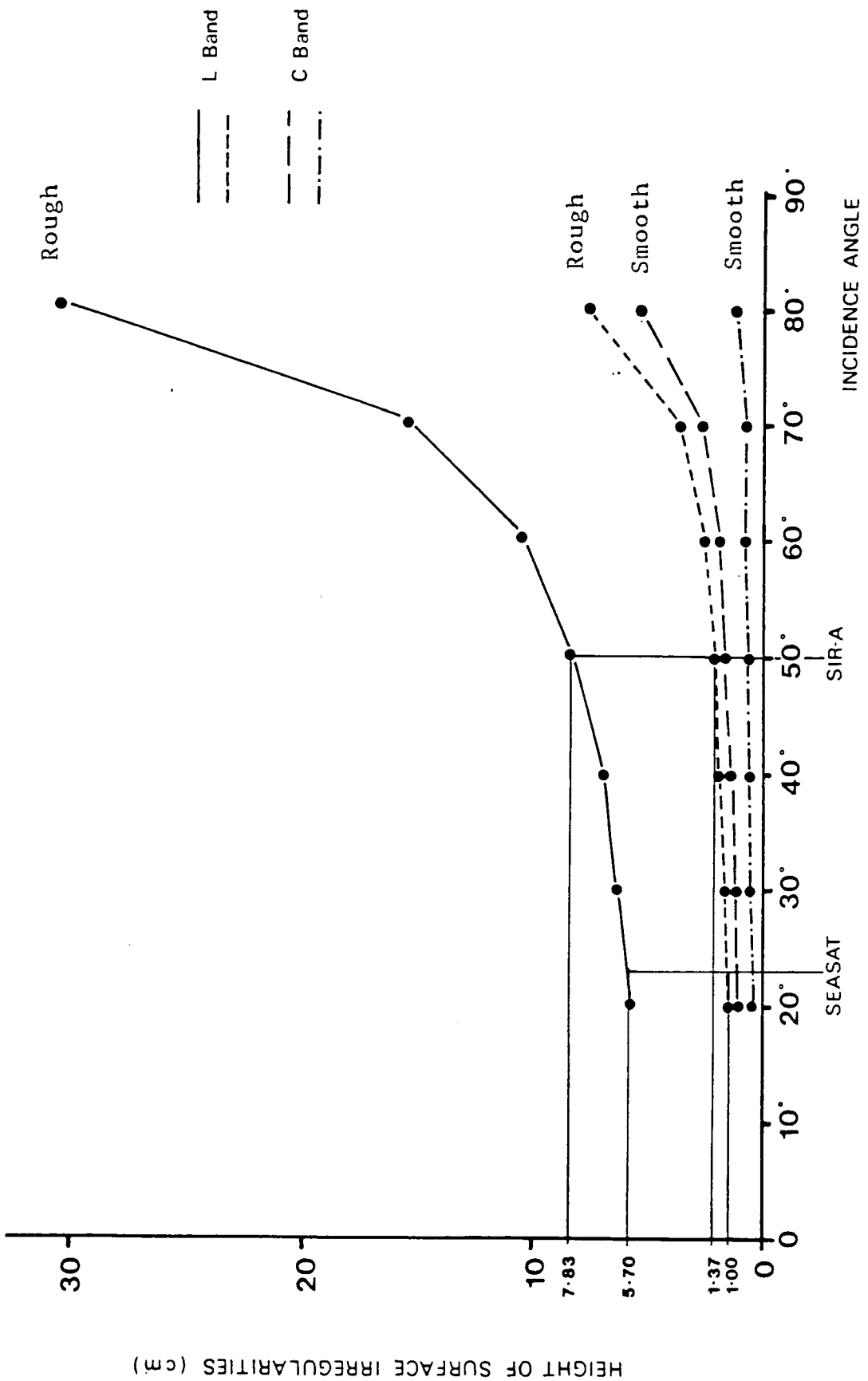

Figure 3.13 Surface roughness as a function of radar incidence angle and wavelength based on Peake and Oliver's roughness criteria. Calculated limits for Seasat and SIR-A are also shown. (after Harris et al, 1984).

The dependence of surface appearance on radar imagery upon system parameters means that the interpreter must be

> "...familiar with the instrument and with the general nature of the scene in order to extract the optimum information" (Bryan and Clark, 1984).

Future multiparameter systems (see Section 3.4) will allow a far greater amount of terrain-related information to be extracted from radar images, enabling surfaces of different roughness to be discriminated more easily. Parameters could be selected to enhance or subdue the effect of relative roughness for different applications.

A normal radar system will hold constant the antenna gain wavelength, the transmitted power and the signal polarization, as described by the backscatter equation (Equation 3.3). The return power will be dependent upon the properties of the target (Fung and Ulaby, 1983). Due to the overriding influence of surface roughness on radar backscatter cross-section, complex mathematical models have been developed to separate areas of different roughness on the basis of backscatter (Simonett and Davis, 1983). The models can be divided into two categories:

(a) surface scattering models that describe the backscatter from randomly rough surfaces; and

(b) volume scattering models that describe the backscatter from heterogeneous media, such as snow or vegetation, where dielectric properties contribute to the return power.

The models are complex and numerous and detailed appraisal is out of place here.

Volume scattering models are particularly useful in studies of backscatter from vegetation canopies (Ulaby, 1982; Ulaby et al., 1982a; Engheta and Elachi, 1982; Brunfeldt and Ulaby, 1984; Wu et al., 1985; Ulaby and Wilson, 1985). Richards et al., (1987) and Simonett et al., (1987) modelled the backscatter contribution from canopy, trunk and ground components of forest stands with considerable success (see Figure 3.14). The general application of these models to the field area in Tunisia is examined in Chapters 6.

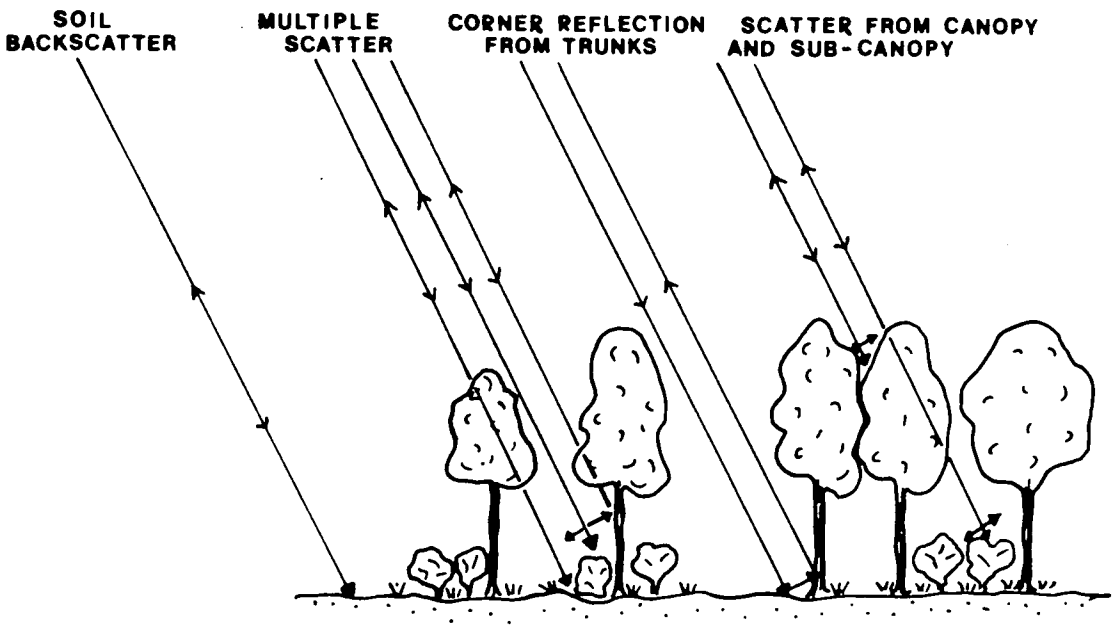

Figure 3.14 Backscattering from forests and other vegetated surfaces (after Simonett et al, 1987).

Vegetation backscatter modelling is not without problems. The size, spacing and direction of crop rows or ploughed fields can exert an additional influence on the backscatter level that is strongly dependent upon radar look angle (Chang et al., 1980; Ulaby et al., 1982b; Blanchard and Chang, 1983; Richards, 1984; Cihlar et al., 1986; Engman and Wang, 1987). Ulaby et al., (1982b) overcame this difficulty by modelling row direction in terms of a random roughness component overlying the periodic component of the soil surface.

Perhaps the greatest problem in backscatter modelling for vegetation or surface features is the requirement for calibration. For any quantitative evaluation of roughness, or comparison of images from different systems or different dates, absolute calibration is necessary to ensure results are "...independent of the measurement tool" (Sieber, 1983). This need has been stressed by numerous authors (Macdonald, 1980a; Chang et al., 1980; Evans and Blom, 1982; Blanchard and Chang, 1983; Krohn et al., 1983; Goldfinger et al., 1983). Empirical and mathematical models are an important method of parameter separation. However, if system effects cannot be held constant with effective calibration, only relative estimates or radar backscatter, and therefore roughness, can be made. Even with calibration, the sheer complexity of natural surfaces, and the difficulty of defining them in simple terms, makes the application of scattering models difficult (Jackson, 1980; Macdonald and Waite, 1973; Hunting Geology and Geophysics, 1981).

> "...We obviously have not reached the point of understanding the complex nature of radar interaction phenomena" (Blanchard, 1980)

but continued refinement of backscatter models in conjunction with improved radar calibration is undoubtedly the way forward.

3.5.9. Complex Dielectric Constant.

The geometrical properties of a surface, that is, surface roughness, are very closely linked to surface electrical properties in determining radar backscatter. These electrical properties are described by the dielectric constant, E, which is a measure of surface response to applied electromagnetic energy. It has two components; real (e') and imaginary (e") as described in Equation 3.9:

$$E = e' - je'' \qquad \text{(Equation 3.9)}$$

where:

$$j = \sqrt{-1}$$

The real component represents the permittivity of the medium, influencing the propagation characteristics of the energy wave within that medium (velocity and wavelength being the most important). The imaginary component represents the conductivity of the medium and is a measure of the electrical losses within it.

The dielectric constant of a surface increases almost linearly with increasing moisture content (Harris et al., 1984; Choudhury et al., 1987), although factors such as rock porosity or gravity, soil texture and salinity have also been found to be important (Xuyan et al., 1984; Dobson et al., 1984; Arcone et al., 1986). Most rocks have

a dielectric constant of between 2.5 and 9.0. Campbell and Ulrichs (1969) measured the dielectric properties of rocks at two microwave frequencies and recorded values of 9.0 for Basaltic rocks, 5.2 for granite and 2.5 for pumice. They suggested that the percentage content of silica or other minerals may have been responsible for some of the observations. When water is added to a soil the dielectric constant rises, slowly at first until a transition point is reached, after which it rises sharply (Wang and Schmugge, 1980). A dry soil commonly has a real dielectric property of 2.8, while the value for wet soil can rise to 19.6 (Harris et al., 1984). The dielectric constant for water in the same frequency range would be nearer 80 (Macdonald and Waite, 1980) due to the ability of water molecules to align themselves in the direction of the applied field (Schmugge, 1980).

The variation in dielectric constant with soil moisture content is further dependent upon soil texture and hence soil type (Dobson and Ulaby, 1980; Njoku and O'Neill, 1982; Ulaby et al., 1984; Blyth , 1984). As moisture is added to soil the water molecules adhere to the soil particles and make only a small contribution to the dielectric constant of that soil. Once all the particle surfaces have been coated with water any excess molecules will align themselves along the applied field, thereby raising the soil's dielectric constant. The larger the surface area on which the molecules can collect, the higher the transition point of that soil. Thus, clay soils are able to hold more moisture and have a higher transition point than sandy soils. Knowledge of the clay content of a particular soil is, therefore, vital to any estimation of moisture content and dielectric constant. Dobson et al., (1984) and Jackson and O'Neill (1986) argued for estimates to be made on the basis of soil bulk

density rather than the percentage field capacity used by Schmugge (1983), stressing that the influence of soil texture was too great to be ignored. In their experiments in soil passive microwave emittance at L band wavelengths, Stroosnijder et al., (1986) found that a 10% alteration in surface clay content could lead to a change in the estimation of soil moisture in the order of $0.02m^3m^3$, again arguing for a rough estimate of soil texture in any study of microwave reflectance or emission. A graphical representation of the effect of soil texture upon dielectric constant is given in Figure 3.15. The influence of soil texture on L-band radar backscatter was examined in the Tunisian test areas and is discussed in Chapter 6.

The importance of soil salinity as a contributing factor to dielectric constant is disputed. Wang and Schmugge (1980) argue for the availability of salinity measurements in the estimation of dielectric constant, while Jackson and O'Neill (1987) conclude that the effects of soil salinity can be ignored when estimating soil moisture in agricultural areas from microwave data of the United States. Whether or not it is important, soil salinity is very closely related to soil texture, being higher in soils with a high clay content (Wang and Schmugge, 1980).

The overall dielectric constant of a soil or surface, as determined by the parameters described above, influences the radar backscatter from that surface. An increase in soil moisture content, and hence dielectric constant, leads to an increase in radar backscatter (and passive microwave emission) from a surface (Schmugge and Choudhury, 1981; Fung and Eom, 1985). The incoming radar waves are reflected back from the surface without penetrating the surface significantly. When the water

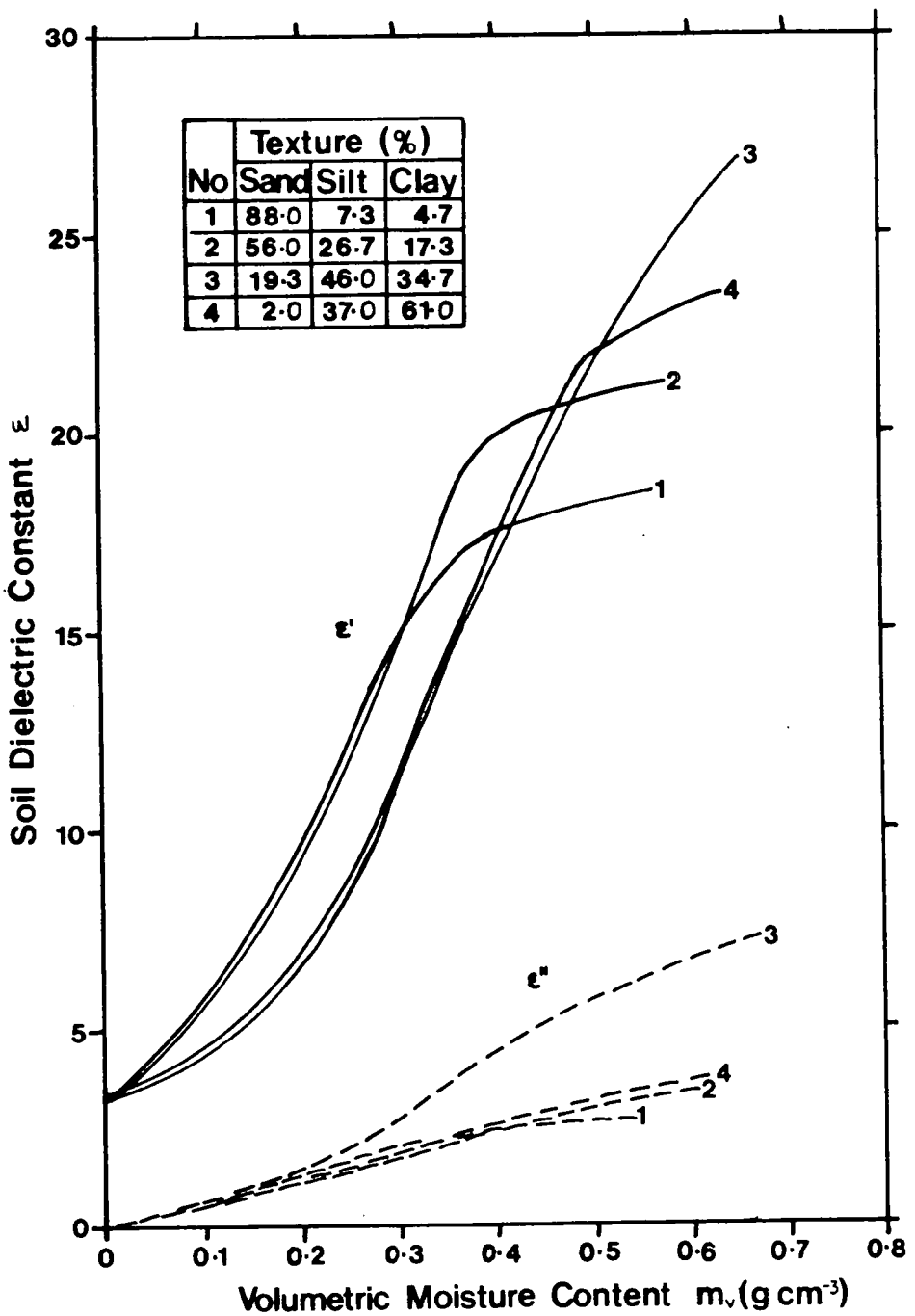

Figure 3.15 Relative Dielectric Constant versus volumetric water content for soils of different texture at 5GHz (Wang and Schmugge, 1980).

table intercepts the surface there will be no penetration (Daily et al., 1978). Thus the depth of radar signal penetration varies inversely with the dielectric constant or moisture content of the medium (McCauley et al., 1982). A critical level of moisture content of 1% has been proposed by Elachi et al., (1984), under which some degree of penetration will result (Berlin et al., 1986).

Signal penetration depends not only upon moisture content, but also upon signal wavelength as described in Section 3.5.3. A longer wavelength signal will ensure greater effective penetration of the surface, thereby allowing some estimation of the dielectric constant to be made (Burke and Schmugge, 1982; Schmugge, 1983; Ulaby and Jedlicka, 1984; Theis et al., 1984). Current remote sensing technology allows the estimation of soil moisture content for the top 5cm of a soil surface (Schmugge, 1983), although the lack of well-calibrated radar systems, particularly at space altitudes, makes quantitative assessment difficult (Chang et al., 1980; Blanchard and Chang, 1983).

Accurate measurement of soil moisture from radar imagery is made all the more difficult by the influence of other parameters such as surface roughness and vegetation cover. All three parameters are so interlinked that in many cases it is virtually impossible to separate out the individual effects (Macdonald and Waite, 1971b; Schmugge et al., 1979; Rosenthal et al., 1985). This is particularly true at short wavelengths where surface roughness and vegetation cover can mask radar contact with the dielectric soil conditions (Malin et al., 1978; Jackson et al., 1982; Ulaby et al., 1982a, 1983; Ulaby and El Rayes, 1987). Longer wavelengths, such as L-band, are regarded as most suitable for microwave estimations of

soil moisture content (Ulaby and Batlivala, 1976; Ulaby et al., 1978; Newton and Rouse, 1980). As Seasat and SIR-A both operate at L-band wavelengths, the complex dielectric constant of the materials within each test area is likely to have some influence on radar backscatter from those regions. This question will be discussed in Chapter 6.

3.5.10. Summary.

Throughout the previous sections (3.5.1. to 3.5.8.) it has become obvious that the various system and ground parameters are very closely related within the radar backscatter cross-section. A considerable wealth of information useful in geological, geomorphological and surface cover studies can be gleaned from qualitative assessment of radar imagery. Nevertheless,

> "...as radar imagery becomes increasingly more popular and available as a research tool questions of system/environment parameter relationships become of crucial importance" (Henderson and Magilski, 1987).

Indeed, if radar data is to be utilized fully a clear understanding of ground-system parameter interaction is vital. The preceding sections provide the basis for the evaluation of Seasat and SIR-A radar imagery of Tunisia and reference is made to them throughout Chapters 5 to 8.

3.6. Landsat Thematic Mapper as a Comparative Tool.

The Landsat series of satellites evolved out of early observations of the earth from space in the 1960s (Freden and Gordon, 1983). The early Return Beam Vidicon (RBV) system was replaced by a Multispectral Scanner (MSS) which was capable of recording passive radiation from the earth in the visible and infra-red wavebands (see Figure 3.1). Between 1972 and the early 1980s Landsats 1, 2 and 3 recorded information from several billion square Km of the earth's surface, providing earth scientists with a great wealth of information which hitherto had been inaccessible. On July 16th 1982 Landsat 4 was launched into a sun synchronous orbit with 16 day repeat cycle at an altitude of 705km. This platform provided scientists with a continuation of MSS information but also carried a new sensor. This new sensor, the Thematic Mapper (TM) had greater spectral, radiometric and geometric sensitivity than the Multispectral Scanner (Freden and Gordon, 1983), as it extended into the far infrared and thermal wavebands (Engel and Weinstein, 1983).

As described in Section 3.1., every feature on the earth's surface has a characteristic spectral response at each wavelength. The seven bands of the Thematic Mapper provide greater powers of discrimination to environmental scientists by increasing the range of wavelengths over which information is recorded. The spectral range of the various bands and the applications in which they are most useful are discussed in turn below.

(a) TM band 1 (0.45-0.52μm).

This band is useful in coastal zone mapping and soil discrimination. Between 70% and 90% of light is absorbed by the chlorophyll of green leaves at these wavelengths making band 1 a useful tool in vegetation and forest studies.

(b) TM band 2 (0.52-0.60μm).

The chlorophyll absorption of green leaves is least at this waveband. High reflectance from vegetation often occurs, making this band useful in vegetation vigour assessment.

(c) TM band 3 (0.63-0.69μm).

Relative radiance spectra from soils and agricultural cover types show the greatest contrast in this waveband. The chlorophyll of green leaves absorbs 70-90% of red light (0.68um). This band is useful in vegetation and soil discrimination (Myers, 1983).

(d) TM band 4 (0.76-0.90μm).

This waveband is the best for discrimination of different plants and for the estimation of biomass. It is useful for identification of water bodies.

(e) TM band 5 (1.55-1.75μm).

This waveband is useful in studies of plant stress through changes in leaf structure and water content (Myers, 1983). It is also helpful in soil moisture and salinity assessment.

(f) TM band 7 (2.08-2.35μm); Added later.

Reflectance decreases in this band making it useful for discrimination of woody and succulent vegetation species. This waveband is sensitive to clay soils and is useful in hydrothermal and geological mapping (NASA, 1982).

(g) TM band 6 (10.40-12.50μm: Thermal infra-red).

This band is useful in soil moisture estimation and salinity assessment. It is an important tool in vegetation stress analysis as it is capable of providing a rough estimation of crop canopy temperature (NASA, 1982).

Numerous excellent studies of Landsat TM data have been published over the years. Canoba (1982) and Pain (1985) used TM imagery to great effect in their studies of the geomorphology of Argentina and Australia respectively, while Wiegand (1984) stressed the advantages of using TM data in crop yield assessment programs.

Landsat Thematic Mapper imagery is available for the western study area in Tunisia around Hadjeb el Ayoun (Path 191, Row 36). It was recorded on the 29th January 1983. Access to this imagery will allow comparison of the response of geomorphological, geological and surface cover features in the study area across a wide range of wavelengths from visible to microwave. Analysis of Landsat TM imagery is undertaken for comparative and supplementary purposes only, and will not be assessed in as much detail as the radar imagery analysis. Reviews of previous studies of Landsat data in Tunisia can be found in Hamza (1982, 1986).

3.7. Conclusions.

This chapter has provided a review of the background and theory of radar remote sensing in the environmental sciences. A general understanding of radar operation and the way in which radar signals interact with the terrain is vital to any meaningful interpretation or application of radar imagery. This interaction is by no means simple, and radar scientists are only just beginning to understand the complexity of microwave response from natural surfaces. The theory presented in this section provides the basis for the interpretation and analysis of the Seasat and SIR-A radar images of central Tunisia (Plates 3.1 to 3.3). The acquisition and pre-processing of the data are discussed in Chapter 4. Visual, digital and statistical analysis of the imagery are discussed in Chapters 5 to 7.

CHAPTER 4. Radar Data Acquisition and Preprocessing.

4.1. Introduction.

Radar imagery for the research project was obtained from two sources outside the United Kingdom. Seasat and SIR-A data are recorded and distributed in different formats (see Chapter 3). Data preparation, consisting of various conversions and preprocessing operations, had to be performed before they could be used for image processing and analysis. This chapter describes the acquisition of the data and the preprocessing in each case.

4.2. Seasat Data Acquisition and Preprocessing.

Digital Seasat data are available for sale from three main sources in Europe and the U.S.A.: the National Remote Sensing Centre at Farnborough; DFVLR in southern Germany; and NASA-Jet Propulsion Laboratory (JPL). Seasat imagery of Tunisia (Rev 719:August 24th 1978) is also held at the Société Européene de Propulsion, Division Traitement d'Images (SEP-DTI), where Dr. Philip Rebillard has used it for his own work on the processing of radar imagery (Rebillard et al., 1984). Dr. Rebillard agreed to supply the required data in exchange for the collection of data from one of his test areas in the field (Plate 3.1).

The image underwent some degree of preprocessing at SEP before being acquired for this project. This preprocessing consisted of the two operations described below. Firstly, raw Seasat data obtained from SEP was in integer format (8 bit). Conversion into logical (16 bit) format is required before the image can be analysed on an image processing system. This was achieved by collecting

the most significant byte (MSB: first pixel or 'picture element') and least significant byte (LSB: second pixel) from each 16 bit equivalent portion of the 8 bit data and generating the true 16 bit pixel value from the equation:

$$MSB \times 256 + LSB = \text{True pixel value} \qquad \text{(Equation 4·1)}$$

This process generates the logical (byte) image with pixel values or digital numbers (DN) in the range from 0 to 255 and is represented schematically in Figure 4.1. Secondly, the logical-format image was gaussian-stretched to adjust the brightness levels in the Seasat image, and thus to improve the contrast within the scene. This is a standard enhancement procedure in the preprocessing of radar imagery (Wadge and Dixon, 1984; Raney, 1980).

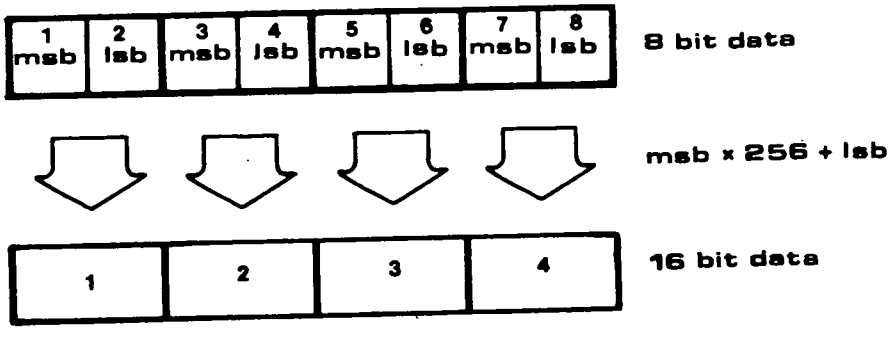

Figure 4.1 Diagram to show conversion of pixels from 8 bit to 16 bit format.

Preprocessing of Seasat SAR data of Tunisia consisted solely of the two operations described above. Both served to improve the interpretability of the image without altering adversely the internal characteristics of the data. Qualitative and quantitative assessment of the image could then be undertaken.

4.3. SIR-A Data Acquisition and Digitization.

SIR-A data of Tunisia (Data take 32-33, 4th November 1981) were obtained from the Jet Propulsion Laboratory in California. As mentioned in Chapter 3, the images were obtained in optical format, the acquired image taking the form of a long strip of positive film 13cm wide at a scale of approximately 1:500,000. Although the optical data contained important spatial and qualitative information, the greyscale had to be quantified before computer analysis and image processing could be carried out. A film digitizer, or densitometer, had to be used to obtain this quantitative information.

The positive film was taken to the Department of Biophysics at the University of Leeds where access to a Joyce Loebel Scandig 3 Microdensitometer had been allowed. The microdensitometer operates by affixing the sample onto a hollow, transparent rotating drum. The optical equipment needed to measure the density of the sample is mounted outside the drum on a carriage which can move freely along the drum axis. One revolution of the drum produces a scan line across the sample in the y direction, while the movement of the carriage represents one scan line in the x direction. Thus the spacing of each axis along the width and length of the drum determines the corresponding pixel size of the final digitized image.

The Scandig microdensitometer incorporates a pixel size selector which allows the user to choose the spacing and size of scan lines. 25, 50 and 100 micrometre sample pitches were available. To obtain the maximum geometric and radiometric resolution, the pixel size had to be chosen with care to correspond with the ground resolution of the SIR-A system. To determine the best pixel size for

the exercise the scale of the optical image was used to calculate the approximate ground resolution at each optical setting. That which corresponded to the nominal SIR-A resolution of 40m would be chosen. The following calculations were made:

Optical SIR-A image scale = 1:460,000 (Based on image and map measurements); where 1cm or 10,000 micrometres on the image represents 4.6km on the ground.

Given a pixel size of 25 micrometres, the number of micrometres on the final image for every 1cm of optical film will be:

$$10,000/25 = 400$$

The distance on the ground represented by one pixel in the final image will be:

$$4.6km/400 = 0.0125km = 12.5m$$

This distance is significantly less than the SIR-A resolution and should not be accepted.

Given a pixel size of 50 micrometres, the same calculations derive figures of 200 micrometres and 23m respectively. Again this is less than the nominal SIR-A resolution and this pixel size should be rejected.

Given a pixel size of 100 micrometres, the number of microns on the final image for every 1cm on the ground will be:

$$10,000/100 = 100$$

Giving a distance on the ground represented by one pixel on the final image of:

4.6km/100=46 m.

This distance corresponds well with the SIR-A ground resolution of 40m.

A 100 micrometre pixel size was chosen for the digitization of the optical data on the basis of these calculations.

The positive film was cut into sections representing the chosen field study areas. A maximum length of 20cm was imposed by the size of the rotating drum, so the edge of the coastal image around Sousse was carefully chosen to coincide with the western margin of the digital Seasat image. Each section was mounted on the drum in turn and digitization commenced.

The optical equipment on the carriage measures the light intensity which is transmitted through film from within the rotating transparent drum. The density of a specific pixel will be dependent upon the incident light (a) and the intensity of the transmitted light (b), where transmittance (T)=b/a, and

$$D = \log \frac{a}{b} = \log \frac{1}{T} \qquad \text{(Equation 4·2)}$$

In this case the image was scanned to 3 optical digits, generating a transmittance value of 1/1000 of the incident light. The received voltage was converted first to analogue density by a logarithmic amplifier and then to a

digital value between 0 and 255 by an eight-bit analogue-to-digital converter (Hills, 1986). To reduce errors in the output system, the Scandig microdensitometer autozeros the amplifier chain after every resolution of the drum by scanning a small area of the drum not covered by data and that is assumed to have zero density (Hills, 1986). Thus, the final density values can be regarded as calibrated.

The final digitized images were written onto tape at 1600 BPI on a DEC PDP 11/45 system. The digitizing process was completed in just over 5 minutes for each scene, the exact time taken depending on the size of the image sections. The two digital SIR-A images were now held on magnetic tape and files 1 and 2, each containing 1300 lines of 2000 records. These files formed the basis for the preprocessing operations discussed in Section 4.4 below.

4.4. SIR-A Preprocessing.

Once digitizing of the SIR-A images had been undertaken it was necessary to apply certain correction procedures before digital processing and analysis could be carried out. Corrections to SAR signals, or image spectra, to rid them of inherent system and scene noise can be both geometric and radiometric. Both were necessary in this case. Plates 4.1 and 4.2 show the eastern and western scenes from the SIR-A swath in their original newly-digitized form. In addition to the more obvious condition of radiance-reversal (black areas appearing white and vice versa), digitization has resulted in serious geometric errors in the planimetric layout of the images through a rotation of the images about the diagonal axis. Both these errors can be reversed with relative ease on an image processing system and are discussed in Section

4.4b. Further geometric correction is more difficult without access to detailed map information or Digital Terrain Models and was not pursued. Important radiometric problems did exist on the images, however, and these will be discussed in some detail below.

4.4.1. SIR-A Scene Fade Correction.

As well as the problems outlined above it can be seen from Plates 4.1 and 4.2 that the images exhibit a 'fading' pattern in the range direction, with the central region containing considerably darker values than the northern and southern margins. Total loss of definition is also present at the near-range and far-range margins. The fading effect occurs in the across-track direction and is constant at any position along-track.

The main reason for the apparent fade lies in the changing angular position of the radar antenna which influences the ability of the radar system to illuminate the surface underneath. In the central part of a SIR-A swath the dynamic range of the various components influencing radar backscatter (i.e. the terrain backscatter) are the predominant factors in the return signal. Any noise present in that part of the image will be data-linked. Towards the near- and far-range the ability of the radar to achieve an accurate representation of the surface is limited by the sensitivity of the SAR and the image will suffer from the radar or receiver noise which saturates the image (Jordan and Rodgers, 1976). In general, the SAR image spectra represent the product of the underlying image spectra multiplied by the transform of the impulse response. At near- and far-range the response factor severely limited the quality of data

available for numerical analysis and had to be removed through radiometric correction.

In order to determine the correction to be applied the image transform, or fading effect, had to be identified. This had to be done in a suitably large area of the image which could be assumed to be both geometrically and radiometrically uniform. In the swath in question the eastern oceanic area fulfills these criteria within acceptable limits. Although minor fluctuations in backscatter will occur as a result of wave patterns for example, any major changes will be the result of the image fading transform. This test area could then be compared with the response recorded in the range direction at any position over land to determine the 'ground' and 'fade' components. The location of test lines selected for the conversion procedure is illustrated in Figure 4.2.

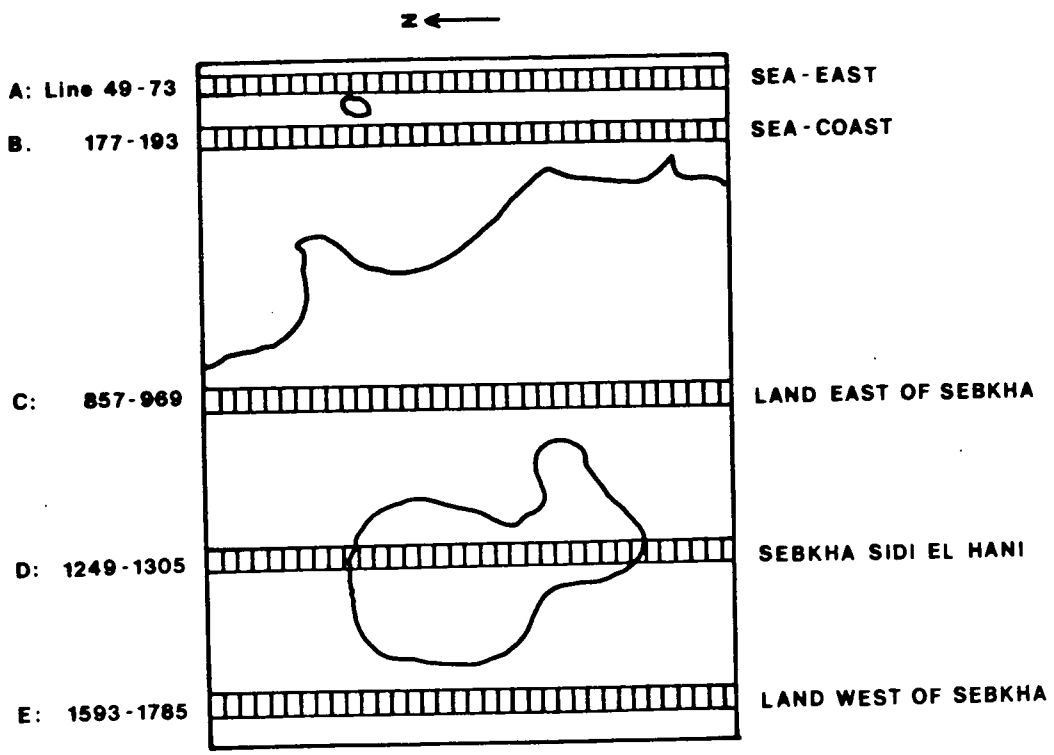

Figure 4.2 Sketch map of approximate locations of selected line batches on eastern SIR-A scene.

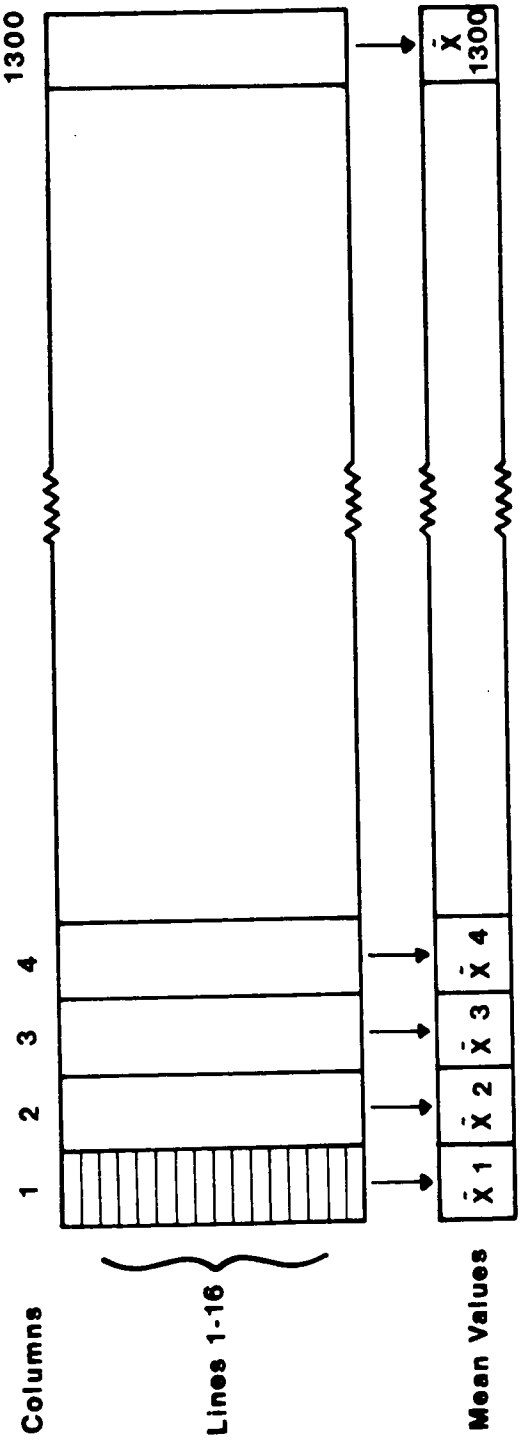

Figure 4.3 Diagram to show calculation of mean pixel values for line batch B.

Once the line batches had been selected on the image processing system the corresponding digital values were extracted from the image computer compatible tape (C.C.T.) and stored in separate files on the computer. Mean backscatter values were calculated for each column of each line batch from near- to far-range. This procedure is shown schematically for line batch B in Figure 4.3. This allowed graphical representation of the variation in value intensity along the selected line batches. The five resultant plots for the eastern test area can be seen in Figures 4.4a to 4.4e. As these plots were derived from the newly-digitized radiance-reversed image, care must be taken when comparing reversed D.N. values given in this section with image analysis results referred to in Chapters 6 and 7.

Comparison of the five graphs highlights the scene fade transform effects clearly. The first two are essentially similar in form, as would be expected in relatively uniform oceanic areas. The minor variations present are probably the result of local wave-form. The remaining three graphs show much greater variations in pixel intensity due to the influence of ground parameters such as surface relief, roughness and soil moisture on radar return. This is particularly evident in Figure 4.4d, where the plateau-like form of the curve for pixel numbers 200 to 900 represents the relatively smooth expanse of Sebkha Sidi el Hani which has a constant backscatter property. The scene fade transform manifests itself within each of these curves, but is shown most clearly in Figures 4.4a and 4.4b where it is undiluted by the overpowering influence of ground parameters. Thus, the dominant form of these two curves represents the shape of the scene fade transform itself and must be the basis of any correction procedures.

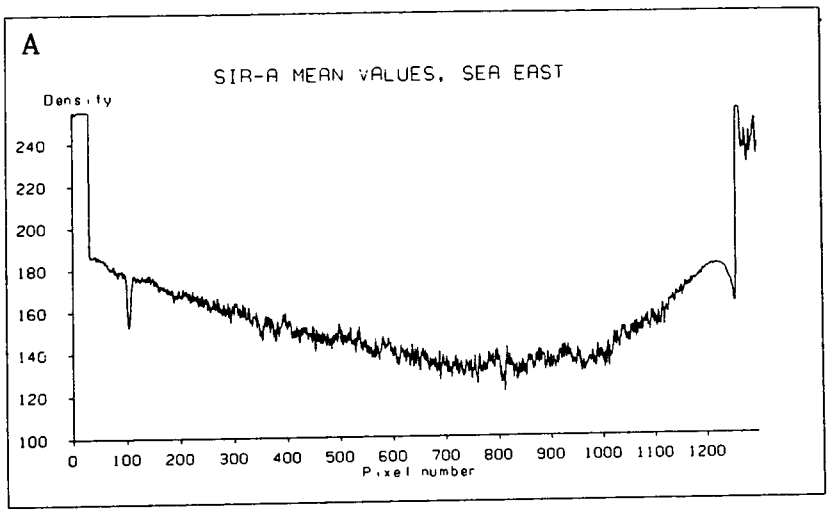

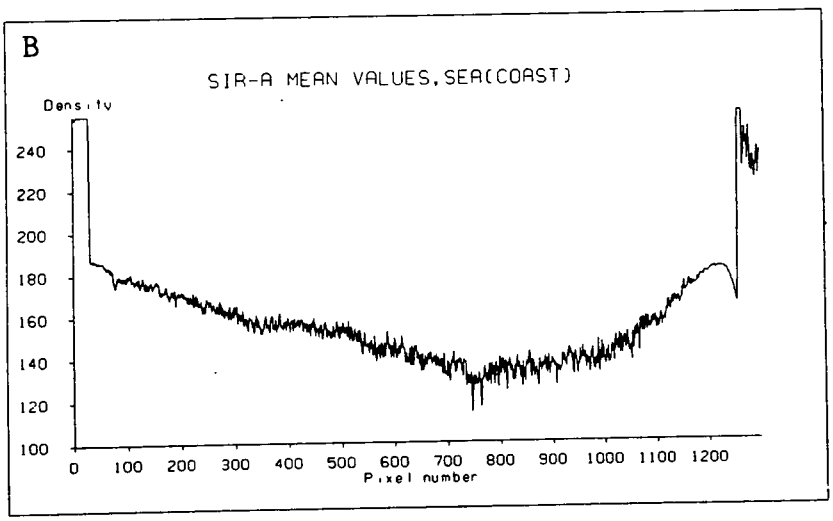

Figure 4.4 Pixel intensity values for the five selected line batches shown in Figure 4.2. (A) Sea east, (B) Sea coast, (C) Area between coast and Sebkha Sidi el Hani, (D) Sebkha Sidi el Hani, (E) Area west of Sebkha Sidi el Hani.

C

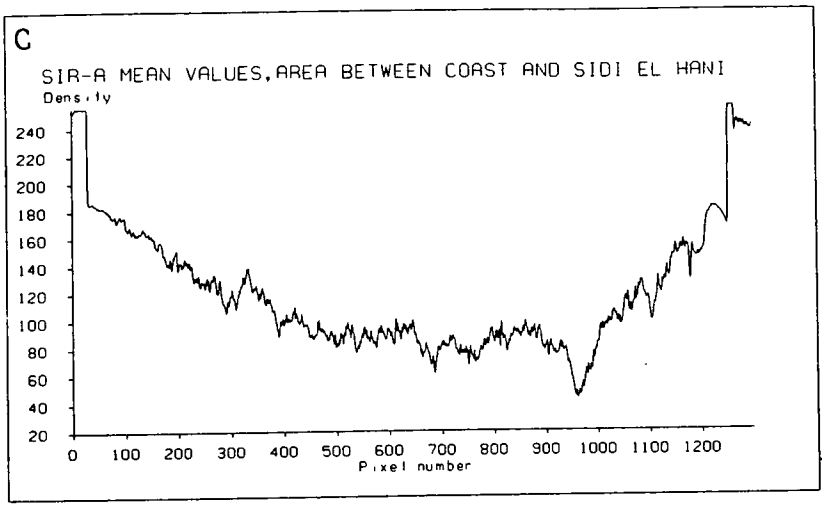
SIR-A MEAN VALUES, AREA BETWEEN COAST AND SIDI EL HANI
Density
240
220
200
180
160
140
120
100
80
60
40
20
0
100
200
300
400
500
600
700
800
900
1000
1100
1200
Pixel number

D

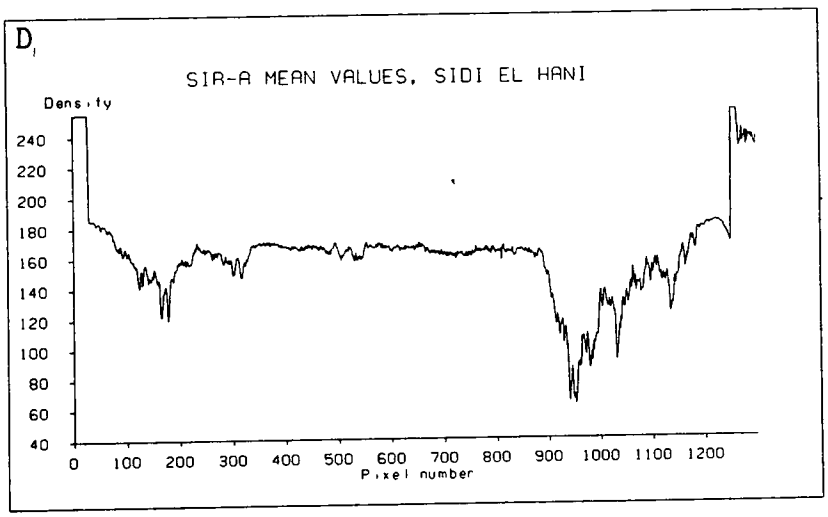
SIR-A MEAN VALUES, SIDI EL HANI
Density
240
220
200
180
160
140
120
100
80
60
40
0
100
200
300
400
500
600
700
800
900
1000
1100
1200
Pixel number

E

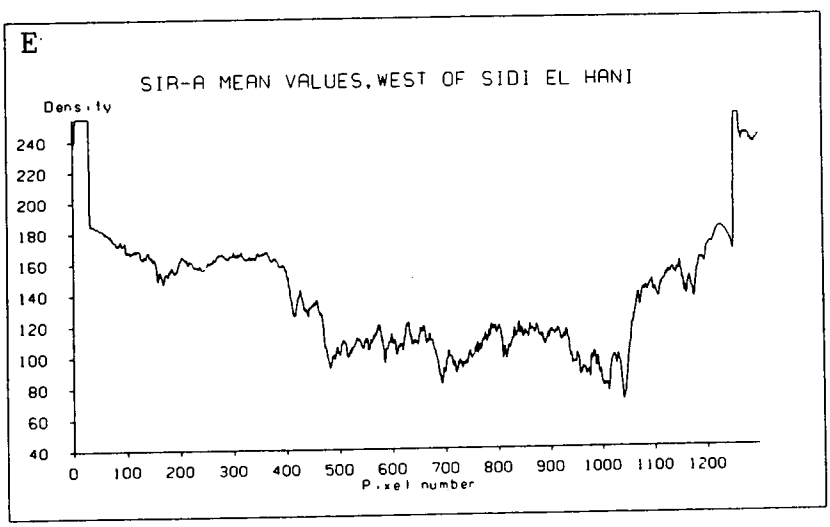
SIR-A MEAN VALUES, WEST OF SIDI EL HANI
Density
240
220
200
180
160
140
120
100
80
60
40
0
100
200
300
400
500
600
700
800
900
1000
1100
1200
Pixel number

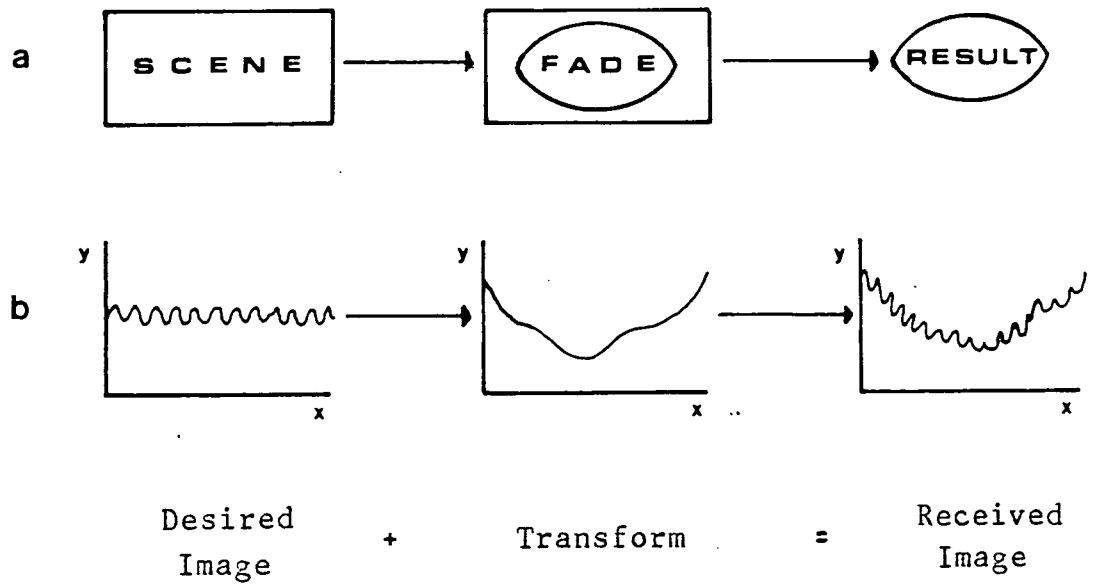

Figure 4.5 Schematic representation of the effect of the scene fade transform upon a SAR image: a) flow diagram, b) relationship between backscatter amplitude (y) and pixel number (x) before and after transformation.

The faded image can be regarded as a correct image onto which a transform has been superimposed (Figure 4.5). Any correction procedure must reverse the effect of the transform to reveal the radiometrically-correct scene beneath. Several correction procedures have been applied to 'faded' SAR images, all with varying degrees of success. Chavez (1981) proposed an automatic shading correction technique involving moving averages within windows across the image. He also assumed minimum fading to be present within the centre of an image. Although deemed successful in the example described, Chavez himself states the difficulty in preserving the material beneath each window. A similar method of fade reductions was described by Begin et al., in 1987. Tests carried out on airborne SAR-580 imagery allowed the material preservation

problem to be overcome by automatically adjusting the length of the window as a function of the variation in the backscatter profile. The authors state that this method can be applied to fading in both the range and azimuth directions, the latter resulting from antenna pattern and spacecraft roll and yaw during imaging. As longitudinal, or azimuth, fade is not present on the Tunisian image only a method of range correction is required.

Because the transform curve identified in the study image has such a definite form it was thought that it could be measured, and hence eliminated, using a best-fit line running through the mean density value curve. Several curve-fitting procedures are available, some having been used in previous fade correction models. Polynomial curve fitting has been adopted in several studies of range fade with encouraging rates of success. Beal and Tilly (1980) used the method on Seasat SAR ocean wave spectra, while Cihlar et al., (1986) and Guindon et al., (1984) applied it in studies of microwave crop classification. Begin et al., (1987) suggested that polynomial fade correction is valid in the range direction while its use in the azimuth direction is disputable. It was, therefore, decided that polynomial curve fitting procedures should be examined closely as a method of fade correction in the current study.

Figure 4.4b was chosen as the basis for the curve-fit procedure, as it incorporated less internal variation resulting from local sea parameters than the curve in Figure 4.4a. Close inspection of the graphs reveals three outliers of response dipping downwards at pixel numbers 76-81, 747-748 and 764-765. These outliers are most likely to be the result of backscatter from ships or the edges of small islands and had to be removed before curve fitting

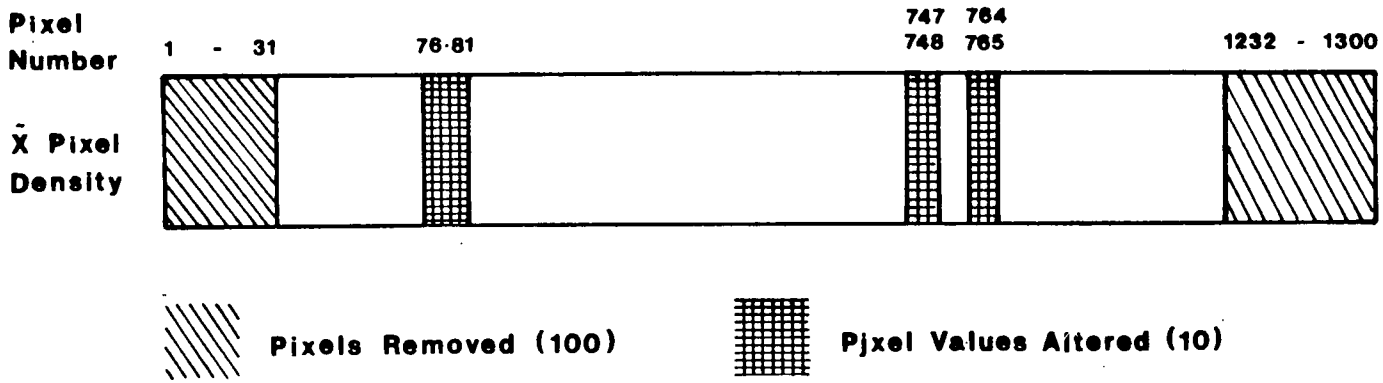

Figure 4.6 Diagram to show location of altered and removed pixels in selected line batch B (sea coast).

could take place. In addition, it was decided to remove the high density values at the beginning and end of the curve which are the product of total SAR system saturation in the near- and far-range. It was thought that the loss of these pixels would not alter the image representation significantly. The values were manually removed from the data or altered to correspond with surrounding pixel values. The form of the edited data file is presented schematically in Figure 4.6. The plot of the cleaned data can be seen in Figure 4.7.

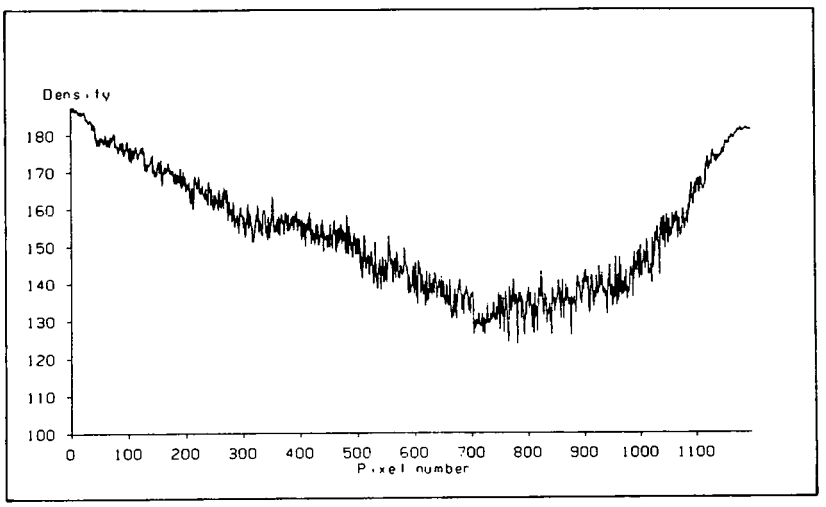

Figure 4.7 Pixel intensity values for 'cleaned' data in line batch B.

Third, fourth, fifth, sixth and seventh order polynomials were calculated from the raw data set. The sixth order polynomial curve was selected as this represented the best fit to the original data (Figure 4.8). The resultant polynomial statistics can be found in Table 4.1, giving the polynomial equation presented in Equation 4.3.

(Equation 4·3)

$$\text{Pixel intensity } (y) = 187{\cdot}56 - 0{\cdot}1376 \times \text{case} + 0{\cdot}1353^{-3} \times \text{case}^2 + 0{\cdot}3816^{-6} \times \text{case}^3 - 0{\cdot}1538^{-8} \times \text{case}^4 + 0{\cdot}1684^{-11} \times \text{case}^5 - o{\cdot}5664^{-15} \times \text{case}^6$$

ANALYSIS AT STEP 6 FOR 2.DENSITY N= 1200 OUT OF 1200

SOURCE	DF	SUM OF SQRS	MEAN SQUARE	F-STAT	SIGNIF
REGRESSION	6	.30305 +6	50509.	5319.7	0.
1.CASE	1	53345.	53345.	5618.4	0.
" **2	1	.21045 +6	.21045 +6	22166.	0.
" **3	1	33965.	33965.	3577.3	0.
" **4	1	3627.0	3627.0	382.01	.0000
" **5	1	1353.6	1353.6	142.56	.0000
" **6	1	309.33	309.33	32.579	.0000
ERROR	1193	11327.	9.4946		
TOTAL	1199	.31438 +6			

MULTIPLE R= .98182 R-SQR= .96397 SE= 3.0813

VARIABLE	PARTIAL	COEFFICIENT	STD ERROR	T-STAT	SIGNIF
CONSTANT		187.56	.62893	298.23	0.
1.CASE	-.26525	-.13760	.14481 -1	-9.5020	.0000
" **2	.03731	.13531 -3	.10491 -3	1.2897	.1974
" **3	.03368	.38166 -6	.32786 -6	1.1641	.2446
" **4	-.08940	-.15389 -8	.49636 -9	-3.1003	.0020
" **5	.13466	.16843-11	.35883-12	4.6939	.0000
" **6	-.16304	-.56649-15	.99247-16	-5.7078	.0000

Table 4.1 Statistics for sixth order polynomial used for SIR-A scene fade correction.

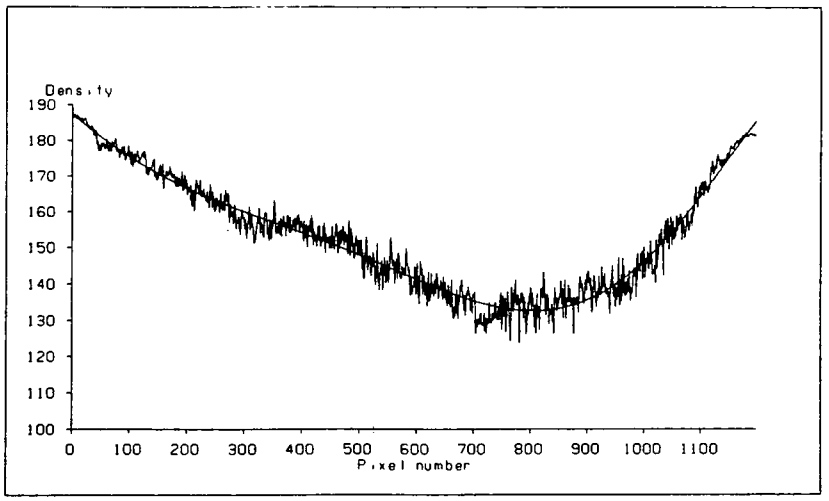

Figure 4.8 Sixth order polynomial superimposed upon 'cleaned' intensity values in line batch B.

Beal and Tilley (1980) used second- and fourth-order polynomials for their conversion procedure but argued for an increase in accuracy of the trend-fitting process. This need has been satisfied by the use of the sixth-order polynomial for this exercise. Close study of the fit of the curve in Figure 4.8 reveals a few minor under- or over-estimations of the trend, for example around pixel numbers 300 and 700. These result from the inability of a polynomial to include a sufficient number of 'waves' to match the form of the curve completely. In theory, a solution to this problem would be the use of a polynomial of a higher order, although, in practice, the accuracy and stability of the statistics tends to decrease with increasing order as the significance level falls. The sixth order polynomial was thought to be the most realistic compromise for the purposes of this exercise.

The main drawback of using a polynomial curve-fit routine is that each individual position of the curve has an influence over the final curve through the equation used. Any major outliers in the data could significantly affect the shape of the resultant curve. However, as the data in question have been edited to remove all the major outliers, this condition can be regarded as of minimal importance.

Once the predicted values for the polynomial were obtained the data could be corrected to remove the inherent trend. Referring back to Figure 4.5; the transform curve (b) can be regarded as the polynomial curve. This being so, the final data must be manipulated to remove this effect. Two alternative methods of correction are possible, each dependent upon the nature of the original data (Equation 4.4).

a) Y NEW = Y RAW - Y POLYNOMIAL

b) Y NEW = Y RAW / Y POLYNOMIAL

(Equation 4·4)

Choice of appropriate correction routine is vital to the success of the operation. Equation 4.4a is justified if it can be assumed that the scene fade transform has no effect upon the amplitude of the backscatter: that is that the two factors are totally independent. Equation 4.4b can be justified if it can be proved that the presence of scene fade has an influence on the amplitude of radar backscatter, such as the relationships shown in Figure 4.9. As there was no obvious evidence of any relationship between backscatter variance and scene fade in the SIR-A image, equation 4.4b is probably inappropriate. Furthermore, when tested against the data, equation 4.4b introduced an erroneous trend effect. Therefore, equation 4.4a was adopted for scene fade correction.

This method is based upon the calculation of 'residual' values of the difference between the original y value and the predicted polynomial value for each pixel number. This is illustrated in Figure 4.10a. The residual values are positive and negative around zero on the y axis (Figure 4.10b). To bring these values up to an appropriate baseline within the pixel intensity greyscale a 'shift'

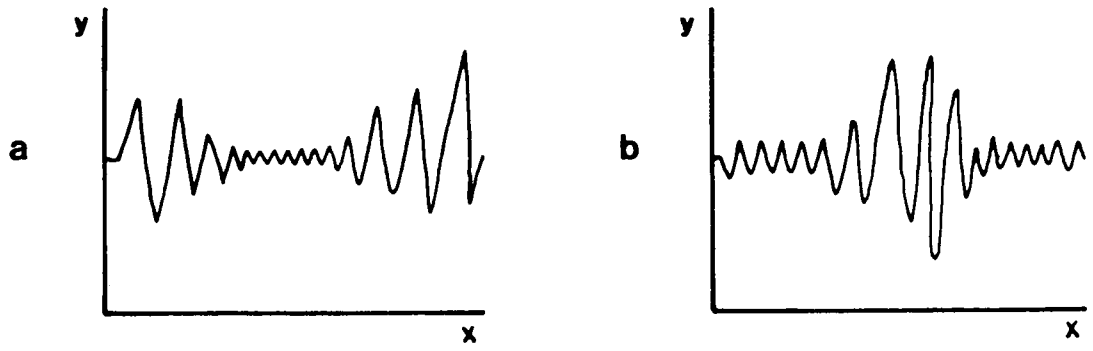

Figure 4.9 Graphical representation of the possible relationship between scene fade and radar backscatter: (a) increasing backscatter with fade, (b) decreasing backscatter with fade.

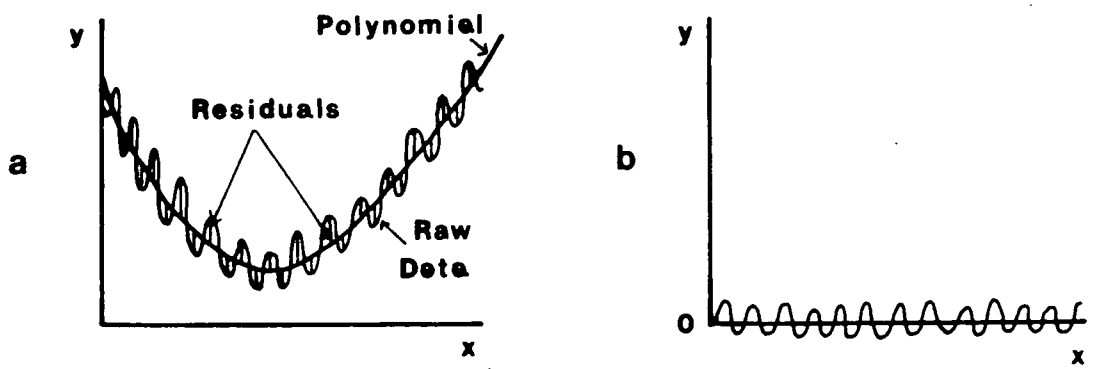

Figure 4.10 (a) Graphical representation of the calculation of residuals from polynomial and raw data values (b) Resultant residuals, fluctuating around zero on the y axis.

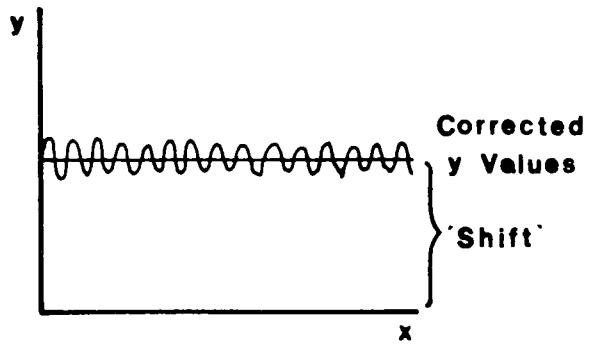

Figure 4.11 Graphical representation of the form of the final y values.

value had to be included in the equation. The shift value was calculated on the basis of the highest predicted polynomial value so as to obtain pixel values in the range 0-255, and to prevent 'wrap around' in digital counting scale from black to white and vice versa. A shift value of 187 was finally chosen.

The final correction equation must take the form:

$$Y\ NEW = Y\ RAW - Y\ POLYNOMIAL + SHIFT(187) \qquad \text{(Equation 4·5)}$$

The resulting values should represent the final scene y values, the scene fade having been removed. The curve should take the form given in Figure 4.11.

A correction program was written to combine the polynomial with the raw data derived from the digitized image C.C.T., to apply the shift value and to write the corrected data to a second C.C.T. The program used can be found in Table 4.2. A flow diagram showing the operation of this program is shown in Figure 4.12. The program was applied to both the coastal image and the area around Hadjeb el Ayoun, using the curve derived from the sea (Figure 4.4b) throughout. Before the corrected image was analysed on the image processing system the original line batches used for the calculation (B: Lines 177-193) were extracted and mean values within columns plotted as before. The resulting curve is shown in Figure 4.13 and represents the corrected pixel intensity values, the scene fade transform having been removed. The success of the operation is clear on comparison of Figure 4.4b and 4.13.

```
      REAL POLY(1200)
      INTEGER DATA(1300),NDATA(1200)
      INTEGER*2 LEN,NLEN/1200/
      LOGICAL*1 BYTES(1300),NBYTES(1200)
      NLEN=1200

      READ (4,*)(POLY(J),J=1,1200)
      DO 100 I=1,2000

      CALL READ(BYTES,LEN,0,ID,1)
      CALL OPENC(BYTES,DATA,1300)

c     Converts logical into integer using routine in OPENC
c     (devised by Bob Nelson)

      DO 99 J=1,1200
      JJ=J+31
99    NDATA(J)=(DATA(JJ)-POLY(J))+187

c     Transforms data to remove fade effect line by line

      CALL SHUTC(NDATA,NBYTES,1200)
      CALL WRITE(NBYTES,NLEN,0,ID,6)

c     Converts integer into logical using routine in SHUTC

 100  CONTINUE
      STOP
      END
 100  CONTINUE
      STOP
      END
```

Table 4.2 SIR-A scene fade correction programme.

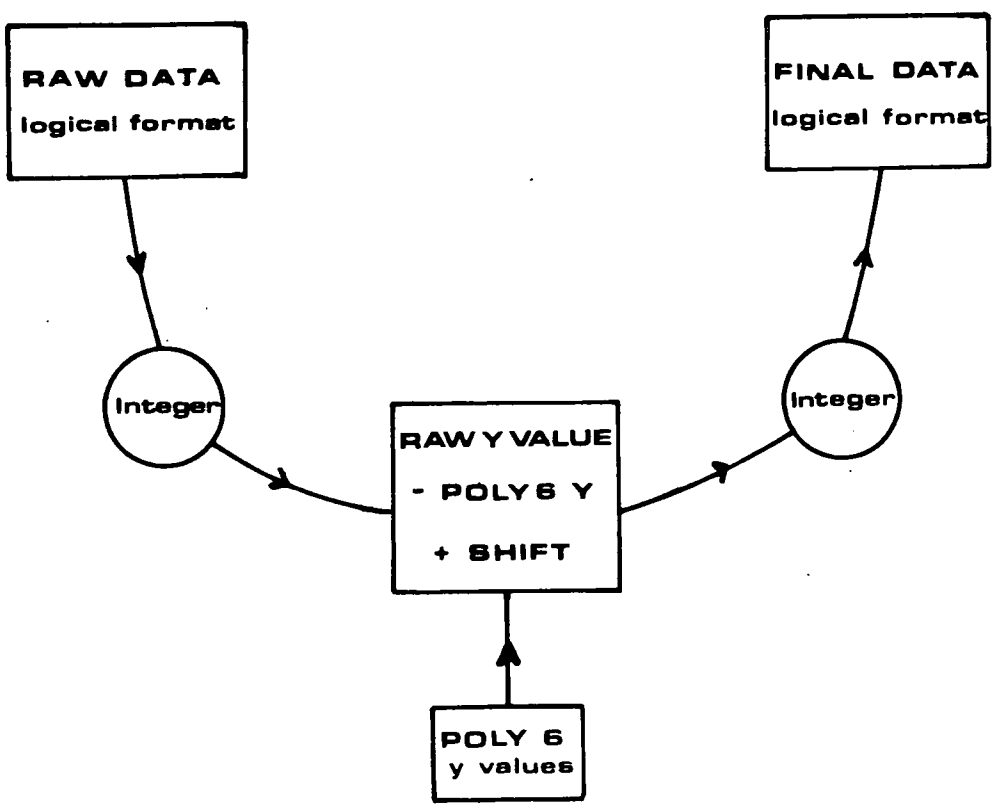

Figure 4.12 Flow diagram showing operation of the final scene fade correction program.

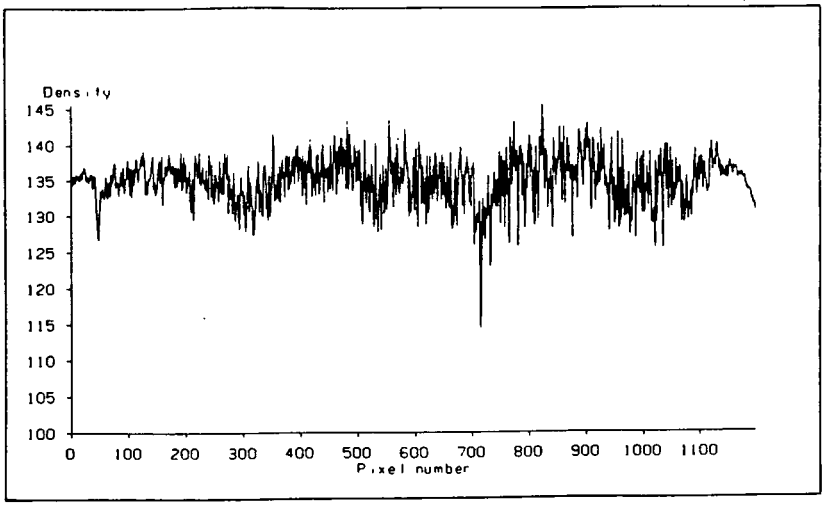

Figure 4.13 Corrected pixel intensity values in line batch B after the removal of scene-fade.

Observation of the corrected image on the I^2S image processing system confirms this result (Plate 4.3). Comparison with the original image shows a great increase in image clarity at both near and far range. The scene still displays some lack of definition at the extreme margins but this is due to internal system effects which saturate the image and cannot be removed (see Section 4.4). The scene-fade corrected western image is given in Plate 4.4. In conclusion, the use of a polynomial seems to be a simple and effective method of curve fitting and can be thoroughly justified as a basis for scene fade correction in the range direction.

4.4.2.SIR-A Geometric and Radiometric Correction.

Once scene fade had been eliminated, the geometric and radiometric reversals which occurred during the digitization process could be corrected. Before the optical SIR-A swath had been obtained from JPL, small areas throughout the length of the image had been covered by sticky tape. When digitized, these areas were void of information and rendered useless in image analysis. Together with the near- and far-range zones of total system saturation (described in the previous section) these areas were removed on the I^2S image processing system using the 'POINTS' and 'COPY' commands. This generated two images of the following specifications:

SIR-A East (Sousse) 1164 Samples x 1923 Lines

SIR-A West (Hadjeb) 1169 Samples x 1641 Lines

Both these images required rotation and reflection about a central point and axis as shown in Figure 4.14 (B requires repositioning at N etc.). In theory, the digitized images have been reflected about a diagonal axis (d) extending from line 1 sample 1164 to line 1923 sample 1. As correction about this axis was difficult to achieve, rectification was carried out in two stages.

The first involved a rotation about the centre by -90° . This was executed through Nearest Neighbour Analysis by the 'C'ROTATE' function on the I^2S image processing system.

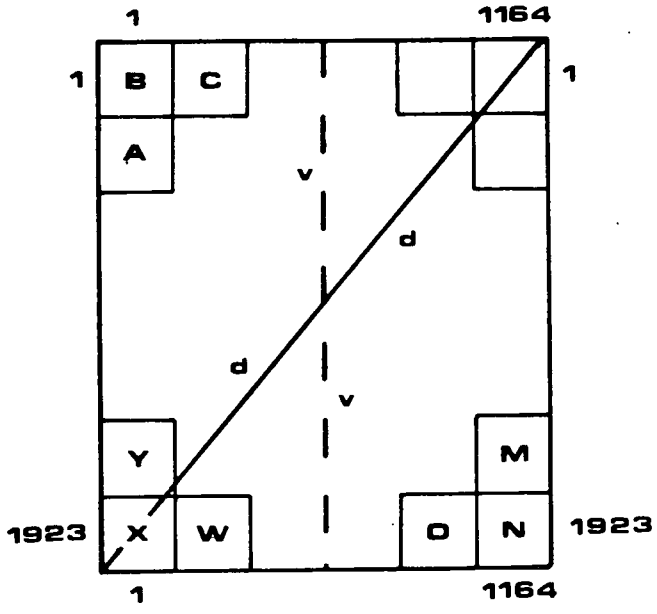

Figure 4.14 Diagram to show the geometric correction required for the eastern SIR-A image.

The second stage required a reflection in the vertical axis (V). As no full-image reflection facility was available on the I^2S at Durham, this procedure had to be carried out on the digital tape file directly. A FORTRAN Vs program was written to conduct the reflection exercise as well as the required radiance-reversal correction. A flow diagram to show the operation of this program is given in Figure 4.15. The program used is presented in Table 4.3. Radiance-reversal was achieved through the equation y=255-x; where x is the input D.N. value and y is the output value. This converts a black pixel of value 0 to a white pixel value of 255. All grey scale values between these two extremes are converted accordingly. Pixel reorganistaion from newly-digitized to final image is shown in Figure 4.14. Rotated point X (originally in position B) moves to point N after reflection. Similarly points W and Y (originally A and C) move to M and O respectively.

```
      INTEGER NEWINT(1644),OLDINT(1644)
      INTEGER *2 LEN,NLEN
      LOGICAL *1 NEWBYT(1644),OLDBYT(1644)
      NLEN=1644
      DO 100 I=1,1195

      CALL READ(OLDBYT,LEN,0,ID,1)
      CALL OPENC(OLDBYT,OLDINT,1644)

c     Reads from tape and converts logical into integer
c     using routine OPENC (devised by Bob Nelson)

      DO 50 J=1,1644
      NEWINT(J)=255-OLDINT(1645-J)
   50 CONTINUE

c     Corrects geometric and radiometric reversals

      CALL SHUTC(NEWINT,NEWBYT,1644)
      CALL WRITE(NEWBYT,NLEN,0,ID,6)

c     Writes to tape and converts integer to logical
c     using routine SHUTC

  100 CONTINUE
      STOP
      END
```

Table 4.3 SIR-A geometric correction programme.

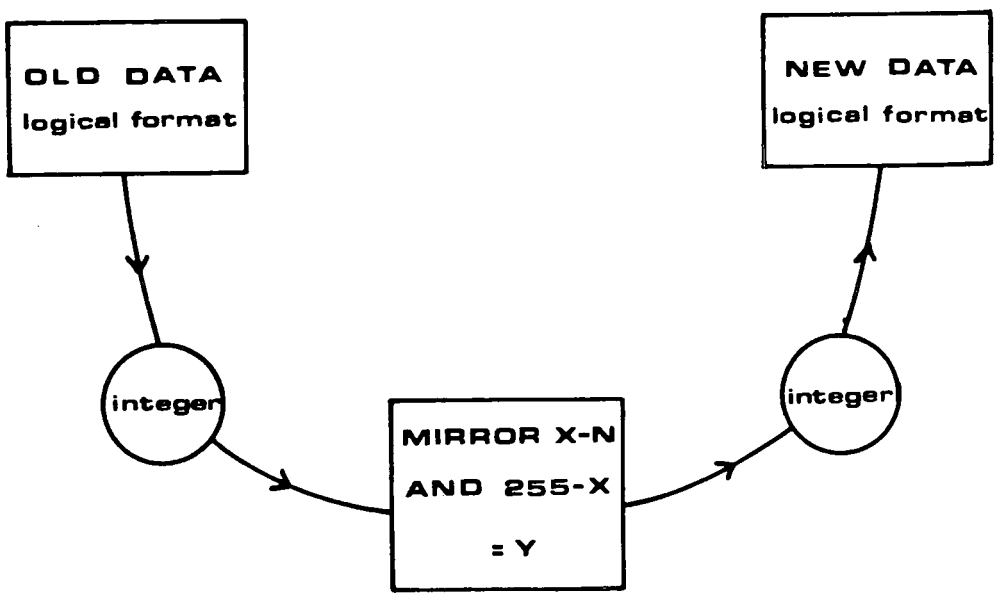

Figure 4.15 Flow diagram to show operation of the image geometric and radiometric program.

After completion of this operation on each of the SIR-A images the requirements for geometric and radiometric correction have been satisfied.

4.5. Summary.

Before Seasat and SIR-A imagery could be analysed using digital image processing techniques, various preprocessing operations were carried out. Digital Seasat data preparation was minimal, the image having been preprocessed at source. To allow comparison with Seasat data, the optically-recorded SIR-A image had to be digitized and geometrically corrected. An erroneous fading transform present in the range direction was also removed. After this data preparation the quantitative and qualitative analysis of the Seasat and SIR-A images could go ahead (See Chapters 5 to 8).

Chapter 5. Image Interpretation and Analysis.

5.1. Introduction.

This chapter describes the various analyses undertaken on the radar and Landsat scenes of the Tunisian study area to allow their full information content to be evaluated. Visual interpretation on the hard-copy radar images is described first in Section 5.2. Once the geometric and radiometric image corrections described in the previous chapter had been applied to the data, a number of digital image processing and analysis techniques were undertaken. The application and evaluation of these techniques is discussed in Sections 5.3 to 5.8. Unless otherwise stated, all images created by the analysis were scaled to exploit the full dynamic range of the data (DN values 0-255).

5.2. Visual Image Interpretations.

Early aerial radar and photographic surveys relied on the visual interpretation of image products in terrain evaluation and mapping studies. A skilled photo-interpreter makes use of his or her professional understanding of image texture, pattern, size, shape and context, together with knowledge of the application in hand, to glean information about an area. Despite the growing importance of digital image analysis, visual image interpretation methods continue to be widely used in the field of applied remote sensing, especially in the rapid assessment of terrain types.

The visual image interpretations of the Seasat image (Plate 3.1) and the two SIR-A swath subscenes (Plates 3.2 and 3.3) are described in this section. Image analysis was

undertaken with reference to the general environmental conditions outlined in Chapter 2. However, the interpretations were made prior to the evaluation of the field data to reduce the likelihood of subjective interpretations biased by field results. Questions raised about the importance of various ground and radar-system parameters are noted for each individual interpretation (Sections 5.2.1. to 5.2.3).

5.2.1. Seasat Image Interpretation .

The Seasat image of the Sahel of Sousse in eastern Tunisia contains a wealth of information on the surface and cover-types existing in the region. The image is dominated by the dark, low backscatter, response of the sea in the Gulf of Hammamet. This response changes from east to west over a dividing line northwards from the coast at Moknine. The near-coastal area west of this line has a near-black response, probably due to low radar backscatter from calm waters sheltered from the prevailing wind by the headland at Moknine. To the east of this headland, the sea has a mid-grey response, signifying increased backscatter from a sea surface affected by higher winds. Individual wave patterns cannot be observed, although some degree of wave structure is evident around the two offshore islands south-east of Monastir.

Sebkha Sidi el Hani and the sebkhas at Monastir and Moknine have a similar dark-grey appearance on the Seasat image. This suggests that these areas are associated with generally low radar backscatter, probably due to smooth surface conditions. The response from Sidi el Hani, however, is not uniform. Concentric bands of light-grey response associated with high radar backscatter are evident near to the sebkha margins and throughout the

southern area of the feature. These high-response areas are likely to be due to one of two factors:

(a) Increased backscatter from areas of increased roughness, perhaps associated with dessication features

(b) Increased backscatter induced by a changing dielectric constant, associated with moisture content, soil type and soil salinity.

The validity of these two theories is examined through statistical analysis of ground conditions in Chapter 6.

Sebkha Kelbia, which lies to the north of the coastal study area, has a very different appearance from the three sebkhas described above. Small areas of low-response do exist but the sebkha is generally characterised by medium to high backscatter, caused by one, or both, of the factors described above. As Sebkha Kelbia lies outside the area studied in detail in the field it is impossible to say with any degree of certainty which of the factors is predominant.

The lunette dunes associated with Sebkhas Sidi el Hani and Kelbia are clearly evident on the Seasat image by their high backscatter responses (Plate 3.1). The dune south-east of Sebkha Kelbia is particularly well defined by its contrast with the surrounding areas of low backscatter associated with areas of flatter terrain. The dune to the south of Sebkha Sidi el Hani is less well defined due to its proximity to an area of hill country in the east. Nevertheless, its form can be identified. Slopes oriented towards the radar look direction are likely to be

the cause of the high radar backscatter from the lunettes, with north-south slopes being preferentially enhanced.

The areas of hill country to the south and east of Sidi el Hani are also easily delimited on the Seasat image. Differential enhancement of shadowing of slopes oriented towards and away from the radar look direction gives a three-dimensional impression of those areas of low-to-moderate relief. The high depression angle and resolution of the Seasat system seems ideal for the detection of areas of relief in the Sahel of Sousse.

Large gullies and wadis dissecting much of the hill country to the north and south of Sousse, and to the south-east of Sebkha Sidi el Hani, are clearly visible on the Seasat image by their high radar backscatter (Plate 3.1). The high response generated by these features is likely to be due to one, or a combination, of the following factors:

(a) Backscatter from wadi/gully sides oriented towards the incoming radar beam

(b) Corner reflection or combined scatter from gully sides and bottoms

(c) Backscatter from rough surfaces on the floor or sides of the wadis.

The dominance of any one of these methods will be assessed in the light of field investigations in Chapter 6.

The wadis and sebkha inflow channels situated around Sebkhas Sidi el Hani and and Kelbia can be distinguished on the Seasat image by their bright radar backscatter response. This response is probably the result of high backscatter from rough gravel or pebble deposits on the floor of the channels together with backscatter from the channel walls. Such gravelly areas would appear particularly rough, or bright, at L-band wavelengths (cf. Section 3.5.8).

The appearance of the Seasat image in agricultural regions is more variable in nature. In the north of the overlap area, between the towns of Sousse and Kairouan, individual fields can be distinguished owing to the high resolution of Seasat. Fields vary from black (low radar backscatter) to white (high radar backscatter) in accordance with the crop grown in the field, or the ground conditions such as furrow size or soil roughness. Fields that appear bright on the radar image must be rough in texture, possibly suggesting the presence of tree or bush crops. Darker fields have radar-smooth surfaces, suggesting the presence of grasses or cereal crops. Further south, the large areas of arboriculture around Monastir, Moknine and Mahdia have a mottled appearance on the image. At the 70° depression angle of Seasat this will be due to combined scatter from ground, trunk and canopy (cf. Figure 3.15). The effect of tree size and spacing on radar backscatter from areas of arboriculture will be assessed quantitatively in Chapter 6 (Section 6.7.3).

Cultural features can be identified in the Seasat image with varying degrees of success. The larger towns of Sousse, Msaken, Djemmel, Moknine, Mahdia and Monastir can be distinguished easily from surrounding areas on account of their size and their high radar backscatter. This high

backscatter is likely to be the result of backscatter from square buildings that act as corner reflectors (Plate 5.1). Smaller towns are not so easily discriminated as they often have the same response as the areas surrounding them. At the 70° depression angle of Seasat, a proportion of the radar signal will penetrate the spaces between buildings (streets, courtyards, etc.) (Figure 5.1). The response from the town as a whole will represent a combination of high backscatter from buildings and low backscatter from areas between buildings. As the towns decrease in size, building spacing is likely to increase, thereby reducing the overall response. This would explain the relative difficulty of identifying smaller settlements on the Seasat image.

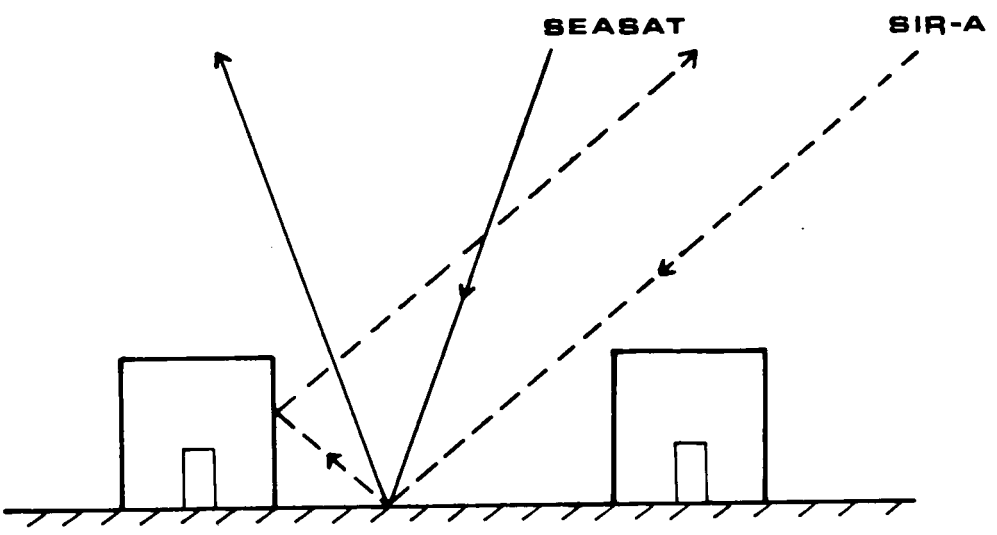

Figure 5.1 Corner reflection in settlement areas. The steeper Seasat signal is able to penetrate the spaces between buildings, while the shallow SIR-A signal produces a high return due to corner reflection.

As far as roads and railways are concerned, only a small proportion of those known to exist can be identified on the Seasat image. The main road and railway line from Msaken to El Djem can be seen, as can the coastal roads near Mahdia and Sousse and the north-south road east of Sebkha Kelbia. Few roads running in an east-west direction can be identified, although notable exceptions can be found in the case of roads from Msaken and Enfidaville to Kairouan. The preferential enhancement of roads running north-south is due to the look direction of Seasat that is unlikely to detect roads normal to it (see Section 3.5.6). All theories of ground-radar interaction proposed in this section will be evaluated in the light of field information in Chapter 6.

5.2.2. Interpretation of the Eastern SIR-A Image.

Like the Seasat image, the SIR-A image of the Sahel of Sousse in eastern Tunisia is dominated by the large areas of dark tone produced by the low radar backscatter from sea and sebkha regions (see Plate 3.2). Both have a uniform near-black response with few internal variations, suggesting that both behave as radar-smooth surfaces. Some variation in tone can be seen within the northern part of Sebkha Sidi el Hani. This may be due to diverse soil type, moisture or salinity conditions which have altered the dielectric constant of the surface. Alternatively, the variation may reflect changes in surface roughness bought about by the changing surface conditions. All possible causes are discussed in Chapter 6 (Section 6.7.2) in the light of information gathered in the field.

The lunette dune on the southern margin of Sebkha Sidi el Hani can be detected on the SIR-A image, although its form is by no means distinct (Plate 3.2). The dune has

a mottled high backscatter response which probably represents a combined response from the slope and microrelief elements of the dune surface. The relative importance of each will discussed in Chapter 6.

The areas of hill country to the south and east of Sebkha Sidi el Hani are not distinct on the SIR-A image. Like the lunette dunes, they have a medium to high response and mottled tone on the image, but no clear relief form can be distinguished. From the lack of slope information recorded it can be deduced that backscatter from these areas is largely dependent on surface roughness at the 43° depression angle of SIR-A. A similar tone and texture can be found in the olive growing regions south and east of Monastir, which are located on level and hilly terrain alike. This adds greater weight to the hypothesis that it is surface roughness (determined by soil and vegetation conditions) and not surface relief, that is largely responsible for variations in SIR-A backscatter (see Chapter 3 and Figure 3.15). The relationship between surface conditions, vegetation size and spacing and SIR-A backscatter is discussed more fully in Chapter 6 (Section 6.7.3) in the light of information collected in the field.

The agricultural regions west of the town of Sousse are clearly evident on the SIR-A image. Individual fields have a dark tone (low backscatter) or light tone (high backscatter) according to crop type and soil conditions. As with the Seasat image, a bright tone suggests that surface conditions and/or crop type of the field in question have created a radar-rough surface. Large furrow sizes, stony ground, or tree or bush crops could generate such conditions. Fields with a dark tone are indicative of a radar-smooth surface, probably associated with cereal crops or level, fallow land.

The large wadis and gullies east of the town of Sousse can be distinguished on the SIR-A image by their speckled bright tone (Plate 3.2). This bright tone is indicative of a high radar backscatter, which is likely to have resulted from a combination of scattering from channel floor and wall components (see previous section). The fact that these features can be distinguished on the SIR-A image with its 40m resolution, albeit with less clarity than on the Seasat image, suggests that they must be either:

(a) very large; or

(b) capable of producing an exceptionally high backscatter response.(See Section 3.5.2)

The gullies in the hill country to the south of Sebkha Sidi el Hani cannot be distinguished easily on the SIR-A image, as their backscatter response is confused by the response from the surrounding hill country. This further supports the assumption the SIR-A is more responsive to microscale, rather than to macroscale, surface features.

The sebkha inflow channels to the north-west of Sebkha Sidi el Hani stand out clearly on the SIR-A image (Plate 3.2). Their bright tone contrasts with the speckled dark grey response of the surrounding area. As on the Seasat image, this bright tone is likely to have been caused by the high radar backscatter from the rough pebbly surface of the channels together with some scattering from the channel walls.

Cultural features stand out particularly clearly on the SIR-A image. All settlements have a very high radar backscatter allowing them to be distinguished easily from

surrounding areas of darker tone. The 43° depression angle of SIR-A ensures that buildings will act as corner reflectors, sending a large proportion of the signal back to the radar sensor (Plate 5.1). At this depression angle, relatively small amounts of the signal will be capable of penetrating between buildings and backscatter will predominantly come from the buildings themselves (Figure 5.1).

The main transport lines can be determined with reasonable ease on the SIR-A image by their linear form and high radar backscatter. However, there is a distinct preferential enhancement of features oriented in an east-west direction, owing to the perpendicular north-south look direction of SIR-A (see Chapter 3, Section 3.5.6). Several explanations for the relatively high backscatter of roads in the area can be proposed:

(a) The aggregate used for construction of the road surfaces could be large enough to behave as a radar-rough surface

(b) The roads could be built upon embankments raised above the surrounding ground level, thereby giving rise to high radar backscatter

(c) The roads could be lined by hedges or tress that are displayed as an area of high backscatter (bright tone) along the road line on the image.

These, and other, theories of ground-radar interaction outlined here will be discussed in Chapters 6 and 7 in the light of information collected in the field.

5.2.3. Interpretation of the Western SIR-A Image.

The SIR-A image of the western study area around Hadjeb el Ayoun (Plate 3.3) reveals very different terrain information from that displayed in the eastern image (Plate 3.2). The image is dominated by the contrasting tone of the high backscatter mountainous environments and the darker lowland regions.

The high surface relief of the mountain environments is responsible for the high radar backscatter and bright tone on the SIR-A image. As would be expected, slopes oriented towards the incoming radar beam tend to have the brightest response, as the local angle of incidence will be minimal (see Chapter 3, Section 3.5.5). This is especially true for slopes of 40° to 50°. For this reason the southern flanks of Djebel Henndi and south-east slopes of Djebels Nara and Cherahil have particularly high levels of radar backscatter.

The incised western and northern flanks of the djebels can be determined clearly, owing to the variations in radar backscatter associated with changes in local incidence angle. Slopes oriented towards the SIR-A system tend to have a bright response on the image, while those oriented away from the system are commonly in radar-shadow.

SIR-A return from the mountain regions of the western study area provides a great deal of relief information. Differential enhancement and shadowing of slopes in accordance with local incidence angle variations gives an excellent impression of relief form and approximate slope angle. This supports the view taken after previous studies

of the great potential of SIR-A in upland areas (Martin-Kaye and Lawrence, 1983a; Rott, 1984a) (see Section 3.5.5).

Other variations in radar backscatter, represented by changes in SIR-A image tone suggest the presence of other geological or morphological features within the mountains. The eroded anticlines of Djebels Cherahil and Henndi can be delimited clearly on account of their unusually low backscatter responses. From this it may be deduced that, in mountainous areas, SIR-A backscatter is largely dependent upon slope form rather than surface roughness conditions. The contribution of microscale roughness and surface relief to SIR-A image appearance is discussed more fully in Chapter 6 in the light of information recorded in the field.

The alluvial fans of the southern tip of Djebel Nara can be distinguished by their mottled mid-grey tone. Their tone and texture suggest the presence of alluvial material of variable size, producing an overall radar medium-to-rough surface. A similar backscatter response can be found in the large areas of exposed calcrete around Djebel Henndi, where exposed nodules have given rise to medium-to-high levels of radar backscatter.

The two small sebkha features to the east of Djebel Nara can just be distinguished on the SIR-A image (Plate 3.3), although their form is less clear. A similarity in surface roughness conditions between the sebkha and its surroundings is the most likely explanation for this lack of definition, as the Cherahil Valley appears to be more radar-smooth than the area surrounding Sebkha Sidi el Hani on the eastern SIR-A image (Plate 5.2).

The large wadis of the western study area, Oued Zeroud and Oued el Hateb, have a distinct mottled mid-grey response on the SIR-A image that contrasts both with the high and low backscatter from mountain and lowland areas respectively. This distinctive tone and texture could have resulted from one or other of several surface conditions:

(a) Gravel and stones on the wadi floor,

(b) Braid bar and channel features on the wadi floor,

(c) Low vegetation clumps on the wadi floor.

At this stage it is not possible to come down in favour of any of these theories. They will be discussed in the light of field information in the following chapter.

Some stretches of the two large wadis are delimited by a line of bright tone associated with high radar backscatter from the channel walls. This type of response is also typical of the smaller wadis and gullies in the region. The line of Oued el Hadjel can be traced clearly along its length on the SIR-A image (Plate 3.3) by its high backscatter response that is well contrasted with the surrounding area of low ground. Furthermore, the numerous gullies that dissect the upper parts of the Hadjel Valley have the same distinctive bright tone. Their response on the SIR-A image is likely to represent a combination of scattering from channel and channel-wall components. The relative importance of each can only be determined in the light of field measurements (see Chapter 6: Section 6.8.2).

The agricultural regions surrounding the mountains of the western study area produce a diversity of tonal

response on the SIR-A image of the area. The black tone associated with the agricultural plains to the east and west of Djebel Cherahil are indicative of smooth surface conditions. From the image response alone, it is not possible to say with any certainty whether or not the areas represented by the dark image tone are cultivated. Any cultivation is likely to take the form of cereal crops or ley grasses. These crops are the most probable cause of the dark tone of many of the individual fields or plots distinguishable on the image. A more detailed analysis of these areas can only be made when reference is made to the results of field investigations (Chapter 6, Section 6.8.3).

Individual fields of brighter tone on the SIR-A are thought to correspond with aboriculture plantations or areas in which bush crops are grown. Large furrow sizes or abnormally stoney ground could also have given rise to the radar-rough surface suggested by the image response. Large areas of the western image to the east of Djebel Cherahil and north Djebel Touil have a similar tone and texture to that found in the olive-growing regions of the Sousse coastal plain. The areas have a bright speckled tone, with individual plot boundaries often distinguishable. The presence of extensive tree plantations in these areas and their effect on radar image tone is discussed in the following chapter.

Hadjeb el Ayoun is the largest settlement within the western study area, and as such is the most easily distinguished on the SIR-A image. Its radial road network is well contrasted with surrounding area on account of its high radar backscatter. Indeed, in this, and other localized areas, SIR-A has demonstrated its ability to discriminate roads that are parallel to the sensor look

direction (see Section 3.5.6). This almost universal bright SIR-A return suggests that the roads themselves must possess certain characteristics that cause them to generate high backscatter response irrespective of look direction (see previous section). Smaller settlements in the area are not so easily distinguished on the image, as the high level of backscatter generated by corner reflection from buildings provides little contrast with the bright tone of mountain and agricultural regions.

5.3. Generation of Landsat Thematic Mapper False-Colour Composites.

Three-band false-colour composite images of the Landsat TM coverage of the western study area were generated to assess the value of information derived from visible and infrared wavelengths by way of comparison with the information recorded at microwave wavelengths by SIR-A and Seasat. The following band combinations were used:

(a) TM4 (red), TM3 (green), TM1 (blue): Plate 5.3.

(b) TM4, TM5, TM2: PLate 5.4.

(c) TM5, TM7, TM1: Plate 5.5.

All three bands in the TM4,3,1 composite (Plate 5.3) are sensitive to variations in vegetation type and to soil moisture and texture conditions (see Section 3.6). As such, this image contains a considerable amount of information in the lowland and valley regions of the study area. The rich agricultural lands east and west of Djebel Cherahil can be clearly distinguished by their predominantly red tone. Individual fields seem to correspond with areas of high and low backscatter on the

SIR-A image, suggesting that it is vegetation intensity and condition, rather than structure, that is important at these wavelengths. Pockets of high near-infrared (band 4) reflectance can be found throughout the image, corresponding to areas of agriculture on the most fertile ground.

The changing soil and land cover conditions of the Hadjel Valley, and lowlands to the north and east of Djebel Henndi, can be distinguished on the image by their green and yellow tones associated with changes in visible light reflectance. The eroded areas of the Hadjel Valley have a considerably lighter tone than areas of more stable soil conditions. All hydrological features have a light green tone on the image resulting from combined reflectance in TM bands 3 and 1. The mountain environments of Djebel Nara and Djebel Henndi have an overall dark brown appearance. Although the general relief form can be distinguished, the amount of morphological information contained within these areas is limited.

The TM 4,5,2 false colour composite image (Plate 5.6) contains similar information to the TM 4,3,1 image. Individual fields can again be discriminated with ease, agricultural areas retaining their prominent red tone. Variations in soil moisture and salinity within the sebkhas and wadi systems are particularly well shown in this image. Moist saline soil conditions are represented by the blue and purple hues associated with high band 4 and 2 reflectance. Furthermore, this band combination gives a better impression of relief form within the Djebel Nara chain.

The false colour composite image of TM bands 5,7,1 (Plate 5.7) reveals a greater amount of geological and pedological information. The internal structure of all the mountain chains in the region can be determined with greater accuracy, as they are no longer confused with upland vegetation reflectance. Hydrological features and soil moisture conditions are shown in blue on the image (note the internal variations with wadis Zeroud and el Hateb). They are well contrasted with the eroded soils of the Hadjel Valley.

In general, the three TM false colour composite images reveal a greater range of information relating to soil and vegetation conditions than the SIR-A image of the area, particularly in the agricultural regions around Djebel Cherahil. However, the impression of relief given by these images is inferior to that given by the SIR-A image. Indeed, Djebels Henndi and Cherahil are not distinct on any of the images, which seem only capable of revealing detailed information about the higher mountains (i.e. Djebel Nara and Djebel Mhrila). The gullies of the Hadjel Valley are much less distinct on the TM images, although variations in soil type and land cover on the interfluves are more readily distinguished. The small sebkha to the east of Djebel Nara can be seen on each of the false colour images, and not on the SIR-A image. This highlights the importance of surface roughness on radar image tone, the variation in which largely determines feature expression. Cultural features too are far less distinct on the false colour images, possibly because they are constructed with local materials, giving them similar reflectance characteristics to the surrounding areas.

5.4. Digital Image Co-registration.

The growth of multi-band and multi-date image collection from the Landsat series of satellites and other systems, such as SPOT, has created the need for faster methods of interpretation that can be carried out at larger scales (Townshend, 1981). Techniques of digital image processing and analysis have been refined over the years to allow the rapid evaluation of multispectral information and the automatic enhancement and transformation of images (Haydn et al., 1982). Although these techniques have serious limitations, they are certainly a useful tool in image interpretation.

Digital image processing of satellite radar data was initiated after the Seasat mission of 1978, although the lack of digitally-processed SIR-A data has tended to restrict its use. The availability of digitally-processed Seasat data and a film-digitized SIR-A product in this study provided a rare opportunity to explore the possibilities offered by a comparison of digital radar imagery. Furthermore, the Landsat TM coverage of the western study area allowed digital combination and comparison of data derived from the visible, infrared and microwave portions of the spectrum.

Although a large amount of information could be gleaned from the single band radar imagery and the Landsat colour composites, it was decided to investigate the possibilities offered by digital image co-registration. Two co-registered data products were prepared. In the eastern study area, the digitized SIR-A image was combined with the Seasat data to produce a two-band image. In the western area, an eight-band image product was produced, by combining the Landsat TM image with the SIR-A scene.

The co-registration process consisted of the selection of common ground points on the images using the "M'GCP'VIRTUAL-DISPLAY" on the I^2S System 600 Image Processing System. Points such as road crossings, headlands and the corners of fields were used, although point selection in the eastern area was hampered by the opposing look directions of the two radar passes which led to preferential feature enhancement. Twenty-two points were selected for the Seasat/SIR-A co-registration and sixteen for the combined TM/SIR-A product.

Once points had been selected, the two SIR-A images were warped to the Seasat and Landsat TM master images using the "M'CPWARP" function on the I^2S image processing system. The Nearest Neighbour Analysis option was adopted for the warp routine as it preserved all DN values on the final images. This procedure created two SIR-A images (SIREWARP and SIRWWARP) with the same geometrical projection as the master images (Plates 5.6 and 5.7). A 30° rotation was required for the co-registration process.

The eastern warped SIR-A scene (SIREWARP) was combined with the Seasat master image and a constant grey-level image to produce a three-band image, using the I^2S "C'MERGE" function. The constant image contained no information, as each pixel had a constant DN value of 127. It was included in the merged product to allow a false colour composite to be generated (Plate 5.8).

Three-band coverage of four selected key subscene images can be found in Plates 5.9 to 5.12. The subscenes, each $(512 \text{ pixels})^2$, were chosen to provide coverage of areas studied in the field and to include the greatest possible range of environmental conditions. Their selection allows the operation of image analysis routines

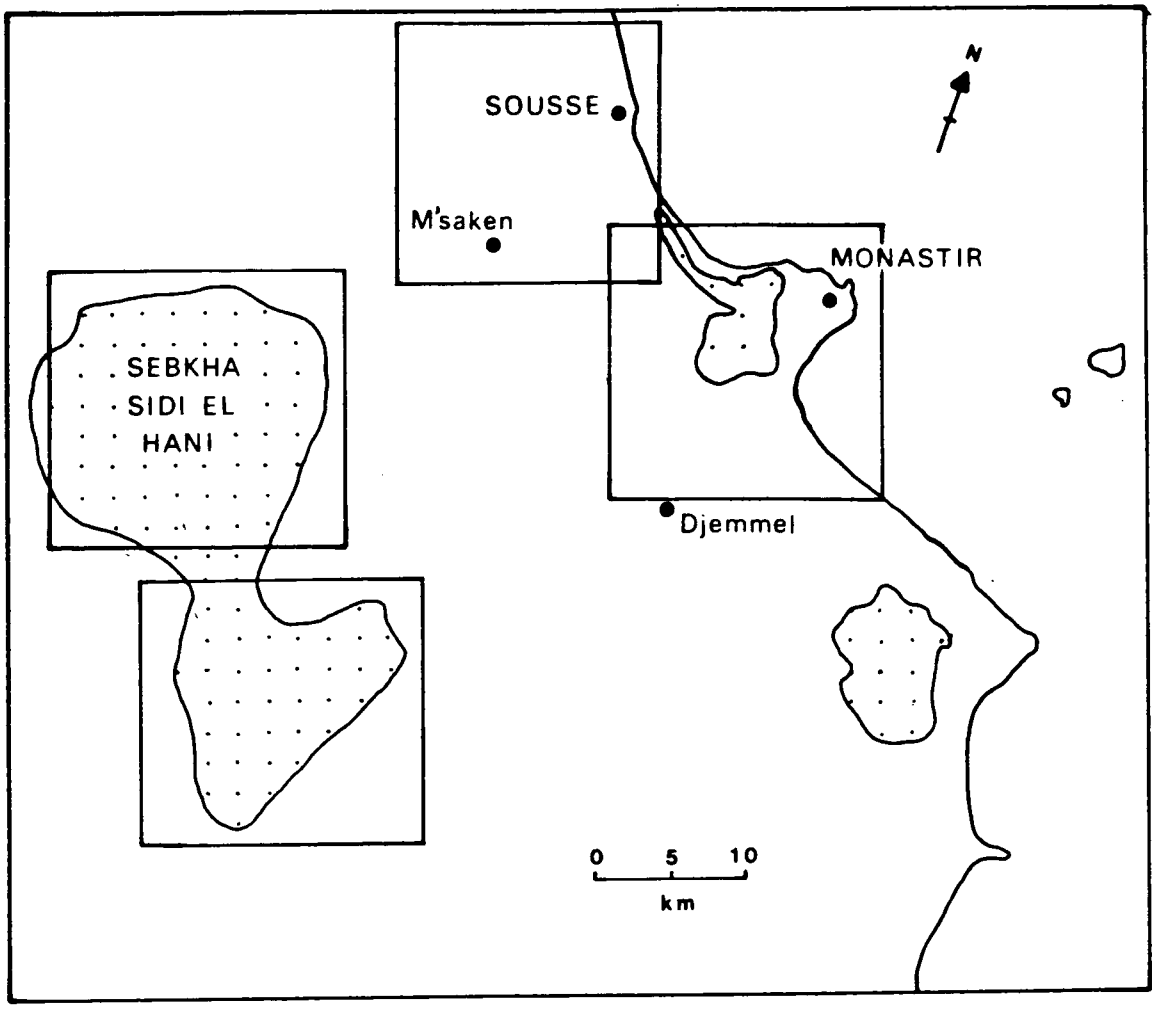

Figure 5.2 Location of the four subscenes chosen for digital image analysis of the eastern Seasat and SIR-A images.

without the need for large amounts of processing time. the four subscenes are shown in Figure 5.2. They are as follows:

(1) Northern part of Sebkha Sidi el Hani

(2) Southern part of Sebkha Sidi el Hani

(3) The environs of Sousse

(4) The ancient coastal sebkha at Monastir.

Seasat and SIR-A coverage of these four areas can be found in Plates 5.13 to 5.20.

The combined image created from Seasat and SIR-A cover of the Sahel of Sousse provides a more detailed picture of the environment of the area than that provided by either one of the individual images. The image displays both surface roughness and relief information allowing the hills and olive-growing regions to be distinguished. Internal variations within Sebkha Sidi el Hani recorded on the Seasat image are highlighted still further by the addition of the SIR-A image where the low response of the sebkha is in marked contrast with the surrounding area (Plates 5.9 and 5.10). Similarly, the extent of the sebkha at Monastir is clarified by the combined image (Plate 5.12).

Combination of information recorded by radar systems with opposing look directions is certainly a bonus for effective image interpretation. Major transport lines can be detected irrespective of orientation and groyne and bar features within the sebkha at Monastir are no longer preferentially enhanced (Plate 5.12). Close inspection of

these features reveals some apparent mis-registration of the images. Although mis-registration is bound to explain, in part, the 'double-image' that appears, preferential backscatter from the sides of features oriented towards the incoming radar signal in each case is an alternative explanation. The combined image formed the basis of several additional analyses that will be discussed later in this chapter.

In the western study area SIRWWARP was combined with the seven band Landsat TM image using the "C'MERGE" function. This enabled various false colour composite images to be produced from selected TM/SIR-A combinations. The following combinations yielded the greatest amount of image information:

(a) TM4 (red), TM7 (green), SIRWWARP (blue) (Plate 5.21).

(b) TM7, TM5, SIRWWARP (Plate 5.22).

(c) TM3, TM5, SIRWWARP (Plate 5.23).

(d) TM3, TM4, SIRWWARP (Plate 5.24).

Additional operations were performed on the combined TM/SIR-A image product and will be discussed later in this chapter.

Many of the digital image processing operations could not be performed easily on the whole image due to the processing time involved. Four subscenes were selected for ease of analysis, each being $(512 \text{ pixels})^2$ (Figure 5.3).

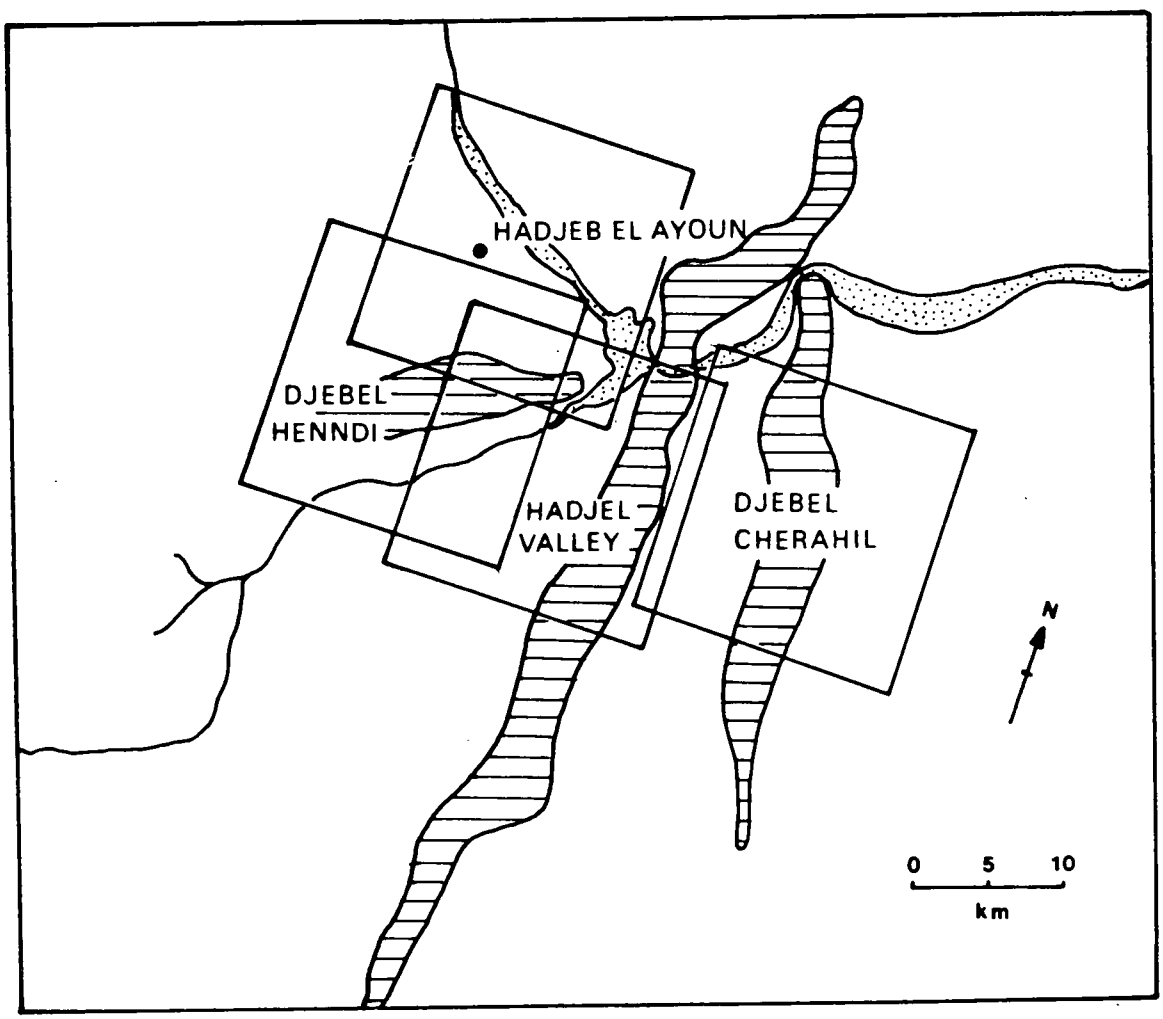

Figure 5.3 Location of the four subscenes chosen for digital image analysis of western SIR-A and Landsat TM data.

The areas were chosen to cover a range of landforms and cover types, including mountains, gullies and agricultural areas, all of which had been studied in the field. Mountains trending north-south and east-west were both represented in the chosen subscenes, which are:

(1) The environs of Hadjeb el Ayoun

(2) Djebel Henndi

(3) The Hadjel Valley and Djebel Nara

(4) Djebel Cherahil

SIRWWARP subscenes for these areas can be found in Plates5.23 to 5.26.

Co-registration of radar and/or Landsat data has been found to be a useful tool in the mapping and analysis of land areas by providing complementary information. Yao and Gilbert (1984) used a co-registered Seasat /TM image over an Iowa test site of the AgRISTARS project (Agriculture Resources Inventory Survey Through Aerospace Remote Sensing). A similar combined Landsat/Seasat product made a significant contribution to rock-type discrimination studies of areas of California, Utah and Haiti (Blom and Daily, 1982). Phillip Rebillard has made use of a number of co-registered Seasat, SIR-A and Landsat images in his studies of land cover and geomorphology in Northern Africa (Rebillard and Nguyen, 1982; Rebillard, 1982; Rebillard and Evans, 1983; Rebillard et al., 1984; Rebillard, 1984).

Inclusion of SIR-A data in the combined false colour image of the western study area enables full advantage to be taken of the range of information recorded by the two

systems. The use of band 7 in two of the three-band combinations makes them ideal for geological and morphological interpretation, due to the combination of relief (SIR-A) and lithological (TM) information. The sensitivity of SIR-A to variations in surface roughness is a bonus in the understanding of soil and surface cover conditions, adding textural information to the spectral response of surfaces at visible and infrared wavelengths.

Combination of information recorded at visible, infrared and microwave wavelengths proves to be advantageous for the detection of hydrological features. In all four composite images the sebkha east of Djebel Nara can be easily distinguished. Internal variations within the sebkha are highlighted by the addition of TM bands 3 and 4, and 4 and 7, to the SIR-A image. The TM3,4, radar and the TM3,5,radar composites are particularly useful for the detection of variations in soil moisture and surface conditions in the large wadis of Zeroud and el Hateb. However, it should be noted that the absence of such variations on the SIR-A image does not necessarily imply that the appropriate surface conditions cannot be detected by radar. The temporal and seasonal differences between the SIR-A and Landsat passes could well account for this. The reservoir at the northern end of the Hadjel valley provides an excellent illustration as, although it stands out clearly on the combined image, it was not constructed until after the date of the Shuttle flight in 1981.

It is not easy to say which of the colour composites provides the 'best' image for investigation of the semi-arid environments around Hadjeb el Ayoun. The choice of combination has to be made in the light of the particular area of interest or application for which it is to be

used. Visual examination of the images allows the following generalizations to be made:

(a) TM4, TM7, SIR-A: useful for discrimination of vegetation and water bodies and for the separation of soil, geological and vegetation information.

(b) TM7, TM5, SIR-A: gives a good impression of relief but tends to confuse soil and vegetation conditions due to the predominance of microwave surface-roughness information.

(c) TM3, TM5, SIR-A: valuable in the detection of moist soil conditions and hydrological features. Again this image seems to highlight surface roughness and relief information.

(d) TM3, TM4, SIR-A: allows the discrimination of vegetated areas and soil moisture conditions.

Each image has its use although the TM4,7,SIR-A combination must be said to take advantage of the full colour spectrum by providing an excellent summary of information derived from visible, near-infrared and microwave wavelengths.

5.5. Principal Components Analysis.

The three-band combinations of the co-registered SIR-A/Landsat image restricted the amount of information that could be displayed in any of the false colour images. In each case only 3/8 of the spectral data was represented in the image. To overcome this problem Principal Components Analysis was applied to the data using the "CPU'STATISTICS" and "M'KL" commands on the I^2S image

processing system. This function maximizes the separation of the differences between bands by redistributing the spread of the data within multi-dimensional image feature space (Drury, 1987). The first principal component (PC) represents the line of maximum data spread and is an average of all the input bands. As such, it is often a useful interpretation tool. The higher orders PC's represent deviations from the average trend and contain larger amounts of noise (Drury, 1987). However, they can contain much useful information and should not be rejected out of hand.

Two principal components analyses were applied to the combined western image. A number of products were created from the resulting components for each of the four test site areas. The analyses are outlined below and final image products are compared for individual test areas.

(1) PCA of Landsat TM.

A principal components analysis was calculated for the four subscenes of the Landsat TM image. As the "M'KL" routine on the I^2S system 600 Image Processing System limits the input bands to 6, TM band 6 (Thermal) was omitted from this analysis on account of its poor spectral information content. Two image products were created from this analysis:

(a) A colour composite image of the three first principal components. These images provided a summary of the information in all 6 TM bands (Plates 5.29-5.32).

(b) An image combining the first two TM principal components with the geometrically altered SIR-A image. The resulting images (Plates 5.33-5.36) contain a summarized visible and infrared component and a full microwave component, a combination that Stewart et al., (1980) found useful in the assessment of wavelength contribution to rock-type discrimination.

(2) PCA of TM bands 7 and 4 and SIR-A Image.

A principal components analysis of this three-band image was calculated to explore the information contained in the colour composite described in Section 5.3. (Plate 5.21). Principal component images for the four subscene areas can be found in Plates 5.37-5.40.

(1a) TM Principal Components Image Analysis (Plates 5.29-5.32).

The four TM principal component image subscenes contain a wealth of information about the soil conditions and vegetation cover of the western study area, with changes in hue representing subtle variations in ground surface characteristics. Vegetated areas are discriminated by combinations of blue, purple and pink, while areas of bare ground are characterized by tones of green and orange. The calcrete levels on the southern and western margins of Djebel Henndi are well shown by their pale-blue appearance on the image. The images give a good impression of relief, and lithological characteristics of upland areas can be discriminated on a general basis, particularly in the Nara Chain. Hydrological features have a bright white tone on all subscenes an account of the overall high spectral response from standing water or

moist soil. The main disadvantage of the image is the lack of information relating to the microrelief of the surface and cultural features.

(1b) Combined TM Principal Component and SIR-A Image Analysis (Plates 5.33-5.36).

These images present a less clear picture of the environmental conditions of the western study area. In general terms areas of relief are less distinct than in the images described in the previous and following sections, although lithological variations can still be discerned. Vegetated areas have an overall red hue on all images, with some areas of yellow and green. This suggests that the SIR-A image has little input value in these areas. Similarly, hydrological features such as the Bourguibà Reservoir are represented by yellow and green, owing to the minimal use of microwave information in these areas. Indeed the Bourguiba reservoir was only constructed some years after the shuttle overflight. Erosion features are well discriminated on the image due to their high SIR-A response. Although all four images reveal valuable textural information relating to surface microrelief or roughness the addition of SIR-A data to the TM PC image introduces excess speckle and confusion to the scene.

(2) Analysis of Principal Component Images of TM bands 4 and 7 and SIR-A (Plates 5.37-5.40).

These images give a particularly good impression of relief with TM band 7 and SIR-A providing alternative illumination directions in mountain regions (by the sun and radar respectively). The opposing look directions reduce the problems of shadowing that arise from single-system image analysis. Furthermore, lithological

variations can be observed in all upland areas, particularly in the Nara Chain.

The clarity of the select-band PCA images is much improved over that of the images described in the previous sections as the scenes are not complicated by vast quantities of data and excessive speckle-noise. Indeed, generation of principal components from satellite radar data has proved to be an effective way of reducing image speckle in this area, as it is not included in any of the first three principal components. The reduction in speckle enables variations in soil condition and vegetation cover to be delimited. Agricultural regions can be identified by their red and green hues, while bare soils tend to be yellow and orange in colour. Hydrological features appear dark on the images and are clearly distinguished from the surrounding areas. Interestingly, the image gives a record of the valley form beneath the Bourguiba reservoir by combining information in pre- and post- construction periods. Cultural features also can be detected (note the town of Hadjeb el Ayoun).

Analysis of the three black and white principal component images of the full scene helps to explain the combined colour image by enabling the dominant component characteristics to be identified. The first principal component (Plate 5.41) contains a considerable amount of information about the macro- and micro-scale relief of the area, with mountains and gullies being particularly well shown. SIR-A and TM band 7 are likely to have given the greatest input to this component. The second principal component (Plate 5.42) reveals information relating to soil and vegetation condition. Bare soils (bright) can be distinguished from vegetated areas (dark). The component is a summary of information found in TM band 4 and the

SIR-A swath. The third principal component (Plate 5.43) is more difficult to interpret, but seems to represent changes in soil moisture and vegetation. SIR-A and TM band 4 both contribute to this component.

In summary it may be said that the TM4,7,SIR-A PCA image reveals information about the relief of the area (at micro- and macro-scales) and the soil and vegetation characteristics. It provides a more effective and useful summary of data recorded at short and longer wavelengths than the full TM SIR-A combined component image.

5.6. Application of Spatial-Frequency Filters.

Application of digital filters to remote sensing images allows certain groups of frequency information to be enhanced or suppressed. These filters can be applied in the frequency domain through a Fourier transform, or in the spatial domain by 'convolution' (Drury, 1987). Low pass and high pass convolution filters were applied to the four subscene radar images in the eastern and western study areas using the I^2S "M'CONVOLVE" function. A 3x3 kernel or window size was used for each filter. The weights applied to the low-pass filter were (1,1,1,1,1,1,1,1,1), while the high pass filter used weights of (-1,-1,-1,-1,8,-1,-1,-1,-1).

In addition to the high- and low-pass filters, a directional filter was applied to each of the radar subscenes. Operated by the "M'COMPASS" command on the I^2S Image Processing System, this convolution filter detects edges with a preferred orientation and is useful in structural geological interpretation (Moore and Camm, 1982). Four directional filters (N, E, NW and NE) were

applied to each image and the optimum filtered image selected using the I^2S "SPLITSCREEN" command.

The three filtered maps derived from each area were combined to create a colour image. SIR-A and Seasat filtered images for the Monastir test area can be found in Plates 5.44 and 5.45. It is interesting to note that, despite the perpendicular look direction of these two satellite SARs, a north-east directional filter produced the most useful result in each case.

The filtered Seasat image (Plate 5.44) gives a three-dimensional impression of the relief of the area, with the patches of hill country around Monastir dominating the image. In local areas relief features may be confused with cultural information (settlements), which have a similar appearance on the image. Low-lying coastal regions, together with the sebkha, can be distinguished by their subtle variation in tone, which is in marked contrast to the areas of relief. Groyne and bar features of opposing orientation within the lagoonal area at Monastir can be determined, although those trending north-south are most prominent.

Cultural features have the greatest clarity within the SIR-A filtered image of Monastir (Plate 5.45). Again, most of the groynes and bars near the coast at Monastir can be distinguished, but the look direction of SIR-A ensures that those trending E-W are emphasised. Filtering of the two images highlights the predominance of textural information in SIR-A data, generated by changes in ground surface roughness. Additional analyses applied to the filtered images are discussed in the following section.

5.7. Application of the Hue-Saturation-Intensity Transform.

Traditional remote sensing colour image displays make use of the red-green-blue colour space, determined by cartesian-coordinates. Such images are well understood within the field of remote sensing but they do have several drawbacks. Firstly, RGB images often generate colours that are very difficult to describe and interpret. Frequently they bear no resemblance to natural relationships between electromagnetic energy and surface material. More importantly, however, the human eye is not particularly sensitive to the chromatic colour space so the full information content of the images cannot be realized (Drury, 1987).

An alternative colour space exists that resembles the human colour perception more closely. This colour space is defined by the spherical co-ordinates of Hue, Saturation and Intensity. Hue is a measure of the average wavelength of the electromagnetic light signal and varies according to the mixtures of adjacent wavelengths. Saturation is determined by the mixture of wavelengths around this average. Pure colour saturation is achieved by a single wavelength, while mixed wavelengths produce pastel shades. The intensity represents the total energy of all the wavelengths (Drury, 1987). This colour system covers a much larger area of colour space than that defined by the RGB co-ordinates (Figure 5.4). The HSI colour space is conical in form, limited in intensity by the 0-255 DN range.

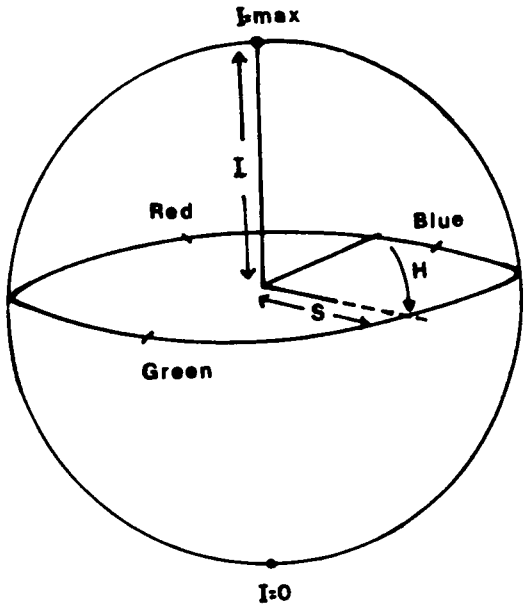

Figure 5.4 HSI and RGB colour space.

Transformation of RGB co-ordinates into HSI colour space enables the three components to be stretched to enhance colour differences before being converted back into RGB for display, thereby revealing the full spread of the data. This provides the image analyst with a powerful interpretation tool. The method has been found to be particularly useful in the analysis of merged image products that combine very different wavelengths. Haydn et al., (1982) stress the value of this technique for enhancing merged Landsat MSS/RBV and MSS/HCMM data of various test sites and state that it seems to "...provide a logical encoding scheme for...highly independent spectral data". This being so, it was decided to apply the transform to the two co-registered images to exploit the full range of information within them. Furthermore, work by Daily (1983) on the split-spectrum processing of a filtered Seasat image prompted the application of the transform to the three-filter subscenes.

Using the I^2S "CPU'RGB_IHS" command and the "Reverse=Yes" option the transformation was used on the following images:

(1) The combined eastern image with intensity held constant, hue determined by Seasat and saturation determined by SIR-A (Plate 5.46)

(2) The combined eastern image with intensity held constant, hue determined by SIR-A and saturation determined by Seasat (Plate 5.47)

(3) The four subscenes of the TM4, TM7, SIR-A image with intensity determined by TM4, hue determined by SIR-A and saturation determined by TM7. The dramatic images produced by this procedure can be found in Plates 5.48 to 5.51

(4) Four filtered subscenes (Monastir: Seasat and SIR-A; Cherahil: SIR-A; Henndi: SIR-A). For each image, intensity was controlled by the directional filter, hue by the low-pass filter and saturation by the high-pass filter (Plates 5.52-5.55).

The images resulting from these processes are evaluated below.

(1) HSI Transform I=Constant, S=SIR-A, H=Seasat.

Use of the HSI transform on this particular image combination is particularly useful for discriminating areas of low radar backscatter associated with hydrological features (Plate 5.46). Subtle changes in tone on the original Seasat image are transformed into dramatic variations of blue and yellow. The areas of hill country

are less distinct, as the purple and red hues associated with the high backscatter response from these regions can be confused with larger settlements and pockets of aboriculture. As on the Seasat image, only the main settlements can be identified.

(2) HSI Transform I=Constant, S=Seasat, H=SIR-A.

The variation in hue generated by SIR-A on this HSI image gives a dramatic visual impression of the environment of the Sahel of Sousse (Plate 5.47). Settlements can be clearly discriminated from the surrounding areas by their red hue. Other regions of high backscatter coincident with areas of arboriculture can be distinguished from radar-smooth surfaces on account of their purple coloration. As surface-roughness is reduced (due to changing soil or vegetation condition), the resultant hues change from purple through blue to green. The darkest areas on the original SIR-A image (regions of low backscatter) are represented by green on the HSI product. Care must be taken when interpreting the variations in saturation generated by the Seasat image, as the highest levels of saturation are coincident with high Seasat backscatter. Thus the normal radar interpretation procedures of "bright response=high backscatter" cannot be used.

Both HSI products generated from the combined eastern image provide a useful summary of the information content found within the input radar data. The image used to determine hue has the greatest influence on the appearance of the final product. For this particular area the second combination (Plate 5.47) generates the most powerful and easily-understood image.

(3) HSI Transforms I=TM4, S=TM7, H=SIR-A.

The value of colour composite and principal component images obtained from this particular combination of TM and SIR-A data has been described in Sections 5.4 and 5.5. Use of the HSI transform on this band combination produces an even more dramatic result. The four subscene transform images for the western study area are given in Plates 5.48 to 5.51. Purple hues represent all upland regions, allowing them to be distinguished from the yellow and blue hues of the badlands. The use of TM7 to determine colour saturation introduces shadowing into these areas, thereby making the images almost three-dimensional in appearance. Other pockets of high radar backscatter, such as settlements and gully walls, have the same purple hue but these can be separated from the mountains by their spatial context.

Flat areas of bare soil can be discriminated easily by their yellow tone on the image, with the intensity of colour determined by soil and moisture conditions (TM band 4). The main drawback of the image is the inability to differentiate rough-surfaces from areas of scrub and bush vegetation, arising from the use of SIR-A to determine hue. Nevertheless, for this particular area and band combination the HSI transform offers a new perspective and greater clarity to combined-wavelength image interpretation.

(4) HSI Transforms of Filtered Subscene Images.

The value of HSI transformations in image interpretation is further exemplified by their application to the filtered images described in Section 5.6. By using the low-pass filtered image to determine hue, a textured

impression of surface cover and relief is obtained. In all images the highest DN values are represented by red and pink hues, hues that progressively change through purple, blue, green, yellow and orange as the DN is reduced. Colour saturation is determined by the high-pass filter, which helps to give a three-dimensional picture of relief at micro- and macro- scales. This adds further texture to the resultant images. The dependence of local intensity values upon the results of the directional filter tends to increase the three-dimensional impression by allowing linear features (roads, groynes, banks, etc.) to stand out from the surrounding areas.

The filtered Seasat subscene image of the Monastir area (Plate 5.52) provides an excellent example of the ability of the HSI transform to highlight variations in relief. While areas of hill country dominate the image the overall information content is significantly greater than the simple filter-derived product described above (Plate 5.44). Similarly, the picture presented by the filtered SIR-A subscene of Monastir (Plate 5.45) is dramatically improved by the application of the HSI transform (Plate 5.53). The combination of hue and texture gives an excellent impression of microrelief characteristics.

The structure of mountain regions and the microrelief and/or vegetation cover of the western study area can be determined from the HSI transforms of the filtered subscene images. Two of these are included in Plates 5.54 (Djebel Henndi) and 5.55 (Djebel Cherahil). Linear features such as roads, wadis and mountain ridges are enhanced by the directional filter. HSI images of this area present the information summarized by the filtered passes in much more clarity and colour than the simple

filter combinations and must be considered successful results of image processing.

The value of HSI transformation in image interpretation has been demonstrated by all four applications described in this section. In all cases, subtle variations in surface expression and dramatic variations in relief alike have been combined in a colourful and valuable summary product.

5.8. Unsupervised Image Classification.

The discrimination capabilities of the combined two-band Seasat/SIR-A, and eight-band SIR-A/TM images was assessed for the eight subscenes using the "M'CLUSTER" command on the I^2S Image Processing System. A method of supervised classification (e.g. maximum likelihood) was rejected in favour of this unsupervised method, due to the difficulties of defining training sets that were fully representative of the area. The limited time available for fieldwork meant that only selected areas could be analysed in detail. Unfortunately, large areas of each study area were mapped on a general level only, and were unsuitable for training set selection. In addition, the presence of inherent image 'speckle' in the radar images was not conducive to the delimitation of homogeneous training areas. Nevertheless, the advantages of unsupervised classification have been extolled in several publications (Nagy et al., 1971; Smedes et al., 1972). Smedes et al., (1972) found that unsupervised classifications of the Yellowstone National Park were almost as accurate as supervised classifications.

Classifications were undertaken on all subscenes using the "M'CLUSTER" command. The number of classes were defined by "M'LEVELSLICE", those classes that appeared similar being combined using the "M'PIECEWISE" function. The key and classes were shaded using the "M'KEYCLASS" and "M'COLOURS" commands. Figures for the number of classes generated and chosen for each subscene are given in Table 5.1.

SCENE	SUBSCENE	CLASSES GENERATED	CLASSES CHOSEN
EAST	SIDI EL HANI NORTH	17	4
	SIDI EL HANI SOUTH	17	6
	BOUSSE	10	4
	MONASTIR	9	6
WEST	HADJEB EL AYOUN	17	7
	DJEBEL HENNDI	17	11
	HADJEL VALLEY	17	11
	DJEBEL CHERAHIL	17	9

Table 5.1 Number of classes chosen for Cluster Classification of the eight subscene image areas.

Class names assigned in each case do not necessarily fully describe the surface conditions at all points within that class. Choice of class names during the classification routine is not meant to preclude further discussion as to the reasons behind the classifications made.

(a) Cluster Analysis of the Eastern Subscenes.

For the two subscenes located on Sebkha Sidi el Hani, Cluster analysis has enabled the separation of areas with different radar backscatter characteristics (Plates 5.56 and Plate 5.57). On the northernmost image (Plate 5.56) the large island within the sebkha has been classified in the same category as the surrounding countryside, thereby clearly differentiating dry-land and sebkha areas. The class named 'shore' represents all areas of moderately high backscatter associated with drier areas on the western shores of the sebkha; areas that are likely to include gravels, flow channels and uneven ground.

Variations in backscatter within the southern tip of Sidi el Hani are clarified significantly by Cluster analysis (Plate 5.57). These variations have been determined largely by the Seasat image. Areas of moderate relief surrounding the sebkha are less distinct, due to the mixed backscatter response on the input radar images. Nevertheless, flat, low-lying areas around the sebkha shore could be discriminated and were coloured dark green on the final image. Once again, most of the agricultural plain surrounding the sebkha has been well-classified (light green).

Settlement areas in the coastal subscenes of Sousse and Monastir were clearly differentiated by the cluster analysis (Plates 5.58 and 5.59), although some confusion has occurred in the areas of hill country in the Sousse subscene. Here, the high backscatter generated by the relief features could not be distinguished from cultural features. Classifications of olive growing regions and agricultural areas is not successful for this subscene, due to the size of fields.

Classification of the Monastir subscene (Plate 5.59), on the other hand, has proved fairly successful. Low backscatter or dark tones on the input radar images have been differentiated from other regions, allowing two classes to be generated for the sea and sebkha areas (dark- and light-blue tones). There is less confusion between settlements and other features in this image, suggesting that settlements have an unusually high radar response in comparison with the surrounding areas. The class identified by its red coloration seems to be coincident with areas of hill country, while classes coloured yellow and green are associated with lowlands (often olive plantations) and rougher surfaces (probably gravel or scrubland).

Cluster analysis of the four subscenes of the combined radar data has generated useful images that enable the differentiation of areas with contrasting levels of DN. The dependence of areas of radar image tone upon microrelief and roughness characteristics, together with the existence of image speckle, prevents a more accurate classification of soil and vegetation types from being made.

(b) Cluster Analysis of Western Subscenes.

Cluster analysis of the combined TM and SIR-A data of the western subscenes has generated classifications of greater clarity than in the eastern area, due to the reduction in image speckle. Around the town of Hadjeb el Ayoun cultural and hydrological features have been fairly well classified, although there is some problem of local mis-classification (Plate 5.60). Wadi and gully locations are also brought out by the cluster classifications of the Hadjel Valley and Djebel Henndi (Plates 5.61 and 5.62).

Flat, radar-smooth areas of agricultural production are well classified on all four subscenes and are shaded dark green. They are especially clear in the ares to the east and west of Djebel Cherahil (Plate 5.63).

Changes in soil type and roughness are well classified on the subscene of the Hadjel Valley (Plate 5.62). The smooth sandy soils towards the centre of the valley contrast with the eroded soils and interfluves of the northern part of the valley. Unfortunately the images are not of sufficiently large scale to show the detail that was apparent on the image processing system.

In upland areas of the western study area unsupervised image classification is largely dependent upon the illumination characteristics of the TM and SIR-A images. These characteristics allow the general separation of slopes into categories, thereby summarizing internal variations within the mountain regions.

For all subscenes, east and west, the results of Cluster analysis have to be interpreted with care, as pockets of mis-classification must be identified before images are used. Where radar imagery is involved, mis-classification is bound to occur as DN values are dependent upon backscatter characteristics that may arise from a number of surface types. This being so, it should be said that the classifications obtained for the test areas have proved successful in the separation of areas of different backscatter and/or spectral characteristics. The discrimination of surfaces by statistical analysis of image data is discussed in Chapter 7.

5.9. Summary.

In the light of a knowledge of the relationships between radar return and system and ground characteristics a wealth of valuable information was gleaned from the single-band radar images. Visual interpretation of these images highlighted the differences between their capabilities for surface discrimination and feature detection in a way that was not possible by digital processing methods. Nevertheless, digital processing and analysis of the three images, together with Landsat TM data of the western study area, provided a means of summarizing and combining the capabilities of each system.

Digital co-registration of eastern and western images was the basis for further analysis. Although the basic co-registered composite images provided a useful summary picture of the combined information content, this was better achieved by principal components analysis and image filtering. Furthermore, application of the Hue-Saturation-Intensity transform proved a valuable way of increasing contrast between areas of different response, and of introducing a three-dimensional impression in the images. The combined SIR-A and Seasat image, and the TM7, TM4, SIR-A image, illustrated this capability dramatically, as did the filtered subscene images. Use of the full band complement of the TM-SIR-A composite was rather less useful than the selective use of bands. Out of all 3-band combinations used, TM7,TM4,SIR-A proved to be the most valuable, a choice that was strengthened by PCA and HSI processing. The great volume of data within the multiband TM image may help to explain the pockets of mis-classification in the western Cluster analysis subscenes, although the complexities of radar signal-ground interactions were the most likely cause.

The link between ground characteristics and radar backscatter is explored in more detail in the following chapter, while statistical image classification procedures are described in Chapter 7.

Chapter 6. Investigation of the Effect of Ground Characteristics on Radar Image Appearance.

6.1. Introduction.

The principal aim of this study has been to exploit the overlap between Seasat, SIR-A and Landsat TM coverage of Tunisia in order to assess the capabilities of satellite radar in the discrimination of semi-arid environments. Determination of the influence of ground and system parameters upon image appearance is at the heart of the study, supported by digital and statistical image classifications. This chapter describes the collection and analysis of data drawn from ground and image sources. The importance of the results for the understanding of radar-ground interactions is also discussed. It should be stressed that the significant time-lag between the satellite passes and the collection of ground data, together with the absence of system calibration, prevents absolute quantitative conclusions from being made (Blanchard and Chang, 1983). Nevertheless, quantitative investigation of parametrical relationships and radar response is valid as a means of providing 'directional' indicators from which assessment of system capabilities can be made.

The parametrical analysis described in this chapter was undertaken to determine the most likely dominant ground controls on Seasat and SIR-A backscatter by studying the response recorded by these two systems for specific features on the coastal plain of Sousse. Ground data were collected from characteristic areas that could be located easily in the field. These data were combined with digital number (DN) information derived from the two radar images and were statistically evaluated. In

addition, the westward extension of the SIR-A swath into the mountain environments of Hadjeb el Ayoun (Figure 2.2b) allowed comparative investigation of the SIR-A response from lowland and mountain regions. On the basis of results derived from both study areas, general conclusions as to the most appropriate system parameters for radar surveys of semi-arid environments could be made. Furthermore, statistical comparisons of the information content of the SIR-A and Landsat TM images of the western study area enabled the relative merits of information collected at visible, infra-red and microwave wavelengths to be assessed. The analyses described in this chapter provide a more sound interpretation of radar-ground relationships than that provided by the visual and digital image analyses discussed in Chapter 5.

Section 6.2 describes the collection of ground data from the sample areas studied in the field. The preparation of these data for the parametrical analysis is discussed in Sections 6.3 and 6.4. The first of these two sections provides a summary of the laboratory analysis of soil samples collected in the field while the second describes the calculation of local radar incidence angle and feature orientation. The collection of image data is discussed in Section 6.5. The organisation of the data for anaysis is outlined in Section 6.6 and the results are discussed in Sections 6.7 to 6.9.

6.2. Ground Data Collection.

Ground data were collected during two spring field seasons to Tunisia in 1985 and 1986. The majority of data were recorded over a period of three weeks in April and May 1986. By no means can the timing of this field season be considered ideal due to the large time-lag between the

collection of image and field data (see Table 6.1). The seasonality of the data also presented problems for effective image interpretation. The field programme was designed to take these problems into account. No detailed crop classification or study of local soil conditions was made in this study on account of the problem of time-lag and seasonality.

DATA COLLECTION SOURCE	DATE
SEASAT PASS	16 August 1978
SIR-A PASS	4 November 1981
LANDSAT TM PASS	29 January 1983
FIRST FIELD SEASON	23 March - 6 April 1985
SECOND FIELD SEASON	24 March - 14 May 1986

Table 6.1 Dates of field and image data collection.

On the whole, ground investigation had to be restricted to areas where annual and seasonal changes could be regarded as minimal. The limited amount of time available for detailed field investigation was an additional factor influencing the design of the field programme.

A two-level approach to data collection in the field was adopted. At one level, general land cover and geomorphological information was recorded, mainly in map form, to assess the discrimination capabilities of the two satellite radar systems. This information was supplemented by published material (eg. République

Tunisienne, 1976) and was used in the verification of the classification studies discussed in Section 5.7 and Chapter 7.

At the second level detailed site-specific information was collected from selected test sites to assess the relationship between the various radar system and ground parameters. The sites were located within characteristic semi-arid environments. The four environments chosen for study, together with their local subset areas, are listed below:

(1) Sebkhas and Associated Features
 (a) Active inland sebkha, Sidi el Hani
 (b) Ancient coastal sebkha at Monastir
 (c) Lunette dune south of Sidi el Hani

(2) Vegetated Regions
 (a) Areas of varied vegetation type in the Sahel of Sousse
 (b) Areas of olive, apricot and almond production in the Sahel of Sousse.

(3) Wadis and Gullies
 (a) Gullies south of Sebkha Sidi el Hani
 (b) Wadis and gullies of the Hadjel Valley
 (c) Major wadis of the western study area

(4) Mountain Environments
(a) Mountain slopes of the western study area
(b) Areas of calcrete

Individual field sites were chosen at easily-located points which were considered to be representative of the key environments listed above. In vegetated regions, for example, individual fields and olive plantations were often recognisable on the radar images by their prominent opuntia hedges or their close proximity to roads, or other distinctive features. Individual gullies and wadis could commonly be located on the images, as were mountain slopes and sebkha regions.

The collection of field data varied from site to site depending upon the dominant ground characteristics in each area. The field program at each site is described later in this section. However, two ground variables were common to each site and formed the basis of the data collection. These variables are terrain slope and surface roughness, both of which are important in radar ground interaction studies (see Chapter 3). The slope angle was measured at each site using an abney clinometer and clino compass to an accuracy of +/- 1°. The Aspect of slope was determined also to the nearest 1°.

6.2.1. The Determination of Surface Roughness in the Field.

The determination of surface roughness in the field was a more complex problem to resolve. It is widely accepted that "no accurate and rapid roughness description method has yet been developed" (Cihlar et al., 1987) and that there is a distinct "lack of any suitable technique or system of microrelief classification" (Carr et al., 1963). However, a number of methods are available, and these are described in turn below:

(1) Measurement of Surface Profiles from a Templet.

This method, designed by Kuiper (1957), involves the use of a metal or wooden board through which vertical rods are inserted at uniform distances throughout its length. The rods are free to move up and down with the microrelief profile of the soil. As all the rods are of equal length, the roughness profile is manifested in the shape of the upper part of the templet (Cihlar et al., 1987), which is photographed against a grid scale for future reference. Schaber et al., (1976) used this method for radar backscatter research in Death Valley, California (Schaber and Berlin, 1980). Although high-resolution measurements can be obtained using this method it does have several distinct disadvantages. Firstly, it is impossible to obtain millimetre scale relief measurements (Schaber and Berlin, 1980). Secondly, the instrument itself often alters the natural surface profile (Cihlar et al., 1987). Finally, the templet is heavy and bulky and difficult to carry over considerable distances in the field. This method was not selected for the measurement of roughness in this study.

(2) Measurement of Surface Profiles Against a Grid.

This method necessitates the insertion of a gridded panel into the soil which is then levelled. The soil profile is photographed against the grid allowing digitization of the profile form. Alternatively, the profile can be recorded by spraying paint horizontally across to the gridded panel. The method was used by Blyth (1984) in his study of the effect of roughness on SAR 580 radar images. The method is unsuitable for use in dry or loosely compacted soils as the natural surface can be easily disturbed by panel insertion (Cihlar et al.,

1987). The equipment required for this method is heavy and bulky, again making it difficult to transport in the field. This method of roughness measurement was rejected during fieldwork design.

(3) Measurement of Surface Profiles from Stereo Photographs.

High resolution surface profiles can be obtained from stereo photographs taken above the soil surface (Schaber and Berlin, 1980). This method produces the most accurate results of all the methods reviewed here but it is time-consuming and expensive to initiate, as specialized equipment must be installed and calibrated at each site (Cihlar et al., 1987). The shortage of time available for fieldwork in Tunisia was not conducive for the adoption of this method.

(4) Quantitative Classification of Surface Roughness.

Owing to the problems associated with the equipment and time required by the three methods described above it was decided to devise a method of roughness measurement that would allow rapid division of surfaces into categories defined by the well-established roughness criteria. The Peake and Oliver roughness criteria described in Chapter 3 were selected as the basis of this approach. Calculation of the smooth and rough criteria for the Seasat and SIR-A system parameters results in the three surface categories 'rough', 'intermediate' and 'smooth' determined by the boundary figures in Figure 3.13. Two additional categories were included to allow more effective division of surfaces (Stone, 1986). Each category was assigned a digital number to allow separation

of categories for Seasat and SIR-A. The field definition of surface roughness is presented in Table 6.2.

Field measurements of the height of surface irregularities above the mean surface level (Figure 3.12) were made at six points within a randomly located $(10m)^2$ grid at each site. The points were chosen to be representative of the area within the grid and measurements made with a metric rule from the mean surface level. Thus, surface features such as boulders, gravel, dessication cracks and hard mounds of vegetation were all included in the classification. The sites were categorised on the basis of the mean height value. Mean roughness measurements and category values were both used in statistical analysis of the field data. The periodic roughness of a surface was also recorded where relevant. This took the form of direction, height and width measurements of crop rows or ploughed furrows in agricultural areas (Cihlar et al., 1987). The relevance of these periodic data to interpretation of the images is questionable, given the seasonal and annual changes in agricultural regions.

This approach to surface roughness quantification allowed rapid and effective assessment in the field without the need for expensive equipment or excessive time and labour. The results were considered to be within acceptable limits considering the time-lag between image and field data collection and the disputed relevance of correlation length in roughness measurement (Engman and Wang, 1987) (see Chapter 3). The ease of surface evaluation with this method enabled comparisons to be made with other field areas, as described later.

The collection of other ground data was dependent

CATEGORY NUMBER	CATEGORY	IMAGE APPEARANCE	ENVIRONMENT	BOUNDARY MEASUREMENT (RMS HEIGHT)	
				SEASAT	SIR-A
1	Seasat very smooth SIR-A very smooth	Black	Absolutely smooth and flat with no surface perturbations, e.g. fine-grained mud or silt		
1.5	Seasat very smooth SIR-A smooth				
2	Seasat smooth SIR-A smooth	Dark grey	Smooth and flat surfaces with minor irregularities, e.g. sand and sebkha areas	< 1.37 cm	< 1 cm
2.5	Seasat smooth SIR-A intermediate				
3	Seasat intermediate SIR-A intermediate	Dark to light grey	Gravelly, stony areas; ploughed fields with shallow furrows; low vegetation	1.37 - 7.83 cm	1 - 5.7 cm
3.5	Seasat intermediate SIR-A rough				
4	Seasat rough SIR-A rough	Light grey	Deeply furrowed fields; cobbles; boulders; rills; low scrub vegetation	7.83 - 30 cm	5.7 - 30 cm
4.5	Seasat rough SIR-A very rough				
5	Seasat very rough SIR-A very rough	White	Boulders; gullies; large vegetation clumps; blocky rock outcrops	> 30 cm	> 30 cm

Table 6.2 Definition of roughness in the field using extended Peake and Oliver roughness criteria. The characteristic image appearance and environment for each class are also shown.

upon the characteristics of each field site and is described in the following sections.

6.2.2. Fieldwork on Sebkhas and Associated Features.

(a) Active Inland Sebkha: Sidi el Hani.

This sebkha must be considered one of the most important natural features of the semi-arid landscape of central Tunisia (see Chapter 2). As surface relief variations are insignificant in sebkha areas the field program was designed to concentrate upon the collection of data relating to the two remaining dominant ground parameters : surface roughness and dielectric constant. Although this area undergoes seasonal and annual fluctuations in moisture content and dessication and variations in water regime, its regional importance demands that it should have a place in the detailed field program. However, results from this area must be considered in the light of its variable nature.

Ground data were sampled within a $(10m)^2$ grid placed every 200m along two transects from the sebkha shore. The first transect was located at the southern end of the sebkha and followed a line in a north-westerly direction towards the sebkha centre. Eight sites were sampled, the first located at the vegetated shoreline. The second transect was located in the northern part of the sebkha, just south of the village of Sidi el Hani. Ten sites were sampled in a south - south easterly direction from the shore. The danger posed by the wet sandy conditions beyond the last sample point of each transect prevented collection of information from the interior of the sebkha. The location of the two sebkha transects are shown in Figure 6.1.

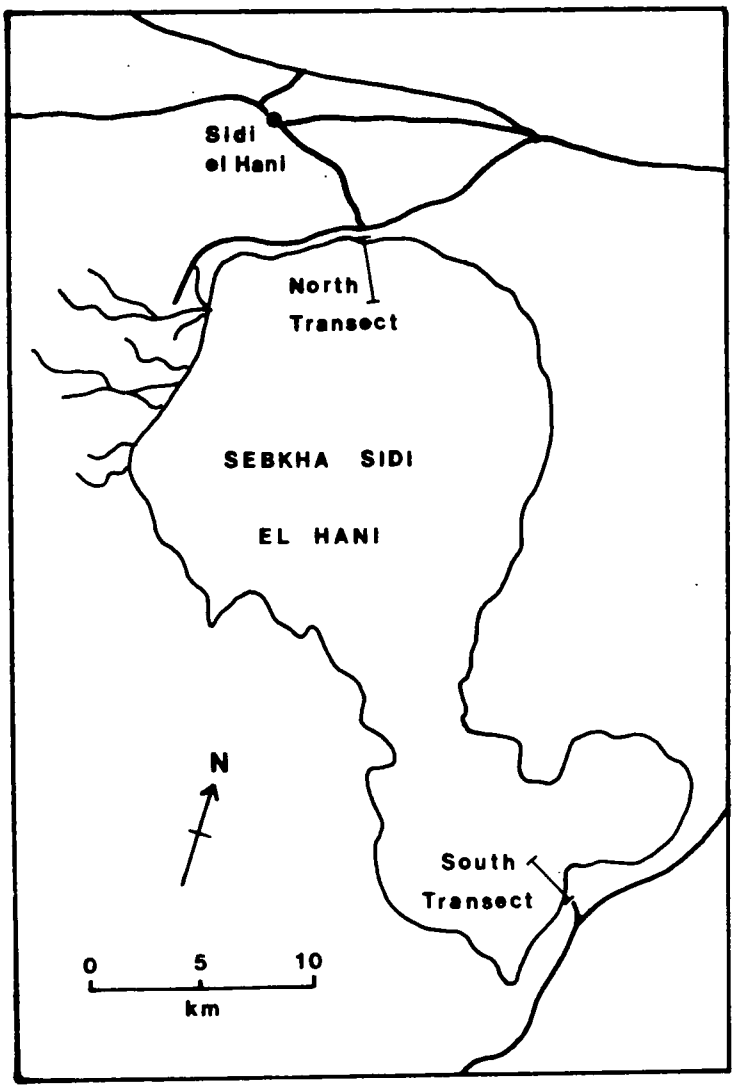

Figure 6.1 Location of the two transects on Sebkha Sidi el Hani. Extention of these transects into the interior of the sebkha was not possible due to dangerous surface conditions.

At each site, the roughness of the sebkha surface was recorded in accordance with the quantitative classification method described above. A soil sample was collected for detailed analysis in the laboratory (see Section 6.4). Field photographs record the nature of surface and subsurface conditions at each site (Plates 2.12 and 6.1).

For samples located at the sebkha shorelines the type, size and spacing of all vegetation present within the $(10m)^2$ grid was noted (Figure 6.2). Along the southern shore tall eucalyptus trees gave way to bushy halophitic species growing on small hummocks (Plate 6.2). To the north, irregular clumps of grass and halophitic plants were found on raised hummocks separated by small inflow channels. The vegetation type was quantified in accordance with the categories listed in Table 6.3.

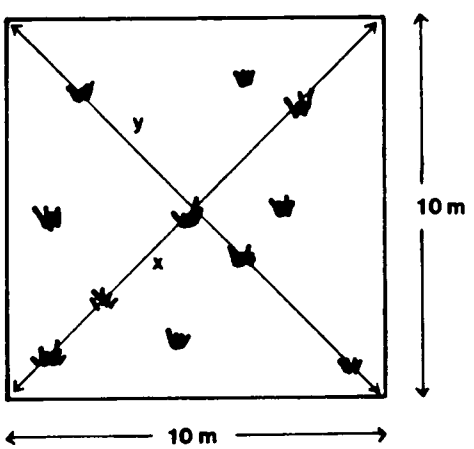

Figure 6.2 Sampling framework for recording vegetation cover.

Category	Vegetation type
1	Cereals
2	Scrub and grass
3	Arboriculture and cereals
4	Arboriculture and bushes
5	Arboriculture
6	Eucalyptus

Table 6.3 Vegetation categories defined from field investigation.

The soil samples were found to exhibit a significantly higher moisture content and increased evidence of gleying with increasing distance from the shore along each transect. In most instances surface salt crystallization increased with soil moisture, as capillary action brought sodium chloride crystals to the surface (see Chapter 2). A layer of salt crust four crystals thick was found to be present at the sixth southern sample site (1200m). The surface conditions at this site are shown in Plate 6.1. Salt polygons of up to 1.5m in diameter were in evidence at the penultimate sample site in the southern transect (1400m) and 1200m into the northern transet. These polygons reduced in size towards the end of each transect. The results of field observations from sebkha Sidi el Hani are recorded in Appendix 1.

(b) Ancient Coastal Sebkha at Monastir.

Once again, the importance of season and the time elapsed since the two radar passes had to be considered when planning the field program in the ancient coastal sebkha behind the Monastir tombolo. Due to time constraints, this area was not chosen for detailed analysis in the field but was used for comparison with the analysis of Sebkha Sidi el Hani.

Five sites were selected from field observations to be typical of the sebkha environment as a whole. Surface roughness measurements and soil samples were collected from each site. Any vegetation present at each site was categorised in accordance with the scheme outlined in Table 6.3. This ancient sebkha was characterized by a more dense vegetation cover, ranging from clumps of halophitic vegetation and grasses at the centre to small areas of olive cultivation towards the sebkha margins. Streams of water and effluent traversed the area, interspersed with pockets of surface salt crystallization (Plate 6.3). All the results from this area are recorded in Appendix 1.

(c) Lunette Dune South of Sebkha Sidi el Hani.

Five typical sample points were selected along the ridge and flanks of the lunette dune south of Sebkha Sidi el Hani. The north side of the dune was characterized by irregularly spaced bushes and low trees with an understorey of grass (Plate 2.12). Three terrace levels were found towards the top of the dune, with soil banks up to 0.5m high separating the fields on either side. The banks and bushes, together with the presence of deeply-ploughed furrows, gave rise to roughness measurements in

excess of 15cm for four out of the five sites. The southern flank of the dune was characterized by generally low-lying vegetation. Vegetation and roughness measurements recorded at each site can be found in Appendix 1.

The soil at all the sites was sandy in texture, formed by coalescence of clay-sized particles on the sebkha and blown southwards during dry periods. A representative sample of the soil was taken from one of the sites (Sample 22) for analysis in the laboratory (see Section 6.3). Unfortunately, constraints on the amount of time available in the field prevented detailed analysis of the possible associations between Seasat and SIR-A system parameters and the ground characteristics of the lunette dune (as depicted by DN). Results from this area are mainly qualitative, supported by limited quantitative field information.

6.2.3. Fieldwork in Vegetated Regions of the Sahel of Sousse

Field data were collected from 20 sites located in vegetated or agricultural areas in the Sahel of Sousse to assess the influence of vegetation upon radar return. The sites were chosen at points which could be located on map and image data and were representative of the full range of vegetation types in the eastern study area. Most were along roads used in the field (Figure 6.3). At each point the following information was noted:

(a) Surface roughness, in accordance with the scheme outlined above

(b) Surface relief and aspect

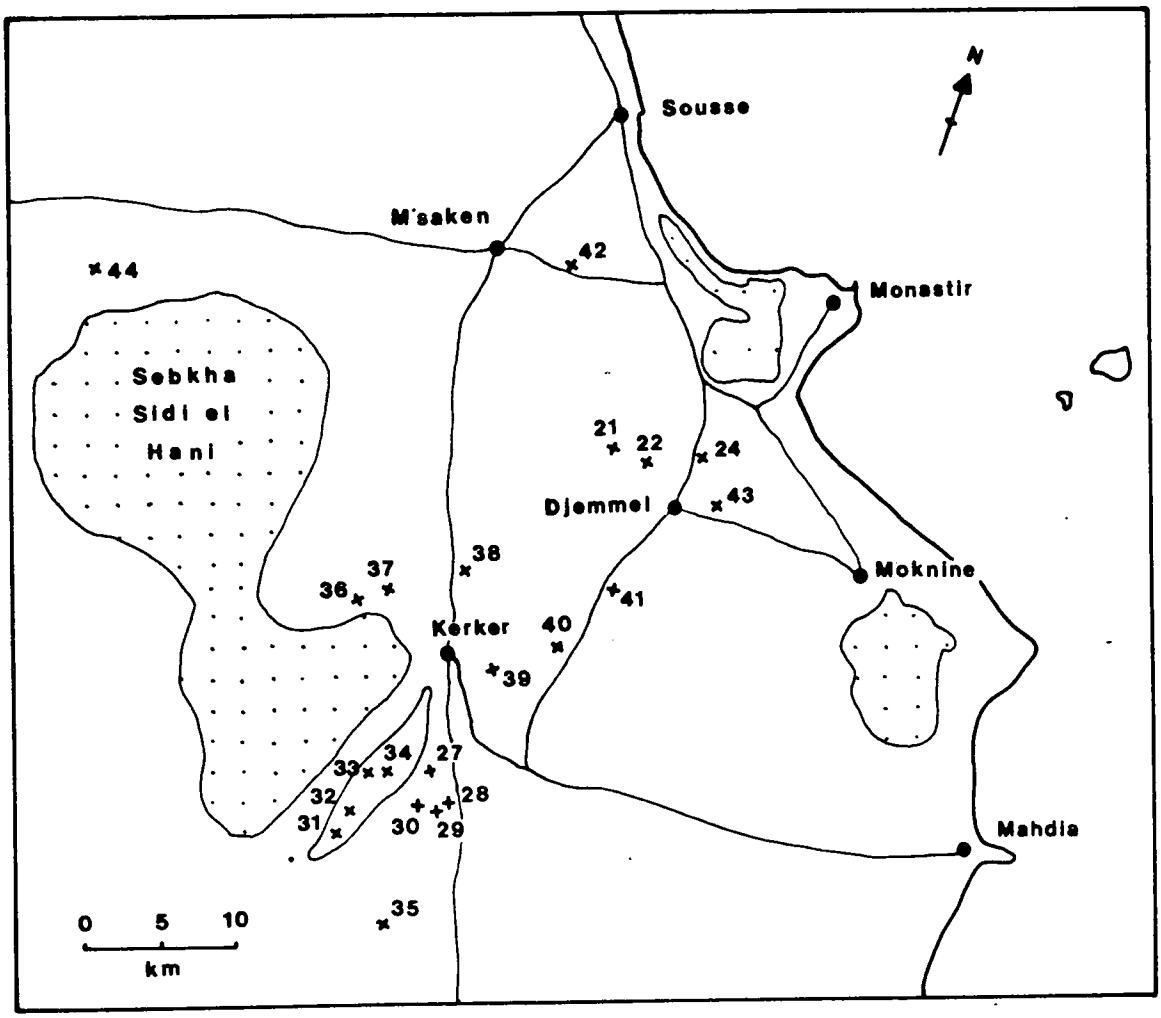

Figure 6.3 Location of vegetation samples in the eastern study area. The numbers refer to sample numbers listed in Appendix 1.

(c) Vegetation type, classified in accordance with the scheme presented in Table 6.3

(d) The mean spacing of vegetation at tree and/or low-canopy levels. Vegetation spacing was measured in two directions over the total area of the plot (or for $100m^2$ of a larger plot) using a survey tape. Results were recorded in units of metres.

(e) The mean height of vegetation at tree and/or low canopy levels in metres

(f) The diameter of vegetation canopies at the two levels in units of metres (Plate 6.4)

(g) The dominant row direction in degrees from north.

All these measurements follow an accepted form of data collection in vegetated regions discussed in Cihlar et al., (1987).

The results from all the sites sampled in the field are presented in Appendix 1. The data were used as the basis of a statistical analysis in which the influence of tree, size, spacing and canopy on radar return were assessed in terms of the depression angles of the two radar systems. The results of this analysis are discussed in Section 6.7.3.

6.2.4. Field study of Wadis and Gullies.

A number of areas in the field are suffering from fluvial erosion (see Chapter 2). Such erosion is widespread in semi-arid environments and a field program was designed to assess its impact upon radar backscatter.

A number of fluvial channels were selected for sampling in the field. The areas, together with the measurements taken in them, are discussed in turn below.

(a) Gullies South of Sebkha Sidi el Hani.

Two large gullies were located on the Seasat radar image in an area of hill country to the south of Sebkha Sidi el Hani. One of these gullies (Plate 6.5) was selected for detailed investigation in the field. Width, depth, roughness and vegetation cover were recorded at a number of sites downstream for 1.3km from the headwall (Plate 6.6). The gully orientation in degrees from north was also noted. A soil sample was taken from five points representative of the area for analysis in the laboratory. The results from these samples are recorded in Appendix 1. The data collected from this gully were used for comparison with gullies studied in the westward SIR-A extension in the Hadjel valley.

(b) Wadis and Gullies of the Hadjel Valley.

As described in Chapter 2, the Hadjel valley is an area of intensive and extensive fluvial erosion, with numerous gullies dissecting the area (Plate 2.6). Most of the gullies are tributaries of the Oued el Hadjel which bisects the plain between Djebels Nara and Henndi. Field investigation of the area was based upon maps prepared by the Tunisian Ministry of Agriculture (République Tunisienne, 1976). The results form the basis of a detailed appraisal of radar capabilities for the discrimination of erosion features (Chapter 8).

In addition to map analysis, cross sections of 36 gullies were sampled in the northern part of the Hadjel

valley from the road crossing over L'Oued el Hadjel to the reservoir at Sidi Saad. The depth and width, orientation, roughness and vegetation cover were recorded at a point approximately 100m from the mouth of each gully. Gully depth and width were measured in metres. The angle of slope of each bank was also noted, as was the presence of any terracing or slumping. The results from twelve of these gullies were selected for inclusion in the statistical analysis and are presented in Appendix 2. One gully representative of the twelve was selected for more detailed field study (Plate 6.7). The cross section of this gully was recorded at ten sites at 100m intervals from the mouth upstream. The resulting cross-sections are given in Figure 6.4.

Downstream of the point at which the road from Hadjeb el Ayoun crosses L'Oued el Hadjel the amount of erosion is significantly reduced, due to the changing soil conditions. Wadis in this area are much shallower than their counterparts to the north (Plate 6.8). They were sampled in a similar way in the field. A comparison between cross sections of typical drainage courses in the north and south of the valley is presented in Figure 6.5b and 6.5c. The cross section of L'Oued el Hadjel just north of the road crossing can be seen in Figure 6.5a (Plate 6.9). The results from this area can be found in Appendix 2.

(c) Major Wadis of the Western Study Area.

The northern part of the western study area is drained by two large wadis: Oued el Hadjeb and Oued Zeroud. Five sites were selected for field analysis which were easily located on the SIR-A image of the area by their proximity to major roads. The width and depth of

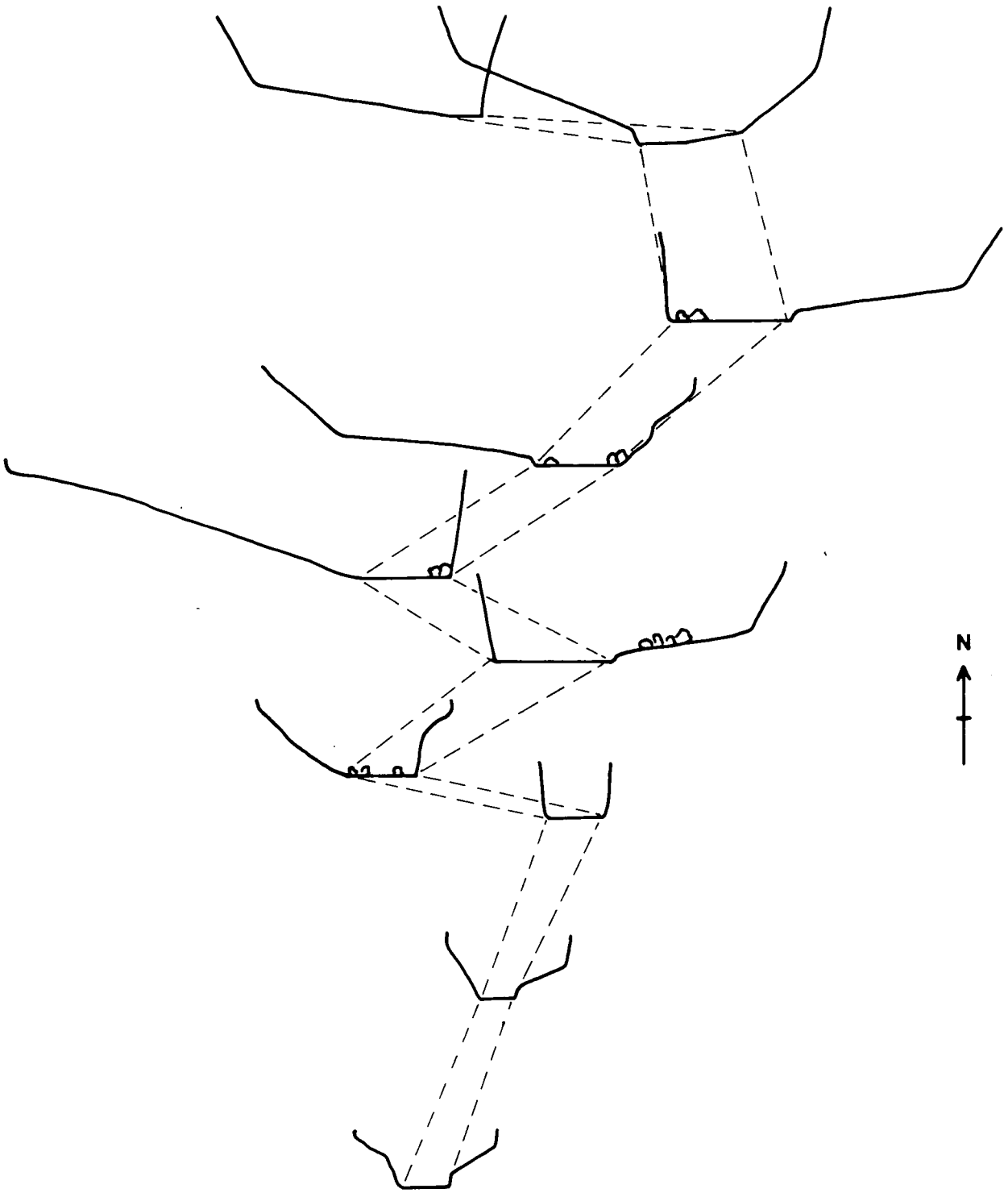

Figure 6.4 A series of cross sections of a typical gully in the northen part of the Hadjel Valley. Samples are located 100m apart in the correct orientation (shown by broken lines). The horizontal scale of each cross section is 1mm=1m. The vertical scale is 2mm=1m.

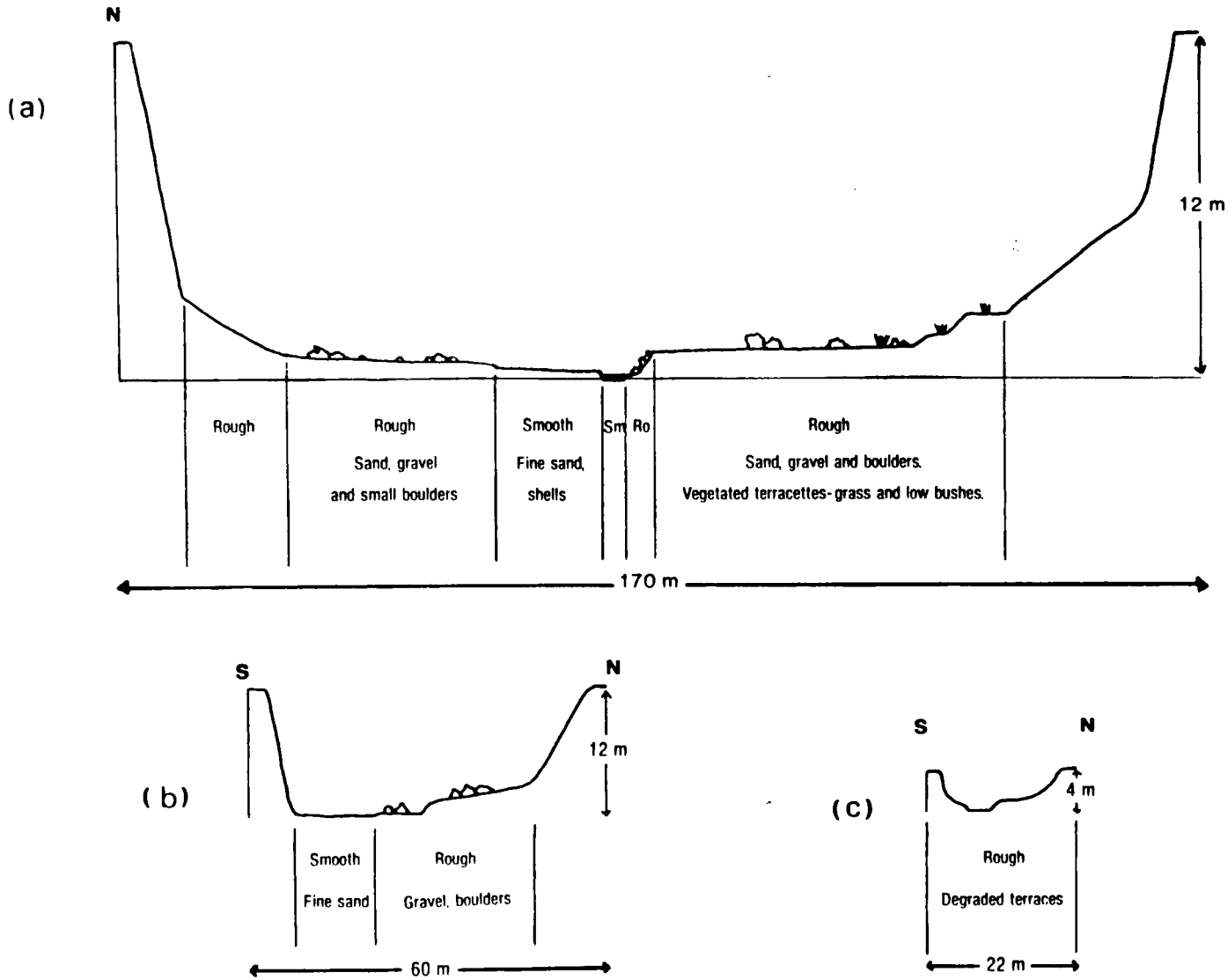

Figure 6.5 Cross sections of (a) L'Oued el Hadjel at road crossing (Plate 6.9), (b) gully in the northern part of the Hadjel Valley and (c) wadi in the southern part of the Hadjel Valley.

each wadi were recorded in metres. The slope of each bank was measured in degrees and the orientation of the wadi in degrees from north was recorded. Surface roughness and the presence of vegetation in the channel were noted at each site.

Both wadis are of considerable width, Oued Zeroud having a width of 804m at the sample points (Plate 6.10). Both are characterised by the presence of braided channels separated by pockets of vegetation that serve to increase the local roughness measurements. However, the seasonality of the vegetation found on the wadis must certainly be considered. Measurements from the five sample points are listed in Appendix 2.

6.2.5. Fieldwork in the Mountain Environments of the Western Study Area.

(a) Analysis of the Mountain Slopes Around Hadjeb el Ayoun

There are three major mountain ranges in the western study area around Hadjeb el Ayoun: Djebels Henndi, Nara and Cherahil (see Chapter 2). A field programme was devised to provide slope and roughness information at sites located on all three. At a total of 30 points the following data were recorded:

(i) Slope angle in degrees

(ii) Aspect of slope in degrees from north

(iii) Surface roughness

(iv) Vegetation type, spacing, height and canopy (if present).

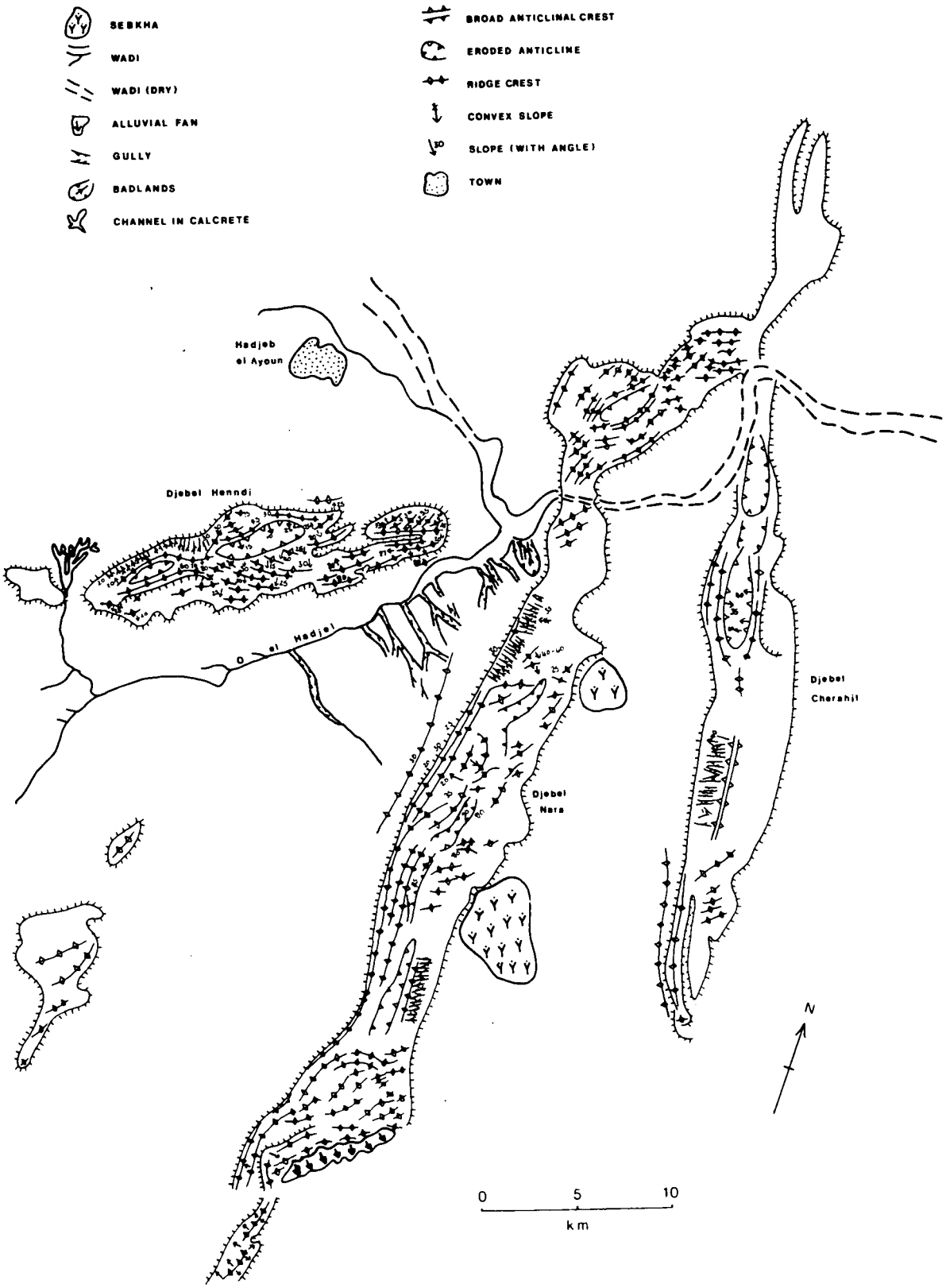

Figure 6.6 Geomorphological map of the mountains of the western study area prepared from field observations and SIR-A image analysis.

A morphological map was prepared for slopes that were included in the transects across the area (Figure 6.6). This maps are used in the evaluation of the capabilities of SIR-A for discriminating mountain slopes and will be discussed in Section 6.8. The results from each sample point can be found in Appendix 2.

(b) Data collection in Areas of Calcrete.

The presence of calcrete over considerable areas around Hadjeb el Ayoun was described in Chapter 2. Four sites were chosen for analysis in the field. Three were located on the northern flank of Djebel Henndi (Plate 2.4). The fourth was located on the calcrete banks of Djebel Mhrila (Plate 2.7). At each site the slope, aspect and surface roughness were recorded and are presented in Appendix 2. Evaluation of the capabilities and applications of radar in the discrimination of calcrete can be found in Chapter 8.

Data collected in the field at all the sites described above were organised and recorded on a site-by-site basis. Before the data could be analysed in more detail or used for statistical analysis additional results had to be processed upon return from the field. These included the generation of local incidence values from slope data and the laboratory analysis of soil samples, and will be discussed in Sections 6.3 and 6.4.

6.3. Laboratory Analysis of Soil Samples.

As described in Section 6.2, soil samples were collected at 36 sites in the field for which pedological data were required for radar analysis. The sites were mainly located in sebkha or near-sebkha areas, where

SOIL SAMPLE	LOCATION
WEST	
1	Northern Sebkha near Djebel Nara
2	Southern Sebkha near Djebel Nara
3	Oued el Hadjel road crossing
4	Oued el Hadjel channel bed
5	Oued el Hadjel north-west channel wall
EAST	
6	Djemmel Valley west
7	Djemmel ancient Sebkha
8	Djemmel ancient Sebkha
9	Djemmel ancient Sebkha
10	Bembla - Monastir road
11	Souk Saydi (North of Kerker)
12	North of Sidi el Hani
13	Sebkha Sidi el Hani South shore A
14	Sebkha Sidi el Hani South shore B
15	Sebkha Sidi el Hani South C
16	Sebkha Sidi el Hani South D
17	Sebkha Sidi el Hani South E
18	Sebkha Sidi el Hani South F
19	Sebkha Sidi el Hani South G
20	Sebkha Sidi el Hani South H
21	Southern tip of Sebkha Sidi el Hani
22	Lunette dune South of Sebkha Sidi el Hani
23	Wadi South of Sebkha Sidi el Hani
24	Gully South of Sebkha Sidi el Hani
25	Gully South of Sebkha Sidi el Hani
26	Gully South of Sebkha Sidi el Hani
27	Sebkha Sidi el Hani North A
28	Sebkha Sidi el Hani North B
29	Sebkha Sidi el Hani North C
30	Sebkha Sidi el Hani North D
31	Sebkha Sidi el Hani North E
32	Sebkha Sidi el Hani North F
33	Sebkha Sidi el Hani North G
34	Sebkha Sidi el Hani North H
35	Sebkha Sidi el Hani North I
36	Sebkha Sidi el Hani North J

Table 6.4 The location of soil samples in the field.

absence of terrain slope would allow the influence of soil conditions upon radar return to be evaluated (see Section 3.59). The location of each sample is given in Table 6.4. The time-lag between image data collection and soil analysis had to be considered, as there is a possibility that local conditions have changed. Results from laboratory analysis can only be used as indicators of the local environment at each site.

Laboratory analysis of the 36 soil samples consisted of four basic procedures:

(1) Determination of soil salinity through measurements of specific conductivity

(2) Evaluation of soil moisture content

(3) Measurement of soil organic matter content

(4) Determination of soil texture

The methods involved in each analysis are described in turn below. Unless otherwise stated, the methods outlined in the Department of Geography Soil Science laboratory handbook were used and information is taken from this publication. The results can be found in Appendix 1.

6.3.1. Determination of Specific Conductivity.

20g of each sample was placed in a 150ml beaker and mixed into a smooth paste with distilled water. The prepared paste was transferred into the constant k=1 cell of a conductivity meter (Plate 6.11). The temperature of the paste was taken and registered on the temperature dial. Care was taken to note the sample temperature and

amount of water added as both of these affect salinity readings (Hesse, 1971). The conductivity was measured in millisiemens CM (mScm-1) by balancing the deflecting needle in the centre of the display. Three measurements were made for each sample and the mean value taken. A salinity class was assigned to each sample on the basis of approximate salt concentrations (Hesse, 1971). In sebkha regions the measurments suggested only slight concentrations of salt were present at the sebkha margins, rising to strong concentration of up to 91,000 mScm-1 (Sample 20). In all other areas samples were relatively free of salt, although strong concentrations of 27,750 mScm-1 were recorded for the sample at the centre of the ancient sebkha near Djemmel and Monastir. The results for all samples can be found in Appendices 1 and 2.

6.3.2 Evaluation of Soil Moisture Content.

It was necessary to acquire an approximate indication of soil moisture content for each of the 36 samples collected in the field. There were, however, several problems associated with evaluation of moisture content. Firstly, only a coarse measurement of sample weight was possible in the field owing to the inadequacies of the spring balance used. Although the balance was calibrated in the laboratory prior to commencement of fieldwork its large scale, coupled with heavy use in the field, rendered accuracies greater than +/- 2 grammes impossible. Therefore, samples could not be calibrated to field capacity, which would allow quantitative comparison of the results.

Furthermore, the time-lag between the collection of image and field data is probably more significant here than for any other variable. Annual, and indeed seasonal,

variations in moisture content could be considerable. Table 6.5 shows rainfall figures taken from records held at the meterological office in Tunis for four weather stations within the study area. The figures for August 1978 and October 1981 are relevant for the satellite coverage of Seasat and SIR-A respectively. They reveal that August 1978 was an unusually wet month while October and November 1981 were unusually dry months. Unfortunately, meteorological records for the field season in Spring 1986 were not available, making detailed analysis of rainfall and moisture figures impossible. Nevertheless, approximate moisture levels were recorded to provide a rough indication of variations between sites, especially in sebkha areas.

Ten grammes of air dried soil from each site was put into a weighed nickel crucible and left in an oven at a constant temperature of 105°C for one to two days. When the weight of each sample had stabilized the crucibles were removed from the oven and left to cool. The samples were then reweighed. The percentage moisture in the oven-dried soil was calculated using the following equation:

$$\% \text{ moisture} = \frac{AC - OC}{OC - C} \times 100 \qquad \text{(Equation 6·1)}$$

Where:

C = Weight of crucible (g)
AC = Weight of crucible and air dried soil (g)
OC = Weight of crucible and oven dried soil (g)
O = Weight of oven dried soil (g)

The results from each site can be found in Appendices 1 and 2.

PRECIPITATION (MM)	MONASTIR	KAIROUAN	SBEITLA	SIDI BOUZID
JULY 1978	0.0	0.0	0.0	0.0
Mean July figure (1950 - 1980)	10.4	61.8	11.07	4.5
AUGUST 1978	10.1	12.1	78.3	22.9
Mean August figure (1950 - 1980)	8.1	13.3	27.9	8.3
OCTOBER 1981	28.7	36.9	NO	27.5
Mean October figure (1950 - 1980)	69.1	54.7	DATA	47.5
NOVEMBER 1981	8.0	9.5	NO	0.2
Mean November figure (1950 - 1980)	41.9	35.78	DATA	24.8

Table 6.5 Rainfall data for four sites within the field area for the two months prior to Seasat and SIR-A overpass dates. The mean monthly rainfall figures measured from 1950-1980 are shown to give some indication of whether conditions at imaging dates were wetter or drier than average.

6.3.3. Measurement of Soil Organic Matter Content.

An approximate value for soil organic matter content was obtained by measuring the percentage loss on ignition for each sample. The oven-dried soil samples used in the determination of soil moisture content were placed in a muffle furnace at a temperature of 357°C for 16 hours. The samples were allowed to cool, removed from the furnace and reweighed. The percentage loss on ignition was calculated for each sample using the equation:

$$\% \text{ loss on ignition} = \frac{OC - IC}{OC - C} \times 100 \text{ g} \qquad \text{(Equation 6·2)}$$

Where IC = weight of crucible and ignited soil (g). The results can be found in Appendices 1 and 2. An alternative temperature of 800°C for 30 minutes could have been used. However, certain minerals are combustible at this temperature and results could be inaccurate. The temperature used has significantly less effect on minerals and water crystallization within the soil and is much more accurate.

6.3.4. Determination of Soil Texture.

The texture of each soil sample was measured using the hydrometer method of particle size analysis. The method cannot be used for samples whose loss on ignition exceeds 25%, but as none of the soils came into this category the method was thought appropriate to obtain approximate measurements of sand, clay and silt content. Detailed reviews of methods of particle size analysis can be found in Akroyd (1964) and Day (1965).

A carefully weighed 50g sample from each site was put into a milk bottle to which 400ml of distilled water and 10ml of sodium hexametaphosphate were added. For a small proportion of samples 25g only was used if less than 50g was available. The prepared samples were shaken end over end for 16 hours before being removed. Each bottle was shaken vigorously and poured into a litre measuring cylinder, care being taken to wash all the mineral matter from the bottle. A Bouyoucos hydrometer was dropped into the suspension and distilled water added to make a total volume of 1 litre.

The hydrometer was temporarily removed while the suspension was shaken end over end for one minute. The cylinder was placed on the bench and the stop watch started. The hydrometer was replaced and readings were taken after 40 seconds and 4 minutes 48 seconds. A third reading was taken after two hours (see Plate 6.12). The temperature of the suspension was recorded after the second and third readings. A correction was applied to all hydrometer readings taken at a temperature above or below 19.5°C. 0.4 was added to hydrometer readings for every degree C above 19.5°C and subtracted for every degree C below this value. USDA textures were calculated from the readings using the following equations:

(Equation 6·3)

$$\%\text{sand}\ (2000\mu\text{m}-50\mu\text{m}) = 100 - \frac{\text{First corrected reading}}{\text{Amount of soil} - (0{\cdot}5 \times \text{Moisture})} \times 100$$

(Equation 6·4)

$$\%\text{clay}\ (<2\mu\text{m}) = \frac{\text{Third corrected reading}}{\text{Amount of soil} - (0{\cdot}5 \times \text{Moisture})} \times 100$$

(Equation 6·5)

$$\%\text{silt}\ (50\mu\text{m} - 2\mu\text{m}) = 100 - (\%\text{sand} + \%\text{clay})$$

For samples 32-36, where % loss on ignition exceeded 4%, a correction of 0.5 x % loss on ignition was subtracted from the sand fraction.

Measurement of soil texture for the samples taken from Sebkha Sidi el Hani (14 to 20 and 27 to 36), together with sample 9 (salt-encrusted ancient sebkha near Djemmel) and samples 22-26 (lunette dune and gullies south of Sidi el Hani), was not straightforward. All these samples suffered from flocculation due to the presence of soluble salts, resulting in the coalescence of clay particles. The salt in samples 23-26 was dispersed by adding an extra 10g of Sodium Hexametaphosphate and stirring vigorously for 20 minutes. The normal test was then applied. This treatment was not sufficient for the remaining samples with higher concentrations of soluble salts. These samples were placed in a Kerry Ultrasonic bath for 1-8 hours until dispersion occurred, and the hydrometer test could be applied. Samples 16,35 and 22 did not respond to Ultrasonic bath treatment. They were passed through a Buckner funnel to disperse the soluble salts still further before being re-tested.

Results were recorded for Samples 16 and 35 but severe flocculation was still present in Sample 22. This sample was taken from the soil pit dug in the top of the lunette dune to the south east of Sebkha Sidi el Hani. This dune was formed by wind-blown clay particles which coalesced and blew from the surface of the sebkha (see Chapter 2). The particles have a high soluble salt content in addition to their tight bonding (Plate 6.13). Dispersion of the particles proved impossible (Plate 6.14) and the test was abandoned. The results from all other sites can be found in Appendices 1 and 2. USDA textures

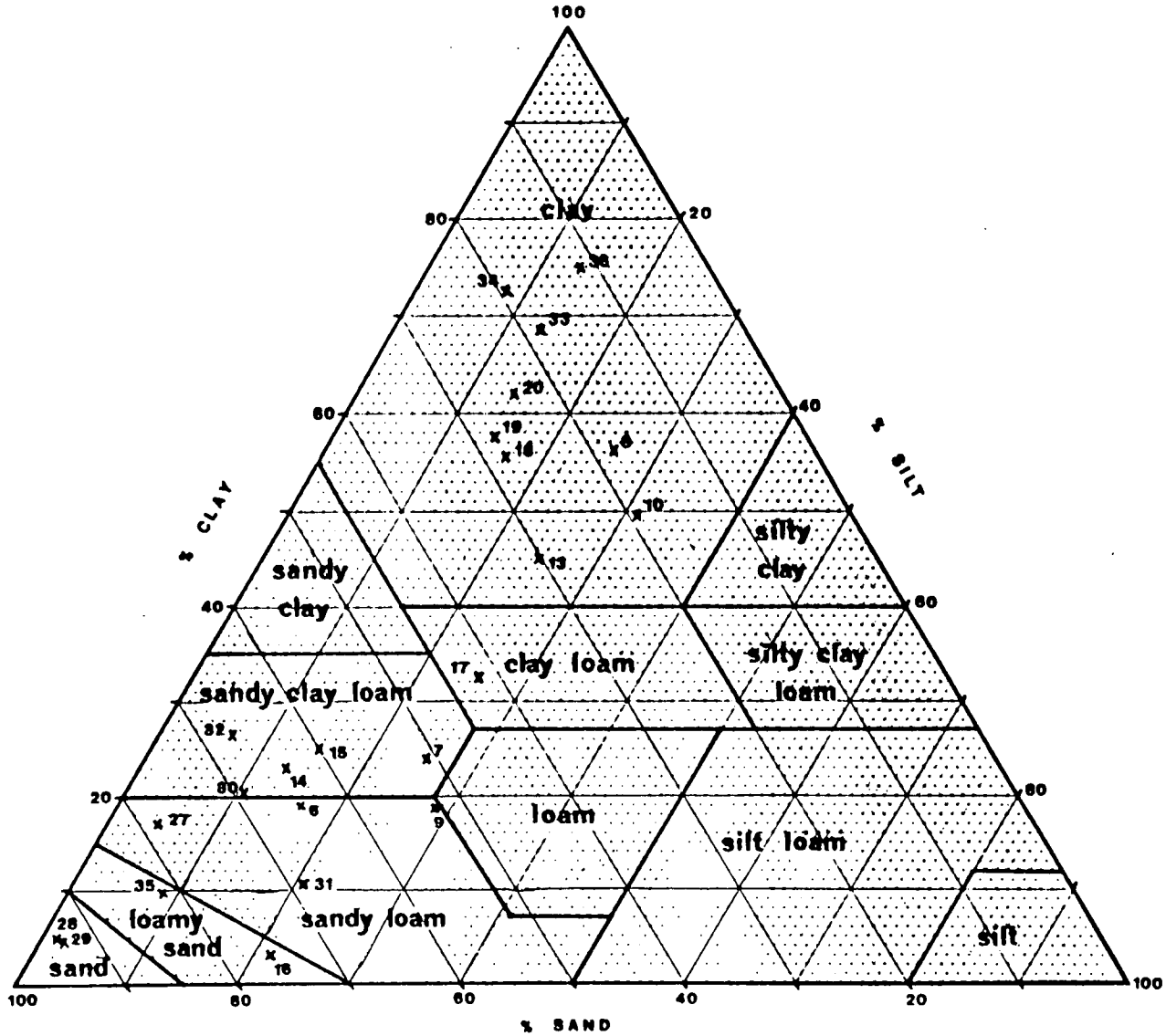

Figure 6.7 Soil textures of samples collected from the sebkhas of the eastern study area.

for Sebkha Sidi el Hani and the ancient sebkha at Monastir are shown in Figure 6.7.

6.4 Determination of Local Radar Incidence Angle and Feature Orientation.

The main problem with statistical analysis of information recorded in the field is associated with the aspect notation and the orientation of linear features. Both were measured in degrees from north and, as such, cannot have a linear relationship with any other variable as 0° and 360° are equal. Thus linear regression and correlation procedures cannot be applied to these variables (see Figure 6.8).

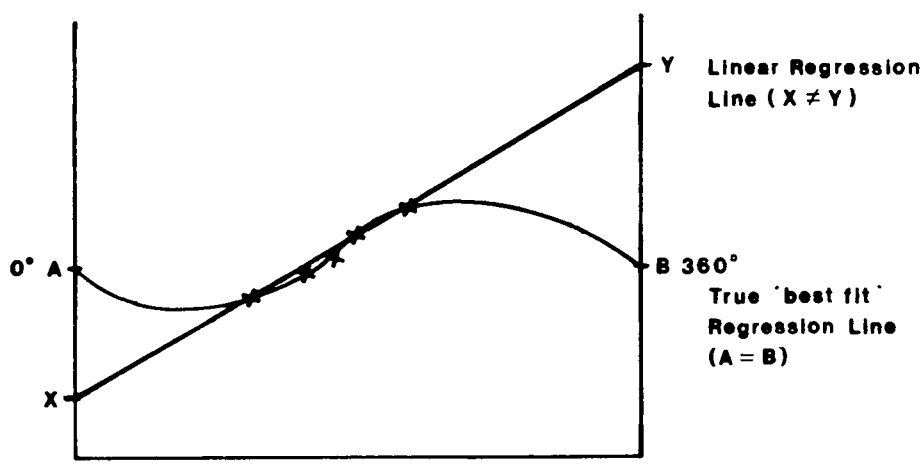

Figure 6.8 Diagram to illustrate the unsuitability of linear rgression for analysis of data recorded through 360° from north.

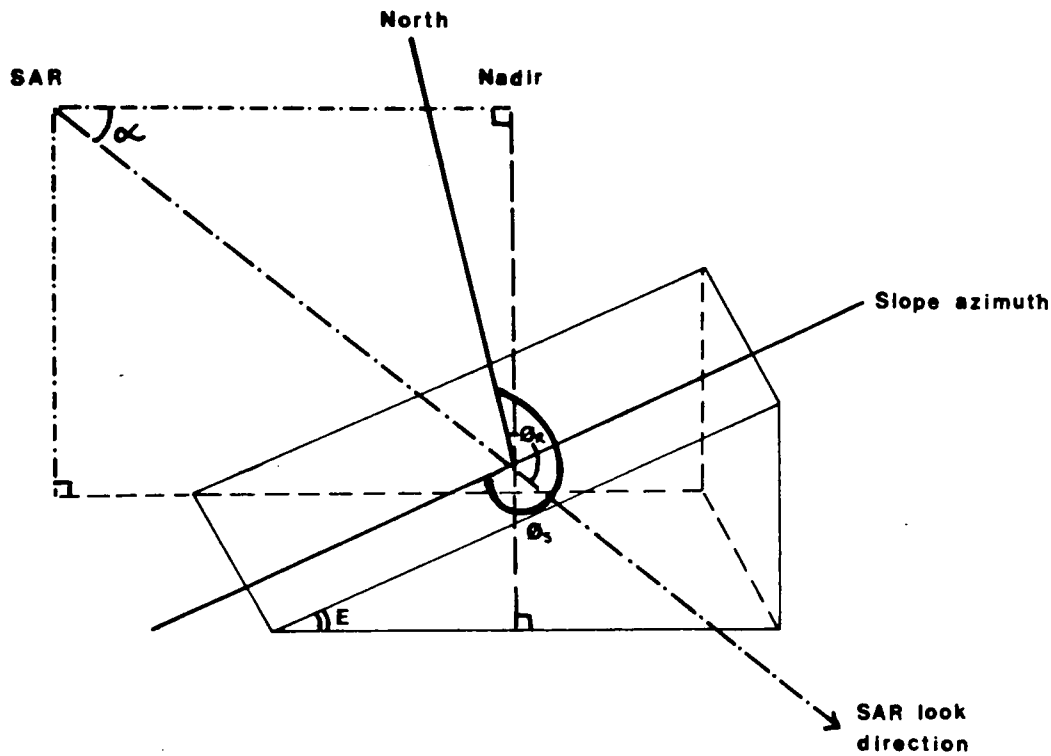

Figure 6.9 Diagram to show the parameters involved in the determination of local incidence angle, where: ϕ_s=aspect; E=gradient; x=radar depression angle and ϕR=radar look direction.

For statistical procedures on slope and aspect information to be meaningful in terms of radar incidence angle and look direction, a new parameter had to be defined to encompass all these elements. The new parameter is a measure of the local incidence angle at each position on a slope and includes the following elements:

(a) Aspect of slope (ϕs) measured in degrees from North

(b) Gradient of slope (E) measured in degrees

(c) Radar depression angle (α) measured in degrees

(d) Radar look direction (ϕR) measured in degrees from north.

All four are illustrated in Figure 6.9. The depression angle for Seasat is 70° and that for SIR-A is 43° (see Figure 3.8). The look directions for Seasat and SIR-A are 86° and 335° respectively (Figure 6.10).

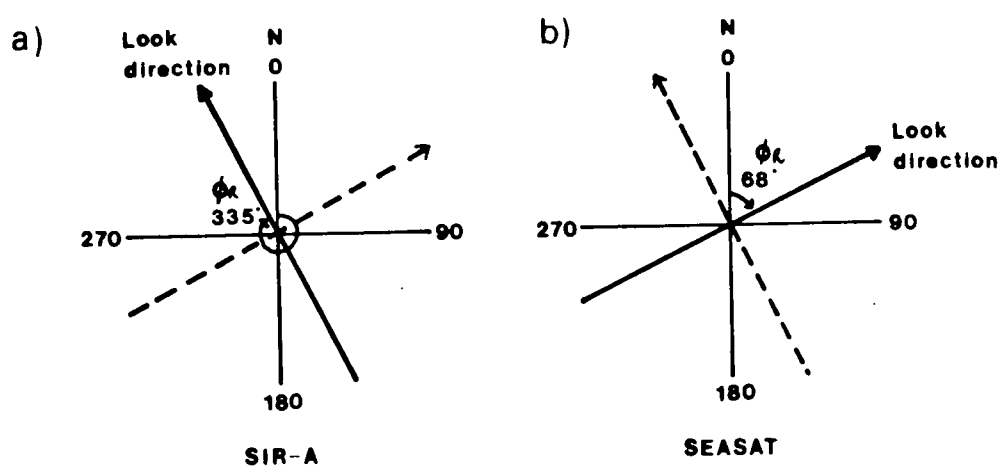

Figure 6.10 Diagram illustrating the look directions used by (a) SIR-A and (b) Seasat.

Geometrical derivation of local incidence angle is made possible owing to the coincident position of the radar signal source and sensor within the radar antenna (Foody, 1986). The solar radiation incidence model, developed by Robinson (1966) and used by Holben and Justice (1980) and Smith et al., (1980) in their analyses of slope effects on Landsat MSS classification, was adapted for the purposes of this study. The following equation was derived:

(Equation 6·6)

$$\theta_A = \cos^{-1} ((\cos E \times \cos \alpha) + (\sin E \times \sin \alpha \times \cos As))$$

Where:

$$As = (\phi R - \phi s) = \text{Apparent Aspect} \qquad \text{(Equation 6·7)}$$

This model was used by Foody (1986) in his assessment of the topographic effects on airborne radar image tone and described by Ford (1980) in the context of Seasat data analysis. The validity of the equation was tested for SIR-A in the case of zero gradient (ie a flat plain). Apparent aspect of slope (As) is also equivalent to zero in this case.

(Equation 6·8)

$$\theta_A = \cos^{-1} ((\cos \theta \times \cos 43) + (\sin \theta \times \sin 43 \times \cos \theta))$$

$$= \cos^{-1} 0{\cdot}73$$

$$= 43°$$

Thus, apparent local incidence (θ_A) is equal to radar incidence angle for a flat plain. Local incidence angle for slopes of opposing aspect angle is illustrated in Figure 6.11.

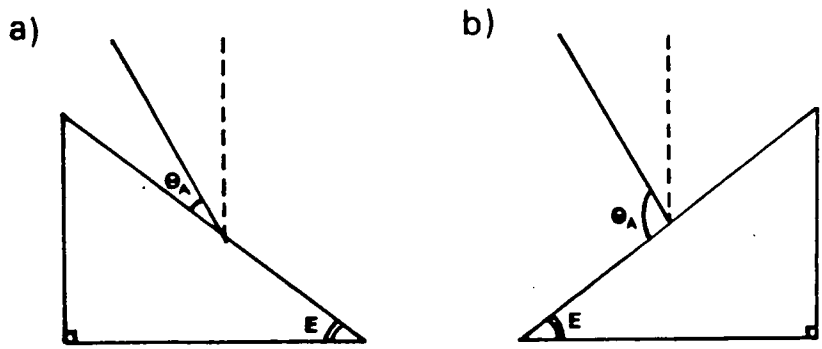

Figure 6.11 Local radar incidence angle for slopes of opposing aspect.

Apparent incidence angles were calculated for each sample site and each radar image. Results were included as an additional variable in the final computer analysis (see Section 6.6). Statistical assessment of the effects of slope on radar backscatter could then be undertaken.

Calculations of the apparent orientation of linear features also had to be made. These linear features included wadis, gullies and crop rows, whose orientation from north was noted in the field. In each case the smallest angle between the radar signal and the feature was calculated and included in the data set. The geometrical relationship between radar look direction, feature direction and apparent feature orientation is shown in Figure 6.12. Figure 6.12a compares the apparent orientation of crop rows (mainly olive and apricot plantations) on the coastal plain calculated for Seasat and SIR-A. Figure 6.12b illustrates the calculation of apparent wadi direction in the western study area around Hadjeb el Ayoun. The results of the calculations were used in the final statistical analysis of field and image data and are given in Appendices 1 and 2.

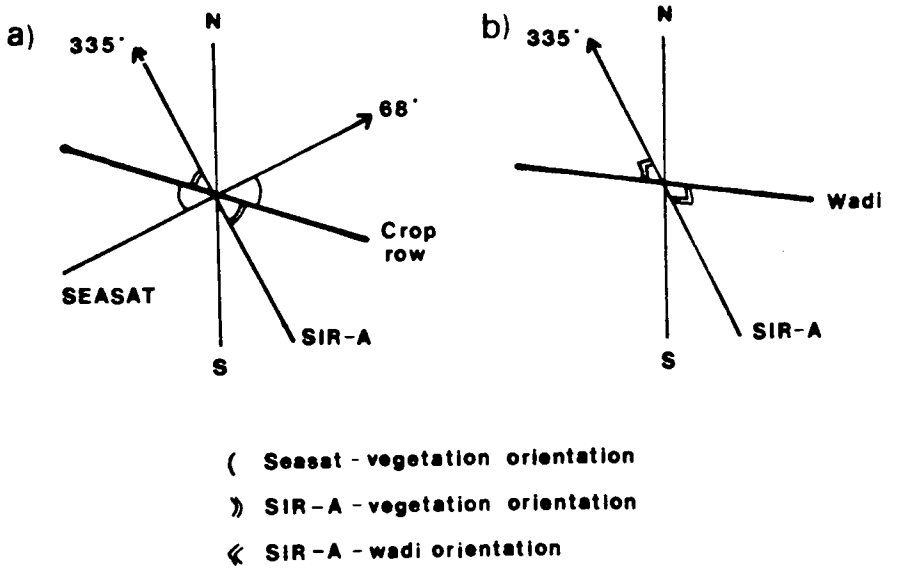

Figure 6.12 Diagram to show the calculation of the apparent orientation of linear features with respect to radar look direction. (a) compares the apparent orientation of crop rows for Seasat and SIR-A, while (b) illustrates the calculation of apparent SIR-A/Wadi orientation.

6.5. Image Data Collection.

As discussed in previous sections, ground data were collected from sites that were located easily in the field and on the images, such as field and road intersections or large gullies. Sites that could not be located exactly, such as on mountain slopes or within large olive plantations, were selected only if they were representative of an area greater than the 40m resolution cell of the SIR-A image. Once ground sites had been located on the map and image data, corresponding image DN values were recorded for each sample. The organisation and methods used on the combined image and ground data are outlined in the following section. The results are discussed in Sections 6.7 to 6.9.

6.6. Organisation of Data for Statistical Analysis.

All data collected from the field, maps and images, including local incidence values and laboratory results, were arranged in tabular form, variable by case, for the eastern and western scenes. The tables were entered into the computer in a format compatible with the operation of the SPSS-X statistics package (see Appendices 1 and 2). The Eastern area had a total of 44 cases, with 25 variables by case. The western area had 60 cases for each of the 34 variables. The variables used for each area are listed in Table 6.6. Class values were assigned to all descriptive variables as described in Section 6.2. The values assigned to the geological units/categories, slope categories and soil categories are shown in Tables 6.7 to 6.9. Missing values were entered as -1 in the SPSS-X file and omitted from the analysis.

The following statistical operations were carried out on the two data sets using the SPSS-X statistical package:

(1) Generation of frequency tables and histograms or bar charts for each variable to determine the nature and spread of the data

(2) Calculation of Pearson Product Moment Correlation Coefficients to determine the strength of the relationships between variables

(3) Graphical representation of bivariate regression plots and stepwise multivariate regression equations to assess the effects of ground variables upon each image variable.

GROUND VARIABLES

EASTERN STUDY AREA (25 variables, 44 cases)	WESTERN STUDY AREA (34 variables, 60 cases)
Seasat DN	SIR-A DN
SIR-A DN	TM band 1 DN
Slope angle (degrees)	TM band 2 DN
Aspect angle (degrees)	TM band 3 DN
Seasat local incidence (degrees)	TM band 4 DN
SIR-A local incidence (degrees)	TM band 5 DN
Roughness (rms height cm)	TM band 6 DN
Roughness category	TM band 7 DN
Conductivity ($mScm^{-1}$)	Slope angle (degrees)
% sand	Aspect angle (degrees)
% silt	SIR-A local incidence (degrees)
% clay	Slope form
Soil texture category	Geological category
% oven-dry moisture	Roughness (rms height cm)
% organic matter	Roughness category
Vegetation type category	% sand
Top layer spacing (m)	% silt
Top layer height (m)	% clay
Top layer canopy width (m)	Soil texture category
Low layer spacing (m)	% oven-dry moisture
Low layer height (m)	% organic matter
Low layer canopy width (m)	Vegetation type category
Vegetation row orientation (degrees)	Vegetation spacing (m)
Seasat - row orientation (degrees)	Vegetation height (m)
SIR-A - row orientation (degrees)	Vegetation canopy width (m)
	Vegetation row orientation (degrees)
	SIR-A - row orientation (degrees)
	Wadi depth (m)
	Wadi width (m)
	Wadi N slope (degrees)
	Wadi S slope (degrees)
	Wadi orientation (degrees)
	SIR-A - wadi orientation (degrees)

Table 6.6 Variables used in the statistical analysis of the eastern and western study areas.

Category	Lithology
1	Modern Alluvium
2	Alluvial deposits (sand and clay)
3	Colluvial deposits
4	Calcrete
5	Limestone and Dolomite
6	Marl, Limestone and Sandstone
7	Calcareous sandstone

Table 6.7 Geological categories used in statistical analysis.

Category	Soil Type
1	Clay
2	Clay loam
3	Sandy clay loam
4	Sandy loam
5	Loamy sand
6	Sand

Table 6.8 Soil categories used in statistical analysis.

Category	Slope form
1	Concave
2	Convex

Table 6.9 Slope form categories used in statistical analysis.

The analyses were not only performed on the complete eastern and western data set, but also on sub-areas with selected ground variables. Full, and sub-areal, analyses are discussed for the eastern and western subscenes in Sections 6.7 and 6.8 below. Additional field material not used in the statistical analysis, together with knowledge of radar theory (Chapter 3), are used to support the statistical results in each section. In all cases, the results must be seen as 'indicators' of relationships between ground and radar parameters rather than direct quantitative associations, owing to the time-lag and calibration difficulties that have been discussed previously.

6.7. Analysis of Eastern Data Set.

6.7.1. Analysis of Full Eastern Data Set

Statistical analysis of the eastern field and image data was accomplished through the SPSS-X statistical package as described in Section 6.6. Before these analyses were applied to the data certain variables were transformed to reduce skewness to acceptable limits for parametrical testing of between +1 and -1. For analyses of the full eastern data set the following variables were transformed:

Transformed Roughness = Log10 (Roughness) = TROUGH
Transformed Organic Matter = $\sqrt{\text{organic matter}}$ = TORGMAT
Transformed Top Spacing = Log10 (Topspacing) = TTOPSPAC
Transformed Top height = Log10 (Top height) = TTOPHT
Transformed Low spacing = Log10 (Low spacing) = TLOWSPAC
Transformed Low height = Log10 (Low height) = TLOWHT
Transformed Local Seasat Incidence = (Local Seasat Incidence)^2 = TSSINC

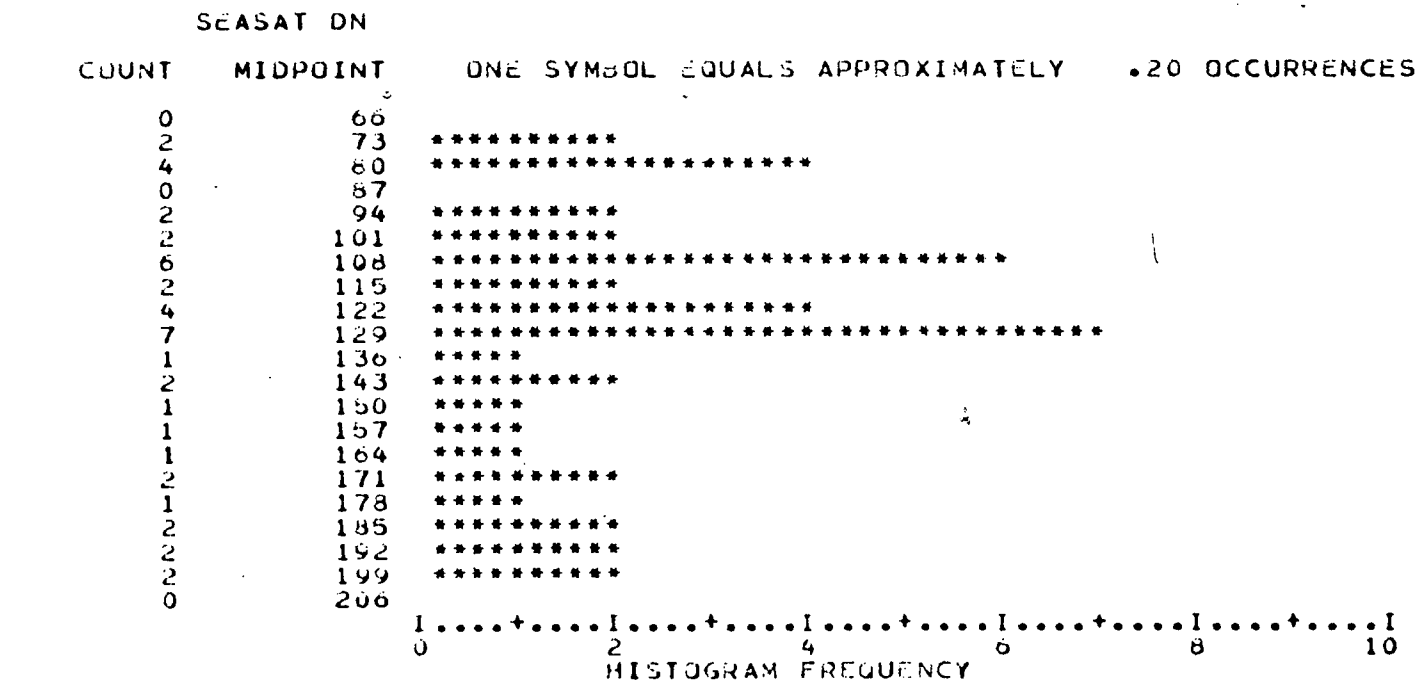

MEAN	129.045	MEDIAN	125.000	MODE	83.000
STD DEV	35.773	VARIANCE	1279.719	KURTOSIS	-.671
SKEWNESS	.455	RANGE	128.000	MINIMUM	72.000
MAXIMUM	200.000				
VALID CASES	44	MISSING CASES	0		

Figure 6.13 Histogram and descriptive statistics for Seasat DN in the full eastern analysis.

SIR-A DN

COUNT	MIDPOINT	ONE SYMBOL EQUALS APPROXIMATELY .20 OCCURRENCES
2	29	**********
1	36	*****
3	43	***************
1	50	*****
8	57	**
5	64	*************************
3	71	***************
1	78	*****
0	85	
1	92	*****
1	99	*****
2	106	**********
1	113	*****
2	120	**********
2	127	**********
3	134	***************
0	141	
2	148	**********
2	155	**********
1	162	*****
3	169	***************

I....+....I....+....I....+....I....+....I....+....I....+....I
0 2 4 6 8 10
HISTOGRAM FREQUENCY

MEAN	91.295	MEDIAN	71.000	MODE	46.000
STD DEV	43.120	VARIANCE	1859.329	KURTOSIS	-1.193
SKEWNESS	.439	RANGE	142.000	MINIMUM	28.000
MAXIMUM	170.000				
VALID CASES	44	MISSING CASES	0		

Figure 6.14 Histogram and descriptive statistics for SIR-A DN in the full eastern analysis.

The transformed variables were used in place of the original variables in the analysis. The remaining variables were untransformed.

The descriptive statistics for the two 'dependent variables', Seasat DN and SIR-A DN, are presented in Figures 6.13 and 6.14. The shape of the two distributions is similar but each has a different spread within the 0-255 DN range. SIR-A DN has a range of 142, from a minimum value of 28 to a maximum value of 170. Seasat DN varies from 72 to 200; a range of 128. To some extent these figures belie the full range of values contained within the two radar images as they do not include values from settlements and other cultural features, which have a higher DN than the surrounding areas. The separability of these features is examined in Chapter 7.

Pearson Product Moment Correlation Coefficients were calculated for the two image variables with each of the ground variables and for selected pairs of ground variables. The results allow the degree of association between variables to be assessed, thereby identifying possible relationships between those variables (Table 6.10). It is not possible to say that any variable 'causes' variation in another variable as indirect relationships between a number of variables may influence the value of the coefficient. This situation is known as 'collinearity' (Ehrenberg, 1982).

The regression line or 'best fit' line was calculated for each of the variable pairs as a summary expression of the relationship between them. Image DN was taken to be the dependent variable in image/ground associations while identification of the dependent variable in associations between two ground variables was a matter of general

GROUND VARIABLE	SIR-A DN R (significance)	SIR-A DN R^2	SEASAT DN R (significance)	SEASAT DN R^2
Slope	0.809 (0.000)	0.654	0.737 (0.000)	0.543
Trans roughness	0.763 (0.000)	0.582	0.692 (0.000)	0.479
Roughness category	0.749 (0.000)	0.561	0.676 (0.000)	0.458
Conductivity	-0.673 (0.000)	0.453	-0.466 (0.004)	0.217
% Sand	0.534 (0.001)	0.285	0.507 (0.002)	0.258
% Silt	-0.421 (0.011)	0.177	-0.583 (0.000)	0.339
% Clay	-0.476 (0.004)	0.227	-0.369 (0.004)	0.136
Texture category	0.494 (0.003)	0.244	0.510 (0.002)	0.260
% Oven dry weight	-0.364 (0.022)	0.132	-0.198 (0.148)	0.039
Trans % organic matter	-0.686 (0.000)	0.471	-0.509 (0.002)	0.259
Trans top spacing	0.717 (0.000)	0.514	0.449 (0.001)	0.201
Trans top height	0.688 (0.000)	0.473	0.426 (0.002)	0.182
Top canopy	0.759 (0.000)	0.576	0.492 (0.000)	0.242
Trans low spacing	0.088 (0.288)	0.007	-0.003 (0.492)	0.000
Trans low height	0.087 (0.289)	0.007	-0.035 (0.411)	0.001
Low canopy	-0.119 (0.230)	0.014	-0.211 (0.095)	0.044
Vegetation type	0.708 (0.000)	0.502	0.433 (0.002)	0.187
SIR-A incidence	-0.398 (0.005)	0.159	———	——
Trans Seasat incidence	———	——	0.052 (0.372)	0.002
SIR-A veg. orientation	-0.388 (0.119)	0.151	———	——
Seasat veg. orientation	———	——	-0.497 (0.060)	0.247

Table 6.10 R and R^2 statistics for ground and image variable pairs in the eastern study area.

knowledge. The regression statistic (R^2) was taken as a measure of the goodness of fit. Correlation (R) and regression (R^2) statistics for the eastern study area can be found in Table 6.10. For SIR-A DN, correlation and regression statistics are fairly high for a number of ground variables (Table 6.10). Thirteen out of nineteen of the correlations are significant at the 95% confidence level, with the highest correlations recorded between SIR-A DN and Slope (.809), Trough (.763) and Topcan (.759). These, and other high correlations, are reinforced by high regression values that suggest the presence of direct relationships between the variables in question.

The close relationship between SIR-A DN and transformed roughness is explained by the depression angle and wavelength of the SIR-A system which makes it ideal for discriminating changes in surface roughness (see Chapter 3). The depression angle of the Seasat system makes it less responsive to changes in roughness and this is reflected in the reduced R and R^2 statistics (Table 6.10). Nevertheless, roughness seems to be an important ground variable influencing Seasat as well as SIR-A backscatter from the region (as represented by image DN).

High correlations also exist between Seasat DN and the majority of the ground variables. As for SIR-A DN, thirteen correlations are significant at the 95% confidence level. The highest correlations are recorded between Seasat DN and Slope (.737), Trough (.692) and the four soil texture variables (Clay, Silt, Sand, PSA). High regression values reinforce the relationship between Seasat and Slope and Roughness, but fail to imply a strong linear relationship with soil-related variables.

It is likely that the significant time-lag and the seasonal differences that exist between the collection of field and image data will have had a considerable effect upon the strength of the relationships between variables. For soil characteristics this effect will have been greatest, as changes in soil moisture, salinity, organic matter and texture can take place over relatively small time scales. Although changes in surface roughness may have occurred during the eight years between the first satellite pass and the last field season, they are unlikely to have been as great as changes in soil condition. Given the landscape, culture and agricultural practices of central Tunisia, one can envisage little, if any, significant alteration in vegetation variables, especially in areas of arboriculture. Thus, time and seasonality is used as an explanation of relationships for selected variables only.

Time-lag and seasonality is one possible explanation for the relatively low R^2 values that exist between Seasat DN and soil characteristics (see Table 6.10), despite their high correlations. This suggests that, although a general relationship between Seasat DN and soil conditions still exists (possibly through multiple or secondary interactions between variable pairs), localized changes over time have eroded any bivariate linear relationships that might have been evident in August 1978. Indeed, complex interactions between groups of variables often result in high correlations between variable pairs within that group. For example, particle size distribution within a soil sample will influence the amount of moisture held within that soil which may in turn influence the roughness of that soil, its conductivity, organic matter content, etc. Some of the correlations for pairs of ground variables are listed in Table 6.11.

VARIABLES	R (significance)		R^2
T. ROUGH/CONDUCT	-0.720	(0.000)	0.519
T. ROUGH/SAND	0.478	(0.004)	0.228
T. ROUGH/SILT	-0.281	(0.070)	0.079
T. ROUGH/CLAY	-0.436	(0.009)	0.190
T. ROUGH/TEXTURE	0.411	(0.013)	0.169
T. ROUGH/OV. DRY WT.	-0.472	(0.004)	0.223
T. ROUGH/T. ORGMAT.	-0.657	(0.000)	0.432
T. ROUGH/SLOPE	0.584	(0.000)	0.341
ROUGHCAT/CONDUCT	-0.729	(0.000)	0.532
VEGTYP/T. TOPSPAC	0.912	(0.000)	0.832
VEGTYP/T. TOPHT	0.918	(0.000)	0.844
VEGTYP/TOPCAN	0.906	(0.000)	0.821
VEGTYP/T. LOWSPAC	0.020	(0.449)	0.000
VEGTYP/T. LOWHT	0.003	(0.491)	0.000
VEGTYP/LOWCAN	-0.011	(0.472)	0.000
VEGTYP/SIR. VEG	-0.090	(0.395)	0.008
VEGTYP/SS. VEG	-0.091	(0.395)	0.008
SLOPE/T. TOPSPAC	0.546	(0.000)	0.298
SLOPE/T. TOPHT	0.608	(0.000)	0.370
SLOPE/TOPCAN	0.617	(0.000)	0.381
SLOPE/T. LOWSPAC	0.004	(0.488)	0.000
SLOPE/T. LOWHT	-0.082	(0.305)	0.006
SLOPE/LOWCAN	-0.117	(0.242)	0.013
SLOPE/VEGTYP	0.589	(0.000)	0.347
SLOPE/TEXTURE	0.538	(0.001)	0.289
SLOPE/SIRINC	-0.557	(0.000)	0.311
SLOPE/SSINC	0.080	(0.309)	0.006
TEXTURE/SAND	0.966	(0.000)	0.934
TEXTURE/SILT	-0.573	(0.001)	0.329
TEXTURE/CLAY	-0.938	(0.000)	0.880
TEXTURE/T. ORGMAT	-0.498	(0.003)	0.248
TEXTURE/OV. DRY WT.	-0.702	(0.000)	0.492
SAND/SILT	-0.626	(0.000)	0.387
SAND/CLAY	-0.949	(0.000)	0.900
SAND/T. ORGMAT	-0.457	(0.006)	0.208
SAND/OV. DRY WT.	-0.703	(0.000)	0.494
SILT/CLAY	0.357	(0.029)	0.127
SILT/T. ORGMAT	0.153	(0.213)	0.023
SILT/OV. DRY WT.	-0.022	(0.453)	0.000
CLAY/T. ORGMAT	0.775	(0.000)	0.600
CLAY/OV. DRY WT.	0.557	(0.001)	0.310
CONDUCT/OV. DRY WT.	0.527	(0.001)	0.277
CONDUCT/ORGMAT	0.840	(0.000)	0.705
OV. DRY WT./ORGMAT	0.550	(0.001)	0.302
T. TOPSPAC/T. TOPHT	0.848	(0.000)	0.719
T. TOPSPAC/TOPCAN	0.929	(0.000)	0.863
T. TOPHT/TOPCAN	0.909	(0.000)	0.826
T. LOWSPAC/T. LOWHT	0.702	(0.000)	0.492
T. LOWSPAC/LOWCAN	1.000	(0.000)	1.000
T. LOWHT/LOWCAN	0.350	(0.013)	0.122

Table 6.11 R and R^2 statistics for selected pairs of ground variables in the eastern study area.

Particularly high correlations are recorded between Trough and Conductivity (-.720), Trough and Torgmat (-.657) and Oven-dried weight, with Sand (-.703), Clay (.775) and Texture category (-.702), all significant at the 99% confidence level. The time-lag can also be used as an explanation for some of the low associations between SIR-A DN and soil variables, although regression values are higher than Seasat-DN for Conductivity (.453) and Torgmat (.471) (see Table 6.11). Seasonality is less of a problem here as, although SIR-A and ground data were collected at different times of the year, the dry season was avoided in each case.

Higher correlations exist for SIR-A DN with vegetation characteristics than for Seasat DN, high R^2 values suggesting close relationships between the variables. Correlations between SIR-A DN and Ttopspac, Ttopht and Topcan are 0.717, 0.688 and 0.759 respectively, all significant at 99% confidence levels. The shallow depression angle of SIR-A ensures that there will be considerable backscattering from canopy and trunk components in areas of arboriculture, with little or no backscatter from the ground (depending on tree spacing) (see Figure 3.14). These areas are therefore likely to be represented by a more distinct backscatter response on the images and a stronger relationship between image DN and Tree variables. The steeper depression angle of Seasat allows greater between-tree penetration in arboriculture plots and a greater contribution of surface conditions to overall DN. Linear relationships between Seasat DN and vegetation variables are less likely to occur.

There are high correlations for Seasat and SIR-DN with Slope. Few of the sites sampled in the eastern study area had slope angles in excess of a few degrees so the

effect of surface relief on backscatter is minimal, except in the small areas of hill country, which were not studied in detail in the field. Thus, the close association between image DN and slope is mainly a product of specular reflection where low slope angles produce low backscatter (assuming zero roughness).

Stepwise multiple regression analysis of the eastern data set revealed little information about the contribution of ground variables to Seasat or SIR-A. In the case of Seasat, none of the variables proved to be significant at 95% confidence levels and consequently the analysis did not proceed. It can be concluded from this that none of the variables recorded during the field season has a significant individual contribution to Seasat DN. Similarly, for SIR-A DN only Vegetation orientation was significant at the 95% confidence level and could be included in the analysis, giving a regression equation of:

$$\text{SIR-A DN} = -0.586\ \text{SIRVEG} + 118.76 \qquad \text{Equation 6.9}$$

and an R^2 value of 0.151. Although the importance of this single variable must not be disputed, the relevance of other ground variables, highlighted through correlation and bivariate regression, should not be underestimated.

6.7.2. Analysis of Eastern Sebkhas (Cases 2-19, Appendix 1)

The nature of the environment in and around Sebkha Sidi el Hani in the eastern study area dictated that there should be a selective inclusion of ground variables in the final statistical analysis. The sebkha is located within a lowland depression, and as such has zero or near-zero slope angles. Hence the slope angle and local incidence

variables were omitted from the analysis. All vegetation variables were omitted also, apart from vegetation type, as vegetation was only recorded at sebkha margins and shoreline regions. The ground variables included in the analysis, together with any transformations applied to them, are listed below:

Transformed Roughness = Log10 (Log10 Roughness) = TROUGH
Roughness Category = RCAT
Conductivity = CONDUCT
Percent Sand = SAND
Percent Silt = SILT
Percent Clay = CLAY
Texture Category = PSACAT
Percent Organic Matter = ORGMAT
Percent Oven-Dried Moisture = OVDRYWT
Vegetation Type = VEGTYP

The Pearson Product Moment Correlation Coefficients and bivariate regression values for Seasat and SIR-A DN and the ground variables listed above are presented in Table 6.12. Correlation coefficients for northern and southern sebkha transects can be found in Table 6.13. For Seasat and SIR-A the highest R and R^2 values occur between image DN and Transformed roughness or Roughness category. For the case of SIR-A each correlation is significant at 99% confidence levels, while for Seasat the confidence level is greater than 90% in each case. A similar situation exists for the two individual sebkha transects, with correlations between SIR-A DN and transformed roughness / roughness category being in excess of the figures for the sebkha as a whole.

GROUND VARIABLE	SIR-A DN R (significance)	R^2	SEASAT DN R (significance)	R^2
Trans roughness	0.810 (0.000)	0.657	0.565 (0.007)	0.319
Roughness category	0.802 (0.000)	0.643	0.630 (0.002)	0.398
Conductivity	-0.667 (0.001)	0.445	-0.223 (0.186)	0.049
% Sand	0.295 (0.117)	0.087	0.217 (0.193)	0.047
% Silt	0.043 (0.432)	0.001	-0.442 (0.033)	0.195
% Clay	-0.307 (0.107)	0.094	-0.080 (0.375)	0.006
Texture category	0.167 (0.254)	0.027	0.222 (0.187)	0.049
% Oven dry weight	-0.603 (0.004)	0.363	-0.131 (0.302)	0.017
% Organic matter	-0.745 (0.000)	0.555	-0.334 (0.088)	0.111
Vegetation type	0.520 (0.013)	0.271	0.037 (0.441)	0.001

Table 6.12 R and R^2 statistics for ground and image variable pairs in Sebkha Sidi el Hani.

Ground variable	SIR-A DN R (significance)		SEASAT DN R (significance)	
	North transect	South transect	North transect	South transect
Roughness	0.832 (0.001)	0.898 (0.001)	0.690 (0.014)	0.470 (0.120)
Roughness category	0.935 (0.000)	0.946 (0.000)	0.694 (0.013)	0.699 (0.027)
Conductivity	-0.932 (0.000)	-0.637 (0.045)	-0.499 (0.071)	-0.086 (0.420)
% Sand	0.541 (0.053)	0.445 (0.135)	0.559 (0.046)	-0.310 (0.227)
% Silt	-0.498 (0.071)	-0.242 (0.282)	-0.471 (0.085)	-0.496 (0.105)
% Clay	-0.483 (0.078)	-0.244 (0.280)	-0.508 (0.067)	0.511 (0.098)
Texture category	0.467 (0.086)	0.260 (0.267)	0.656 (0.020)	-0.383 (0.174)
% Oven dry weight	-0.723 (0.009)	-0.477 (0.116)	-0.658 (0.019)	0.375 (0.179)
% Organic matter	-0.740 (0.007)	-0.620 (0.050)	-0.668 (0.017)	0.002 (0.498)

Table 6.13 Correlations between ground and image variable pairs for northern and southern transects located on Sebkha Sidi el Hani.

Strong correlations also exist between SIR-A DN and Conductivity (-.667), Oven-dried moisture (-.603) and Organic matter (-.745). None of the soil texture variables are highly correlated with SIR-A or Seasat DN. This is perhaps surprising as, although direct linear relationships between image DN and soil texture were not expected, the close relationship between soil texture (namely clay content) and soil moisture revealed by the high correlation values shown in Table 6.14 were expected to produce a correlation between DN and texture from their common association with soil moisture. Indeed, the importance of soil texture upon variations in soil moisture (and hence dielectric constant) has been stressed by Stroosnijder et al., (1986) amongst other scientists and was described in Chapter 3 (Section 3.5.9). However, the lack of any significant correlation between DN and soil texture does serve to highlight the overall importance of surface roughness upon the radar response from Sebkha Sidi el Hani.

Conductivity has a high negative correlation with SIR-A DN (-.667), significant at the 99% confidence levels; the R^2 value is 0.445. This suggests that high salinity levels are associated with low SIR-A backscatter, or DN. Such a relationship is indeed possible (see Chapter 3), as is an indirect link through soil moisture. Oven-dried moisture content and Organic matter have high negative correlations of their own with SIR-A DN (see Table 6.12). There is a high positive correlation between these two ground variables (.835), suggesting a close association between them.

Variables	R (significance)		R^2
T.ROUGH/CONDUCT	-0.713	(0.000)	0.509
T.ROUGH/SAND	0.351	(0.076)	0.123
T.ROUGH/SILT	-0.149	(0.277)	0.022
T.ROUGH/CLAY	-0.295	(0.117)	0.087
T.ROUGH/TEXTURE	0.238	(0.130)	0.056
T.ROUGH/OV. DRY WT.	-0.563	(0.007)	0.317
T.ROUGH/ORGMAT	-0.633	(0.002)	0.401
T.ROUGH/VEGTYP	0.424	(0.040)	0.180
ROUGHCAT/CONDUCT	-0.699	(0.001)	0.489
CONDUCT/OV. DRY WT.	0.654	(0.002)	0.427
CONDUCT/ORGMAT	0.592	(0.005)	0.350
TEXTURE/SAND	0.966	(0.000)	0.934
TEXTURE/SILT	-0.440	(0.034)	0.194
TEXTURE/CLAY	-0.932	(0.000)	0.868
TEXTURE/OV. DRY WT.	-0.661	(0.001)	0.437
OV. DRY WT./SAND	-0.678	(0.001)	0.459
OV. DRY WT./CLAY	0.737	(0.000)	0.544
OV. DRY WT/ORGMAT	0.835	(0.000)	0.697
SAND/SILT	-0.421	(0.041)	0.177
SAND/CLAY	-0.963	(0.000)	0.927
SAND/OV. DRY WT.	-0.678	(0.001)	0.459
SAND/ORGMAT	0.835	(0.000)	0.697
CONDUCT/SAND	-0.333	(0.088)	0.110
CONDUCT/SILT	-0.055	(0.414)	0.003
CONDUCT/CLAY	0.341	(0.083)	0.116

Table 6.14 R and R^2 values for selected pairs of ground variables on Sebkha Sidi el Hani.

The statistical results suggest that SIR-A DN seems to respond to variations in roughness, moisture, organic matter and salinity, while Seasat DN is closely associated with roughness measurements only. This observation is reinforced by the results of the stepwise multiple regression calculated for each image. In the case of Seasat the multiple regression equation is as follows:

Seasat DN = 14.66 Roughcat + 74.611 Equation 6.10

With an R^2 value of 0.398. Thus, nearly 40% of the variation in Seasat DN can be accounted for by a variation in Roughness category. None of the other ground variables is significant at the 95% confidence limit used by the SPSSX package and is omitted from the analysis. For SIR-A, the regression equation after the first step is:

SIR-A DN = 80.34 Trough + 42.863 Equation 6.11

With an R^2 value of 0.657. Thus, Transformed roughness is able to account for 65% of the variation in SIR-A DN. Organic matter is also significant at the 95% confidence levels and is included in the second step of the equation giving an equation of:

SIR-A DN = 56.03 Trough x -3.130 Orgmat + 55.824 Equation 6.12

With an R^2 value of 0.747. Thus, by the addition of Organic matter nearly 75% of the variation in SIR-A DN has been accounted for. It should not be assumed in either case that none of the other ground variables is able to account for any of the variation in image DN. Ground variables that are highly correlated will not all be selected for inclusion in the equation as they will not

account for any additional variation in DN (Ehrenberg, 1982). Thus, it is likely that oven-dried moisture content and Conductivity both account for some of the variation in SIR-A DN but they are so highly correlated with Organic matter content that it is not necessary to include them in the regression equation.

There are a number of explanations for the results observed. Firstly, the time-lag and seasonal difference between the Seasat pass at the collection of ground data may have been enough to eliminate any association between DN and soil conditions. Although the time-lag is obviously important, it is unlikely to be the sole explanation, as it should also be relevant to SIR-A. A second explanation is that the different incidence angles of the Seasat and SIR-A systems have recorded similar ground conditions existing at the two overpass dates in different ways. However, if this were the case it would be expected that the higher DN values in the Seasat image of the southern part of Sidi el Hani would have coincided with high statistical associations between image DN and soil conditions. The highest statistical associations are in fact recorded for the SIR-A image of Sidi el Hani, which has less visible variation in DN, especially in its southern region. If applied together, both of these explanations could account for the results observed; that is, ground conditions observed by different systems could produce differences in DN that, because of internal changes since 1981, do not correspond to ground conditions recorded during the field season.

The most likely explanation for the observations can be found when comparing the statistical results and image data. For both Seasat and SIR-A the highest correlations and R^2 values were recorded between DN and surface

roughness, suggesting that it is this parameter that dominates the backscatter recorded by each system. The roughness measurements taken in the field for Sidi el Hani fall mainly into the 'smooth' and 'very smooth' categories defined by the extended Peake and Oliver roughness criteria in Section 6.2 (see Appendix 1). Such low roughness (smoothness) conditions are depicted by the uniformly low DN/backscatter on the SIR-A image of the Sebkha, suggesting that roughness measurements recorded in the spring of 1986 are similar to those existing in November 1981. The low levels of backscatter from the sebkha allow variations in other surface conditions, such as soil moisture or salinity, to be picked out by the radar sensor and recorded on the image.

The DN values on the Seasat image of Sidi el Hani are significantly higher than the corresponding values on the SIR-A image, while retaining a similar form (see Figures 6.15 and 6.16). This may well reflect an overall increase in surface roughness, caused by hummocks, salt polygons and cracks on the sebkha surface present during the dry season. Such surface conditions would be capable of producing the bright tone seen in the southern part of the sebkha, through high levels of radar backscatter. The image resulting from radar interaction with the ground conditions would be dominated by roughness information and would reveal few of the subtle variations in DN caused by changes in soil condition.

Comparative analysis of this SIR-A image with a scene from the same data-take over sebkha environments in eastern Oman gave further weight to the hypothesis proposed above. The Omani sebkha was characterized by a high backscatter (DN) with a dark edge effect, a very different appearance from the uniform dark tone of the

SEASAT DN

COUNT	MIDPOINT	ONE SYMBOL EQUALS APPROXIMATELY .10 OCCURRENCES
2	72	**********
1	77	*****
1	82	*****
0	87	
0	92	
3	97	**********
1	102	*****
4	107	**********
1	112	*****
0	117	
1	122	*****
1	127	*****
0	132	
0	137	
1	142	*****
0	147	
0	152	
1	157	*****
0	162	
0	167	
1	172	*****

I....+....I....+....I....+....I....+....I....+....I....+....I
0 1 2 3 4 5
HISTOGRAM FREQUENCY

MEAN	108.833	MEDIAN	105.500	MODE	72.000
STD DEV	27.620	VARIANCE	762.853	KURTOSIS	.568
SKEWNESS	.881	RANGE	101.000	MINIMUM	72.000
MAXIMUM	173.000				
VALID CASES	18	MISSING CASES	0		

Figure 6.15 Histogram and descriptive statistics for Seasat DN in Sebkha Sidi el Hani.

SIR-A DN

COUNT	MIDPOINT	ONE SYMBOL EQUALS APPROXIMATELY .10 OCCURRENCES
0	24	
1	27	**********
0	30	
1	33	**********
1	36	**********
0	39	
1	42	**********
2	45	********************
1	48	**********
0	51	
3	54	**********
1	57	**********
3	60	**********
2	63	********************
0	66	
1	69	**********
0	72	
0	75	
0	78	
1	81	**********
0	84	

I....+....I....+....I....+....I....+....I....+....I
0 1 2 3 4 5
HISTOGRAM FREQUENCY

MEAN	53.278	MEDIAN	55.000	MODE	46.000
STD DEV	13.288	VARIANCE	176.565	KURTOSIS	.141
SKEWNESS	-.089	RANGE	53.000	MINIMUM	28.000
MAXIMUM	81.000				
VALID CASES	18	MISSING CASES	0		

Figure 6.16 Histogram and descriptive statistics for SIR-A DN in Sebkha Sidi el Hani.

Tunisian sebkha. Field measurements were made in each sebkha environment during the spring of 1986 and results presented in a series of three comparative papers (Stone and McBean, 1987; 1988; McBean and Stone, In Press). Levels of moisture, conductivity and organic matter, together with soil texture measurements, were found to be very similar, suggesting a similarity between the complex dielectric constants of the two sebkhas. Roughness measurements which were all made according to the scheme described in Section 6.2, were quite different.

In Tunisia roughness measurements ranged from 0.0 to 5.6cm, with a mean value of 1.3cm. For Oman, measurements ranged from as low as 0.0cm to as high as 40.0cm, giving a mean value of 9.75, which falls within the 'rough' and 'very rough' categories of the enhanced Peake and Oliver roughness criteria. As temporal and system parametric consistency could be guaranteed in the comparative study, the results highlight the tremendous importance of surface roughness upon SIR-A backscatter from sebkha regions, supporting the conclusions of Macdonald and Waite (1973).

The ancient sebkha near the coast at Monastir has a similar low-to-medium backscatter response on the Seasat and SIR-A images, suggesting that surface conditions were not significantly different at each overpass date. Although this sebkha was not studied in as great detail as Sidi el Hani, fieldwork in 1986 revealed considerable variations in surface condition and cover. Towards the coast the surface moisture content increased and there were large areas of standing water. This generated a radar-smooth surface giving rise to low Seasat and SIR-A DN. Inland surface moisture was reduced and pockets of halophytic vegetation and salt crystallization were noted

(Plate 6.3). The roughness of the surface increased, an increase seen in the higher DN or brighter image response.

The time-lag factor, together with the lack of system calibration prevents direct quantitative conclusions from being made about radar backscatter and sebkha ground conditions. However, one important conclusion must be made, namely; surface roughness has a considerable influence upon variations in DN on radar images of sebkha environments. Studies using calibrated imagery and concurrently collected ground measurements would do much to clarify and quantify the results of this research.

6.7.3. Analysis of Eastern Vegetated Areas (Cases 27-44: Appendix 1).

Statistical analysis was undertaken on the vegetation subset in the eastern field area to assess the influence of vegetation parameters upon Seasat and SIR-A backscatter. Ground parameters thought to be of little relevance to the study were omitted from the analysis. These included variables relating to soil type or condition. The ground variables used in the analysis, together with transformations applied to them are listed below:

Transformed slope = Arctan Slope = TSLOPE
Roughness = ROUGH
Roughness category = ROUGHCAT
Tree spacing = TOPSPAC
Tree height = TOPHT
Transformed tree canopy = Tree canopy^2 = TTOPCAN
Low vegetation cover = LOWCAN
Local SIR-A incidence = SIRINC

Transformed Local Seasat Incidence = Local Seasat incidence^2 = TSSINC

Transformed SIR-A/vegetation orientation = Log10 (SIR-A/vegetation orientation) = TSIRVEG

Transformed Seasat/vegetation orientation = Log10 (Seasat/vegetation orientation) = TSSVEG

	SIR-A DN		SEASAT DN	
Ground variable	R (significance)	R^2	R (significance)	R^2
Roughness	0.358 (0.072)	0.128	0.490 (0.019)	0.240
Roughness category	0.337 (0.085)	0.114	0.399 (0.050)	0.159
Trans slope	0.570 (0.006)	0.336	0.550 (0.009)	0.303
Trans SIR-A incidence	-0.131 (0.302)	0.017	———	—
Trans Seasat incidence	———	—	0.431 (0.037)	0.186
Top spacing	-0.189 (0.226)	0.035	-0.443 (0.033)	0.196
Top height	-0.112 (0.328)	0.012	-0.311 (0.104)	0.096
Trans top canopy	0.243 (0.166)	0.059	-0.047 (0.426)	0.002
Vegetation type	-0.167 (0.253)	0.028	-0.397 (0.051)	0.157
Trans SIR-A vegetation orientation	-0.627 (0.003)	0.393	———	—
Trans Seasat vegetation orientation	———	—	-0.825 (0.000)	0.680

Table 6.15 R and R^2 statistics for pairs of ground and image variables in the vegetated regions of the sahel of Sousse.

Correlation coefficients for the vegetated regions of the eastern study area show some interesting and unexpected results (Table 6.15). For both Seasat and SIR-A the highest R values are recorded between image DN and Transformed slope and Transformed vegetation orientation. None of the other correlation coefficients is significant at 90% confidence levels. Stepwise multivariate regression analyses calculated for the two dependent variables

(Seasat DN and SIR-A DN) confirm the results of the bivariate analyses. For Seasat DN the regression equation is:

$$\text{Seasat DN} = -18.694\ \text{Tssveg} + 157.31 \qquad \text{Equation 6.13}$$

The R^2 value of 0.681 suggests that Transformed Seasat-vegetation orientation accounts for 68% of the variation in DN. A similar result was obtained for SIR-A DN where:

$$\text{SIR-A DN} = -11.204\ \text{Tsirveg} + 136.49 \qquad \text{Equation 6.14}$$

The R^2 value of 0.386 suggests that over 38% of the variation in SIR-A DN is accounted for by variations in Transformed SIR-A vegetation orientation. For both Seasat and SIR-A none of the remaining ground variables added significant predictive power at the 95% confidence levels adopted as a cut off for stepwise multiple regression and were omitted from the analysis.

The orientation of the vegetation, particularly in areas of arboriculture, seems to have a significant influence on levels of backscatter from vegetated regions of the Sahel of Sousse. This is hardly surprising, as rows of vegetation perpendicular to radar look direction will generate increased levels of trunk and canopy backscatter, thereby increasing image DN. What is perhaps more surprising is the absence of any significant association between image DN and other vegetation variables, such as tree height, spacing and canopy. It was expected that these variables would influence the amount of signal penetration between trees or bushes and therefore the overall contribution of soil, trunk or canopy to the backscatter response. It was also expected that these measurements would highlight differences in DN

SEASAT DN

COUNT	MIDPOINT	ONE SYMBOL EQUALS APPROXIMATELY .10 OCCURRENCES
1	116	**********
2	120	********************
1	124	**********
2	128	********************
3	132	******************************
0	136	
1	140	**********
0	144	
0	148	
1	152	**********
0	156	
1	160	**********
0	164	
0	168	
0	172	
1	176	**********
0	180	
2	184	********************
0	188	
1	192	**********
2	196	********************

I....+....I....+....I....+....I....+....I....+....I....+....I
0 1 2 3 4 5
HISTOGRAM FREQUENCY

MEAN	150.222	MEDIAN	136.500	MODE	126.000
STD DEV	29.403	VARIANCE	864.536	KURTOSIS	-1.535
SKEWNESS	.469	RANGE	80.000	MINIMUM	116.000
MAXIMUM	196.000				
VALID CASES	18	MISSING CASES	0		

Figure 6.17 Histogram and descriptive statistics for Seasat DN in the vegetated regions of Sousse.

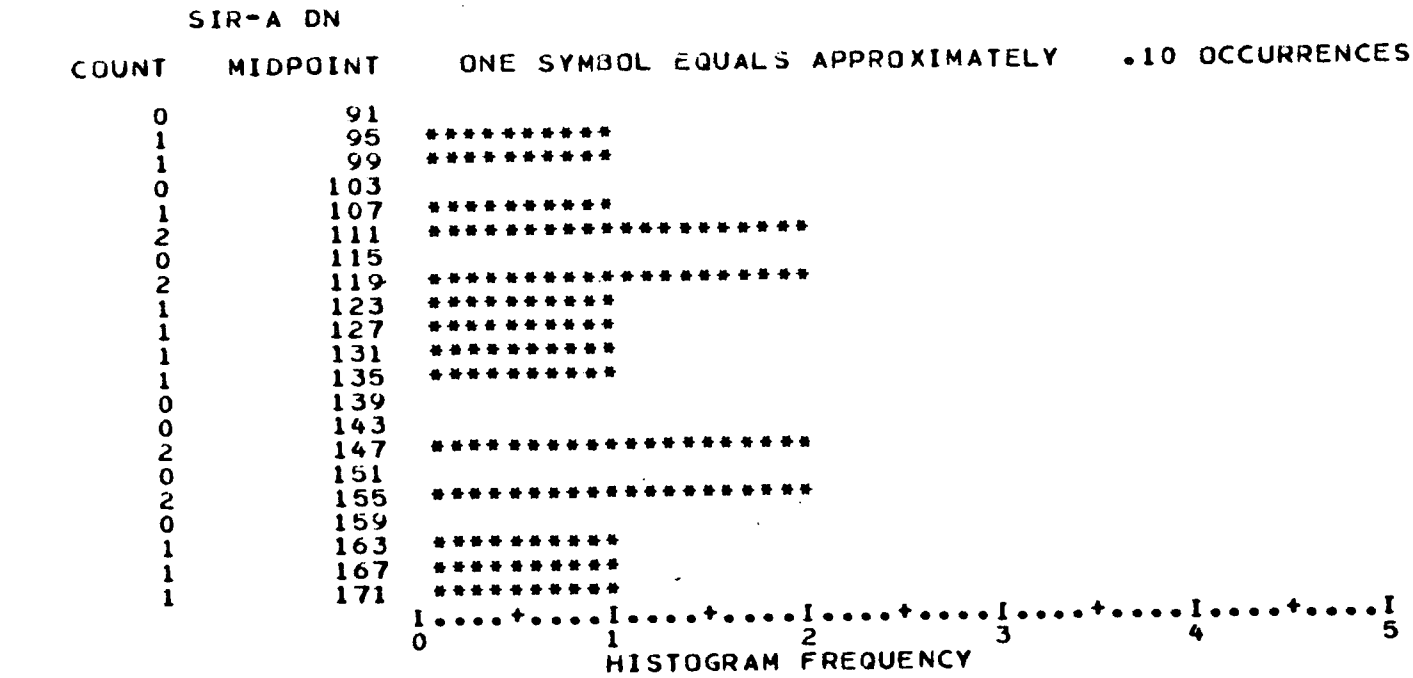

Figure 6.18 Histogram and descriptive statistics for SIR-A DN in the vegetated regions of Sousse.

within tree plantations recorded by the differing radar depression angles, with greater ground-tree interaction being detected by the steeper Seasat signal.

The distribution of SIR-A and Seasat DN are not dissimilar (see Figures 6.17 and 6.18) with descriptive statistics showing a remarkable degree of similarity. The ranges of values are almost identical, being 77 for SIR-A and 80 for Seasat. Maximum and minimum values agree to within 26 DN in each case. From this it may be concluded that radar depression angle has little effect upon the backscatter from vegetated areas of eastern central Tunisia. Furthermore, the structure and size of tree- or bush-level vegetation is of lesser importance to DN than row orientation. Although these results seem to be fairly conclusive, studies using a larger population of concurrently recorded field and image data would be advisable to test these hypotheses further. It is regretted that time constraints during the field programme limited the effective sample size to less than twenty cases.

6.8 Analysis of Western Data Set.

6.8.1 Analysis of Full Western Data Set (Cases 1-60: Appendix 2)

Before statistical analysis of the western data set could commence, several transformations had to be applied to reduce skewness to within acceptable limits. The following variables were transformed:

TM band 4, where TTM4 = $(TM4)^2$
TM band 5, where TTM5 = $(TM5)^2$
Slope, where Tslope = Log10 (Slope)
Roughness, where TROUGH = Log10 (Rough)
Vegetation spacing, where TVEGSPAC = Log10 (VEGSPAC)
Wadi width, where TWADWID = Log10 (WADWID)
Local SIR-A Incidence Angle, where TSIRINC =
Log10 (SIRINC)

The remaining variables listed in Table 6.6 were not transformed. Statistical analyses were undertaken on the full data set to allow the most important ground variables contributing to changes in DN to be assessed at all eight wavelengths covered by SIR-A and TM. The results for the TM bands are not analysed in detail but are used for comparative tools only.

Pearson product moment correlation coefficients for ground and image variable pairs are presented in Table 6.16. For SIR-A, correlations significant at the 90% confidence level are found between SIR-A DN and Transformed roughness (0.486), Roughness category (.487) and Transformed slope (0.316). These three variable pairs have bivariate regression values of 0.236, 0.237 and 0.099 respectively. Other notable associations are SIR-A DN with Transformed wadi width ($R = 0.47$; $R^2 = 0.23$) and SIR-A DN with Wadi height ($R = 0.44$; $R^2 = 0.20$). Four out of the seven TM bands are well correlated with Geological category; R values are -.514, -.514, -.492 and -.425 recorded for bands TM,2,3 and 7 respectively. The bands 1,2 and 3 have correlations significant at the 90% level with Transformed slope and Vegetation height (see Table 6.16). TM band 6 is well correlated with Transformed wadi width.

	PEARSON PRODUCT MOMENT CORRELATION COEFFICIENTS: R (SIGNIFICANCE)								R^2
	SIR-A DN	TM1 DN	TM2 DN	TM3 DN	Trans TM4 DN	Trans TM5 DN	TM6 DN	TM7 DN	SIR-A DN
Trans slope	0.316 (0.007)	-0.311 (0.008)	-0.374 (0.002)	-0.326 (0.005)	-0.066 (0.30)	-0.092 (0.242)	-0.166 (0.101)	-0.159 (0.112)	0.099
Trans roughness	0.486 (0.00)	0.051 (0.34)	0.007 (0.47)	0.009 (0.47)	0.043 (0.37)	-0.070 (0.29)	-0.220 (0.045)	0.068 (0.30)	0.236
Geology	-0.002 (0.49)	-0.514 (0.00)	-0.514 (0.00)	-0.492 (0.00)	-0.019 (0.468)	-0.150 (0.165)	-0.254 (0.04)	-0.425 (0.00)	0.000
Sand	0.582 (0.15)	0.108 (0.43)	0.240 (0.34)	0.417 (0.24)	0.043 (0.47)	0.350 (0.28)	-0.690 (0.09)	0.340 (0.285)	0.338
Silt	-0.498 (0.19)	-0.031 (0.48)	-0.150 (0.40)	-0.359 (0.27)	-0.140 (0.41)	-0.529 (0.17)	0.561 (0.16)	-0.400 (0.25)	0.248
Clay	-0.679 (0.10)	-0.240 (0.34)	-0.390 (0.25)	-0.480 (0.20)	0.159 (0.39)	0.040 (0.47)	0.860 (0.02)	-0.184 (0.38)	0.461
Texture	0.480 (0.20)	0.030 (0.48)	0.150 (0.40)	0.350 (0.27)	0.090 (0.44)	0.500 (0.19)	-0.560 (0.16)	0.400 (0.25)	0.230
Oven dry	-0.700 (0.09)	-0.210 (0.36)	-0.350 (0.27)	-0.500 (0.19)	-0.090 (0.44)	-0.230 (0.35)	0.800 (0.05)	-0.300 (0.30)	0.490
Organic matter	-0.480 (0.20)	-0.030 (0.46)	-0.150 (0.40)	-0.350 (0.27)	-0.090 (0.44)	-0.500 (0.19)	0.560 (0.16)	-0.400 (0.25)	0.230
Trans veg. spacing	0.120 (0.17)	-0.260 (0.02)	-0.270 (0.02)	-0.230 (0.04)	-0.030 (0.40)	-0.120 (0.18)	-0.060 (0.32)	-0.110 (0.20)	0.014
Veg. height	0.100 (0.21)	-0.330 (0.005)	-0.320 (0.007)	-0.290 (0.091)	-0.172 (0.098)	-0.236 (0.03)	0.196 (0.07)	-0.158 (0.118)	0.010
Veg. canopy	0.090 (0.23)	-0.300 (0.01)	-0.290 (0.01)	-0.250 (0.02)	-0.150 (0.118)	-0.190 (0.07)	0.200 (0.05)	-0.118 (0.18)	0.008
Veg. type	0.028 (0.41)	-0.220 (0.04)	-0.210 (0.05)	-0.190 (0.06)	-0.130 (0.148)	-0.180 (0.08)	0.124 (0.17)	-0.080 (0.26)	0.000
Trans wadi width	-0.470 (0.02)	0.040 (0.43)	-0.030 (0.44)	-0.090 (0.36)	-0.130 (0.30)	-0.310 (0.11)	0.750 (0.00)	0.020 (0.45)	0.220
Wadi height	0.440 (0.03)	-0.230 (0.17)	-0.160 (0.26)	-0.030 (0.35)	0.100 (0.35)	-0.290 (0.12)	0.000 (0.48)	-0.130 (0.30)	0.193
North slope	-0.190 (0.22)	0.30 (0.11)	0.190 (0.22)	0.180 (0.23)	-0.050 (0.42)	-0.050 (0.42)	-0.110 (0.32)	0.210 (0.20)	0.036
South slope	0.180 (0.24)	-0.040 (0.43)	-0.060 (0.39)	0.050 (0.42)	0.070 (0.39)	-0.170 (0.24)	0.060 (0.49)	-0.030 (0.45)	0.032
Slope form	0.240 (0.028)	-0.290 (0.01)	-0.300 (0.01)	-0.240 (0.02)	-0.060 (0.30)	-0.060 (0.31)	-0.070 (0.288)	-0.050 (0.34)	0.057
Trans SIR-A incidence	0.120 (0.16)	—	—	—	—	—	—	—	0.014
SIR-A gully orientation	0.150 (0.27)	—	—	—	—	—	—	—	0.022

Table 6.16 R and R^2 values for ground and image variable pairs in the western field area.

The results obtained from the Pearson Product Moment Correlations highlight the difference between the capabilities of radar data from SIR-A and visible and infrared Landsat data. For radar, it is the relief of the surface that is important, both at the macro- (slope) and micro- (roughness) level. Physical dimensions of morphological features are also important. At visible and infrared wavelengths, radiometric characteristics of vegetation and lithology are more important, although terrain slope still has a considerable influence on DN. Thus, even the general results presented here confirm the theoretical points discussed in Chapter 3 and observations made in Chapter 5.

The bivariate relationships discussed above are reinforced by the results of the multivariate analysis, namely stepwise multiple regression. For SIR-A, Roughness category is selected in step 1 of the analysis giving an equation of:

SIR-A DN = 32.03 Roughcat + 14.73 Equation 6.15

With an R^2 value of 0.237, SIR-A/gully orientation is added at step 2 to raise the R^2 value to 0.507, while the addition of Slope form increases R^2 to 0.869, giving the equation:

SIR-A DN = 119.55 Roughcat +4.68 Sirgul + Equation 6.16
-94.32 Slopeform = -364.32

Geology is selected at the first step of multiple regression equations calculated for TM1, TM2 and TM3 and at the second step of TM6. R^2 values of 0.26, 0.26 and 0.24 are achieved for bands 1-3 respectively.

Variables	R	(significance)
ROUGH/SLOPE	0.480	(0.000)
ROUGH/ROUGHCAT	0.950	(0.000)
ROUGH/GEOLOGY	0.420	(0.002)
ROUGH/VEGSPAC	0.370	(0.002)
ROUGH/SLOPEFORM	0.400	(0.001)
SLOPE/ROUGHCAT	0.400	(0.000)
SLOPE/GEOLOGY	0.780	(0.000)
SLOPE/SLOPEFORM	0.740	(0.000)
GEOLOGY/SLOPEFORM	0.650	(0.000)
GEOLOGY/VEGSPAC	0.600	(0.000)
GEOLOGY/VEGHT	0.680	(0.000)
GEOLOGY/VEGCAN	0.530	(0.000)
GEOLOGY/VEGTYP	0.550	(0.000)
GEOLOGY/WADWID	-0.750	(0.000)
GEOLOGY/WADHT	-0.070	(0.380)
VEGTYP/VEGSPAC	0.860	(0.000)
VEGTYP/VEGHT	0.800	(0.000)
VEGTYP/VEGCAN	0.830	(0.000)
VEGSPAC/VEGHT	0.750	(0.000)
VEGSPAC/VEGCAN	0.810	(0.000)
VEGHT/VEGCAN	0.940	(0.000)

Table 6.17 R and R^2 values for selected pairs of ground variables in western study area.

The inclusion of SIR-A/gully orientation and Slope form in the second and third steps of the regression analysis for SIR-A DN further highlights the influence of geometry upon variations in image tone. However, there is a need for caution when interpreting the statistical results obtained from the images of this area. One has to be aware of the close associations between ground variables and hence the problem of collinearity. Pearson Product Moment Correlation Coefficients are presented for selected pairs of ground variables in Table 6.17. High correlations are recorded for slope form with slope (0.74) and with geology (0.65). The complex interactions that exist between these and other variables are likely to result in only some of them being included in the multiple regression analysis.

6.8.2 Analysis of Gullies of the Western Study Area (Cases 7-18: Appendix 2).

Data collected from the gully sites in the western study area were analysed statistically to try to identify any general associations between channel form and image DN. The following variables and transformations were used:

SIR-A DN
Transformed TM 1 DN = $(\text{TM1 DN})^2$
TM2 DN
Transformed TM3 DN = $(\text{TM3 DN})^2$
TM4 DN
Transformed TM5 DN = $(\text{TM5 DN})^2$
Transformed TM7 DN = $(\text{TM7 DN})^2$
Roughness
Transformed wadi width = Log10 (wadi width)
Wadi depth

SIR-A/wadi (or gully) orientation
Southern Gully slope
Northern Gully slope

The Pearson Product Moment Correlation Coefficients for SIR-A DN with ground variables can be found in Table 6.18. Two coefficients significant at the 97% confidence level can be identified, namely SIR-A DN with Transformed wadi width (.808) and Southern slope (.742). These two variable pairs have R^2 values of 0.65 and 0.55 respectively, reinforcing the associations identified by correlation.

Stepwise multiple regression identifies the same two variables as being of most importance when accounting for the variation in SIR-A DN. After step 1 of the analysis the following regression equation is obtained:

SIR-A DN = 48.60 Twadwid +120.933 Equation 6.17

An R^2 value of 0.65 suggests that 65% of the variation in SIR-A DN can be accounted for by the variation in Wadi width. With the addition of south slope at step 2, where:

SIR-A DN = 38.68 Twadwid + 0.97 Sslope +79.71 Equation 6.18

The R^2 value rises to 0.92, indicating that together these two variables account for 92% of the variation in SIR-A DN.

The bivariate statistics reveal few strong relationships between pairs of ground variables. The only correlations significant at the 90% confidence level are noted in Table 6.19. From this it can be concluded that

Ground variable	SIR-A DN R (significance)	R^2	TM1 DN R	TM2 DN R	TM3 DN R	TM4 DN R	TM5 DN R	TM7 DN R
Roughness	-0.83 (0.398)	0.688	-0.170 (0.298)	0.233 (0.232)	-0.293 (0.177)	-0.063 (0.422)	-0.202 (0.264)	-0.109 (0.368)
Roughness category	-0.262 (0.205)	0.068	0.052 (0.434)	-0.026 (0.467)	-0.096 (0.383)	0.163 (0.306)	0.012 (0.485)	0.090 (0.390)
Slope	0.534 (0.037)	0.280	-0.131 (0.342)	-0.104 (0.373)	-0.006 (0.493)	0.157 (0.312)	0.177 (0.290)	0.218 (0.247)
Slope form	0.517 (0.043)	0.267	-0.128 (0.346)	-0.103 (0.374)	-0.005 (0.493)	0.158 (0.312)	0.167 (0.301)	0.212 (0.254)
South slope	0.742 (0.003)	0.550	-0.156 (0.314)	-0.094 (0.386)	-0.011 (0.485)	-0.188 (0.279)	-0.086 (0.395)	-0.062 (0.423)
North slope	-0.054 (0.433)	0.003	0.245 (0.221)	0.200 (0.266)	0.149 (0.322)	0.120 (0.355)	0.050 (0.438)	0.133 (0.340)
Trans wadi width	0.808 (0.001)	0.650	-0.642 (0.012)	-0.543 (0.034)	-0.415 (0.090)	-0.404 (0.096)	-0.352 (0.131)	-0.355 (0.128)
Wadi height	0.452 (0.070)	0.200	-0.143 (0.329)	-0.006 (0.492)	0.005 (0.493)	-0.017 (0.479)	-0.011 (0.486)	-0.010 (0.487)
SIR-A gully orientation	0.637 (0.013)	0.400	—	—	—	—	—	—
Geology	-0.446 (0.050)	0.198	0.352 (0.131)	0.252 (0.214)	0.217 (0.249)	0.468 (0.062)	0.354 (0.129)	0.395 (0.103)

Table 6.18 R and R^2 values for image and ground variable pairs in the gullies and wadis of the western study area.

wadi width and southern slope are important variables in their own right and have not been selected on the basis of any complex collinear relationships between ground variables.

Variables	R (significance)
ROUGHCAT/GEOLOGY	0.768 (0.002)
SIRGULORIEN/GEOLOGY	-0.670 (0.008)
SIRGULORIEN/ROUGHCAT	-0.670 (0.008)
SIRGULORIEN/SSLOPE	0.690 (0.006)
SIRGULORIEN/NSLOPE	-0.300 (0.172)
SLOPE/SLOPEFORM	0.998 (0.000)
SLOPE/SIRINC	-0.997 (0.000)
SLOPEFORM/SIRINC	-0.992 (0.000)
NSLOPE/ROUGH	0.673 (0.008)

Table 6.19 Correlations between selected pairs of ground variables in the gullies and wadis of the western study area.

The importance of wadi width and the slope of the channel walls upon SIR-A DN in this area suggests that it is the amount of radar signal able to enter the channel that is the controlling factor. The wider the wadi, the more likely the radar signal will penetrate between the channel walls and into the channel bottom. If significant penetration of the gully does occur, combined scatter from the floor and walls of the channel will increase the overall backscatter response. At the shallow depression angle of SIR-A, the width of the channel is of tremendous importance.

Most of the gullies in the western study area have a similar orientation. This means that the effective orientation of the gully in relation to the SIR-A look direction does not vary to any significant degree. This explains the relatively low correlation between SIR-A DN and Gully orientation. Results obtained from gullies of varying orientation would be expected to highlight the effect of look direction in much the same way as the vegetation studies to the east (see Section 6.7.3). In the majority of cases the effective gully orientation is greater than or equal to 30°. The northern slope of the channel is oriented towards the incoming SIR-A signal in the case of each gully, and would be expected to influence the amount of radar backscatter from the feature. However, the southern slope of the channel has been identified as exerting a more important influence on backscatter and hence DN. Again, this seems to be a matter of gully penetration, as a steeper channel wall down range will allow greater effective penetration beyond it. The steeper the southern channel wall (ie. the nearer the angle approaches the depression angle of SIR-A), the greater the amount of signal penetration and the greater the possibility of corner reflection, both of which will produce high levels of radar backscatter. Even for gullies oriented within a few degrees of radar look direction, near-range channel slope will influence SIR-A return.

The lack of any significant correlation between any TM band and any ground characteristic in this study (see Table 6.18) further highlights the important relationships identified from the radar imagery. The results of this study imply that SIR-A data responds to variations in the geometrical properties of gullies in the area covered by the study. The value of SIR-A for discriminating gullies

in the Hadjel Valley is examined through discriminant analysis in Chapter 7. Applications of SIR-A data to problems of gully erosion in central Tunisia are discussed in Chapter 9.

6.8.3 Analysis of The Mountain Environments of Hadjeb el Ayoun (Cases 26-54: Appendix 2).

The data collected from the mountain regions of the western study area were used in four separate analyses to determine the influence of relief and morphology upon radar image tone. For the first analysis, all 29 cases were included, irrespective of slope or aspect. Transformations were applied to:

TM5, where TTM5 = $(TM5)^2$
TM7, where TTM7 = $(TM7)^2$
Roughness, where TROUGH = $\sqrt{ROUGH}$

The second analysis included cases 26-39 which were all located on Djebel Henndi. Transformations were applied to:

TM7, where TTM7 = $(TM7)^2$
Slope, where TSLOPE = log10 (slope).

The third analysis included all cases located on Djebels Nara and Cherahil (Cases 40-54). TM5 and TM7 were both cubed to reduce skewness and a square root transformation was applied to roughness.

Finally, cases located on Djebel Nara (cases 40-48) were analysed separately. The following transformations were applied to this subset:

$TTM3 = (TM3)^2$
$TTM4 = (TM4)^2$
$TTM5 = (TM5)^4$
$TTM7 = (TM7)^4$
$TROUGH = (Rough)^2$

The purpose of the four separate analyses was to investigate the possible influence of aspect angle, and therefore effective look direction, upon signal response from the mountains of the study area.

Pearson Product Moment Correlation Coefficients for the full mountain data set (Table 6.20) revealed close associations between SIR-A DN and three variables : slope (.586), Roughness category (.490) and SIR-A incidence (.442). All three correlations are significant at a 90% confidence level and have R^2 values that are greater than those of other ground variables. Stepwise multiple regression analysis reveals that slope angle accounts for 34% of the variation in SIR-A DN, this association having an R^2 value of 0.34 and the following equation:

$$\text{SIR-A DN} = 0.86 \text{ Slope} + 114.04 \qquad \text{Equation 6.19}$$

Slope is the only variable to be significant at the 95% confidence level used by SPSS-x as the regression threshold but it should not be assumed that SIR-A incidence and Roughness are not important. Indeed, Slope and SIR-A incidence have a moderate correlation of 0.51 and collinearity must be a factor here. The analysis does seem to highlight the importance of relief upon variations in SIR-A DN.

Ground Variable	R (significance)	R^2
Slope	0.586 (0.000)	0.340
Trans roughness	0.320 (0.042)	0.102
Roughness category	0.490 (0.003)	0.240
Geological category	0.400 (0.020)	0.160
Vegetation spacing	0.115 (0.279)	0.013
Vegetation height	0.260 (0.080)	0.260
Vegetation canopy	0.150 (0.217)	0.022
Vegetation type	0.100 (0.330)	0.010
Slope form	0.130 (0.240)	0.016
SIR-A local incidence	0.442 (0.008)	0.195

Table 6.20 R and R^2 values for SIR-A DN and ground variables in the mountain environments of Hadjeb el Ayoun.

Ground Variable	R (significance)	R^2
Trans slope	0.810 (0.000)	0.656
Roughness	0.415 (0.070)	0.172
Roughness category	0.579 (0.015)	0.335
Geological category	0.441 (0.057)	0.194
Slope form	0.296 (0.152)	0.087
Vegetation type	0.174 (0.315)	0.030
SIR-A local incidence	0.458 (0.050)	0.209

Table 6.21 R and R^2 values for SIR-A DN and ground variables on Djebel Henndi.

Analysis of samples located on Djebel Henndi gives further weight to the conclusions drawn from the combined mountain study. Transformed slope is the single variable with which SIR-A DN is highly correlated. This pair of variables has a correlation coefficient of 0.81 and a bivariate regression value (R^2) of 0.65 (Table 6.21). SIR-A incidence and Roughness do not have significant correlations with SIR-A DN in this analysis. Transformed slope is the only variable included in the multiple regression equation:

SIR-A DN = 65.01 Tslope + 55.98 Equation 6.20

This relationship has an R^2 value of 0.66 suggesting that 66% of the variation in SIR-A DN can be explained by variations in slope. The influence of slope on SIR-A return from mountain environments was noted in the previous chapter (see Section 5.2.3). In the remaining two analyses none of the ground variables was found to be correlated with SIR-A DN (see Tables 6.22 and 6.23). Slope, Roughness category and SIR-A incidence have the highest correlations in each case but none was significant at 99% confidence levels. Furthermore, none of the variables was able to satisfy the threshold significance for stepwise multiple regression and thus these equations could not be calculated.

The lack of any significant association between SIR-A DN and ground characteristics on Djebel Nara and Djebel Cherahil is likely to be a function of the aspect angle of foreslopes and backslopes in these mountains. Both mountain chains are part of the Tunisian North-South Axis described in Chapter 2 (Figure 2.3) and have the majority of slope faces oriented towards the east or west. These slopes are normal, or near-normal, to the SIR-A look

Ground Variable	R (significance)	R^2
Slope	0.515 (0.024)	0.266
Trans roughness	0.287 (0.149)	0.082
Roughness category	0.418 (0.060)	0.174
Slope form	-0.047 (0.433)	0.002
Geological category	0.358 (0.172)	0.128
SIR-A local incidence	0.502 (0.028)	0.252

Table 6.22 R and R^2 values for SIR-A DN and ground variables on Djebels Nara and Cherahil.

Ground Variable	R (significance)	R^2
Slope	0.389 (0.150)	0.151
Trans roughness	0.366 (0.166)	0.133
Roughness category	0.637 (0.032)	0.405
Geological category	0.358 (0.172)	0.128
Slope form	-0.126 (0.373)	0.015
SIR-A local incidence	0.504 (0.083)	0.254

Table 6.23 R and R^2 values for SIR-A DN and ground variables on Djebel Nara.

direction and, according to the radar theory outlined in Chapter 3 (Section 3.5.6), variations within them will be subdued on the resultant image. The slopes Djebel Henndi, on the other hand, are perpendicular to the SIR-A look direction and will be enhanced on the final image.

None of the ground variables included in the study was found to be significantly correlated with any of the TM bands, with the exception of Roughness category and Slope form which had correlations with TM band 3 of -0.632 and -0.623 respectively for Djebel Henndi. This lack of correlation between relief or morphology and visible or infrared DN provides some of the best possible evidence in support of the theory that radar data is of much greater value in mountain environments than traditional short-wave remote sensing. Similar conclusions were drawn from the results of digital image analysis described in the previous chapter (Section 5.3). The relative merits of SIR-A and TM for discriminating slopes in the western study area is further examined in Chapter 7.

Statistical analysis of field and image data from the mountain environments around Hadjeb el Ayoun has demonstrated the importance of slope, look direction and aspect angle upon SIR-A DN and, therefore, backscatter. Microscale variations in surface roughness have also been shown to be significant (Plate 6.15). The relative contributions of relief and roughness to SIR-A backscatter could be determined more accurately if they were to be separated from each other and analysed independently. Without an accurate digital terrain model of the area this separation is impossible. The effect of slope and aspect angle upon SIR-A image DN in this area is examined in Chapter 7 with the aid of discriminant analysis.

Chapter 7. Radar Classification of Semi-arid Environments

7.1. Introduction.

This chapter investigates the ability of Seasat and SIR-A to discriminate surfaces and cover types in semi-arid Tunisia. Discriminant analysis of image data taken from homogeneous areas identified in the field facilitates the assessment of the relative merits of these two systems as classification tools. The availability of Landsat TM data for the western study area allowed the classification accuracies of visible, infrared and microwave data to be compared. The results are used in support of the image-based and parameter-based studies described in Chapters 5 and 6, allowing conclusions to be made as to the most appropriate system for terrain classification in semi-arid Tunisia.

7.2. Discriminant Analysis as a Classification Tool.

Discriminant analysis is a common technique used in remote sensing to determine the optimum bands for area classifications, as it:

> ".. provides a powerful technique for examining differences between two or more groups of objects with respect to several variables simultaneously" (Klecka, 1980)

This method was used by Hobbs and Shennan (1986) in their studies of salt marsh reclamation in the Wash and by Asrar et al., (1986) for distinguishing among prairie grass types. Other publications on the application of discriminant analysis include: Morrisey et al., (1984), Adams and McLeod (1984) and Labovitz (1986). Discussion

of the methods involved in the analysis are reviewed in Jennrich (1977) and Klecka (1980).

Classes to be included in the analysis were selected in the field to be typical of surfaces found in semi-arid Tunisia. Sixteen classes were chosen in the eastern area, while twenty-two classes were included in analysis of the western area. All the classes are listed in Table 7.1.

CLASSES USED FOR DISCRIMINANT ANALYSIS

	EASTERN STUDY AREA		WESTERN STUDY AREA
1	Sea	1	Sebkhas
2	Coastal Sebkha: Monastir	2	Settlements
3	Ancient coastal Sebkha (extension of 2): Bembla	3	Roads
4	Inland Sebkha: Moknine	4	Wadis
5	Large Active Inland Sebkha: Sidi el Hani	5	Gullies
6	Sebkha shore	6	Calcrete
7	Settlements	7	Olives and scrubland
8	Roads East-West	8	Agriculture: cereals and pasture
9	Roads North-South	9	Bare ground
10	Inflow channels	10	Low slopes North (<30°)
11	Lunette dune	11	Low slopes South (<30°)
12	Hill country	12	Low slopes East (<30°)
13	Arboriculture in East (mainly olives)	13	Low slopes West (<30°)
14	Arboriculture in West (mainly olives)	14	Medium slopes North (30°-55°)
15	Tree and bush plots	15	Medium slopes South (30°-55°)
16	Cereal plots and pasture	16	Medium slopes East (30°-55°)
		17	Medium slopes West (30°-55°)
		18	High slopes North (>55°)
		19	High slopes South (>55°)
		20	High slopes East (>55°)
		21	High slopes West (>55°)
		22	Alluvial fans

(Note. Sebkha classes 2-5 will be referred to by name and not condition in tables and text to follow)

Table 7.1 Classes used for Discriminant Analysis in the eastern and western study areas.

Forty DN samples were extracted from each image for every class, taking care to avoid boundary areas and mixed pixels. The data were entered into the computer in tabular form compatible with the operation of the discriminant analysis function of the SPSS-x statistics package, with DN values for classes listed in turn for each image variable and a class number and case number was assigned to each line of data. The final input file took the following form:

Case Number	Class Number	Image 1	Image 2
001	01	240	62
002	01	180	71
...	..	...	..
...	..	...	..
...	..	...	..
041	02		
042	02		

A stepwise discriminant analysis function was calculated for each separate image or band and for various band and image combinations. The minimum Mahalanobis distance (D squared) between groups was maximized in every analysis . This analysis allowed the classification capabilities of single-wavelength or multi-wavelength data to be assessed. The analysis command was run on the full number of classes in each area. Selected classes were 'regrouped' or 'reclassified' into larger, general classes, allowing analyses of all eastern sebkha areas and of western mountain slopes classifed by slope and aspect. The results obtained from the discriminant analysis are discussed for eastern and western areas separately in Sections 7.3 and 7.4.

7.3. Discriminant Analysis Results for Eastern Study Area

Three analyses were undertaken on the eastern data set. For the first analysis all sixteen classes were used (see Table 7.1), while for the second and third analyses classes of similar type were combined into larger redefined categories. In each case, the discriminant analysis programme was applied separately to the Seasat and SIR-A data and then to the combined image data.

CLASS (number of cases)		SIR-A and SEASAT	SIR-A	SEASAT
SEA	(40)	17.5 (7)	10.0 (4)	8.0 (2)
SEBKHA: MONASTIR	(40)	77.5 (31)	15.0 (6)	75.0 (30)
SEBKHA: BEMBLA	(40)	5.0 (2)	17.5 (7)	5.0 (2)
SEBKHA: MOKNINE	(20)	20.0 (8)	0.0 (0)	27.5 (11)
SEBKHA: SIDI EL HANI	(40)	35.0 (14)	62.5 (25)	10.0 (4)
SEBKHA SHORE	(40)	65.0 (26)	47.5 (19)	0.0 (0)
SETTLEMENTS	(40)	100.0 (40)	100.0 (40)	67.5 (27)
ROADS E - W	(40)	32.5 (13)	2.5 (1)	17.5 (7)
ROADS N - S	(40)	7.5 (3)	7.5 (3)	25.0 (10)
INFLOW CHANNELS	(40)	57.5 (23)	12.5 (5)	30.0 (12)
LUNETTE DUNE	(40)	7.5 (3)	2.5 (1)	20.0 (8)
HILL COUNTRY	(40)	37.5 (15)	42.5 (17)	10.0 (4)
ARBORICULTURE (OLIVES) E	(40)	35.0 (14)	40.0 (16)	17.5 (7)
ARBORICULTURE (OLIVES) W	(40)	30.0 (12)	5.0 (2)	15.0 (6)
TREE AND BUSH PLOTS	(40)	12.5 (5)	2.5 (1)	5.0 (2)
CEREALS AND PASTURE	(40)	13.5 (5)	5.4 (2)	0.0 (0)
TOTAL		34.69	23.39	20.63

Table 7.2 Discriminant Analysis results for all sixteen classes in the eastern study area. Figures represent the percentage number of cases correctly classified in each class. The number of cases is shown in brackets.

The classification results from the analysis of all sixteen classes (Table 7.2) show a considerable variation in the classification accuracy between the single-image and dual-image analyses. The figures represent the percentage number of grouped cases that have been correctly classified, and vary from 0% to 100% according to class and image.

For Seasat, the sebkha at Monastir and the settlement cases have been particularly well classified, with accuracy figures at 75% and 67.5% respectively. Internal variations in DN within both of these classes is minimal, with the sebkha at Monastir having a low backscatter (DN) response and the settlements having high levels of backscatter. None of the other classes was well classified, with correct classifications being less than, or equal to, 30% for each class. Predicted group membership figures (not listed) indicate that there has been considerable confusion between the four sebkha classes and between channels, lunettes, roads and settlements. The two agricultural classes were particularly poorly classified. Only 5% of the tree and bush plots were correctly classified, the majority of cases having been assigned to road, settlement, upland and channel classes. None of the cereal plots was classified correctly, most cases having been assigned to the sea and sebkha classes. This confusion between classes is a function of the restricted range of DN values within the data set and the large variations in DN within most of the classes. The overall classsification accuracy of Seasat for the sixteen-class analysis is 20.63%, a figure which suggests that, by itself, Seasat data is not suitable for discriminating the classes given.

The classification of the sixteen classes by the SIR-A data shows little improvement over the Seasat data, with an overall accuracy result of only 23.39% (Table 7.2). However, in general, more of the classes have been well classified, with accuracies exceeding 40% recorded for five classes. All settlement cases have been correctly classified due to their high DN values. Sebkha Sidi el Hani, the sebkha shore, hill country and eastern olive-growing areas have been well discriminated also, with accuracy values of 62.5%, 47.5%, 42.5% and 40% respectively. As with the Seasat data, there has been significant confusion between sebkha classes, between sebkhas and cereal-growing areas and between roads, channels, olives and upland regions. Furthermore, there has been considerable confusion between sebkha cases and cases located on the shores of the sebkhas, arising from the similarity of their roughness condition and backscatter response.

When both Seasat and SIR-A data are used together the number of grouped cases correctly classified rises to 34.69% (Table 7.2). As with the SIR-A analysis, 100% of settlement cases have been classified correctly. Other results of note include the sebkha at Monastir (77.5%), sebkha shorelines (65%) and channels (57.5%). A further five classes have classification results greater than, or equal to, 30% (see Table 7.2). However, the combined analysis still shows considerable misclassification of, and confusion between, the individual sebkha classes, roads, the lunette and the various vegetation categories. The results indicate that even a combination of Seasat and SIR-A data is not adequate to discriminate between the sixteen chosen classes in the eastern study area.

STATISTIC		SIR-A and SEASAT	SIR-A	SEASAT
Eigen values	F1	9.680	7.470	2.330
	F2	0.508	—	—
% variance	F1	94.960	100.000	100.000
	F2	5.040	—	—
Canonical correlation	F1	0.950	0.939	0.836
	F2	0.580	—	—
Chi^2	F1	1736.000	1341.400	755.520
	F2	257.610	—	—
Degrees of freedom	F1	30.000	15.000	15.000
	F2	14.000	—	—
Significance	F1	0.000	0.000	0.000
	F2	0.000	—	—

IMAGE		SIR-A	SEASAT	SIR-A	SEASAT
Wilks λ		0.117	0.062	0.117	0.299
Standardized canonical discriminant function	F1	0.890	-0.440	1.000	1.000
	F2	0.480	0.870	—	—

Table 7.3 Statistical results of the discriminant analysis of all sixteen classes in the eastern study area.

The statistical results associated with the discriminant analyses (Table 7.3) enable the associations between the variables (Seasat and SIR-A) and the discriminant functions to be examined more closely. In the case of the combined analysis, the standardized canonical discriminant function coefficients show that, with a coefficient of 0.89, SIR-A is of relatively more importance in determining the first discriminant function, and that Seasat (with a coefficient of 0.87) is of more importance in the determination of the second discriminant function. The first function has a high association with the classes, as shown by the canonical correlation of 0.95, and accounts for 94.96% of the discrimination power (% variance). Canonical correlations, chi-squared statistics and eigenvalues from the two single-image analyses reflect the results described above, with SIR-A showing a slight improvement in discrimination over Seasat.

For the second discriminant analysis of the eastern study area the four sebkha classes (Monastir, Bembla, Moknine and Sidi el Hani) are combined, as are the two road classes (north-south and east-west) and the two olive classes (east and west). These classes are combined as they represent similar field and backscatter conditions. This similarity is the most likely explanation for the problems of discrimination, or statistical separation, experienced by the first analysis.

Redefinition of the classes does indeed help to raise the overall classification accuracy of the single-image and dual-image analysis (Table 7.4). The total number of correctly classified Seasat cases is now 37.97%, with high classifications for Sebkha (91.9%) and settlement (67.5%) cases. Roads, channels and olives all show classification

accuracies of around 35%. However, it is interesting to note that all of the other classes have been entirely incorrectly classified. Roads, channels, olives and sebkhas are the most common classes to which mis-classified cases have been assigned, with sebkhas causing the greatest confusion due to their considerable range of backscatter response.

In the case of SIR-A, class reorganisation has increased the overall classification accuracy to 39.09% (Table 7.4). Settlements, sebkhas and olives have been particularly well classified, with correct classifications of 100%, 62.5% and 50% respectively. There is still confusion between hill, lunette and vegetation classes.

The combination of Seasat and SIR-A data achieves an overall classification accuracy of 46.47% (Table 7.4). Five out of the eleven classes have more than 50% of their cases correctly classified (see Table 7.4), which marks a significant improvement over the results from the single-image analyses. However, there are still some major areas of mis-classification, hills, lunettes, roads and agriculture being the most important.

The standardized canonical discriminant function coefficients (Table 7.5), reveal that, once again, SIR-A is largely responsible for determining the first discriminant function. This function has a high degree of association with the classes used in the analysis and accounts for 96.11% of the discriminating power. For the single-image analysis, the improved classification of SIR-A is seen in the relatively high chi-squared statistic (1326.4) at a confidence level of 99%, and by the higher eigenvalue.

CLASS (number of cases)		SIR-A and SEASAT	SIR-A	SEASAT
SEA	(40)	25.0 (10)	10.0 (4)	0.0 (0)
SEBKHA	(160)	63.8 (102)	62.5 (100)	91.9 (147)
SEBKHA SHORE	(40)	67.5 (27)	47.5 (19)	0.0 (0)
SETTLEMENTS	(40)	100.0 (40)	100.0 (40)	67.5 (27)
ROADS	(80)	15.0 (12)	6.3 (5)	36.3 (29)
INFLOW CHANNELS	(40)	60.0 (24)	15.0 (6)	30.0 (12)
LUNETTE DUNE	(40)	7.5 (3)	10.0 (4)	0.0 (0)
HILL COUNTRY	(40)	40.0 (16)	42.5 (17)	0.0 (0)
ARBORICULTURE (OLIVES)	(80)	56.3 (45)	50.0 (40)	35.0 (28)
TREE PLOTS	(40)	17.5 (7)	22.5 (9)	0.0 (0)
CEREALS AND PASTURE	(40)	27.0 (10)	13.5 (5)	0.0 (0)
TOTAL		46.47	39.09	37.97

Table 7.4 Discriminant Analysis results for the eastern study area after re-grouping of Sebkha, road and arboriculture cases. Figures represent the percentage number of cases correctly classified in each class.

STATISTIC		SIR-A and SEASAT	SIR-A	SEASAT
Eigen values	F1	8.990	7.210	1.940
	F2	0.360	—	—
% variance	F1	96.110	100.000	100.000
	F2	3.890	—	—
Canonical correlation	F1	0.948	0.937	0.812
	F2	0.516	—	—
Chi^2	F1	1644.500	1326.400	680.600
	F2	195.370	—	—
Degrees of freedom	F1	20.000	10.000	10.000
	F2	9.000	—	—
Significance	F1	0.000	0.000	0.000
	F2	0.000	—	—

IMAGE		SIR-A	SEASAT	SIR-A	SEASAT
Wilks λ		0.121	0.073	0.121	0.339
Standardized canonical correlation function	F1	0.900	-0.420	1.000	1.000
	F2	0.450	0.890	—	—

Table 7.5 Statistical results from the Discriminant Analysis of the eastern study area after re-grouping of sebkha, road and arboriculture cases.

For the final discriminant analysis of the eastern study area, the hill country and lunette classes are combined to create one upland class. In addition, the small plots of tree or bush cultivation are combined with cases from the extensive areas of arboriculture to form a single tree-crop class. Thus, the original sixteen classes have been reduced to nine, more clearly defined, classes.

Redefinition of cases into fewer classes had led to more accurate classifications of single and dual-image data (Table 7.6). It is interesting to note that the Seasat data has now produced a slightly higher classification accuracy result (43.59%) than the SIR-A data (42.54%), suggesting that it is more suited to the discrimination of these classes, although this is not borne out by the canonical correlations or eigenvalues (see Table 7.7). However, four out of the nine classes have classification accuracies of 0% when Seasat is the sole variable. Three of these classes (sea, sebkha shore and roads) have relatively high DN values and have been confused with sebkha and tree-crop classes. The fourth (cereal crop), has generally low DN values, but has also been largely classified as sebkha. All these mis-classifications illustrate that for Seasat the classes have high within-class variance and low between-class variance, a fact that can be observed in the image itself (see Figure 3.1).

Results for the combined Seasat and SIR-A data show a significant improvement over the single-image results, the total number of correctly classified cases being 50.24%. All nine of the classes have over 25% of their cases correctly classified, with settlements, sebkha shores, sebkhas and channels having accuracy figures in excess of 60%. These results indicate that a combination of Seasat

CLASS (Number of cases)		SIR-A and SEASAT		SIR-A		SEASAT	
SEA	(40)	25.0	(10)	10.0	(4)	0.0	(0)
SEBKHA	(160)	63.8	(102)	62.5	(100)	91.3	(146)
SEBKHA SHORE	(40)	72.5	(29)	50.0	(20)	0.0	(0)
SETTLEMENTS	(40)	100.0	(40)	100.0	(40)	67.5	(27)
ROADS	(80)	30.0	(24)	11.3	(9)	0.0	(0)
INFLOW CHANNELS	(40)	60.0	(24)	10.0	(4)	20.0	(8)
HILL COUNTRY AND LUNETTE	(80)	42.5	(34)	48.8	(39)	10.0	(8)
ARBORICULTURE	(120)	39.2	(47)	41.7	(50)	75.0	(90)
CEREALS AND PASTURE	(40)	27.0	(10)	13.5	(5)	0.0	(0)
TOTAL		50.24		42.54		43.59	

Table 7.6 Discriminant Analysis results for eastern study area after re-grouping of sebkha road, arboriculture and upland cases. Figures represent the percentage number of cases correctly classified in each class.

STATISTIC		SIR-A and SEASAT	SIR-A	SEASAT
Eigen values	F1	6.91	5.69	1.74
	F2	0.31	—	—
% variance	F1	95.71	100.00	100.00
	F2	4.29	—	—
Canonical correlation	F1	0.93	0.92	0.79
	F2	0.48	—	—
Chi^2	F1	1474.50	1199.90	637.11
	F2	170.26	—	—
Degrees of freedom	F1	16.00	8.00	8.00
	F2	7.00	—	—
Significance	F1	0.00	0.00	0.00
	F2	0.00	—	—

IMAGE		SIR-A and SEASAT		SIR-A	SEASAT
Wilks λ		0.096	0.364	0.149	0.364
Standardized canonical correlation function	F1	0.880	-0.460	1.000	1.000
	F2	0.420	0.900	—	—

Table 7.7 Statistical results from the Discriminant Anlysis of the eastern study area after re-grouping of sebkha, road, arboriculture and upland cases.

and SIR-A data allows a useful separation of cases into nine broad categories in the eastern study area. SIR-A retains its place as having the greatest influence on the first discriminant function, as illustrated by the standardized canonical discriminant function coefficients in Table 7.7.

The results from the three discriminant analyses of the eastern image data highlight the problems involved in the classification of semi-arid environments using radar data alone. The response of a surface at microwave wavelengths is largely dependent upon the micro- and macro- scale relief of that surface, as illustrated by the statistical results discussed in Chapter 6. However, variations in backscatter response may also result from changes in vegetation cover within a given area; changes that serve to alter the local surface roughness profile. Thus, a variety of environmental conditions will be capable of producing similar responses in radar backscatter through similarities in their apparent roughness profiles.

The capacity of radar to respond to changes in surface geometry presents problems when discriminating between different features, or areas of vegetation, which may have similar roughness characteristics. This is exemplified in the results described above, which show considerable confusion between classes of similar backscatter response. Only when surface properties are such that they generate a unique and consistent response such as SIR-A settlement cases, will they be successfully discriminated from other areas. The larger the number of classes, the greater the problem of mis-classification, as backscatter profiles of different classes overlap.

In all of the analyses described above, SIR-A data has been shown to produce a 'better' classification, either in terms of the total percentage of cases correctly classified, or in terms of the least confusion between the classes. SIR-A also makes the biggest contribution to the discriminant power of the combined image analysis, irrespective of the number of classes used. The most likely explanation for this is the difference in depression angle used by the two systems. The shallow 43° depression angle of SIR-A is more responsive to variations in surface roughness (see Section 3.5.5 and Figure 3.9), thereby allowing greater separation of areas on the image. The lower spatial resolution of SIR-A will also help to improve discrimination by reducing within-class DN variations.

7.4. Discriminant Analysis Results for Western Study Area

Three analyses were performed on the SIR-A and Landsat TM data of the Western study area around Hadjeb el Ayoun. Twenty-two classes were used in the first analysis (see Table 7.8), twelve of which covered the full range of slope conditions (low, medium and high; north, south, east and west). The upland cases were combined according to slope and aspect for the second and third analyses. The classification accuracies of SIR-A and six of the TM bands were examined in each case. Several band combinations were also analysed to allow easier comparison with the results of the digital image analysis (Chapter 5).

When all twenty-two classes are used in the analysis, the total percentage of correctly classified SIR-A DN values is 22.90% (see Table 7.8), a similar figure to that achieved in the sixteen class analysis of the eastern study area. East-facing high slope angles have the

CLASS (Number of cases)		SIR-A and TM bands 1 - 7	SIR-A	TM bands 1 - 7	TM band 1	TM band 2	TM band 3	TM band 4	TM band 5	TM band 7	SIR-A and TM bands 4 and 7	SIR-A and TM bands 3 and 5	SIR-A and TM bands 5 and 7	SIR-A and TM bands 4 and 3
SEBKHA	(40)	62.5 (25)	12.5 (5)	62.5 (25)	2.5 (1)	0.0 (0)	5.0 (2)	0.0 (0)	42.5 (17)	45.0 (18)	52.5 (21)	60.0 (24)	45.0 (18)	65.0 (26)
SETTLEMENTS	(40)	70.0 (28)	30.0 (12)	25.0 (10)	32.5 (13)	15.0 (6)	10.0 (4)	0.0 (0)	2.5 (1)	0.0 (0)	45.0 (18)	47.5 (19)	45.0 (18)	45.0 (18)
ROADS	(80)	30.0 (24)	3.8 (3)	37.5 (30)	0.0 (0)	7.5 (6)	5.0 (4)	5.0 (4)	1.3 (1)	26.3 (21)	15.0 (12)	38.8 (31)	16.3 (13)	6.3 (5)
WADIS	(80)	35.0 (28)	0.0 (0)	51.3 (41)	7.5 (6)	18.8 (15)	22.5 (18)	2.5 (2)	0.0 (0)	33.8 (27)	7.5 (6)	38.8 (31)	1.3 (1)	21.3 (17)
GULLIES	(40)	90.0 (36)	62.5 (25)	55.0 (22)	10.0 (4)	62.5 (25)	60.0 (24)	27.5 (11)	65.0 (26)	42.5 (17)	85.0 (34)	80.0 (32)	90.0 (36)	80.0 (32)
CALCRETE	(40)	67.5 (27)	15.0 (6)	20.0 (8)	55.0 (22)	10.0 (4)	17.5 (7)	52.5 (21)	25.0 (10)	0.0 (0)	72.5 (29)	5.0 (2)	60.0 (24)	70.0 (28)
OLIVES AND SCRUB	(80)	47.5 (38)	23.8 (19)	36.3 (29)	5.0 (4)	5.0 (4)	2.5 (2)	5.0 (4)	2.5 (2)	28.8 (23)	25.0 (20)	57.5 (46)	8.8 (7)	33.8 (27)
CEREALS AND PASTURE	(40)	67.5 (27)	62.5 (25)	47.5 (19)	5.0 (2)	17.5 (7)	0.0 (0)	0.0 (0)	0.0 (0)	0.0 (0)	60.0 (24)	70.0 (28)	55.0 (22)	65.0 (26)
BARE GROUND	(40)	72.5 (29)	32.5 (13)	25.0 (10)	20.0 (8)	15.0 (6)	0.0 (0)	32.5 (13)	15.0 (6)	0.0 (0)	77.5 (31)	65.0 (26)	77.5 (31)	72.5 (29)
LOW SLOPES N	(40)	55.0 (22)	17.5 (7)	17.5 (7)	5.0 (2)	0.0 (0)	0.0 (0)	12.5 (5)	0.0 (0)	0.0 (0)	50.0 (20)	10.0 (4)	20.0 (8)	35.0 (14)
LOW SLOPES S	(40)	27.5 (11)	20.0 (8)	12.5 (5)	5.0 (2)	7.5 (3)	15.0 (6)	7.5 (3)	0.0 (0)	0.0 (0)	5.0 (2)	2.5 (1)	2.5 (1)	10.0 (4)
LOW SLOPES E	(40)	22.5 (9)	2.5 (1)	10.0 (4)	12.5 (5)	10.0 (4)	7.5 (3)	0.0 (0)	10.0 (4)	0.0 (0)	25.0 (10)	0.0 (0)	2.5 (1)	32.5 (13)
LOW SLOPES W	(40)	55.0 (22)	12.5 (5)	10.0 (4)	0.0 (0)	0.0 (0)	2.5 (1)	0.0 (0)	2.5 (1)	0.0 (0)	37.5 (15)	7.5 (3)	25.0 (10)	35.0 (14)
MEDIUM SLOPES N	(40)	27.5 (11)	7.5 (3)	7.5 (3)	0.0 (0)	5.0 (2)	10.0 (4)	0.0 (0)	0.0 (0)	0.0 (0)	30.0 (12)	17.5 (7)	10.0 (4)	10.0 (4)
MEDIUM SLOPES S	(40)	42.5 (17)	60.0 (24)	22.5 (9)	17.5 (7)	32.5 (13)	22.5 (9)	5.0 (2)	22.5 (90)	0.0 (0)	45.0 (18)	50.0 (20)	47.5 (19)	40.0 (16)
MEDIUM SLOPES E	(40)	37.5 (15)	17.5 (7)	15.0 (6)	5.0 (2)	5.0 (2)	2.5 (1)	12.5 (5)	10.0 (4)	0.0 (0)	37.5 (15)	32.5 (13)	40.0 (16)	35.0 (14)
MEDIUM SLOPES W	(40)	42.5 (17)	10.0 (4)	0.0 (0)	2.5 (1)	2.5 (1)	5.0 (2)	10.0 (4)	2.5 (1)	0.0 (0)	22.5 (9)	12.5 (5)	35.0 (14)	20.0 (8)
STEEP SLOPES N	(40)	45.0 (18)	32.5 (13)	5.0 (2)	0.0 (0)	0.0 (0)	0.0 (0)	5.0 (2)	2.5 (1)	0.0 (0)	27.5 (11)	30.0 (12)	45.0 (18)	42.5 (17)
STEEP SLOPES S	(40)	40.0 (16)	22.5 (9)	32.5 (13)	7.5 (3)	12.5 (5)	15.0 (6)	12.5 (5)	5.0 (2)	0.0 (0)	22.5 (9)	20.0 (8)	12.5 (5)	30.0 (12)
STEEP SLOPES E	(40)	65.0 (26)	85.0 (30)	62.5 (25)	62.5 (25)	60.0 (24)	60.0 (24)	55.0 (22)	0.0 (0)	2.5 (1)	52.5 (21)	60.0 (24)	52.5 (21)	60.0 (24)
STEEP SLOPES W	(40)	65.0 (26)	7.5 (3)	70.0 (28)	0.0 (0)	7.5 (3)	2.5 (1)	5.0 (2)	35.0 (14)	0.0 (0)	30.0 (12)	42.5 (17)	55.0 (22)	20.0 (80)
ALLUVIAL FANS	(40)	47.5 (19)	7.5 (3)	20.0 (8)	35.0 (14)	0.0 (0)	12.5 (5)	7.5 (3)	7.5 (3)	0.0 (0)	20.0 (8)	27.5 (11)	30.0 (12)	37.5 (15)
TOTAL		49.10	22.90	30.80	12.10	13.00	12.30	10.80	10.20	10.70	35.70	36.40	32.10	37.10

Table 7.8 Discriminant Analysis results for 22 classes in the western study area. Figures represent the percentage number of cases correctly classified in each class. The number of cases classified correctly is given in brackets.

highest classification accuracy (85%) and 60% of the cases on south-facing medium slopes are correctly classified. Gullies and areas of cereal production are also well classified, with accuracy levels of 62.5% for each class. There is, however, much confusion between the slope classes and between slope and other land use or land cover classes.

None of the single TM bands has been capable of assigning more than 13% of the total number of cases (1000) to the correct class, with many classes containing no correctly assigned cases. Gullies, calcrete areas and east-facing slopes over 55° have the highest percentage of correctly classified cases (see Table 7.8). As these classes are well discriminated by all TM bands, it must be concluded that they have unique spectral signatures across the range of visible and infrared wavelengths used. If all six TM bands are combined the total classification accuracy rises to 30.8%. Nine of the twenty two classes have more than 30% of their cases classified correctly, with wadis (51.3%), gullies (55%), sebkhas (62.5%), east-facing high slopes (70%) having the best classifications. Nevertheless, it is important to note that the six TM bands allow only a further 8% of western cases to be correctly classified, over and above the single band SIR-A image.

When two TM bands are selected and combined with the SIR-A data the total classification accuracy rises to well over 30% (see Table 7.8). Sebkhas, gullies, calcrete, cereal crops and bare ground are particularly well discriminated, as are east-facing slopes over 55°. These results suggest that a combination of information from visible, near infrared, infrared and microwave wavelengths is valuable in the discrimination of semi-arid

environments. The combined SIR-A and six-band TM analysis reinforces this point, as the total number of cases correctly classified rises to 49.10%. Settlements, low slopes north and west and high western slopes are added to the list of well-classified groups identified by the three-band analyses. There is, however, still considerable confusion between the majority of the slope/aspect categories.

The confusion between the various slope and aspect classes used in the analyses of the western area prompted two further studies to be made in which slopes were grouped first by angle and then by aspect. The object of this exercise was twofold; firstly to ease the problem of misclassification and secondly, to investigate whether system look direction and local incidence angle had any noticeable effect upon slope classification.

The reorganisation of slope cases into low, medium and high slope angles, irrespective of aspect, results in a considerable increase in the total number of correctly classified cases for all single-band and multi-band analyses (see Table 7.9). The SIR-A image alone produces an overall classification accuracy of 30%. settlements (65%), gullies (75%), cereal crops (62.5%) and medium slope angles (64.4%) are particularly well discriminated. However, the similarities in the backscatter response from a number of the other classes leads to considerable misclassification.

The combined six-band TM analysis has correctly classified 35.20% of all cases, with eleven out of thirteen classes having more than 20% of their cases classified accurately. When the SIR-A image is added as an additional variable, the total classification accuracy

CLASS (Number of cases)		SIR-A and TM bands 1 - 7	SIR-A	TM bands 1 - 7	TM band 1	TM band 2	TM band 3	TM band 4	TM band 5	TM band 7	SIR-A and TM bands 4 and 7	SIR-A and TM bands 3 and 5	SIR-A and TM bands 5 and 7	SIR-A and TM bands 4 and 3
SEBKHA	(40)	70.0 (28)	15.0 (6)	62.5 (25)	10.0 (4)	0.0 (0)	0.0 (0)	42.5 (17)	42.5 (17)	42.5 (17)	60.0 (24)	60.0 (24)	60.0 (24)	65.0 (26)
SETTLEMENTS	(40)	67.5 (27)	65.0 (26)	22.5 (9)	32.5 (13)	15.0 (6)	0.0 (0)	0.0 (0)	25.0 (10)	0.0 (0)	65.0 (26)	52.5 (21)	55.0 (20)	50.0 (20)
ROADS	(80)	33.8 (27)	5.0 (5)	32.5 (26)	6.3 (5)	13.8 (11)	0.0 (0)	5.0 (4)	1.3 (1)	0.0 (0)	25.0 (20)	20.0 (16)	12.5 (10)	22.5 (18)
WADIS	(80)	40.0 (32)	0.0 (0)	47.5 (38)	7.5 (6)	18.8 (15)	62.5 (50)	2.5 (2)	0.0 (0)	32.5 (26)	15.0 (12)	15.0 (12)	1.3 (1)	36.3 (29)
GULLIES	(40)	90.0 (36)	75.0 (30)	50.0 (20)	10.0 (4)	62.5 (25)	0.0 (0)	27.5 (11)	65.0 (26)	35.0 (14)	92.5 (37)	85.0 (34)	87.5 (35)	80.0 (32)
CALCRETE	(40)	62.5 (25)	15.0 (6)	20.0 (8)	55.0 (22)	10.0 (4)	0.0 (0)	52.5 (21)	40.0 (16)	0.0 (0)	72.5 (29)	62.5 (25)	60.0 (24)	62.5 (25)
OLIVES AND SCRUB	(80)	51.3 (41)	26.3 (21)	23.8 (19)	11.3 (9)	5.0 (4)	0.0 (0)	7.5 (6)	5.0 (4)	0.0 (0)	26.3 (21)	61.3 (49)	25.0 (20)	32.5 (26)
CEREALS AND PASTURE	(40)	65.0 (26)	62.5 (25)	47.5 (19)	0.0 (0)	0.0 (0)	0.0 (0)	0.0 (0)	0.0 (0)	0.0 (0)	57.5 (23)	75.0 (30)	57.5 (23)	62.5 (25)
BARE GROUND	(40)	75.0 (30)	32.5 (13)	5.0 (2)	20.0 (8)	15.0 (6)	0.0 (0)	32.5 (13)	25.0 (10)	0.0 (0)	77.5 (31)	70.0 (28)	77.5 (31)	65.0 (26)
LOW SLOPES	(160)	56.9 (91)	32.5 (52)	36.9 (59)	8.8 (14)	15.0 (24)	38.8 (62)	15.6 (25)	9.4 (15)	40.0 (64)	43.8 (70)	21.3 (34)	25.6 (41)	49.4 (79)
MEDIUM SLOPES	(160)	40.6 (65)	64.4(103)	22.5 (36)	3.8 (6)	3.8 (6)	9.4 (15)	9.4 (15)	15.6 (25)	43.1 (69)	30.6 (49)	45.0 (72)	58.8 (94)	28.1 (45)
STEEP SLOPES	(160)	50.6 (81)	6.9 (11)	56.9 (91)	58.1 (93)	59.4 (95)	58.1 (93)	10.0 (16)	1.3 (2)	5.6 (9)	40.6 (65)	28.1 (45)	6.9 (11)	41.3 (66)
ALLUVIAL FANS	(40)	70.0 (28)	7.5 (3)	0.0 (0)	35.0 (14)	40.0 (16)	0.0 (0)	7.5 (3)	25.0 (10)	0.0 (0)	25.0 (10)	72.5 (29)	55.0 (22)	40.0 (16)
TOTAL		53.70	30.00	35.20	19.80	21.20	22.00	13.30	13.60	19.90	41.70	41.90	35.80	43.30

Table 7.9 Discriminant analysis results for western study area after re-grouping of slope cases by slope angle. Three slope classes were used (low = <30 degrees; medium = 30-55 degrees; high - >55 degrees, irrespective of aspect. Figures represent the percentage number of cases correctly classified in each class.

rises to 53.7% (see Table 7.9). All classes have classification accuracies in excess of 30%, with only three classes having less than 50% of their cases assigned to the correct class. Gullies are particularly well discriminated, with 90% of cases accurately classified.

Most of the land use and land cover classes are well discriminated by SIR-A and two Landsat bands. Once again, gullies show the highest classifications, accuracies being in excess of 80% in each case. In comparison, all three slope classes are poorly classified, with most confusion occurring between these classes.

Classification of upland areas by aspect proved to be less successful than classification by slope angle in all analyses in which SIR-A was used (Table 7.10). Where SIR-A alone is used, the total classification accuracy falls to 19.6%, with only cereal-growing regions and eastern-facing slopes having more than 60% of cases correctly classified (see Table 7.10). The combined SIR-A/TM analysis yields an overall accuracy figure of 44.1%, almost ten percentage points lower than the slope-based study. It is interesting to compare the slope and aspect analysis on a class-by-class basis (see Table 7.9 and 7.10), as although classifications for lowland and land-cover classes are very similar, upland classifications by aspect are considerably poorer than those by slope. Total percentages of correctly classified cases for individual and combined TM bands are little changed by the division of upland cases by aspect.

The dependence of SIR-A backscatter from mountain regions upon radar look direction and depression angle, and upon slope and aspect, was discussed in Chapter 6. The results from the upland areas in all three analyses of

CLASS (Number of cases)		SIR-A and TM bands 1 - 7	SIR-A	TM bands 1 - 7	TM band 1	TM band 2	TM band 3	TM band 4	TM band 5	TM band 7	SIR-A and TM bands 4 and 7	SIR-A and TM bands 3 and 5	SIR-A and TM bands 5 and 7	SIR-A and TM bands 4 and 3
SEBKHA	(40)	70.0 (28)	17.5 (7)	62.5 (25)	2.5 (1)	5.0 (2)	15.0 (6)	42.5 (17)	42.5 (17)	42.5 (17)	62.5 (25)	60.0 (24)	52.5 (21)	65.0 (26)
SETTLEMENTS	(40)	60.0 (24)	40.0 (16)	22.5 (9)	32.5 (13)	15.0 (6)	10.0 (4)	0.0 (0)	17.5 (7)	0.0 (0)	50.0 (20)	57.5 (23)	0.0 (0)	37.5 (15)
ROADS	(80)	31.3 (25)	5.0 (4)	35.0 (28)	6.3 (5)	7.5 (6)	8.8 (7)	5.0 (4)	1.3 (1)	0.0 (0)	18.8 (15)	22.5 (18)	12.5 (10)	13.8 (11)
WADIS	(80)	41.3 (33)	7.5 (6)	48.8 (39)	7.5 (6)	18.8 (15)	22.5 (18)	2.5 (2)	0.0 (0)	30.0 (24)	10.0 (8)	21.3 (17)	23.8 (19)	42.5 (34)
GULLIES	(40)	82.5 (33)	45.0 (18)	52.5 (21)	10.0 (4)	62.5 (25)	60.0 (24)	27.5 (11)	65.0 (26)	37.5 (15)	92.5 (37)	87.5 (35)	72.5 (29)	80.0 (32)
CALCRETE	(40)	57.5 (23)	15.0 (6)	20.0 (8)	55.0 (22)	10.0 (4)	17.5 (7)	52.5 (21)	40.0 (16)	0.0 (0)	75.0 (30)	62.5 (25)	5.0 (2)	70.0 (28)
OLIVES AND SCRUB	(80)	36.3 (29)	12.5 (10)	22.5 (18)	5.0 (4)	5.0 (4)	0.0 (0)	6.3 (5)	5.0 (4)	0.0 (0)	21.3 (17)	46.3 (37)	1.3 (1)	31.3 (25)
CEREALS AND PASTURE	(40)	65.0 (26)	62.5 (25)	47.5 (19)	67.5 (27)	0.0 (0)	0.0 (0)	0.0 (0)	2.5 (1)	0.0 (0)	60.0 (24)	77.5 (31)	52.5 (21)	65.0 (26)
BARE GROUND	(40)	72.5 (29)	32.5 (13)	12.5 (5)	20.0 (8)	15.0 (6)	27.5 (11)	32.5 (13)	25.0 (10)	0.0 (0)	70.0 (28)	67.5 (27)	37.5 (15)	65.0 (26)
SLOPES N	(120)	35.8 (43)	3.3 (4)	36.7 (44)	10.0 (12)	9.2 (11)	6.7 (8)	13.3 (16)	1.7 (2)	33.3 (40)	17.5 (21)	9.2 (11)	25.8 (31)	10.0 (12)
SLOPES S	(120)	30.0 (36)	0.0 (0)	30.8 (37)	5.0 (6)	5.8 (7)	3.3 (4)	9.2 (11)	4.2 (5)	8.3 (10)	16.7 (20)	9.2 (11)	25.8 (31)	2.5 (3)
SLOPES E	(120)	44.2 (53)	66.7 (80)	47.5 (57)	0.0 (0)	52.5 (63)	57.5 (69)	10.8 (13)	16.7 (20)	40.8 (49)	48.3 (58)	59.2 (71)	59.2 (71)	55.0 (66)
SLOPES W	(120)	31.7 (38)	3.3 (4)	39.2 (47)	8.3 (10)	5.0 (6)	9.2 (11)	17.5 (21)	4.2 (5)	14.2 (17)	3.3 (4)	10.8 (13)	45.8 (55)	11.7 (14)
ALLUVIAL FANS	(40)	52.5 (21)	7.5 (3)	0.0 (0)	35.0 (14)	40.0 (16)	30.0 (12)	7.5 (3)	25.0 (10)	0.0 (0)	20.0 (8)	75.0 (30)	0.0 (0)	55.0 (22)
TOTAL		44.10	19.60	35.70	13.20	17.10	18.10	13.70	12.40	17.20	31.50	37.30	30.60	34.00

Table 7.10 Discriminant Analysis results for western study area after re-grouping of slope cases by aspect. Four aspect classes are used (north, south, east, west), irrespective of slope. Figures represent the percentage number of cases correctly classified in each class.

SIR-A data must be interpreted in the light of these parameters for them to be fully understood.

The high classification accuracies of east facing slopes over 55° (Table 7.8) and all east-facing slopes in the aspect study (Table 7.10) are explained by the look direction of SIR-A which highlights slopes facing east-south-east. East-facing steep slopes have the highest response in the first analysis as they tend to act as corner reflectors, sending most of the incoming radar signal directly back to the sensor (Plate 7.1). Local incidence angles on eastern-facing slopes of 30° to 55° also generate high levels of radar backscatter but the slopes are not well classified as they tend to be confused with the steeper eastern-facing slopes. High and medium southerly slope angles also have relatively high classification accuracies due to local incidence angle considerations (see Table 7.8 and Plate 7.2).

All other slopes in the aspect study have low classification accuracies (Table 7.10). The failure of the analysis to classify these slopes correctly stems from the large range in backscatter from the foothills to the summits which does not facilitate their classification as one slope unit. The relatively high classification accuracy of north-facing steep slopes (Table 7.8) is only due to their being in radar shadow, which gives them a unique backscatter response.

The fact that northerly slopes over 55° are in radar shadow accounts for the low classification accuracy of high slopes in the slope angle analysis (Table 7.9). The wide range of backscatter response in this category makes it impossible for all steep slopes to be classified in one unit. Slopes with angles between 30° and 55° have the

most even radar response over the four aspects measured and therefore have the largest number of correctly classified cases (see Table 7.9). Similarly, slopes of low angle have fairly constant backscatter levels and produce a classification accuracy of 32.5%.

Radar system and ground parameters impose serious limitations upon the accurate discrimination of mountain slopes from SIR-A data in the western study area. Division of slopes by angle produces the best results but there is still considerable confusion between slope cases and between slope and settlement, calcrete, gully and slope cases. This confusion results from the sensitivity of radar to variations in slope at a macro- and micro-level which may well produce a like-response from very different areas (see previous section).

Nevertheless, for surfaces or features that have a unique and constant backscatter response SIR-A data demonstrates its greatest powers of discrimination. In all three analyses, a large number of cases in gully areas and regions of cereal cultivation have been classified correctly (see Tables 7.8 to 7.10), due to their respective high and low DN values. The potential application of SIR-A to soil erosion studies in the dissected areas of the Hadjel valley is explored more fully in Chapter 9.

The combination of SIR-A with visible and infrared data recorded by the Landsat TM Satellite leads to a considerable improvement in surface discrimination. All three-band analyses allow a higher percentage of cases to be correctly classified than when SIR-A alone is used. This supports the results obtained by digital image analysis (Chapter 5). When all TM bands are combined with

SIR-A data the overall classification accuracy rises still further, illustrating the value of multi-wavelength data in discriminant analysis.

All the statistical results from the discriminant analysis of the western study area reveal the importance of SIR-A in determining the first discriminant function in each analysis (Tables 7.11 to 7.13). The canonical correlations for the SIR-A image analyses exceed those obtained by the corresponding single-band TM analyses. In each of the combined SIR-A-TM studies, SIR-A accounts for a higher percentage of the discriminant power (as shown by the % variance). All these results highlight the relative value of SIR-A in the discrimination of the surfaces and cover types around Hadjeb el Ayoun and support the conclusions made after the digital and statistical studies described in Chapters 5 and 6.

7.5 Summary.

Discriminant analysis of the eastern and western study areas in Tunisia highlighted the advantages and limitations of using Seasat and SIR-A data for environmental classification. When surface conditions (i.e. slope and roughness) and system parameters work together to produce a unique and consistent radar response, the feature or area in which those conditions occur will be easily discriminated on the image. Examples of this can be seen in the eastern areas, in the form of gullies, cereals and slopes where local incidence angles are approximately equal to the complement of the depression angle (see Chapter 6, Section 6.4). Where local conditions produce a response similar to that produced by other areas, the feature in question will not be discriminated. Several examples of this condition can

be seen in each test area. Class size seems also to be an important factor influencing the accuracy of the classification procedure, with classes covering little of the total image area (e.g. roads) being less easily discriminated.

Surface roughness and local incidence angle have been identified as the two most important parameters influencing the radar return from the two study areas, and hence the capacity of the two systems to discriminate surfaces within them. Radar depression angle and look direction are both closely related to these parameters and are also important. The sensitivity of SIR-A to variations in surface roughness makes this system more appropriate than Seasat for the separation of semi-arid surfaces in Tunisia. However, when two or more systems or bands are combined the accuracy of statistical class separations increases significantly, with the best results being achieved by a combination of data across the full range of wavelength from visible to microwave.

Chapter 8. Conclusions.

8.1 General Introduction.

The overlap of Seasat and SIR-A satellite passes in central Tunisia provided an excellent opportunity to consider the response of semi-arid surfaces at two radar depression angles and opposing look directions. Previous publications by Rebillard and others have examined Seasat/SIR-A co-registrations over various parts of northern Africa, including Tunisia (Rebillard, 1982; Rebillard and Nguyen, 1982; Rebillard and Evans, 1983; Rebillard et al., 1984). Interpretations were made using digital image processing techniques, and the authors came to various important conclusions about the dependency of feature expression upon look angle. However, field information was not gathered for any of these studies and the results are general. The present research project has allowed a more detailed investigation of Seasat and SIR-A coverage of Tunisia by a combination of field, laboratory and computer analysis. Furthermore, the availability of Landsat Thematic Mapper data for the western study area around Hadjeb et Ayoun enabled the relative merits of data recorded at visible, infrared and microwave wavelengths to be evaluated.

The research objectives outlined in Chapter 1 were addressed through visual and digital image analysis and statistical analysis of data collected in the field and laboratory. Recognising the importance of the various radar system and ground parameters outlined in Chapter 3, the research sought to assess the influence of each upon radar image appearance in semi-arid Tunisia. Future multi-parameter radar systems promise to provide a wealth of information to radar and application scientists alike. Until then, comparative studies of SAR image products of a

variety of environments is the only means of furthering the field of spaceborne radar remote sensing.

The results from this research have to be assessed in the light of various factors. Firstly, there was a significant time-lag between the collection of field and image data; eight years in the case of Seasat (see Table 6.1). This is not likely to have had an appreciable effect upon measurements made in areas such as mountain slopes or established olive plantations where land form and land cover will have remained constant in the short term. However, it certainly had to be borne in mind when assessing the influence of soil characteristics, surface roughness and seasonal vegetation cover.

Secondly, the time available for field work was limited severely by factors beyond the control of the research project. This limited the amount of detailed information that could be collected in the field, necessitating the examination of selected test sites. Furthermore, neither radar system was calibrated, either internally of externally, making absolute quantitative comparisons impossible.

Given these factors, the results presented in this thesis must be considered as general indications about the capabilities of microwave remote sensing in semi-arid areas. Satellite radar is a new tool for environmental scientists. The field is in its infancy and much work has to be done before it is well established. Only by trying to test its capabilities in a scientific manner can advancement be made. Thus, while the scientific framework for this research project cannot be regarded as perfect, any contribution it may make to the understanding of radar-ground interaction, however small, may be regarded as useful.

The main conclusions drawn from this research project can be divided into a number of key areas defined by the research objectives given in Chapter 1.

8.2 Identification of the Dominant Ground Parameters.

Combined fieldwork and image analysis identified two ground parameters as having the greatest influence upon radar backscatter, and hence image appearance, in semi-arid Tunisia. These two parameters are surface roughness and surface relief. In low-lying areas, surface roughness is the dominant parameter influencing radar return from a surface. This is exemplified in the analysis of Sebkha Sidi el Hani in the eastern study area, where roughness information dominates the return from both Seasat and SIR-A. Pearson Product Moment Correlation Coefficients and regression values derived from statistical analysis of the sebkha data and discussed in Chapter 6 (Section 6.7.2) suggest that variations in surface roughness account for at least 40% of the variation in Seasat or SIR-A DN levels. Comparison of SIR-A coverage of the Tunisian sebkhas with similar imagery of the coastal sebkhas of Oman reinforces this conclusion. The uniformly-low roughness profiles of the Tunisian sebkhas is the main reason for the classification accuracies of 62.5% and 91.9% achieved for SIR-A and Seasat respectively by the discriminant analysis procedure (Chapter 7 : Section 7.3).

The importance of rouhgness for image appearance can also be seen in the western study area, where increased surface roughness on alluvial fans and areas of calcrete gives these areas a characteristic medium-to-high backscatter response on the SIR-A image (Chapter 5 : Section 5.2.3). The smooth areas of exposed sand on the interfluves in the southern part of the Hadjel valley have

a correspondingly low backscatter response on the SIR-A image, as does the large expanse of cereal cultivation and pasture land in the Cherahil valley.

In upland areas, such as the mountains of central Tunisia, surface relief is the dominant parameter influencing radar return. Slope angle and aspect angle are both important, and are closely related to the system parameters of depression angle and look direction. Because of the interaction between these four parameters, it was necessary to define the effective local incidence angle for each slope, thereby allowing the influence of slope upon radar return to be determined more accurately (Chapter 6 : Section 6.3.1). For mountain slopes oriented towards the incoming radar signal, the effective angle of slope with respect to radar depression angle determines the amount of radar backscatter from that feature (see Sections 5.2.3, 6.8.3 and 7.4). The appearance of slopes oriented away from the incoming radar signal will be confused by radar shadow, the extent of the problem being determined by the effective local incidence angle. Slopes perpendicular to SIR-A look direction are less well defined on the resultant image, highlighting still further the importance of aspect angle upon radar response from mountain regions.

The geometry of surface features such as gullies and settlements largely determines the radar response from these features. Feature size and spacing, together with the angle of the slopes delimiting the feature, are all important (see Sections 5.2.1, 5.2.2 and 6.8.2). Feature geometry is closely related to surface roughness and relief and serves to highlight the importance of 'form' upon radar backscatter from semi-arid areas.

The time-lag and calibration constraints imposed upon this research project prevented a detailed assessment of the influence of the complex dielectric constant upon radar image appearance. It is suggested that, when surface roughness and surface relief are minimal, factors such as soil moisture, organic matter, texture and salinity may exert some influence upon radar backscatter levels (see Chapter 6). However, field investigation in sebkha regions suggests that these ground characteristics are of lesser importance than the surface roughness profile.

The sensitivity of radar to variataions in surface roughness and surface relief make it an ideal tool in applied studies of semi-arid areas. Three such studies will be described in Chapter 9, each revealing the tremendous value of radar in the field of environmental management. The quantitative assessment of surface roughness adopted in this research project has provided an adequate measure for all the purposes described in this thesis. Some applied studies may require a more detailed evaluation of surface roughness, especially if calibrated radar imagery is available. Therefore, it is recommended that further research be undertaken to devise a rapid, effective and less-cumbersome means of determining roughness than the practical methods outlined in Chapter 6 (Section 6.2.1).

8.3 Identification of the Dominant System Parameters.

As described in the previous section, the various ground characteristics influencing radar backscatter from a surface are closely related to the system parameters of the radar sensor (see Chapter 3). Therefore, recognition of the dominant system parameters must be made in the light of comments made in Section 8.2.

Radar depression angle also determines the amount of signal penetration between features, such as gully walls or tall buildings. Statistical analysis of wadis and gullies in the Hadjel Valley (Section 6.8.2) revealed that SIR-A depression angle, together with the slope of the gully walls, largely determined the amount of backscatter from a feature, and whether dominant scattering came from the walls or floor of the channel. Similar characteristics were observed in the settlements of the coastal plain. The steeper depression angle of Seasat allowed more signal penetration of the spaces between tall buildings, while the 43° angle of SIR-A allowed less penetration and led to an increase in radar backscatter through the actions of corner reflectors (see Figure 5.1).

It is considered surprising that the statistical analysis of vegetated regions revealed no conclusive evidence for a link between radar depression angle, tree spacing and image appearance (Section 6.7.3). It is possible that the sample size from these areas was not sufficient for statistical results to be valid. It is recommended that future research programs should extend this work in other comparable areas.

A link between vegetation row direction and radar look direction was identified from the statistical analysis of field and image data. For both Seasat and SIR-A, the effective orientation of the crop with respect to look direction is the dominant parameter influencing radar backscatter from vegetated regions (Section 6.7.3). The findings contradict research by Nithack (1982), who found that rows of trees could be discriminated on vertically polarised radar imagery, irrespective of look direction. It is recommended that further research be undertaken to asses the effect of signal polarisation and wavelength upon linear feature detection.

Radar look direction is clearly important in mountainous regions through its influence on local incidence angle. The south-facing slopes of Djebel Henndi are discriminated most easily by SIR-A which has a look direction from south-south-east. This look direction produces less definition on the eastern and western flanks of Djebels Nara and Cherahil (Section 7.4).

The importance of radar look direction upon feature expression is illustrated most clearly by the road networks and coastal-bar features in the eastern study area. The raised banks within the ancient sebkha at Monastir are preferentially enhanced by the opposing look directions of the two systems (see Plates 5.19 and 5.20). Similarly, wadis and gullies perpendicular to radar look direction are discriminated most easily by the two systems. However, where local surface conditions lead to an unusually high level of radar backscatter, linear features normal to radar look direction can be detected (Section 5.2.3). This is illustrated by the radial road networks around the town of Hadjeb el Ayoun (Plate 5.25).

The detectability of linear features on radar imagery raises the question of image resolution. Many of these features are smaller than the resolution cell of the radar, but produce such a characteristic backscatter response that they are able to be 'detected'. In general, however, the effective radar resolution exerts the greatest influence on the size of features that may be detected on an image. This is the case in the agricultural regions east of Sousse, where the finer Seasat resolution enables individual fields to be distinguished (Section 5.2.1; Plate 5.17); these fields are virtually indistinct on the equivalent SIR-A image (Plate 5.18). It is recommended that future satellite SAR systems adopt as small a resolution cell as is feasible if

the full potential of the imagery they produce is to be realized.

It is not easy to come to a conclusion as to which of the two radar products used for this research is most appropriate for the identification and analysis of semi-arid surfaces and cover types. The various system parameters of Seasat and SIR-A interact with the ground surface in different ways, revealing different information on the final image product. The shallow depression angle of SIR-A tends to reveal more roughness information, while, the 70° depression angle of Seasat makes it more sensitive to variations in relief from. Whilst producing areas of radar shadow in mountainous regions, the SIR-A incidence angle does reduce the problems of excessive layover.

The choice of the most appropriate depression angle depends largely upon the area in which it is to be used, together with the application for which it is needed. When roughness information is required, a shallower depression angle is appropriate. Steeper angles should be used in geomorphological and geological studies in areas of moderate relief. The multi-incidence angle capability of SIR-C will provide an excellent solution to this problem, by enabling imagery to be recorded for the same area at a variety of depression angles. Studies using SIR-C imagery will allow a more accurate assessment of the effect of depression angle upon the information content of radar imagery.

8.4. Limitations of Radar Remote Sensing.

Although it is advantageous in many applications, the sensitivity of radar to variations in surface roughness and feature geometry can often lead to serious

discrimination problems. When different surfaces or features have similar roughness profiles they will not be separated on the resulting image (Chapter 7: Section 7.3). Thus, areas of contrasting lithology, or land use, may be entirely mis-classified, as illustrated by the results discussed in Chapter 7 (see Chapter 3: Section 3.5.8).

Excellent classification accuracies may be achieved when surface conditions produce a unique and consistent response throughout an area (Section 7.5). Automatic classification procedures, therefore, should be applied to radar imagery with extreme caution. The results derived from them must be analysed with the overriding influence of roughness in mind and conclusions drawn accordingly. It should be born in mind, however, that all single-band remote sensing images, whatever their wavelength, will have limited discrimatory power

A further limitation of radar remote sensing is its inability to reveal 'spectral' information about surfaces or vegetation types. Variations in lithology, for example, will only be detected if they give rise to unique roughness conditions or landforms. Vegetation communities are discriminated only on the basis of surface roughness. Cereals and pasture have radar-smooth surfaces and produce low levels of radar backscatter. Tree crops generate a higher backscatter response. However, variations of type within these communities cannot be identified from L-band satellite data.

Recent results from studies of airborne multi-wavelength and multi-polarization SAR are most encouraging (see Sections 3.5.3 and 3.5.4). Work by Stewart et al. (1980) and Blom et al. (1987), amongst others, suggest that such multi-parameter systems can be

used to discriminate between lithological units, surface types and vegetation communities. Much work needs to be done in this area before the full information content of radar images can be understood, but we are certainly entering an exciting era of advancement in radar remote sensing.

8.5 Radar and Landsat as Complementary Tools

The main conclusion to be drawn from this research concerns the close link between radar and surface relief at the micro- and macro-scale. This sensitivity to surface form makes radar a valuabale tool in geomorphological and structural geological studies. In the discrimination of lithology soil or vegetation, however, fixed-parameter radar systems have serious limitations. It is in these circumstances that supplementary information recorded at visible and infrared wavelengths is most useful.

In the study area around Hadjeb el Ayoun, Landsat Thematic Mapper and SIR-A provided complementary information about the environment. The value of the combined Landsat and radar study was apparent from the results of the digital image analysis (Section 5.3) and from the discriminant analysis (Section 7.5). In both cases, Landsat TM increased the discriminatory power by increasing the range of the electromagnetic spectrum over which information was recorded (Section 3.6). These results support the findings of previous research scientists (Blom et al., 1981; Ford et al., 1983; Hartl et al., 1983; Paris, 1984; NOAA, 1984; Yao and Gilbert, 1984; Merrifield and Yang, 1985; Green, 1986).

The highest levels of discrimination were achieved when information from all of the seven TM bands was

combined with the SIR-A data. However, in digital image analyses where only three channels could be used the choice of the two most appropriate TM bands was made in the light of the application for which the final image product was to be used. Various band combinations were found to be useful in the western study area (Chapter 5). A combination of TM band 7, TM band 4 and SIR-A was found to produce a useful image product for general landscape evaluation purposes.

8.6 Useful Methods in Radar Image Analysis

Several methods were adopted for the analysis of radar imagery in this research project. Visual interpretation of the images yielded a considerable amount of information about the morphology and roughness condition of each study area. The differences between the discrimination capabilities of Seasat and SIR-A were made apparent during visual interpretation, with digital image analysis revealing little information that was not contained in the original images. Nevertheless, digital image processing did provide a useful means of summarizing the information contained within the combined images (Chapter 5).

Principal components Analysis of the combined Landsat/SIR-A data enabled useful three-band composite images to be produced from the dominant components of the summarized image data (Section 5.5). Principal components 1, 2 and 3 from the TM7, TM4, SIR-A combination generated the most useful summary product.

Unsupervised classification of combined Landsat/SIR-A data and combined Seasat/SIR-A data yielded useful image products. The former produced a first-order separation of surfaces and land forms in the western study area, while

the latter generated a classification of surfaces on the basis of their roughness condition. While the products generated by Cluster analysis do have their use in radar image analysis, the comments made in Section 8.4 about the problems of discriminating surfaces from variations in surface roughness have some relevance at this point.

The two most valuable radar image processing techniques in this research project were the application of spatial filters, and the application of the HSI transform. The former served to highlight the relative roughness, relief and texture content of the Seasat and SIR-A images. The latter made variations in roughness and relief in image combinations and filtered products more apparent by allowing the full spread of the data to be colour-encoded (Section 5.7). The results support those obtained from previous analyses of radar imagery (Haydn et al., 1982; Daily, 1983).

8.7 Conclusions and Recommendations for the Future

Given the constraints within which this research was undertaken; namely time-lag and seasonality problems, lack of radar calibration and limited fieldwork time, a number of important conclusions were made about the suitability of radar for environental investigation in semi-arid Tunisia. Surface roughness and slope angle were identified as the dominant ground parameters influencing Seasat and SIR-A backscatter. The amount of roughness and slope information contained in an image was found to depend upon the depression angle of the radar system, with a shallower angle revealing more roughness information. Depression angle and look direction were both identified as key factors influencing radar return from mountain regions.

A combination of statistical and image analysis was found to be useful in the evaluation of radar images. The lack of digital SIR-A data proved not to be an obstruction, as digitization and scene-fade correction were undertaken with relative ease. Once this had been accomplished, both visual interpretation and digital image processing revealed valuable information about the environment of central Tunisia. Digital radar data and information recorded at visible and infra-red wavelengths were found to provide complementary information in semi-arid mountain environments.

All the results discussed in this thesis are important steps towards a fuller understanding of the information content of radar images. Radar remote sensing is a growing field and has recieved considerable interest in recent years. Many of the limitations imposed upon this research will be removed in future satellite radar programmes which will provide:

(1) Multi-depression angle, multi-wavelength, and multi-polarization capabilities.

(2) Internal and external calibration.

(3) Digital image products.

(4) Well-organised programs for the simultaneous collection of data from satellite, airborne and ground sources.

It is recommended that the conclusions drawn from this research be extended to other semi-arid areas (and, indeed, other environments) within the framework of these advances.

The sensitivity of radar to variations in surface profile and relief make it a valuable tool in applied studies. This is of particular importance in arid and semi-arid areas, where vegetation cover is limited. The potential of radar in applied environmental research is considered in Chapter 9, illustrated by case studies from Tunisia.

Chapter 9. Prospective Applications of Satellite Radar Imagery to Environmental Management in Semi-arid Areas

9.1 Introduction.

Perhaps the most important conclusion to have come from this research project concerns the sensitivity of satellite radar imagery to variations in surface form at the macro-and micro-scale. The results from Chapters 5, 6 and 7 all highlight the link between radar image tone and surface roughness or geometry, and thus the ability of radar to distinguish between areas with distinct roughness characteristics. This chapter investigates the extent to which radar's sensitivity to surface form makes it an appropriate tool for morphological and geomorphological analysis in semi-arid environments.

Radar offers considerable potential in hydrological studies through its capacity to discriminate between areas of erosion or deposition on the basis of surface roughness. Areas of active deposition within wadis or sebkhas, for example, where clay or sand-sized particles are being deposited, will generate a dark response on a radar image. Conversely, areas where active erosion is taking place, will tend to generate a brighter response on a radar image through backscatter from freshly-exposed rough surfaces and different erosion levels. This is especially important in arid and semi-arid areas where vegetation cover is limited. Thus, where radar is able to penetrate between channel walls, such as in the case of the larger wadis in the western study area, it can be used to distinguish between areas of erosion and deposition on the channel floor on the basis of surface roughness characteristics. These capabilities offer the hydrologist

a means of assessing the general flow characteristics or degree of incision of a particular channel without the need for field observation. This is particularly important for reconnaissance studies of inaccessible areas.

The sensitivity of radar to changes in surface relief make it an ideal tool for geomorphologiacl studies, where changes in surface form at both the macro- and micro-level are important. It offers a means of distinguishing features such as alluvial fans, duricrusts or areas of instability, as well as breaks of slope and other morphological characteristics.

The possibilities offered by radar in the field of environmental management and other applied studies are numerous. A full invesigation of the potential of radar in such studies is beyond the bounds of this thesis. However, three case studies brought to light by the research are considerd in the following sections. Particular attention is paid to a case study in the Hadjel valley, in which remote sensing data were used to map and monitor the soil loss from the area (Section 9.4).

9.2. Applications of Radar in Saline Environments.

A good understanding of the hazards posed by saline environments in all parts of the world is crucial for the effective management of natural resources and agriculture, and for commercial concerns, such as construction and highway engineering (Stone and McBean, 1988). In arid and semi-arid areas the problems of distintegration increase, due to the large diurnal temperature range and to the rapid growth of salt crystals (Goudie, Cooke and Evans, 1970; Goudie, 1974; Cooke et al.,(1982). Rocks or buildings located in saline arid areas may well undergo

considerable splitting or granular disintegration caused by the thermal expansion of salt crystals. Salt crystal growth is often more destructive than the thermal expansion of salt crystals. This is especially true in seasonally wetted sebkha regions where the ground surface may be contorted into salt polygons by the growth of gypsum or sodium chloride crystals (Brunsden, 1979).

The recognition of saline areas from remote sensing imagery is of great value in the planning stages of commercial or environmental management projects (Stone and McBean; 1988). Identification of the forms and processes within those areas is of equal importance when assessing the feasibility of construction, extraction, exploitation or cultivation. Throughout the 1970s and 1980s satellite imagery has been used with increasing success in the mapping of sebkhas (Townshend and Hancock, 1981). Krinsley (1976) used Landsat MSS data to choose appropriate road locations in playa areas of Iran. However, at visible and infrared wavelengths salt deposits and standing water can give rise to a wide range of tonal characteristics that may confuse the determination of sebkha boundaries (MacDonald and Waite, 1973).

In the eastern study area on the Sahel of Sousse Seasat and SIR-A imagery have proved to be of great value in the identification of sebkhas and their associated features (see Chapters 5 and 7). The ease with which these systems are able to discriminate sebkha areas is largely a function of radar depression angle and wavelength, together with the roughness and electrical conductivity of the surface: parameters that were described at length in Chapter 3. Field investigation in and around Sebkha Sidi el Hani revealed surface roughness to be of prime importance in determining radar backscatter

from the sebkha (Chapter 6 : Section 6.7.2). Comparison of this feature with the Sebkhas near Ra's Jibsh in eastern Oman in two papers by Stone and McBean (1987;1988) has strengthened this conclusion (see Chapter 6).

Once a sebkha has been identified, the sensitivity of radar data to variations in surface roughness permits an easier classification of surface characteristics than that achieved by visible or infrared data. For example, standing water will produce a uniform low-backscatter response on a radar image, while the same area recorded at visible wavelengths will contain considerable tonal variations produced by variations in depth, salinity or suspended sediment (MacDonald and Waite, 1973). Similarly, a radar-rough sebkha surface, caused by large salt polygons or extensive mud cracking, will have a uniformly bright return, allowing it to be easily discriminated on a radar image. For a radar image to be as sensitive to variations in moisture and salinity as it's visual counterpart, MacDonald and Waite (1973) suggest that the antenna gain of the imaging system would have to be adjusted to such an extent that all roughness information would be lost in signal saturation. However, if radar imagery and multi-spectral data of sebkha areas are used together the environmental scientist can derive complementary information allowing surface characteristics and subsurface conditions to be assessed.

9.3. Application of Radar to the Identification of Material Resourses in Semi-arid Areas

Many landforms of semi-arid areas provide vital sources of materials for the construction and building industries. Large amounts of gravel are required for road and railway construction and for the production of

concrete. Gravel deposits, which by definition have grains with diameters of 2-64mm, commonly occur in fluvial environments, or on slopes where they may be the products of weathering and erosion processes. The two most important slope deposits in semi-arid areas are duricrusts and alluvial fans, both of which were discussed in Chapter 2. Both can be used in the construction industry, although care has to be taken to assess the physical and chemical suitability of the deposit (Cooke et al., 1982). Large quantities of sand (0.06 - 2mm) are also in demand for plastering in the building industry. Sand deposits can be found in the channels and terraces of wadis or in areas of aeolian deposition. Sandy deposits in saline areas should be avoided on account of the problems of salt weathering (Cooke et al., 1982).

Both sand and gravel deposits have been located successfully from aerial photographs and satellite imagery in arid and semi-arid areas. Scientists involved in the Bahrain surface materials resources survey in the late 1970s were able to locate the materials required for an extensive building program from aerial photographs of the whole island (Brunsden et al., 1979). All previous attempts to locate suitable deposits had failed, and the government had even considered the possibility of importing aggregate. Incidently, areas of salt weathering were also identified on the air photographs and were avoided during the construction programme.

In Botswana, research scientists from the Overseas Section of the Transport and Road Research Laboratory used Landsat MSS and TM imagery to map the location of calcrete-bearing landforms. 97% of all large pans, in which calcrete was likely to be found, were identified on the imagery of the area (Lawrance and Toole; 1984). Small

pans less than 200m across, however, were not easily distinguished as they often had spectral characteristics similar to the surrounding area.

The value of conventional remote sensing techniques in materials location should not be disputed. However, as products of weathering and erosion processes often have similar spectral responses to their source rocks, there can be problems associated with aggregate identification. These problems are not experienced when radar imagery is used, as the radar is sensitive to the micro and macro-scale variations in land form, and not to chemical or thermal effects. The response of radar to surface roughness conditions makes it an ideal tool for the identification of aggregate deposits and sand areas, which will have a direct relationship with image tone (see Table 6.2). Furthermore, the ability of radar to penetrate the surface in arid areas allows suitable deposits to be distinguished several metres beneath the surface.

In the western study area around Hadjeb el Ayoun, alluvial fans and pockets of calcrete have similar SIR-A backscatter characteristics (see Section 5.2.3). Both produce a mottled medium-to-light grey tone on the image, indicative of rough surface conditions. The fact that these areas were not well classified by the discriminant analysis is mainly a function of the similarity in their surface roughness condition and the relatively small area from which the sample cases were extracted. Results from a study of alluvial fans in the Winnemucca area of the Nevada desert (MacDonald and Waite, 1973) suggested that Ka-band radar was capable of distinguishing between older, radar-smooth, fan deposits and younger, radar-rough, deposits. The response from both these fans was in contrast to the dark tone produced by the smooth alluvial

deposits in the valley floor (Macdonald and Waite, 1973). Similarly, smooth sandy areas can be delimited easily on the western SIR-A image by their low backscatter response.

The sensitivity of radar to variations in surface roughness is of tremendous importance in the search for surficial materials in arid and semi-arid areas where vegetation cover is limited. In all the examples in this Section and in Section 9.2 it is assumed that the presence of vegetation is not sufficient to alter the roughness profile of the surface significantly, and that the resulting radar return is a function of the materials or bare surface alone. If this is so, when used together with data recorded at visible and infrared wavelengths, radar imagery provided complementary information about an area or deposit, allowing both surface form and spectral characteristics to be determined. Detailed site investigation will still be required to determine chemical characteristics or engineering properties, for example, but geomorphological analysis of remote sensing data can certainly help in the location of material resources.

9.4. Application of Radar to Soil Erosion Studies.

9.4.1. The Problem.

The hazard of soil erosion is a growing concern in widely differing geographical and geoclimatic environments. In semi-arid areas, extensive land clearance and intensive cultivation leads to gully erosion that quickly spreads, rendering large areas unsuitable for agriculture. More land is cleared to replace that already lost and the problem intensifies, often accompanied by increased sheet wash and rill erosion. Despite the areal extent of soil erosion, detailed studies have been

undertaken largely in accessible areas on account of the need for regular monitoring. However, it is often in remote localities, which have remained outside the watchful eye of governments or management teams for many years, that the problems of soil erosion are most severe.

The extent of gully erosion in the Hadjel Valley in central Tunisia was described in Chapter 2 (Section 2.4.1). The erosion owes its existence to land clearance and intensive agricultural production that began in the Roman period and still continues today (Bonvallot, 1977; Hamza, 1985). The severity of the problem was first recognised by the Tunisian Ministry of Agriculture in the 1970s while reconnaissance work for the construction of the Bouguiba reservoir was being undertaken. The most severely eroded areas were mapped by the Ministry from sequential aerial photographs dating from 1963 to 1973 (see Figure 9.1). Estimates of the volume of soil lost from wadi banks and by sheet and rill erosion were made from the analysis of aerial photographs and supported by measurements of suspended sediment yield at the dam construction site at Sidi Saad. A figure of 246.5 tonnes hectare^{-1} year^{-1} was achieved for mean annual soil loss in the area of study (République Tunisienne, 1976). As mentioned in Chapter 2, the high sediment yield of L'oued el Hadjel has been sufficeint to cause substantial silting of the reservoir since its completion in 1981 (Hamza, 1986; Personal communication). Recognition of the problem has led to the introduction of strict management practices and conservation measures in the most severely affected areas.

The value of aerial photographs in the identification of eroded areas was first noted in the 1920s, and by 1938 most soil surveys in the United States were based upon photographic interpretations (Weismiller and Kaminsky,

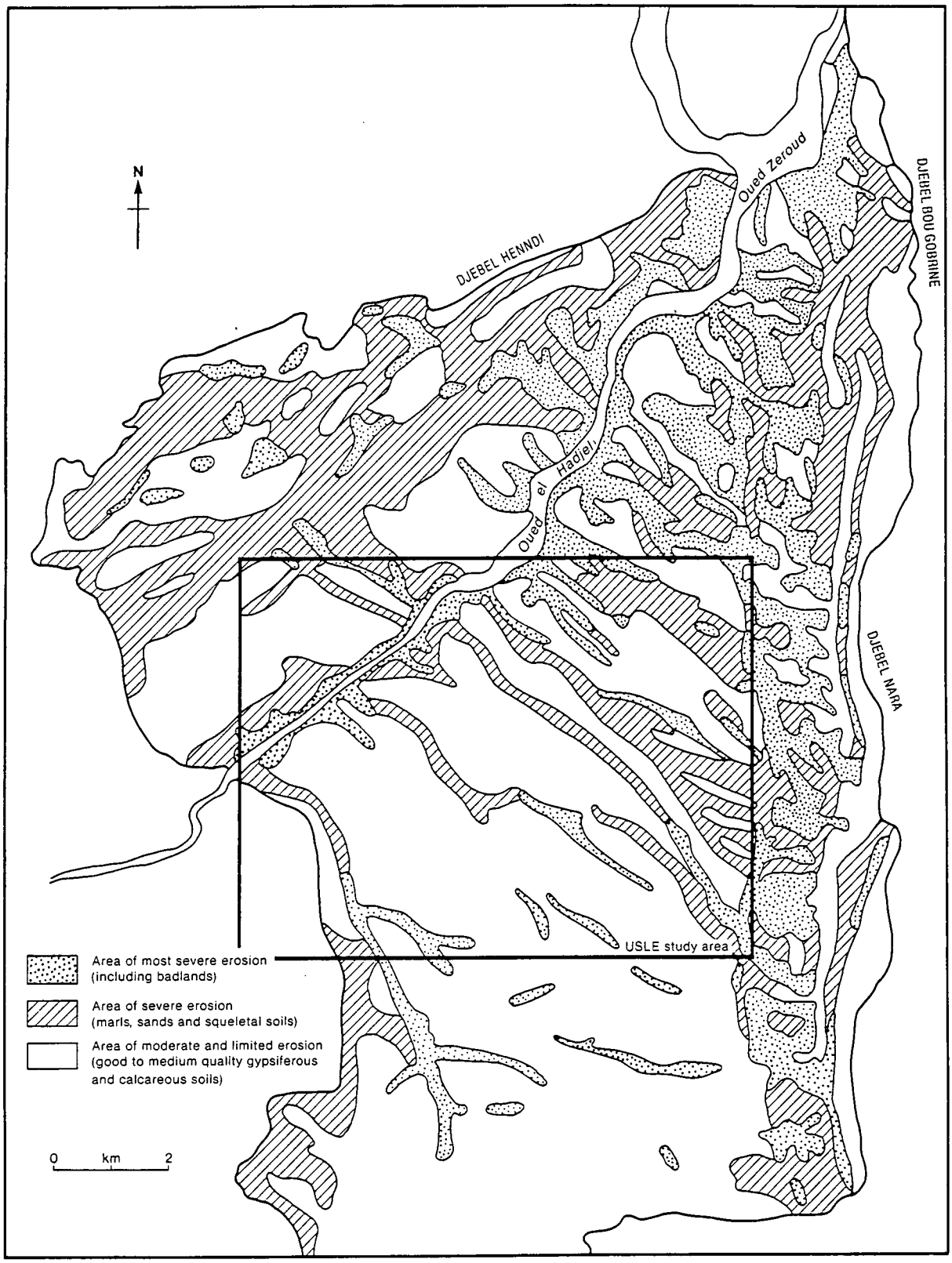

Figure 9.1 The extent of erosion in the Hadjel Valley mapped from aerial photographs dating from 1963 and 1973. (Source: République Tunisienne, 1976).

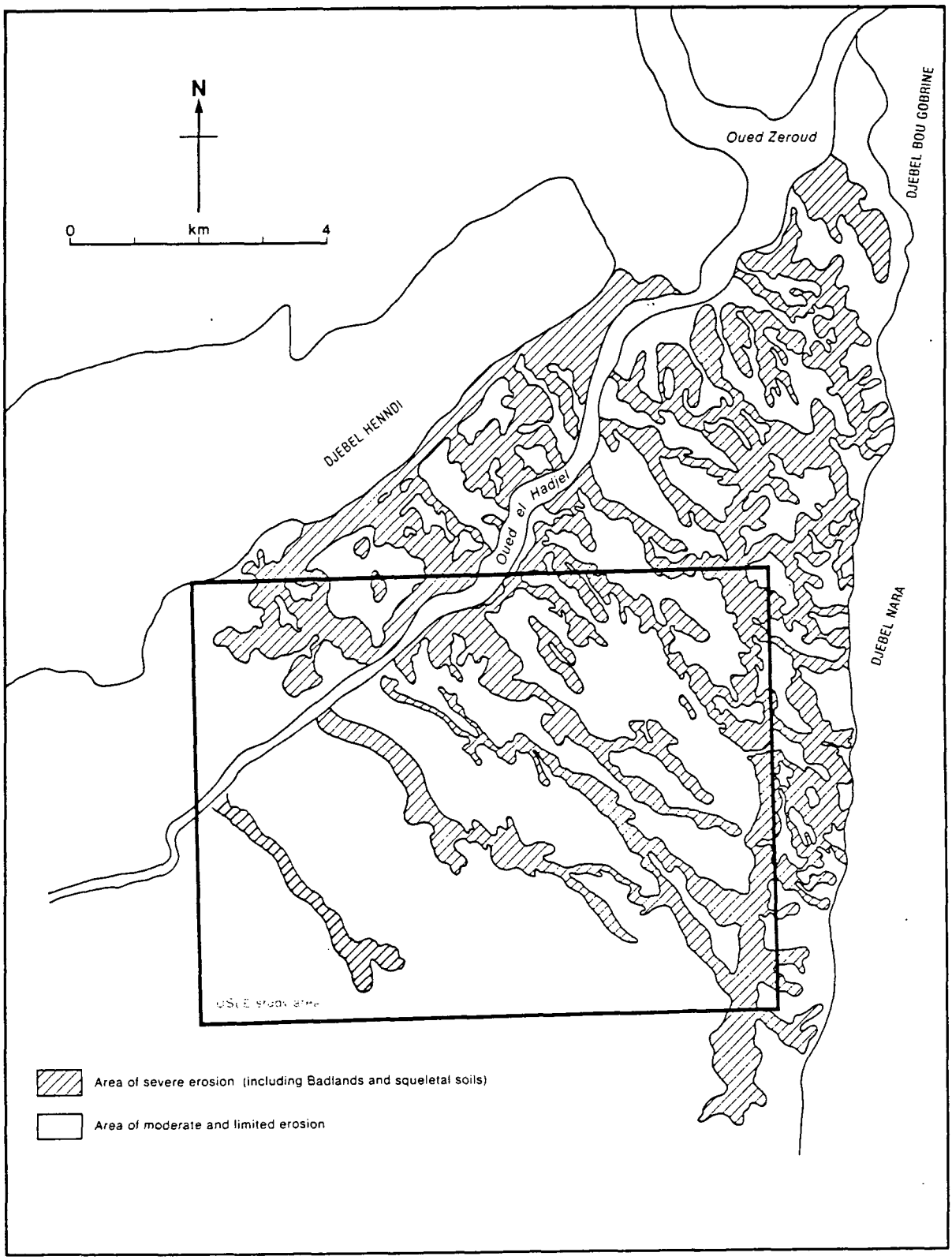

Figure 9.2 The extent of erosion in the Hadjel Valley mapped from SIR-A coverage dating from 1981.

1978). Satellite remote sensing imagery further transformed the study of soil erosion by providing synoptic and more frequent ground coverage at a range of wavelengths. Areas of erosion and potential erosion that had previously gone unnoticed could now be identified.

The pattern of gully erosion in the Hadjel valley can be clearly identified on the SIR-A image (Plate 3.3) as a series of linear concentrations of high backscatter (Chapter 5 : Section 5.2.3). Field investigation revealed a correspondence between areas of high backscatter and gully locations. Results from the discriminant analysis of the area discussed in Chapter 7 reinforce the value of SIR-A data in the mapping of eroded areas, with up to 75% of gully cases being correctly classified. The ability of SIR-A to discriminate the gullies is largely a function of gully width and depth, together with the slope of the channel walls with respect to local radar incidence angle and look direction (see Chapter 6 : Section 6.8.2). For this reason, the areas of most severe erosion in the Hadjel valley could be mapped with relative ease from the SIR-A imagery (Figure 9.2). The resulting map is very similar to that produced from the air photograph interpretation (Figure 9.1).

9.4.2. The Model.

The apparent value of satellite radar imagery in the identification of the extent of the erosion problem in the Hadjel valley prompted an investigation into the possibilities of deriving some quantitative measure of soil loss from the SIR-A image. Over the years, a wide range of models have been developed to estimate soil loss or sediment yield from a variety of environments. Based on extensive research in the United States and Southern

Europe, the Universal Soil Loss Equation, or USLE, developed by Wischmeier and Smith (1965) has come to be widely known and has been regarded as a useful means of quantifying long term soil loss from rill and sheet erosion in certain areas. Despite its name, the universal applicability of the model is questionable, but the relative ease with which it may be calculated using remote sensing data as an input, led to its adoption as a means of quantifying the level of erosion in the Hadjel valley.

The model allows the calculation of predicted soil loss for a given area using the equation:

$$A = R.\ K.\ LS.\ C.\ P \qquad \text{Equation 9.1}$$

Where:

R = Rainfall erosivity index (a function of kinetic energy of storm rainfall and rainfall intensity, and dependent upon mean annual and monthly rainfall).

K = Soil erodibility factor (determined from physical and chemical analysis of field samples and/or published pedological information)

LS = Topographic Factor (derived from measurements of slope length and angle on a topographic map).

C = Cover management factor (determined from information on vegetation type and cover).

P = Soil conservation practices (relevant only once control has been implemented).

Most of the factors within the Universal Soil Loss Equation must be derived from documentary records, or specific field information for a given area, as described above. If regular monitoring of an identified problem area is required, frequent field visits are necessary to record any changes that may occur. Since the rainfall, soil and topographic indices (R,K,LS) are generally static over the time scales in which a project will be implemented, changes will only be relevant in the cover management factor (C), and eventually the conservation factor (P). Thus, once initial field data have been collected, any cost or time-saving measure that reduces the need for subsequent field survey will be a positive advantage, especially in the poorer and less accessible areas of the world. Recent studies have highlighted the importance of airborne and satellite remote sensing products in the rapid assessment of the cover management factor (C) for the USLE (Morgan et al., 1980; Patterson and McAdams, 1980; Fenton, 1982). This being so, it was decided to investigate the possibility of deriving the c factor from the SIR-A image of the Hadjel Valley.

The cover management factor (C) was derived on the basis of variations in SIR-A backscatter. Four general categories of radar response were identified and found to correspond with the four main cover types mapped in the field: arboriculture (bright), cereals and pasture (intermediate to dark), bare soil (dark) and eroded wadi banks (very bright). These were mapped on a transparent sheet placed over the SIR-A image. The cover management factor for each area was obtained using the scheme devised by Wischmeier and Smith (1978) for pasture and idle land. The values and their derivation are given in Table 9.1.

Cover type	Per cent cover	SIR-A response	C factor
Grass, small weeds and cereals	40 - 60%	Medium to low backscatter	0.13
Arboriculture with no understory	60%	High backscatter	0.14
No appreciable canopy	0.0%	Low backscatter	0.45

Table 9.1 Derivation of USLE C factor from SIR-A coverage of the Hadjel Valley using the scheme devised by Wischmeier and Smith (1978)

A grid square approach was adopted to measure and map the c factor and each of the other USLE parameters. The area chosen for study (see Figures 9.1 and 9.2) was subdivided into a series of squares of equal area and values for the equation were calculated on a grid-by-grid basis to produce a two-dimensional record for each variable. The values for each grid were subsequently fed into the Universal Soil Loss Equation to produce an output grid for estimated soil loss (A) that could be spatially overlain and compared with each input file (Figure 9.3).

The grid square approach was first used by Alam (1987), and afterwards by Stone and Alam (1987) for a comparative study of erosion in Tunisia and the UK. For a more detailed discussion of the grid-mesh USLE model reference should be made to these publications, which are included at the back of this thesis. The main advantage of the model is the capacity to calculate, not only an overall estimate of soil loss for a given area, but also totals for individual grid squares, thereby

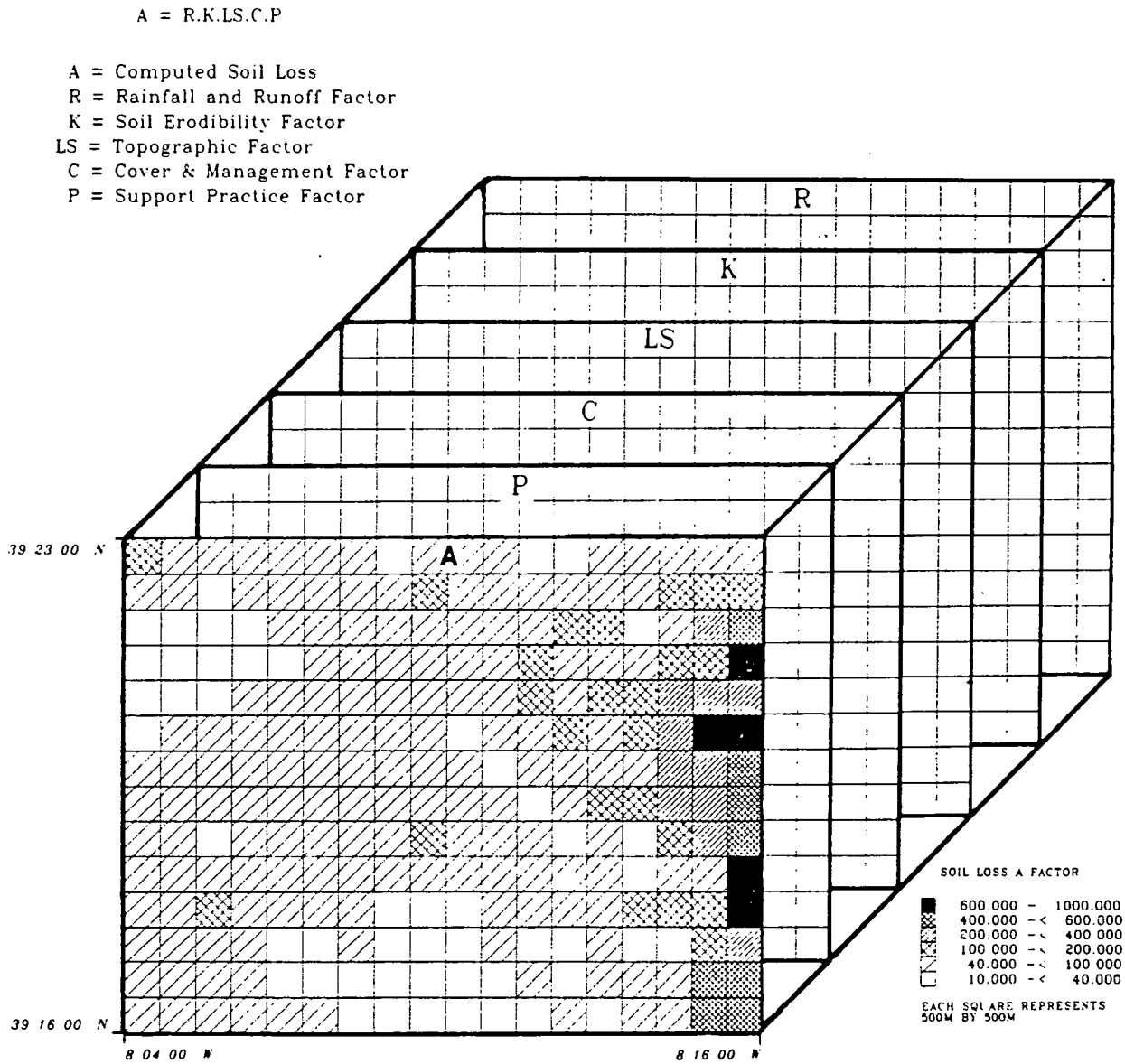

Figure 9.3 The grid-mesh approach to the calculation of soil loss by the Universal Soil Loss Equation. Each input factor is calculated within a two-dimensional grid framework. Once all the input factor grids have been prepared they are multiplied together in accordance with the equation to produce an output grid for estimated soil loss A.

allowing more careful erosion control and implementation of management practices. Furthermore, updated information can be fed into the model for selected grids only, and temporal changes easily compared. This is an important consideration for conservationalists and land management teams in all areas, particularly in the developing world, where a trained labour force and financial resources are limited.

Once all the input factors for the universal soil loss equation had been obtained, the values were combined in accordance with the equation to produce a predicted soil loss value for each grid. (Figure 9.4a). A total figure of 261.8 tonnes / hectare / year was achieved for the area as a whole. This figure compares favourably with the value of 246.5 tonnes / hectare / year obtained from the measurements of suspended sediment yield at the Sidi Saad dam site, with a margin of error of only 6%. The value is also very similar to that achieved by using aerial photographic coverage of the area to derive the cover management factor (C) (Stone and Alam, 1987). The soil loss values derived from the three sources are compared in Table 9.2. The minimal difference between the aerial and satellite studies is further exemplified by the spatial distribution on the two grid-mesh files in Figure 9.4.

SOURCE	PREDICTED EROSION RATE (tonnes/hectare/year)
Field Measurements (Republique Tunisienne 1976)	246.5
Aerial Photographs (May-June 1963)	258.8
SIR-A (November 11th 1981)	261.8

Table 9.2 Predicted soil loss values for the study area in the Hadjel Valley derived from field measurements and from the USLE, where air photographs and SIR-A are used as alternative sources of crop management information.

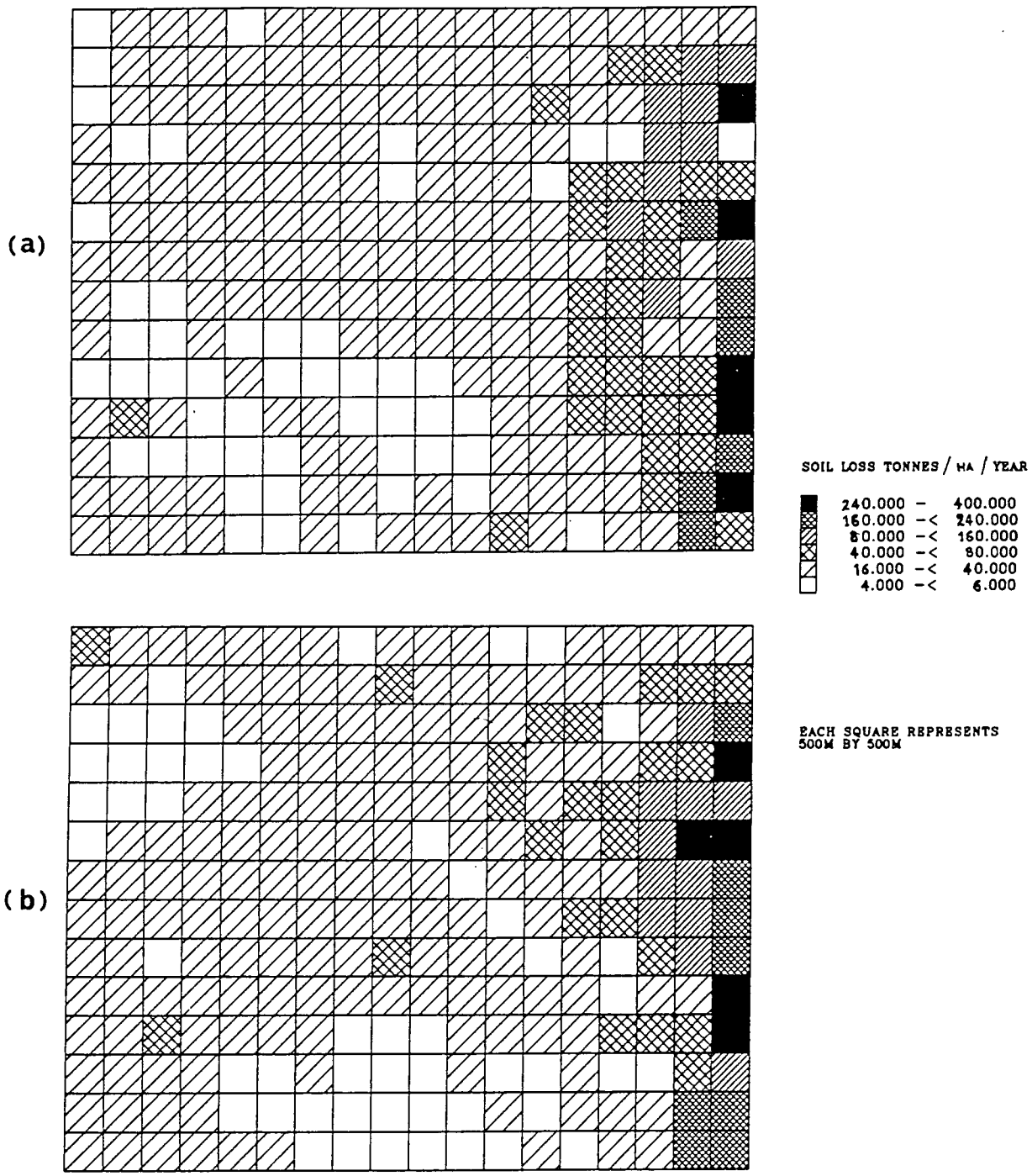

Figure 9.4 Output grid files for estimated soil loss in the Hadjel Valley produced by using (a) SIR-A and (b) air photographs to derive the USLE crop management factor, C.

9.4.3. Conclusions.

The sensitivity of SIR-A to variations in surface form associated with land cover and erosion makes it an ideal tool for the mapping and monitoring of soil erosion, especially in semi-arid areas where vegetation cover is limited. The results from the SIR-A derived USLE model described above are most encouraging, and suggest that SIR-A imagery can be used effectively in management programmes in areas such as Tunisia. The viability of this proposition should be tested by applying satellite radar imagery in similar studies throughout the semi-arid world.

9.5. Summary and Conclusions.

The three applications of radar imagery in semi-arid areas discussed in this chapter have all highlighted the tremendous contribution it can make in the identification and mapping of hazard and resource areas. The unique sensitivity of radar to surface form, whether at the macro-scale (slope) or micro-scale (roughness) provides the environmental scientist with vital information about the landscape that cannot be derived from conventional remote sensing systems. This is of particular importance in semi-arid or arid areas where vegetation cover is limited and surface features are more prominent. Applied studies of radar imagery are in their infancy, but there can be no doubt that radar offers a valuable contribution to the field of geomorphology and environmental management.

Bibliography

Adams S.L. and Mcleod A.G. (1984), Land resources management. In Schiffman Y.M. et al. (editors), Methods and models for spatial data bases: Proceedings of 1983 National Conference on Resource Management, 1st April, 1983, Vol. VIII, S.F. California.

Akroyd T.N.W. (1964), Laboratory Testing in Soil Engineering, Soil Mechanics Ltd., London, 233pp.

Alam M.S. (1987), The application of remote sensing in open moorland soil erosion studies: a case study of Glaisdale Moor, Northern England, Unpublished PhD. thesis, Department of Geography, University of Durham, 281pp.

Allan T.D. (1983), A review of Seasat. In Allan T.D. (editor), Satellite Microwave Remote Sensing, Ellis Horwood Ltd, Chichester.

Anderson J.G.C. (1978) The structure of Western Europe., Pergamon Press, Oxford, 250pp.

Arcone S.A., Gow A.J. and McGrew S. (1986), Microwave dielectric, structural and salinity properties of simulated sea ice, IEEE Transactions on Geoscience and Remote Sensing, Vol. 24, No. 6., p.832-39.

Asrar G., Weiser R.L., Johnson D.E., Kanemasu E.T. and Killeen J.M. (1986), Distinguishing among tallgrass prairie cover types from measurement of multispectral reflectance, Photogrammetric Engineering and Remote Sensing, Vol. 19(2), p.159-169.

Attema E.P.W., Van Kats P. and Krul L. (1982), A radar signal model for partially coherent scattering from irregular surfaces, EEE Transactions on Geoscience and Remote Sensing, Vol. 20(1), p.76-84.

Bahar E. and Fitzwater M.A. (1984), Comparison of backscatter cross sections for composite rough surfaces with different mean square slopes, International Journal of Remote Sensing, Vol.5(2), p.451-462.

Baird D.W. (1967), The Permo-Carboniferous of Spouthern Tunisia. In Martin L. (Editor), Guidebook to the Geology and History of Tunisia, Petroleum Society of Libya, 9th annual field conference, pp85-107.

Bannour H., Bonvallot J. and Hamza A. (1981). Erosion et aménagement antiérosif d'un bassin versant de la Tunisie Centrale: L'oued el Foul. Sols de Tunisie 12.

Beal R.C and Tilley D.G. (1980). Optimal Spatial filtering and transfer function for SAR ocean wave spectra. SAR Image Quality ESA sp-172, pp59-65.

Beckman P. and Spizzichino A. (1963), The scattering of electromagnetic waves from rough surfaces, Macmillan, New York.

Bégin D., Gwyn Q.H.J. and Bonn F. (1987) Radiometric correction of SAR images: a new correction algorithm. International Journal of Remote Sensing 8(3), pp385-398.

Bennett J.R., Cumming J.G. and Deane R.A. (1980), The digital processing of Seasat synthetic aperture radar data, IEEE International Radar Conference, p.168-175.

Benson M. (1984), The use of linear approximations to the cell migration curves for the high resolution processing of Seasat SAR images, Canadian Journal of Remote Sensing, Vol.10(1), p.57-66.

Berlin G.L., Tarabzouni M.A., Al-Naser A.H., Sheikho K.M. and Larson R.W. (1986), SIR-B subsurface imaging of a sand-buried landscape: Al Labbah Plateau, Saudi Arabia, IEEE Transactions on Geoscience and Remote Sensing, Vol.24(4), p.595-602.

Berlin G.L., Tarabzouni M.A., Munshi Z.M.N. and Chavez P.S. Jr. (1984), Application of SIR-B data for groundwater exploration in the Arabian Shield and sand drift monitoring in the An Nafud and Al Jafurah Fringe areas, Kingdom of Saudi Arabia, JPL Publication 84-3, p.4.19-4.21.

Bienvenu L. and Pascucci R. (1962), Engineering geology from side looking radar records, Autometric Corporation, Alexandria, Virginia, 13pp.

Bishop W.F. (1975) Geology of RTunisia and adjacent parts of Algeria and Libya. Bulletin of the American Association of Petroleum Geologists 59(3), pp413-450.

Blanchard B.J. (1980), Realistic earth/land radar models, JPL Publication 80-61 Radar Geology: An Assessment, p.200-222.

Blanchard B.J. and Chang A.T.C. (1983), Estimation of soil moisture from Seasat SAR data, Water Resources Bulletin, Vol.19(5), p.803-810.

Blom R. and Daily M. (1982), Radar image processing for rock type discrimination, IEEE Transactions on Geoscience and Remote Sensing, Vol 20, p.343-351.

Blom R. and Elachi C. (1981), Spaceborne and airborne imaging and radar observations of sand dunes, Journal of Geophysical Research, Vol.86(B4), p.3061-73.

Blom R. Abrams M. and Conrad C. (1981), Rock-type discrimination techniques using Landsat and Seasat image data, Digest 1981 International Geoscience and Remote Sensing Symposium (IGSARSS '81), Vol.2, p.597-602.

Blom R.G., Crippen R.E. and Elachi C. (1984), Detection of subsurface features in Seasat images of Means Valley, Mojave Desert, California, Geology, Vol.12, p.346-349.

Blom R.G., Schenck L.R. and Alley R.E. (1987), What are the best radar wavelengths, incidence angles and polarizations for discrimination among lava flows and sedimentary rocks? A statistical approach, IEEE Transactions on Geoscience and Remote Sensing, Vol. 25(2), p.208-213.

Blyth K. (1984), Analysis of digital radar data from SAR-50 in relation to soil/vegetation moisture and roughness, Institute of Hydrology Report No.93 (NERC), November 1984.

BNSC (1987), AMI: Synthetic aperture radar-image mode ERS-1 Users product support team publication DC-HO-PST-SY-0004, BNSC, 2pp.

Bonnefous J. (1967). Jurassic stratigraphy of Tunisia: a tentative synthesis (Northern and Central Tunisia; Sahel and Chotts area). In Martin L. (Editor), Guidebook to the Geology and History of Tunisia, Petroleum Society of Libya, 9th annual field conference, p109-130.

Bonvallot J. (1977) Causes et modalite de l'érosion dans le bassin versant inférieur de l'oued el Hadjel (Tunisie Centrale), Comm. Symp. Erosion et transport soldie dans les eaux continentales, UNESCO-AIHS , Paris, Juillet 1978. IASH-AISH Publication 122, pp260-268.

Bonvallot J. and Delhoume J.P. (1978) Etude de differentes accumulations carbonatées d'une toposéquence du centre Tunisien (Djebel Semmama), 103 Congrès National des Sociétés Savantes, Nancy, Sciences, Fasc iv pp281-292.

Borengasser M.X. and Taranik J.V. (1985), The application of shuttle imaging radar (SIR-B) to tectonic analysis of the Candelaria region, Nevada (Summary), International Symposium on Remote Sensing of the Environment 4th Thematic Conference Remote Sensing in Exploration Geology (ERIM), p.19-20.

Born G.H., Dune J.A. and Lame D.B. (1979), Seasat mission overview, Science, Vol.204, p.1405-6.

Born G.H., Held D.N., Lame D.B., Lipes R.G., Montgomery D.R., Rygh P.J. and Scott J.F. (1982), Seasat Data Utilization Project Report, NASA-JPL D-36, 72pp.

Boulaine J. (1958) Sur le formation des carapaces calcaires accumulation de carbonates et de sulfates dans les sols bien draines, Publication du Service de la Carte Géologique de L'Algerie (Nouvelle Serie), Bulletin no 20. p7-19.

Bowler J.M. (1973) Clay dunes: their occurrence, formation and environmental significance, Earth Science Reviews 9, pp315-338.

Brechtel R. and Rohmer W. (1980) Bodenkunde-Nordafrica (Tunisien, Algerien). Africa Kartenwerk no4, Gebruder Borntraeger, Berlin. 67pp.

Breed C.S., Schaber G.G., McCauley J.F., Grolier M.J., Haynes C.V., Elachi C., Blom R., Issawi B. and McHugh W.P. (1983), Subsurface geology of the western desert in Egypt and Sudan revealed by Shuttle Imaging Radar (SIR-A) Spaceborne Imaging Radar Group Symposium, JPL 83-11, p.10-12.

Brierly G.J. 91981). The wadis of the Sousse region, Central Tunisia. In Harris R. and Lawless R. (editors) Field studies in Tunisia, Department of Geography, University of Durham, p4-17.

Brogan O.(1967) Roman Tunisia. In Martin L. (Editor), Guidebook to the Geology and History of Tunisia, Petroleum Society of Libya, 9th annual field conference, p17-35.

Brown J.W., Cleven G.C., Klose J.C., Lame D.B. and Yamarone C.A. (1979), Seasat low-rate data system, Science, Vol.204, p.1407-8.

Brunfeldt D.R. and Ulaby F.T. (1984), Measured microwave emission and scattering in vegetation canopies, IEEE Transactions on Geoscience and Remote Sensing, Vol. 22(6), p.520-25.

Brunsden D. (1979), Weathering. In Embleton C. and Thornes J. (editors), Process in Geomorphology, Edward Arnold, 436pp.

Brunsden D., Doornkamp J.C. and Jones D.K.C. (1979), The Bahrain surface materials resources survey and its

application to regional planning, Geographical Journal, Vol.145, p.1-35.

Bryan K. (1935). The formation of pediments. 16th International Geological Congress Report pp765-775.

Bryan M.L. (1979), The effect of radar azimuth angle on cultural data, Photogrammetric Engineering and Remote Sensing, Vol.45(8), p.1097-1107.

Bryan M.L. and Clark J. (1984), Potentials for change detection using Seasat Synthetic Aperture Radar data, Remote Sensing of Environment, Vol. 16(2), p.107-124.

Buchanan G.S. and Schwab R.F. (1966) Middle Jurassic triugh of Central Tunisia. 51st annual A.A.P.G and 40th S.E.P.M. conference. Resume in American Society of Petroleum Geologists 50(3i) p606.

Burke H.H.K. and Schmugge T.J. (1982), Effects of varying soil moisture contents and vegetational canopies on microwave emissions, IEEE Transactions on Geoscience and Remote Sensing, Vol. 20(3), p.268-274.

Burollet P.F. (1967), Tertiary Geology of Tunisia. In Martin L. (Editor), Guidebook to the Geology and History of Tunisia, Petroleum Society of Libya, 9th annual field conference, p215-225.

Busson G. (1967) Mesozoic of Southern Tunisia. In Martin L. (Editor), Guidebook to the Geology and History of Tunisia, Petroleum Society of Libya, 9th annual field conference, p131-151.

Campbell M.J. and Ulrichs J. (1969), Electrical properties of rocks and their significance for lunar radar observations, Journal of Geophysical Research, Vol.74, p.5867-5881.

Canoba C.A. (1982), Geomorphological mapping using Landsat imagery: a case study in Argentina, ITC Journal, Vol.3, p.324-9.

Car D.C., Becker R.E. and Van Lopik J.R. (1963), Terrain Quantification Phase II Playa and Miscellaneous Studies, Final Report Contract AF 19(628)-2786 Project Terrestrial Sciences Laboratory, Airforce 7628 Cambridge Research Centre, 70pp.

Castany G.(1953) Carte géologique de la Tunisie. Notice explicative. Deuxième édition, Régence de Tunis-Protectorat Francais, Direction des Travaux Publics, Service des Mines, de L6industrie et de l'énergie. 141pp.

Chang A.T.C., Atwater S.G., Salomonson V.V., Estes J.E., Simonett D.S. and Bryan M.L. (1980), L-band radar sensing of soil moisture, IEEE Transactions on Geoscience and Remote Sensing, Vol.18(4), p.303-310.

Chavez P.S. (1981) Automatic shading correction and speckle noise mapping/removal techniques for radar image data. In Radar Geology: an assessment. JPL Publication 81-60, pp251-262.

Choudhury B.J., Owe M., Goward S.N., Colus R.E., Ormsby J.P., Chang A.T.C. and Wang J.R. (1967), Quantifying spatial and temperature variabilities of microwave brightness temperature over the U.S. Southern Great Plains, International Journal of Remote Sensing, Vol.8(2), p.177-191.

Choudhury B., Schmugge T., Newton R.W. and Chang A.T.C. (1979), Effect of surface roughness on the microwave emission from soils, Journal of Geophysical Research, Vol.84, p.5699-5706.

Cihlar J., Dobson M.C., Schmugge T., Hoogeboom P., Janse A.R.P., Baret F., Guyot G., Le Toan T. and Pampaloni P. (1987), Review Article: Procedure for the description of agricultural crops and soils in optical microwave remote sensing studies, International Journal of Remote Sensing, Vol.8(3), p.427-39.

Cimino J.B. (1985), The SIR-B experiment-preliminary results, International Symposium on Remote Sensing of the Environment 4th Thematic Conference Remote Sensing in Exploration Geology (ERIM), p.107.

Cimino J.B. and Elachi C. (editors), (1982), Shuttle Imaging Radar (SIR-A) Experiment, JPL Publication 82-77.

Cimino J.B. and Wall S. (1985), Multiple incidence angle SIR-B imagery of the Chubut Province of southern Argentina (Summary), International Symposium on Remote Sensing of the Environment 4th Thematic Conference Remote Sensing in Exploration Geology (ERIM), p.18.

Cimino J.B., Brandani A., Casey D., Rabassa J. and Wall S.D. (1986b), Multiple incidence angle SIR-B experiment over Argentina: Mapping of forest units, IEEE Transactions on Geoscience and Remote Sensing, Vol.24(4), p.498-509.

Cimino J.B., Elachi C. and Settle M. (1986a), SIR-B The Second Shuttle Imaging Radar Experiment, IEEE Transactions on Geoscience and Remote Sensing, Vol.24(4), p.445-454.

Colwell R.N. (editor), (1983), Manual of Remote Sensing, (2nd edition). American Society of Photogrammetry. 2440pp.

Cooke R.U. and Warren A. (1973). Geomorphology in deserts Batsford, London, 394pp.

Cooke R.U., Brunsden D., Doornkamp J.C. and Jones J.K.C. (1982), Urban Geomorphology in Drylands, Oxford University Press, 324pp.

Correa A.C. (1980), Geological mapping in the Amazon jungle-a challenge to side-looking radar, Radar Geology: an assessment. Snowmass Colorado (1979), JPL Publication 80-61, pp.385-416.

Coque R. (1955) Morphologie et croûtes dans le sud-saharienne. A. Geographie Paris 64(345) pp359-370.

Coque R. (1958) Morphologie de la Tunisie pre-saharienne. Trav. Inst. Rech. Sahariennes 17, pp59-80.

Coque R. and Jauzein A. (1965). Essai d'une carte néotectonique de la Tunisie au 1/1,200,000, Revue de Géographie Physique et de Géologie Dynamique 2 vii, Fasc 3, Paris, pp253-265.

Coque R. and Jauzein A. (1967). The Geomorphology and Quaternary Geology of Tunisia. In Martin L. (Editor), Guidebook to the Geology and History of Tunisia, Petroleum Society of Libya, 9th annual field conference, p227-257.

Daily M. (1983), Hue-saturation-intensity split-spectrum processing of Seasat radar imagery, Photogrammetric Engineering and Remote Sensing, Vol.49(3), p.349-55.

Daily M., Elachi C., Farr T. and Schaber G. (1978), Discrimination of Geologic units in Death Valley using dual frequency and polarization imaging radar data,Geophysical Research Letters, Vol.5(10), p.889-891.

Daily N.I., Farr T., Elachi C. and Schaber G. (1979), Geologic interpretation from composited radar and Landsat imagery, Photogrammetric Engineering and Remote Sensing,Vol.45(8), p.1109-16.

Day P.R. (1965), Partical fractionation and particle size analysis. In Black C.A. (editor), Methods of soil analysis part 1 - Physical and mineralogical properties, including statistics of measurement and sampling p.545-87.

DeLauder D.H. and Balanis C.A. (1984), Numerical comparisons of short pulse scattering models for rough

surfaces, IEEE Transactions on Geoscience and Remote Sensing, Vol.22(6), p.585-592.

Dellwig L.F. and Moore R.K. (1966), The geological value of simultaneously produced like-and cross-polarized radar imagery, Journal of Geophysical Research, Vol.71(14), p.3597-3601.

Dellwig L.F., Kirk J.W. and Walters R.L. (1966), The potential of low-resolution radar imagery in regional geologic studies, Journal of Geophysical Research, Vol.71(2), p.4995-8.

Dellwig L.F., Macdonald H.C. and Kirk J.N. (1968), The potential of radar in geological exploration, Proceedings 5th Symposium Remote Sensing of the Environment, Ann Arbor, Michigan, ERIM p.747-764.

Dixon T.H. (1984), SIR-B analysis of the Precambrian Shield of Sudan and Egypt: Penetration studies and subsurface mapping, JPL Publication 84-3, p.4.39-4.40.

Dixon A.D.G., Munday T.J. and Lake S.D. (1985), Structural and lithological mapping in the Wessex Basin of southern England using Seasat SAR data (summary), International Symposium on Remote Sensing of the Environment 4th Thematic Conference Remote Sensing in Exploration Geology (ERIM), p.42-3.

Dobson M.C. and Ulaby F. (1981), Microwave backscatter dependence on surface roughness soil moisture and soil texture: Part III soil tension, IEEE Transactions on Geoscience and Remote Sensing, Vol.19(1), p.51-61.

Dobson M.C. and Ulaby F.T. (1986), Preliminary evaluation of the SIR-B response to soil moisture, surface roughness and crop canopy cover, IEEE Transactions on Geoscience and Remote Sensing, Vol.24(4), p.517-526.

Dobson M.C., Kouyate F. and Ulaby F.T. (1984), A re-examination of soil textural effects on microwave emission and backscattering, IEEE Transactions on Geoscience and Remote Sensing, Vol.22(6), p.530-36.

Domik G., Leberl F. and Cimino J.B. (1986), Multiple incidence angle SIR-B experiment over Argentina: Generation of secondary image products, IEEE Transactions on Geoscience and Remote Sensing, Vol.24(4), p.492-497.

Dornier (System GMBH), (1984), ERS-1 ESA Remote Sensing Satellite and ERS-1 Newsletter

Drury S.A. (1987), Image Interpretation in Geology, Allen and Unwin, 243pp.

Ehrenberg A.S.C. (1982), A primer in data reduction. An introductory statistics textbook. John Wiley and Sons. 305pp.

Dutcher L.C. and Thomas H.E. (1966) The occurrence, chemical quality and use of groundwater in the Tabulbah area, Tunisia. United States Geological Survey Water Supply Paper, 1757-E.

Elachi C. (1980), Spaceborne imaging radar: geologic and oceanographic applications, Science, Vol.209(4461), p.1073-1082.

Elachi C. (editor) (1981), Earth observation with the Seasat Spaceborne Imaging Radar, Revue Photo-interpretation, 81-4/1-5, 31pp.

Elachi C. (1983), Spaceborne radar research in the '80's. Spaceborne Radar Symposium, Jan 17-20 J.P.L. California, JPL Publication 83-11, p.131-135.

Elachi C., Blom R., Daily M., Farr T. and Saunders R.S. (1980), Radar imaging of volcanic fields and sand dune fields: Implications for VOIR, radar geology: An assessment, Snowmass Colorado, JPL Publication 80-61, p.114-150.

Elachi C., Brown W.E., Cimino J.B., Dixon T., Evans D.L., Ford J.P., Saunders R.S., Bread C., Masursky H., McCauley J.F., Schaber G., Dellwig L., England A., Macdonald H., Martin-Kaye P. and Sabins F. (1982), Shuttle imaging radar experiment, Science, Vol.218(4576), p.996-1003.

Elachi C., Roth L.E. and Schaber G.G. (1984), Spaceborne radar surface imaging in hyperarid regions, IEEE Transactions on Geoscience and Remote Sensing, Vol.22(4), p.383-387.

Engel J.L. and Weinstein O. (1983), The Thematic Mapper-An Overview, IEEE Transactions on Geoscience and Remote Sensing, Vol.21(3), p.258-265.

Engheta N. and Elachi C. (1982), Radar scattering from a diffuse vegetation layer over a smooth surface, IEEE Transactions on Geoscience and Remote Sensing, Vol.20(2), p.212-216.

Engman E.T. and Wang J.R (1987), Evaluating roughness models of radar backscatter, IEEE Transactions on Geoscience and Remote Sensing, Vol.25(5), p.709-713.

Eom H.J. (1986), Regression models for vegetation radar backscattering and radiometric emission, Remote Sensing of Environment, Vol.19, p.151-157.

Eom H.J. and Fung A.K. (1984), A scatter model for vegetation up to Ku-Band, Remote Sensing of Environment, Vol.15, p.185-200.

Eom H.J. and Boerner W-M., (1986), A re-examination of radar terrain backscattering at nadir, IEEE Transactions on Geoscience and Remote Sensing, Vol.24(2), p.232-234.

Eppes T.A. and Rousse J.W. Jr. (1984), Viewing-angle effects in radar images, Photogrammetric Engineering, Vol.40(2), p.169-173.

ESA (1984a), Earthnet's experience with Seasat-SAR image processing-based on article by J.P. Guignard in ESA Bulletin No.24. In Earthnet, the Story of Images ESA BR-18, March 1984, p.8-11.

ESA (1984b), Looking ahead to ERS-1; a new tool for marine applications and science. In Earthnet, the Story of Images ESA BR-18, p.50-52.

ESA, (1985), Preliminary announcement of opportunity for ERS-1, Earth Observation Quarterly, No.11, Sept.'85, ESA publications.

Evans D.L. and Blom R. (1982), Potential of multisensor data and strategies for data acquisition and analysis, In Proceedings of the workshop on the use of future multispectral imaging capabilities for lithologic mapping, California Institute of Technology, J.P.L. 82-93, p.2.15-2.18.

Evans D.L., Elachi C. and Zebkher H.A. (1985), Multipolarization and multifrequency imaging radars: scientific rationale and future plans (summary), International Symposium on Remote Sensing of the Environment 4th Thematic Conference Remote Sensing in Exploration Geology (ERIM), p.2.

Evans D.L., Farr T.G., Farr J.P., Thompson T.W. and Werner C.L. (1986), Multipolarization radar images for geologic mapping and vegetation discrimination, IEEE Transactions on Geoscience and Remote Sensing, Vol.24(2), p.246-257.

Evans D.L., Farr T.G., Tapponier P. and Elachi C. (1988), Imaging radar observations of Normal Faults in Tibet. In Remote Sensing moving towards the 21st Century, Proceedings of ICARSS '88 Symposium, Edinburgh September 13-16th, Ref ESA SP-284, p.357.

Evans R. and Carroll D.M. (1986), Radar images for soil survey in England and Wales, ITC Journal, Vol.1986-1, p.88-93.

Farr T.G. (1983), Use of radar image texture in geologic mapping, JPL Publication 83-11, p.73-75.

Farr T.G. (1984), Quantitative use of multi-incidence-angle SAR for geologic mapping, JPL Publication 84-3, p.4.41-4.43.

Farr T.G. and Massonnet D. (1985), The use of multi-incidence angle radar systems for geologic mapping (summary), International Symposium on Remote Sensing of the Environment 4th Thematic Conference Remote Sensing in Exploration Geology (ERIM), p97.

Fenton T.E. (1982), Estimating soil erosion by remote sensing techniques. In Johansen C.J. and Saunders J.L. (editors), Remote Sensing for Resource Management, Soil Conservation Society, America, p.217-241.

Fielding E.J., Knox W.J. and Bloom A.L. (1986), SIR-B radar imagery of volcanic deposits in the Andes, IEEE Transactions on Geoscience and Remote Sensing, Vol.24(4), p.582-589.

Foody G.M. (1986), An assessment of the topographic effects on SAR image tone, Canadian Journal of Remote Sensing, Vol.12(2), p.124-131.

Ford J.P. (1980), Seasat orbital radar imagery for geological mapping: Tennessee-Kentucky-Virginia, AAPG Bulletin, Vol.64(20, p.2064-2094.

Ford J.P. (1981), Analysis of Seasat orbital radar imagery for geologic mapping in the Appalachian Valley and Ridge Province, Tennessee-Kentucky-Virginia. In Radar Geology: An Assessment JPL Publication 81-60, p.75-113.

Ford J.P. (1982), Resolution v's speckle relative to geologic interpretability of spaceborne radar images: a survey of user preferences, IEEE Transactions on Geoscience and Remote Sensing, Vol.20(4), p.434-444.

Ford J.P. and da Cunha R. (1985), Spaceborne radar images for geologic mapping in tropical rainforest (summary), International Symposium on Remote Sensing of the Environment 4th Thematic Conference Remote Sensing in Exploration Geology (ERIM), p119.

Ford J.P. and Sabins F.F. Jr. (1985), Space Shuttle radar investigations in Indonesia (summary), International

Symposium on Remote Sensing of the Environment 4th Thematic Conference Remote Sensing in Exploration Geology (ERIM), p21.

Ford J.P., Blom R.G, Bryan M.L., Daily M.I., Dixon T.H., Elachi C., and Xenos E.C. (1980), Seasat views of North America, the Carribean and Western Europe with imaging radar, JPL Publication 80-67.

Ford J.P., Cimino J.B. and Elachi C. (1983), Space Shuttle Columbia views the world with imaging radar: the SIR-A experiment, JPL Publication 82-95, 179pp.

Ford J.P., Wickland D.E. and Ocamp A. (1985), Mapping diverse vegetation with multichannel radar image data sets (summary), International Symposium on Remote Sensing of the Environment 4th Thematic Conference Remote Sensing in Exploration Geology (ERIM), p128-129.

Francis C.R. (1983), Radar altimeter calibration, Radar Calibration, Proceedings of EARSeL workshop, Austria 6-10 Dec 1982, p.69-79.

Freden S.C. and Gordon F. Jr. (1983), Landsat Satellites. In Colwell R.N. (editor), Manual of Remote Sensing (Second Edition), American Society of Photogrammetry, p.517-570.

Frost V.S. (1984), Probability of error and radiometric resolution for target discrimination in radar images, IEEE Transactions on Geoscience and Remote Sensing, Vol.22(2), p.121-126.

Frost V.S., Shanmugan K.S. and Holtzman J.C. (1984), The influence of sensor and flight parameters on texture in radar images, IEEE Transactions on Geoscience and Remote Sensing, Vol.22(5), p.440-449.

Fung A.K. (1967), Theory of cross-polarized power returned from a random surface, Applied Science Research, Vol.18, p.50-60.

Fung A.K. (1981), A review of surface scatter theories for modelling applications, Coherent and incoherent radar scattering from rough surfaces and vegetated areas, Proceedings of ESA-EARSel Workshop in Alpbach Austria March 1981, ESA SP-166, p.71-82.

Fung A.K. and Eom H.J. (1981), A theory of wave scattering from an inhomogeneous layer with an irregular interface, IEEE Transactions on Geoscience and Remote Sensing, Vol.29(6), p.899-910.

Fung A.K. and Eom H.J. (1983), Effects of a rough boundary surface on polarization of the scattered field from an inhomogeneous medium, IEEE Transactions on Geoscience and Remote Sensing, Vol.21(3), p.265-71.

Fung A.K. and Eom H.J. (1985), A comparison between active and passive sensing of soil moisture from vegetated terrains, IEEE Transactions on Geoscience and Remote Sensing, Vol.25(5), p.768-775.

Fung A.K. and Ulaby F.T. (1978), A scatter model for leafy vegetation, IEEE Transactions on Geoscience Electronics, Vol.16(4), p.281-6.

Fung A.K. and Ulaby F.T. (1983), Matter-energy interaction in the microwave region. In Colwell R.N. (editor), Manual of Remote Sensing (Second Edition), American Society of Photogrammetry, p.115-164

Gelnett R.H. (1978), Importance of look direction and depression angles in geologic applications of SLAR, Motorola MARS Technical Report TR-04823, Phoenix, Arizona, 15pp.

George P. and Guignard J.P. (1987), ERS-1 synthetic aperture radar fast delivery processor, IEEE Transactions on Geoscience and Remote Sensing, Vol.25(6), p.770-774.

Glennie K.W. (1970) Desert sedimentary environments, Developments in sedimentology, 14 Elsevier, Amsterdam, 222pp.

Goldfinger A.D., Beal R.C., Irvine D.E., Monaldo F.M. and Tilly D.G. (1983), SAR calibration: a users viewpoint, Radar Calibration Proceedings of EARSel Workshop, Austria 5-10 Dec 1982, p.95-99.

Gonzalez F.I., Beal R.C., Brown W.E., Deleonibus P.S., Sherman J.W. III, Gower J.F.R., Lichy D., Ross D.R., Rufenach C.L. and Shuchman R.A., (1979), Seasat synthetic aperture radar: ocean wave detection capabilities, Science, Vol.204, p.1418-1421.

Goudie A. S. (1973) Duricrusts in Tropical and sub-tropical landscapes. Clarenden Press, Oxford, 174pp.

Goudie A.S. (1974), Further experimental investigation of rock weathering by salt and other mechanical processes, Zeitschrift Fur Geomorpologie, Suppl.21, p.1-12.

Goudie A.S. (1985) Duicrusts and landforms, in Richards K.S., Arnett R.R. and Ellis S. (editors) Geomorphology and soils. George Allan and Unwin, London, pp37-57.

Goudie A.S., Cooke R.U. and Evans I. (1970), Experimental investigation of rock weathering, Area, Vol.42, p.8.

Green G.M. (1986), Use of SIR-A and Landsat MSS data in mapping shrub and intershrub vegetation at Koonamore, South Australia, Photogrammetric Engineering and Remote Sensing, Vol.52(5), p.659-70.

Guindon B., Teillet P.M., Goodenough D.G, Palimaka J.J. and Sieber A. (1984) Evaluation of the crop classification performance of X, L and C-band SAR imagery. Canadian Journal of Remote Sensing 10(1) pp4-16.

Hadley R.F. (1967). Pediments and pediment-forming processes. Journal of Geological Education 15 pp83-89.

Hallows R.W. (1947), Radar: radiolocation simply explained. Scientific Book Club, London, 140pp.

Hamza A. (1977). Typologie des érosions à partir d'une détermination à grande échelle des divers compartiments morphopedologique du bassin versant de l'oued el Hadjel (Tunisie Centrale). These 3 cycle,Strasbourge, DRES, Tunis, 3 volumes, 409pp.

Hamza A. (1985), Contribution a l'etude de la morphogenese historique en Tunisie Centrale: le cas du bassin versant de l'Oued el H'jel. Recherches Géographiques à Strasbourg.Numero special 22.23 p55-68.

Hamza A. (1986), Technical note: remote sensing for developing countries. A case study of Tunisia, International Journal of Remote Sensing, Vol.7(2), p.283-6.

Hamza A., Mami A. and Sadowski F. (1982), Land-use mapping from Landsat imagery applied to Central Tunisia, International Symposium on Remote Sensing of the Environment 1st Thematic Conference, Remote Sensing of Arid and Semi Arid Lands, p.1099-112.

Harger R.O. (1970), Synthetic aperture radar systems: theory and design, Academic Press, New York.

Harris P.T., Ashley G.N., Collins M.B. and James A.E. (1986), Topographic features of the Bristol Channel seabed: a comparison of Seasat (synthetic aperture radar) and side-scan radar images, International Journal of Remote Sensing, Vol.7(1), p.119-136.

Harris R., Hobbs A. and Munday T.J. (1984), Study of microwave remote sensing techniques for land surface and hydrological applications, Final Report prepared for the

Natural Environment Research Council under contract F60/GG/08, May 1984, Department of Geography, University of Durham, 447pp.

Hartl P.H. (1983), Radar measurement instruments, Radar Calibration Proceedings of EARSel Workshop, Austria 6-10 Dec 1982 p.25-44.

Hartl P.H., Sieber A., Weiss C.H. and Theilen-Willige B. (1983), Remote sensing correlation study- a comparison of airborne and satellite SAR and multispectral data, ISPRA Report, p.138-220.

Haskell A. (1983a), European Space Agency, ERS-1 program, spaceborne imaging radar symposium Jan 17-20, JPL Publication 83-11, p.140-142.

Haskell A. (1983b), The active microwave instrument (AMI) for ERS-1, Radar Calibration Proceedings of EARSel Workshop, Austria 6-10 Dec 1982, p.133-7.

Haskell A. (1983c), The ERS-1 programme of the European Space Agency, ESA Journal, Vol.7, p.1-13.

Haskell A. and Sorensen B. (1982), The European SAR 580 Project, Digest International Geoscience and Remote Sensing Symposium.

Haydn R., Dalke G.W., Henkel J. and Bare J.E. (1982), Application of the IHS colour transform to the processing of multisensor data and image enhancement, Presented at the International Symposium on Remote Sensing of Arid and Semi-arid lands, Cairo, p.599-616.

Henderson F.M. and Mogilski K.A. (1987), Urban land-use separability as a function of radar polarization, International Journal of Remote Sensing, Vol.8(3), p.441-448.

Hesse P.R. (1971), A textbook of soil chemical analysis, John Murray (Publishers) Ltd., London, 520pp.

Hills R. (1986) What's in the picture? - film digitizers provide the answer. Sensor Review 7(1), pp12-14.

Hobbs A.J. and Shennan I. (1986), Remote sensing of salt marsh reclamation in the Wash, England, Journal of Coastal Research, Vol.2(2), p.181-198.

Hoffer R.M. (1984), Microwave and optical remote sensing of forest vegetation, JPL Publication 84-3, p.4.71-4.73.

Holben B.N. (1980), The topographic effect on spectral response from nadir-pointing sensors, Photogrammetric Engineering and Remote Sensing, Vol.46, p.1191-1200.

Hollis G.E. and Kallel M.R. (1986). Modelling natural and man-induced hydrological changes on Sebket Kelbia, Tunisia. Transactions of the Institute of British Geographers 11, pp86-104.

Horta J.C. de O.S. (1979). Les encroûtements calcaires et les encroûtements gypseaux en géotechnique routière, B.E.T., Laboratoire des Méchaniques des Sols, Memoire Technique no1, 105pp.

Hunting (Geology and Geophysics Ltd.), (1981), Seasat-A: the evaluation of the data content of overland Seasat SAR imagery, Unpublished report prepared for RAE, Farnborough (2 Volumes).

Imhoff M.L., Vermillion C., Story N.H., Choudhury A.H., Gafoor A. and Polcyn F. (1987), Monsoon flood boundary delineation and damage assessment using spaceborne imaging radar and Landsat data, International Journal of Remote Sensing, Vol.3(4), p.405-413.

Jackson P.L. (1980), Multichannel SAR in geologic interpretation: an appraisal, Radar Geology: and assessment, JPL Publication 80-61, p.233-250.

Jackson T.J. and O'Neill P. (1986), Microwave dielectric model for aggregate of soils, IEEE Transactions on Geoscience and Remote Sensing, Vol.24(6), p.920-929.

Jackson T.J. and O'Neill P. (1987), Salinity effects on the microwave emission of soils, IEEE Transactions on Geoscience and Remote Sensing, Vol.25(2), p.214-220.

Jackson T.J., Schmugge T.J. and Wang J.R. (1982), Passive microwave sensing of soil moisture under vegetation canopies, Water Resources Research, Vol.18(4), p.1137-1142.

Jennrich R.I. (1977), Stepwise discriminant analysis. In En Slein K., Ralson A. and Wilf H.S. (editors), Statistical method for digital computers, Vol.III of Mathematical Methods for Digital Computers, p.76-95.

Jensen H., Graham L.C., Purcello L.J. and Leith E.N. (1977), Side looking airborne radar, Scientific American, Vol.237(1), p.84-95.

Jiyuan L, Xuyan T. and Jinkai X. (1986), Application of Shuttle imaging radar data for land-use investigations, Remote Sensing of Environment, Vol.19, p.291-301.

Jones M., Degavre J.C.L. and Guignard J.P. (1983), High throughput digital SAR processing, ESA Journal, Vol.7(2), p.145-162.

Jordan R.L. (1980), The Seasat-A Synthetic Aperture Radar System, IEEE Journal of Oceanic Engineering, Vol.OE-5(2), p.154-163.

Jordan R.L. and Rodgers D.H. (1976??), A Seasat-A synthetic aperture imaging radar system AIAA Paper, Vol.76-966, p.1-10.

Kaupp V.H. (1984), Evaluation of the L-band scattering characteristics of volcanic terrain in aid of lithologic identification. Assessment of SIR-B calibration and development of planetary geomorphic analogs, JPL Publication 84-3, p.4.83-4.85.

Kaupp V.H., Waite W.P. and Macdonald H.C. (1982), Incidence angle considerations for spacecraft imaging radar, IEEE Transactions on Geoscience and Remote Sensing, Vol.20(3), p.384-389.

Kaupp V.H., Bridges L.C., Pisaruck M.A., Macdonald H.C. and Waite W.P. (1983), Simulation of spaceborne stereo radar imagery: environmental results, IEEE Transactions on Geoscience and Remote Sensing, Vol.21(3), p.400-405.

Keydel W. (1982), Application and experimental verification of an empirical backscattering cross section model for the earth's surface, IEEE Transactions on Geoscience and Remote Sensing, Vol.20(1), p.67-71.

Klecka W.R. (1980), Discriminant Analysis, Sage University Applications in the Social Sciences, 71pp.

Kobrick M. (1984), SIR-B cartography and stereo topographic mapping, JPL Publication 84-3, p.4.92-4.94.

Koopmans B.N. (1980), Side-looking radar, a tool for geological surveys. In de Loor G.P. (editor) Remote Sensing Reviews : Radar Remote Sensing. Harwood Academic Publishers, 33pp.

Koopmans B.N. (1982), Some comparative aspects of SLAR and airphoto images for geomorphologic and geologic interpretation, ITC Journal, Vol.1982-3, p.330-337.

Koopmans B.N. (1983), Spaceborne Imaging Radars, present and future, ITC Journal, Vol.1983-3, p.223-231.

Koopmans B.N. (1985), Report on the results in geology and geomorphology of the European SAR-580 experiment, ITC Journal, Vol.1985-3, p.203-206.

Koopmans B.N. (1986), A comparative study of lineament analysis from different remote sensing imagery over areas in the Benue Valley and Jos Plateau, Nigeria, International Journal of Remote Sensing, Vol.7(12), p.1763-1771.

Krinsley D.B. (1976), Selection of alignment through the Great Kavir in Iran. In Williams R.S. and .Carter W.D. (editors), ERTS-1a New Window on our Planet, U.S.G.S. Professional Paper 929, p.296-302.

Krohn M.D., Milton W.M. and Segal D.B. (1983), Seasat synthetic aperture radar (SAR) response to lowland vegetation types in eastern Maryland and Virginia, Journal of Geophysical Research, Vol.8(3), p.1937-1952.

Kuiper H. (1957), A reliefmeter for soil cultivation studies, Netherlands Journal of Agricultural Science.

Labovitz M.L. (1986), Issues arising from sampling designs and band selection in discriminating ground reference attributes using remotely sensed data, Photogrammetric Engineering and Remote Sensing, Vol.52(2), p.201-211.

Lawrance C.J. and Toole T. (1984), The location, selection and use of calcrete for bituminous road construction in Botswana, Transport and Road Research Laboratory Report No.1122, 47pp.

Le Houerou J.C. (1959) Récherches écologiques et floristiques sur la vegetation de la Tunisie méridionale. Inst. Rech. Sah., Univ. Alger. 501pp.

Leader J.C. (1972), Bidirectional scattering of electromagnetic waves from rough surfaces, Presented at the spring meeting of USNC/URSI of the IEEE, April, 1970.

Leader J.C. and Dalton W. (1972), Bidirectional scattering of electromagnetic waves from the volume of dielectric materials, Journal of Applied Physics, Vol.43(?), p.3080.

Leader J.C. (1975), Polarization dependence of E.M. scattering fro Rayleigh Scatterers embedded in a dielectric slab 2. Experiment, Journal of Applied Physics, Vol.46(10), p.4386-4391.

Leberl F. (1978), Current status and perspectives of active microwave imaging for geoscience applications, ITC Journal, p.167-190.

Leberl F., Raggam J. and Kobrick M. (1985), On stereo viewing of SAR images, IEEE Transactions on Geoscience and Remote Sensing, Vol.23(2), p.110-117

Leberl F., Domik G., Raggam J. and Kobrick M. (1986), Radar stereomapping techniques and application to SIR-B images of Mt. Shasta, IEEE Transactions on Geoscience and Remote Sensing, Vol.24(4), p.473-481.

Leberl F., Domik G., Raggam J., Cumino J.P. and Kobrick M. (1986), Multiple incidence angle SIR-B experiment over Argentina: stereo-radargrammetric analysis, IEEE Transactions on Geoscience and Remote Sensing, Vol.24(4), p.482-491.

Leonardo E.S. (1983), Stereo models from synthetic aperture radar. In Hopkins P.F. (editor), Extraction of information from Remotely Sensed Images, Proceedings of Conference, American Society of Photogrammetry, Society of Photographic Scientists and Engineers, p.105-114.

Levine D.M. (1982), Comparison of σo obtained from the conventional definition with σo appearing in the radar equation for randomly rough surfaces, IEEE Transactions on Geoscience and Remote Sensing, Vol.20(1), p.85-90.

Lewis A.J. (1971), Geomorphic Evaluation of Radar Imagery of Southern Panama and North Western Columbia, Unpublished PhD Thesis, Department of Geography, University of Kansas, 178pp.

Lewis A.J. and Waite W.P. (1973), Radar shadow frequency, Photogrammetric Engineering, Vol.39(2), p.189-196.

Li F., Croft C. and Held D.N. (1983), Comparison of several techniques to obtain multiple look SAR imagery, IEEE Transactions on Geoscience and Remote Sensing, Vol.21(3), p.370-375.

Li F., Held D.N., Curlander J.C. and Wu C. (1985), Doppler parameter estimation for spaceborne synthetic-aperture radars, IEEE Transactions on Geoscience and Remote Sensing, Vol.23(1), p.47-56.

Lipes R.G., Bernstein R.L., Cardone V.J., Njoku E.G., Riley A.L., Ross D.B., Swift C.T. and Wentz F.J. (1979), Seasat scanning multichannel microwave radiometer: results of the Gulf of Alaska Workshop, Science, Vol.204, p.1415-1417.

Lo C.P. (1984), Chinese settlement pattern analysis using Shuttle Imaging Radar- a data, International Journal of Remote Sensing, Vol.5(6), p.959-967.

Long M.W. (1983), Radar Reflectivity of Land and Sea, Artech House Inc, Dedham, 385pp.

Longoria J.F. (1985), Spaceborne radar imagery in regional geologic mapping of the Sierra Madre Oriental, Northwestern Mexico (Summary), International Symposium on Remote Sensing of the Environment 4th Thematic Conference Remote Sensing in Exploration Geology (ERIM), p.75.

Lowman P.D., Harris J., Masouka P.M., Singhroy V.H. and Slaney V.R. (1987), Shuttle Imaging Radar (SIR-B) investigations of the Canadian Shield: initial report, IEEE Transactions on Geoscience and Remote Sensing, Vol.25(1), p.55-66.

Lynne G.J. and Taylor G.R. (1986), Geological assessment of SIR-B imagery of the Amadeus Basin, N.T. Australia, IEEE Transactions on Geoscience and Remote Sensing, Vol.24(4), p.575-581.

Macdonald H. (1969), Geologic evaluation of radar imagery from Darien Province, Panama, Modern Geology, Vol.1, p.1-63.

Macdonald H. (1980a), Historical sketch-radar geology, Radar Geology: An Assessment, JPL Publication 80-61, p.23-33.

Macdonald H. (1980b), Techniques and applications of imaging radars. In Siegal B.S. and Gillespie A.R. (editors), Remote Sensing In Geology, John Wiley and Sons, New York, p.297-336.

Macdonald H. and Waite W.P. (1971a), Optimum radar depression angles for geological analysis, Modern Geology, Vol.2, p.179-193.

Macdonald H. and Waite W.P. (1971b), Soil moisture detection with imaging radars, Water Resources Research, Vol.7(1), p.100-110.

Macdonald H. and Waite W.P. (1973), Imaging radars provide terrain texture and roughness parameters in semi-arid environments, Modern Geology, Vol.4, p.145-158.

Macdonald H. and Wing R.S. (1972), Petroleum exploration with radar- Eastern Panama and North-western Columbia, 57th Annual Meeting AAPG, Denver, April 1972

Mackenzie J.S. and Ringrose P.S. (1986), Use of Seasat SAR imagery for geological mapping in a volcanic terrain: Askja Caldera, Iceland, International Journal of Remote Sensing, Vol.7(2), p.181-194.

Malin M.C., Evans D. and Elachi C. (1978), Imaging radar observations of Askja Caldera, Iceland, Geophysical Research Letters, Vol.5(11), p.931-934.

Martin-Kaye P.H.A. and Lawrence G.M. (1983a), The application of satellite imaging radars over land to the assessment, mapping and monitoring of resources, Philosophical Transactions of the Royal Society London, Series A,(309), p.295-314.

Martin-Kaye P.H.A. and Lawrence G.M. (1983b), SIR-A aids regional geology: comparisons of SIR-A imagery with SLAR and Landsat over Guyana, Venezuela, Nicaragua and Mali, Spaceborne Imaging Radar Symposium, Jan 17-20 JPL Pasadena, JPL Publication 83-11, p.56-72.

Martin-Kaye P.H.A., Mcdonough M. and Deane G.C. (1983), Seasat over land. In Allen T.D. (editor), Satellite Microwave Remote Sensing, Ellis Horwood Ltd, Chichester.

Matthews R.G. (editor), (1975), Active Microwave Workshop Report. NASA SP376 NASA/JSC, 502pp.

Mehta N.C. (1984), Separability of agricultural crops with airborne multiparameter radars, IEEE Transactions on Geoscience and Remote Sensing, Vol.22(6), p.540-545.

Mo T., Schmugge T.J. and Jackson T.J. (1984), Calculations of radar backscattering of vegetation-covered soils, Remote Sensing of Environment, Vol.15, p.119-133.

Moore R.K. (1983), Imaging radar systems. In Colwell R.N. (editor) Manual of Remote Sensing (second edition), p.429-474.

Moore J. McM. and Camm S. (1982), Interactive enhancement of Landsat imagery for structural mapping in Tin-Tungsten prospecting: a case history of the S.W. England orefield (U.K.), Paper Presented at the International Symposium of Remote Sensing of Environment, Second Thematic Conference, Remote Sensing for Exploration Geology, Fort Worth, Texas, p.727-740.

Morgan K.M., Lee G.B., Kiefer R.W., Daniel T.C., Bubenzer G.D. and Murdock J.T. (1978), Prediction of soil loss on cropland with remote sensing, Journal of Soil and Water Conservation, Vol.33(6), p.291-293.

Morrissey L.A., Weinstock K.J., Mouat D.A. and Card D.H. (1984), Statistical analysis of TM simulated data for the geobotanical discrimination of rock types in South-west Oregon, IEEE Transactions on Geoscience and Remote Sensing, Vol.22(6), p.525-530.

Motts W.S. (1965) Hydrologic types of playas and closed valleys and some relations of hydrology to playa geology. in Neal J.T. (Editor) Geology, mineralogy and hydrology of U.S. playas. Air Force Cambridge research Laboratories, Environmental Research Paper 96, pp73-104.

Myers V.I. (1983), Remote sensing applications in agriculture. In Colwell (editor), Manual of Remote Sensing (Second Edition), American Society of Photogrammetry, p.2111-2228.

McCauley J.R. (1972), Surface configuration as an explanation for lithology-related cross-polarized radar image anomalies, Fourth Annual Earth Resources Program Review NASA/JSC, Vol.2, p.36.1-36.6

McCauley J.F., Breed C.S., Schaber G.G., McHugh W.P., Issawi B., Haynes C.V., Grolier M.J. and Elkilani A. (1986), Palaeodrainages of the Eastern Sahara- the radar rivers revisited (SIR-A/B IMplications for a Mid-Tertiary Trans african Drainage System), IEEE Transactions on Geoscience and Remote Sensing, Vol.24(4), p.624-648.

McCauley J.F., Schaber G.G., Breed C.S., Grolier M.J., Haynes C.V., Issawi B., Elachi C. and Blom R. (1982), Subsurface valleys and geoarcheology of the eastern Sahara by Shuttle radar, Science, Vol.218, p.1004-1019.

McClain E.P. and Marks R.A. (1979), Seasat visible and infrared radiometer, Science, Vol.204, p.1421-1424.

McCoy R.M. and Lewis A.J. (1976), Use of radar in hydrology and geomorphology. In Lewis A.J. (editor), Geoscience Application of Imaging Radar Systems, RSEMS, V#3, p.105-121.

McDonough M. and Deane G. (1979), Preliminary Results of an evaluation of the land-use and geologic data content of Seasat imagery, Huntings, p.9-18.

McGinn A. and Sykes J. (1980), Microwave scattering from natural targets. UK Atomic Energy Authority, Harwell, AERE Report, 9768.

Merifield P.M. and Yang W.W. (1985), Landsat Thematic Mapper and Seasat SAR data for mapping desert alluvial deposits (summary), International Symposium on Remote

Sensing of the Environment 4th Thematic Conference Remote Sensing in Exploration Geology (ERIM), p94.

Nagy G., Shelton G. and Toloba J. (1971), Procedural questions in signature analysis, Proceedings 7th International Symposium on Remote Sensing of the Environment, Ann Arbor, Michigan, p.1387-1401.

NASA-JPL (1982) The SIR-B Science Plan. Imaging Radar Science Working Group, December 1982, NASA-JPL Publication 82-78.

NASA-JPL (1983a), Shuttle Imaging Radar-C (SIR-C Executive Summary, JPL Publication 83-47.

NASA-JPL (1983b), Spaceborne Imaging Radar Symposium, Jan 17-20, 1983, NASA-JPL Publication 83-11, 159pp.

NASA-JPL (1984), The SIR-B Science Investigations Plan, SIR-B Science Team, JPL Publication 84-3.

NASA-JPL (1986), Shuttle imaging radar-C Science Plan, NASA-JPL Publication 86-29.

NASA (1982), Landsat data users notes, Issue No. 23, U.S. Geological Survey.

Newton R.W. and Rouse J.W. Jr. (1980), Microwave radiometer measurements of soil moisture content, IEEE Trans Ant. Prop, Vol.AP-28, p.680-686.

Nithack J. (1982), Visual evaluation of SLAR imagery, European Space Agency Technical Translation ESA-TT-734 of "Visuelle Auswertung von E-SLAR-Aufnahmen", DFVLR-FB 81-11, 63pp.

Njoku E.G. and O'Neill P.E. (1982), Multifrequency microwave radiometer measurements of soil moisture, IEEE Transactions on Geoscience and Remote Sensing, Vol.20(4), p.468-475.

NOAA (1984), Imaging radar: a companion for Landsat, Landsat Data Users Notes, No.32 Dec 1984, 12pp.

Noack W., Popella A. and Schreier G. (1987), Knowledge-based SAR processing and geocoding: the elementary components of the German processing and archiving facility for high throughput and high precision processing of ERS-1 SAR data, IEEE Transactions on Geoscience and Remote Sensing, Vol.25(6), p.758-769.

Noureddine L.(1979) Remarques sur les croûtes calcaires dans la Beqa a meridionale (Liban), Récherches Géographiques a Strasbourge, no12, pp5-11.

O'Leary D.W., Friedman J.D. and Pohn H.A. (1976), Lineament, linear, lineation: some proposed new standards for old terms, Geological Society of America Bulletin, Vol.87, p.1463-1469.

Olsson L. and Stern M. (1981), Large area data sampling for remote sensing applications and statistical analysis of environment exemplified by an experiment in the Sudan, Lund Universitets Naturgeografiska Institution Repporter Och Notiser 49, 51pp.

Ottl H. and Valdoni F. (1985), The X-SAR Science Plan, DFVLR-Mitteilung, 85-17, 160pp.

Pain C.F. (1985), Mapping of landforms from Landsat imagery: an example from eastern New South Wales, Australia, Remote Sensing of the Environment, Vol.17(1), p.55-65.

Paris J.F. (1984), Development and evaluation of techniques for using combined microwave and optical image data for vegetation studies, JPL Publication 84-3, p.4.113-4.115.

Parr J.T. (1984), Investigation of SIR-B images for lithologic mapping, JPL Publication 84-3, p.4.116-4.117.

Parry D.E. and Trevett J.W. (1979), Mapping Nigeria's vegetation from radar, The Geographical Journal, Vol.145(2), p.265-281.

Patterson F.A. and McAdams P.M. (1980), The use of Landsat data to produce erosion hazard potential maps: NASA National Space Technology Laboratories, 18pp.

Peake W.H. and Oliver T.L. (1971), The response of terrestrial surfaces at microwave frequencies, Ohio State University Technical Report, Columbus, Ohio, p.2440-2447

Podwysocki M.H., Power M.S. and Koslow M.H. (1985), Use of multifrequency radar images for botanical and lithological mapping in an arid terrain, International Symposium on Remote Sensing of the Environment 4th Thematic Conference Remote Sensing in Exploration Geology (ERIM), p98-9.

Pravdo S.H., Huneycutt B., Holt B.M. and Held D.N. (1983), Seasat synthetic aperture radar data users manual, JPL Publication 82-90.

Raney R.K. (1980) SAR processing of partially coherent phenomena. International Journal of Remote Sensing 1(1), pp29-51.

Rapp A. and Hellden U. (1979) Research on environmental monitoring methods for land-use planning in African drylands. Lunds Universitets Naturgeografiska Institution, Rapporter och Notiser 42, 124pp.

Rayleigh Lord (1884), The theory of Sound, New York: Dover (1945).

Rebillard P. (1980), L-band radar and geology: some results in south-east of France remote sensing and mineral exploration. In Carter W.D. (editor), Proceedings of workshop 22nd Plenary Meeting of COSPAR Bangalore India, Pergamon Press. p.169-172.

Rebillard P. (1982), Seasat/SIR-A digital registration over north-eastern Algeria. In Cimino J.B. and Elachi C. (editors), Shuttle Imaging Radar-A (SIR-A) Experiment, JPL Publication 82-77, p.4.35-4.43.

Rebillard P. (1984), An example of multidate and multispectral spaceborne data registration applied to Tunisia SEP:5 Information No 10, p.8-9.

Rebillard P. and Nguyen T.P. (1982), An exploration of coregistered SIR-A, Seasat and Landsat images, Paper presented at International Symposium on Remote Sensing of Environment, 2nd Thematic Conference, Remote Sensing for Exploration Geology, Fort Worth, Texas, Dec 6-10.

Rebillard P. and Evans D. (1983), Analysis of coregistered Landsat, Seasat and SIR-A images of varied terrain types, Geophysical Research Letters, Vol.10(4), p.277-280.

Rebillard P., Pascaud P.N. and Sarrat D. (1984), Merging Landsat and spaceborne radar data over Tunisia, Paper presented at 25th COSPAR at Graz 27 June-7th July.

République Tunisienne (1976) Planification des actions antiérosive a mettre en oeuvre dans le bassin versant de l'oued el Hadjel, Project FAO-SIDI TF/TUN 5 and 13 SWE, Ministère de l'Agriculture, Direction des Forêts, 98pp.

République Tunisienne (1984) Rapport annuel d'activite 1983. Ministère de L'Agriculture, Office de mise en valeur de Nebhana, Sousse, 287pp.

Rice S.O. (1950), Reflection of electromagnetic waves from slightly rough surfaces, Symposium on the theory of electromagnetic waves.

Richards J.A. (1984), Australian multiexperimental assessment of SIR-B (AMAS), JPL Publication 84-3, p4.121-4.123

Richards J.A., Woodgate P.W. and Skidmore A.K. (1987a), An exploration of enhanced radar backscatter from flooded forests, International Journal of Remote Sensing, Vol.8(7), p.1093-1100.

Richards J.A., Sun Guo-Qing, Simonett D.S. (1987b), L-Band radar backscatter modelling of forest stands, IEEE Transactions on Geoscience and Remote Sensing, Vol.25(4), p.487-498.

Robinson N. (1966), Solar Radiation, Elsevier Publishing Co., New York, 347pp.

Rosenthal W.D., Blanchard B.J. and Blanchard A.J. (1985), Visible/infrared/microwave agriculture classification, biomass and plant height algorithms, IEEE Transactions on Geoscience and Remote Sensing, Vol.23(2), p.84-90.

Rott H. (1983), SAR data analysis for an Alpine test site, Proceedings of the SAR-580 investigations workshop, Joint Research Centre, Ispra, Italy, p.1-14.

Rott H. (1984a), Synthetic aperture radar capabilities for snow and glacier monitoring, Advances in Space Research, Vol.4(110), p.241-246.

Rott H. (1984b), The analysis of backscattering properties from SAR data of mountain regions, IEEE of Oceanic Engineering, Vol.OE-9(5), p.347-355.

Sabins F.F. Jr. (1978), Remote Sensing: Principles and Interpretations, San Francisco, W.H. Freeman and Co., 426pp.

Sabins F.F. Jr. (1983a), Geological interpretation of Space Shuttle radar images of Indonesia, Annals of the Association of Petroleum Geologists Bulletin, Vol.67(11), p.2075-2099.

Sabins F.F. Jr. (1983b), Geologic application of spaceborne radars, Spaceborne Imaging Radar Symposium, Jan 17-20 '83, JPL Publication 83-11, p.5-9.

Sabins F.F. Jr., Blom R. and Elachi C. (1980), Seasat radar image of San Andreas Fault, California, Annals of the Association of Petroleum Geologists Bulletin, Vol.64(5), p.619-628.

Schaber G.G. (1984), Application and calibration of the subsurface mapping of SIR-B in desert regions, JPL Publication 84-3, p.4.125-4.129.

Schaber G.G. and Berlin G.L. (1981), Terrain analysis procedures for modelling radar backscatter, Radar Geology: An Assessment, JPL Publication 81-60, p.168-199.

Schaber G.G., Berlin G.L. and Brown W.E. (1976), Variation in surface roughness within Death Valley, California - geologic evaluation of 25cm wavelength radar images, Geological Society of America Bulletin, Vol.84, p.29-41

Schaber G.G., Pike R.J. and Berlin G.L. (1980), Terrain analysis procedures for modelling radar backscatter, Radar Geology; An Assessment, JPL Publication 80-81, p.168-199.

Schaber G.G., McCauley J.F., Breed C.S. and Olhoeft G.R. (1986), Shuttle Imaging Radar: physical controls on signal penetration and subsurface scattering in the Eastern Sahara, IEEE Transactions on Geoscience and Remote Sensing, Vol.24(4), p.603-623.

Schanda E. (1986), Physical Fundamentals of Remote Sensing, Springer-Verlag, Berlin, 187pp.

Schanda E. (1987), On the contribution of volume scattering to the microwave backscattered signal from wet snow and wet soil, International Journal of Remote Sensing, Vol.8(10), p.1489-1500.

Schmugge T. (1980a), Soil moisture sensing with microwave techniques, NASA GLAS-Lab for Atmospheric Sciences, p.487-505.

Schmugge T.J. (1983), remote sensing of soil moisture: recent advances, ITC Journal, Vol.21, p.336-344.

Schmugge T.J. and Choudhury B.J. (1981), A comparison of radiative transfer models for predicting the microwave emission from soils, Radio Science, Vol.16(5), p.927-938.

Schmugge T.J., Jackson T.J. and McKim H.L. (1979), Survey of in situ and remote sensing methods for soil moisture determination. In Deutsch M., Wiesnet D.R. and Rango A. (editors), Satellite Hydrology 5th Annual William T. Pecora Memorial Symposium, American Water Resources Association, p.333-352.

Sieber A.J. (1983), Calibration needs and problems, Radar Calibration Proceedings of EARSeL Workshop Austria 6-10 Dec 1982 ESA SP-193, p.5-10.

Sieber A.J. (1984), German radar observation satellite experiment (ROSE), JPL Publication 84-3, 4.130-4.131.

Sieber A. and Noack (1986), Results of an airborne synthetic-aperture radar (SAR) experiment over a SIR-B (Shuttle Imaging Radar) test site in Germany, ESA Journal, Vol.10(3), p.291-310.

Sieber A.J. and Trevett J.W. (1983), Comparison of multifrequency band radars for crop classification, IEEE Transactions on Geoscience and Remote Sensing, Vol.21(3), p.285-294.

Simonett D.S. and Davis R.E. (1983), Image analysis-active microwave. In Colwell R.N. (editor), Manual of Remote Sensing (2nd Edition, American Society of Photogrammetry. p.1125-1187.

Simonett D.S., Strahler A.H., Sun G. and Wang Y. (1987), Radar forest modelling: potentials, problems, approaches, models, Advances in Digital Image Processing, Proceedings of the annual conference of the remote sensing society, Nottingham, p.256-270.

Simons J.H. and Beccasio A.D. (1964), An evaluation of geoscience applications of side-looking airborne mapping radar, autometric facility, Raytheon Co, 70pp.

Smedes H.W., Linnerud H.L., Laver L.B., Su M.Y. and Jayroe R.R. (1972), Mapping terrain by computer clustering techniques using multispectral scanner data and using colour aerial film, 4th NASA Earth Resources Program Review, Vol.3, p.61.1-61.30.

Smith B.J. and Whalley W.B. (1982) Observations on the composition and mineralogy of an Algerian Duricrust Complex. Geoderma 28, pp285-311.

Smith J.A., Lin T.L. and Ransom K.J. (1980), The Lambertian assumption and Landsat data, Photogrammetric Engineering and Remote Sensing, Vol.46, p.1183-1189.

Sood R.K., Mehta N.S., Dhate V.D. and Sharma S.B. (1985), Geological studies at microwave frequencies-a case study in central India (Summary), International Symposium on Remote Sensing of the Environment 4th Thematic Conference Remote Sensing in Exploration Geology (ERIM), p76.

Stewart H.E., Blom R., Abrams M. and Daily M. (1980), Rock type discrimination and structural analysis with Landsat and Seasat data, Radar Geology: An Assessment, JPL Publication 80-61, p.151-167.

Stiles J.A., Frost V.S., Holtzman J.C. and Shanmugan K.S. (1982), The recognition of extended targets: SAR images for level and hilly terrain, IEEE Transactions on Geoscience and Remote Sensing, Vol.20(2), p.205-211.

Stone R.J. (1985), Remote Sensing of Semi-Arid Terrain: A case study of Central Tunisia, University of Durham, Department of Geography Graduate Discussion Paper, 33pp.

Stone R.J. (1986), Radar system and ground parameters- an interactive case study of semi-arid terrain in Tunisia, Mapping from Modern Imagery- Acquisition and Revision of spatial information, International Archives of Photogrammetry and Remote Sensing, Vol.26(4), p.261-270.

Stone R.J. and Alam M.S. (1987), Satellite remote sensing and the USLE model, Advances in digital image processing, Proceedings of the Annual Conference In Remote Sensing Society. Nottingham, 1987, p.602-610.

Stone R.J. and McBean C.W. (1987), Radar discrimination of sebkha environments: a comparison of SIR-A backscatter from Tunisia and Oman, Advances in digital image processing, Proceedings of the Annual Conference In Remote Sensing Society. Nottingham, 1987, p.611-617

Stone R.J. and McBean C.W. (1988), SIR-A sebkha response: the story so far, Proceedings of the Postgraduate Workshop on applications of remote sensing Durham, Remote Sensing Monograph No.2, p.48-55.

Stroosnijder L., Lascano R.J., Van Bavel C.H.M. and Newton R.W. (1986), Relation between L-band soil emittance and soil water contact, Remote Sensing of the Environment, Vol.19, p.117-125.

Taket N.D., Hall T.J. and Burge R.E. (1988), SAR imaging of volume scatterers, IEEE Transactions on Geoscience and Remote Sensing, Vol.26(2), p.133-139.

Taranik J.V. (1984), Analysis of SIR-B illumination geometry for depth penetration and surface feature and vegetation detection, Nevada and California, JPL Publication 84-3, p.4.140-4.142.

Theilen-Willige B. (1984), The use of spaceborne radar images (Shuttle Imaging Radar) from arid and semi-arid environments for mapping soil erosion features and drainage systems, Paper presented at World Conference on Remote Sensing, 8-10 October 1984 at Bayreuth F.R.G.

Theilen-Willige B. (1985), The use of spaceborne radar images for agricultural resources survey, a comparative

Ulaby F.T. and El Rayes M.A. (1987), Microwave dielectric spectrum of vegetation. Part 1: Experimental Observation. Part 2: Dual Dispersion Model, IEEE Transactions on Geoscience and Remote Sensing, Vol.25(5), p.541-557.

Ulaby F.T., Batlivala P.P. and Dobson M.C. (1978), Microwave backscatter dependent on surface roughness, soil moisture and soil texture, part 1: Bare Soil, IEEE Transactions on Geoscience and Electronics, Vol.16, p.286-295.

Ulaby F.T., Moore R.K. and Fung A.K. (1981), Microwave remote sensing: active and passive, Volume I: Microwave remote sensing fundamentals and radiometry, Addison-Wesley Publishing Co, Reading, Mass.

Ulaby F.T., Moore R.K. and Fung A.K. (1982a), Microwave remote sensing active and passive, Volume II: radar remote sensing and surface scattering and emission theory, Addison-Wesley Publishing Co., Reading, Mass., p.457-1064.

Ulaby F.T., Kouyate F., Fung A.K. and Sieber A.J. (1982b), A backscatter model for a randomly perturbed periodic surface, IEEE Transactions on Geoscience and Remote Sensing, Vol.20(4), p.518-528.

Ulaby F.T., Aslam A. and Dobson M.C. (1982c), Effects of vegetation cover on the radar sensitivity to soil moisture, IEEE Transactions on Geoscience and Remote Sensing, Vol.20(4), p.476-481.

Ulaby F.T., Li R.Y. and Shanmugan K.S. (1982d), Crop classification using airborne radar and Landsat data, IEEE Transactions on Geoscience and Remote Sensing, Vol.20(1), p.42-50.

Ulaby F.T., Razani M. and Dobson M.C. (1983), Effects of vegetation cover on the microwave radiometric sensitivity to soil moisture, IEEE Transactions on Geoscience and Remote Sensing, Vol.21(1), p.51-61.

Ulaby F.T., Held D., Dobson M.C., Macdonald K.C. and Senior T.B.A. (1987), Relating polarization phase differences of SAR signals to scene properties, IEEE Transactions on Geoscience and Remote Sensing, Vol.25(1), p.83-92.

Valenzuela G.R. (1968), Scattering of electromagnetic waves from a tilted slightly rough surface, Radio Science, Vol.3(11),(new series).

Vincent R.K. (1980), The use of radar and Landsat data for mineral and petroleum exploration on the Los Andes Region,

Venezuela, Radar Geology: An Assessment, JPL Publication 80-61, p.367-384.

Wadge G. and Dixon T.H. (1984), A geological interpretation of Seasat-SAR imagery of Jamaica, Journal of Geology, Vol.92, p.561-581.

Wang J.R. (1984), Remote sensing of soil moisture, JPL Publication 84-3, p.4.154-4.157.

Wang J.R. and Schmugge T.J. (1980), An empirical model for the complex dielectric permittivity of soils as a function of water content, IEEE Transactions on Geoscience and Remote Sensing, Vol.18(4), p.283-295.

Wang J.R., O'Neill P.E., Jackson T.J. and Engman E.T. (1983), Multifrequency measurements of the effects of soil moisture, soil texture and surface roughness, IEEE Transactions on Geoscience and Remote Sensing, Vol.21, p.44-51.

Wang J.R., Engman E.T., Shiue J.C., Rusek M. and Steinmeier C. (1985), The SIR-B observations of microwave backscatter dependence on soil moisture, surface roughness and vegetation covers, IEEE Transactions on Geoscience and Remote Sensing, Vol.24(4), p.510-516.

Watson A. (1979) Gypsum crusts in deserts, Journal of Arid Environments, 2, pp20-22.

Weigand C.L. (1984), The volume of direct observations of crop canopies for indicating growing conditions and yield, 18th International Symposium on Remote Sensing of the Environment, 10pp.

Weismiller R.A. and Kaminsky S.A. (1978), Application of remote sensing technology to soil survey research, Journal of Soil and Water Conservation, Vol.33(6), p.287-289

White F. (1983), The vegetation of Africa, Descriptive memoirs to accompany UNESCO AETFET/UNSO vegetation map of Africa. 356pp.

White K. (1987). Piedmont surface mapping in the Tunisian Southern Atlas: use of Landsat Thematic Mapper Data. In Advances in Digital Image Processing, Proceedings of the annual conference of the Remote Sensing Society, Nottingham, pp641-649.

Wischmeier W.H. and Smith D.D. (1965), Predicting rainfall-erosion losses from cropland east of the Rock Mountains, Agricultural Handbook No.282, U.S. Department of Agriculture, Washington D.C.

Wischmeier W.H. and Smith D.D. (1978), Predicting rainfall erosion losses, USDA Agricultural Research Service Handbook No. 537, Washington D.C.

Wilhelmi G.J., Rouse J.W. Jr. and Blanchard A.J. (1975), Depolarization of light backscattered from rough dielectrics, Journal of the Optical Society of America, Vol.65(9).?

Wing R.S. (1970), Structural analysis from radar imagery, Eastern Panama Isthmus, Technical Report No. 133-15, CRES, University Kansas.

Wing R.S. and Dellwig L.F. (1970), Tectonic development of the eastern Panamanian Isthmus as revealed through analysis of radar imagery, Paper presented at the annual meeting of the Geological Society of America, 1970.

Woldai T. (1983a), Landsat and SIR-A interpretation of the Kaplin Chol and Chong Korum Mountains of China, ITC Journal, Vol.1983(3), p.250-252.

Woldai T. (1983b), Lop-Nur (China) studied from Landsat and SIR-A imagery, ITC Journal, Vol.1983(3), p.253-257.

Wu C., Barkan B., Huneycutt B., Leang C. and Pang S. (1981), An introduction to the interim Digitar SAR Processor and the characteristics of the associated Seasat SAR imagery, JPL Publication 81-26, 82pp.

Wu C., Barkan B., Karplus W.J. and Caswell D. (1982), Seasat SAR data reduction using parallel programmable array processors, IEEE Transactions on Geoscience and Remote Sensing, Vol.20(3), p.352-357.

Wu L-K., Moore R.K. and Zoughi R. (1985), Sources of scattering from vegetation canopies at 10GHZ, IEEE Transactions on Geoscience and Remote Sensing, Vol.23(5), p.737-745.

Wu S-T. and Sader S.A. (1987), Multipolarization of SAR data for surface feature delineation and forest vegetation characterisation, IEEE Transactions on Geoscience and Remote Sensing, Vol.25(1), p.67-76.

Xuyan T., Changqing S., Xian P.H., Zhaosheng L. and Bolin Y. (1984), Pressure microwave radiometry in the Gobi desert region, Remote Sensing of the Environment, Vol.15, p.37-46.

Yamaguchi Y. (1985), Image-scale and look-direction effects on the detectability of lineaments in radar

images, Remote Sensing of the Environment, Vol.17(2), p.117-128.

Yao S.S. and Gilbert J.R. (1984), Registration of a synthetic aperture radar image to Thematic Mapper imagery for remote sensing applications, IEEE Transactions on Geoscience and Remote Sensing, Vol.26(6), p.557-563.